

**Engineering Zeolite Catalysts with Improved Performance for Aromatics  
Production**

by  
Yunwen Zhou

A dissertation submitted to the Department of Chemical and Biomolecular  
Engineering

Cullen College of Engineering

in partial fulfillment of the requirements for the degree of

Doctor of Philosophy

in Chemical Engineering

Chair of Committee: Dr. Jeffrey D. Rimer

Committee Member: Dr. Lars C. Grabow

Committee Member: Dr. Michael P. Harold

Committee Member: Dr. Yan Yao

Committee Member: Dr. Travis Conant

University of Houston

May 2020

Copyright 2020, Yunwen Zhou

## ACKNOWLEDGMENTS

I am very grateful for my Ph.D. advisor, Dr. Jeffrey Rimer, for all his support and guidance throughout my study at the University of Houston. My research would have been impossible without his help and mentorship. I would like to thank my committee members for evaluating my work, Dr. Michael Harold, Dr. Lars Grabow, Dr. Yan Yao, and Dr. Travis Conant. I would also like to acknowledge my collaborators for their contributions to our work.

I was lucky to have the opportunity to work in a wonderful research group at the University of Houston. I would like to express special thanks to our catalysis subgroup, Dr. Ming-Feng Hsieh, Dr. Yufeng Shen, Dr. Wei Qin, Dr. Seung Hyeok Cha, Thuy T. Le, Heng Dai, Xiaohui Zhao, and Deependra Parmar for their inspiring discussions about research. I will always remember the time we spent on building reactors and troubleshooting equipment.

Finally, I would like to thank my parents for everything you have done for me. Without you, I would not be the person I am today. I love you more than anything.

## ABSTRACT

Zeolites are shape-selective microporous crystals that are widely used in refining and (petro)chemical processes owing to their unique porous topologies, high thermal stability, and tunable acidity. This dissertation aims to improve the performance of zeolite catalysts by optimizing some essential design parameters such as framework topology, morphology, and Brønsted and Lewis acidity.

We first investigated the synthesis of 2-dimensional (2D) zeolites due to their superior catalytic properties, particularly in applications involving large (bulky) molecules. We selected a common layered zeolite, MCM-22 (MWW framework), to explore methods of preparing 2D nanosheets via a one-pot synthesis in the absence of complex organic templates. Using a combination of high-resolution microscopy and spectroscopy, we show 2D MWW-type layers with an average thickness of 3.5 nm (ca. 1.5 unit cells) can be generated using the surfactant cetyltrimethylammonium (CTA), which operates as a dual organic structure-directing agent (OSDA) and exfoliating agent to affect Al siting and eliminate the need for post-synthesis delamination, respectively. We tested these 2D catalysts using a model reaction to assess external (surface) Brønsted acid sites and observed a marked increase in the conversion relative to 3-dimensional MCM-22 and 2D layered MWW (ITQ-2) prepared by post-synthesis exfoliation. To this end, our findings highlight a facile, effective route to directly synthesize 2D MWW-type materials, which may prove to be more broadly applicable to other layered zeolites.

Driven by the limited supply of fossil fuels, it is highly desirable to develop high-performance zeolite catalysts with improved selectivity to aromatics, particularly from diversified (non-petroleum) feedstocks. The catalyst ZSM-5 (MFI framework)

was chosen to examine more efficient routes to aromatics given its reported shape-selectivity for  $C_6 - C_8$  products. In this dissertation, we examine ethylene dehydroaromatization (DHA) over metal-exchanged ZSM-5 (both Ag-ZSM-5 and Ga-ZSM-5) and show that extra-framework Lewis acid sites promote DHA reactions with enhanced selectivity to toluene and xylenes. We observe that metal-exchanged ZSM-5 enhances aromatic selectivity approximately 3-fold compared to H-ZSM-5, which tends to produce light olefins and other aliphatic hydrocarbons. Through systematic studies of metal-exchanged ZSM-5 using a combination of experiments and density functional theory (DFT) calculations, we have been able to differentiate the roles of metal species in ethylene activation with enhanced product selectivity to value-added aromatics.

Lastly, we have studied the challenges associated with synthesizing ZSM-5 at low temperature (ca.  $100^\circ\text{C}$ ), which is often necessary to generate small crystals ( $< 200$  nm) with an appreciable quantity of acid sites (i.e.,  $\text{Si}/\text{Al} < 25$ ). We show that synthesis at low temperature, and most notably in growth mixtures containing high aluminum concentration, results in the incomplete incorporation of Al in ZSM-5 that can be partially removed through post-synthesis mild acid treatment. Our findings suggest that ZSM-5 may be more difficult to synthesize than is commonly perceived, most notably when examining the various types of defects (i.e., extra-framework octahedral- and penta-coordinated Al) that can be incorporated in crystalline products over a wide range of synthesis conditions.

## TABLE OF CONTENTS

ACKNOWLEDGMENTS .....	iii
ABSTRACT.....	iv
TABLE OF CONTENTS.....	vi
LIST OF TABLES .....	ix
LIST OF FIGURES .....	x
Chapter 1.....	1
1.1 Zeolite Catalysts: Synthesis Approaches and Nature of Active Sites .....	1
1.2 Two-dimensional Zeolite Catalyst.....	5
1.3 Bifunctional Metal-exchanged Zeolite Catalyst .....	9
1.4 Recent Development in Aromatics Production over Zeolites .....	14
1.5 Dissertation Outline.....	16
Chapter 2.....	18
2.1 Motivation .....	18
2.2 Experimental Methods.....	20
2.2.1 Material .....	20
2.2.2 Synthesis of MWW Materials .....	21
2.2.3 Characterization .....	23
2.2.4 Catalytic Measurements .....	27
2.3 Results and Discussion .....	28
2.3.1 Preparation of Disordered MWW-type Nanosheets.....	28
2.3.2 Putative Role of CTA as an OSDA .....	35
2.3.3 Enhanced surface catalytic activity .....	40
2.4 Summary.....	46
Chapter 3.....	48
3.1 Motivation .....	48
3.2 Experimental Methods.....	50
3.2.1 Zeolite Catalyst Preparation .....	50
3.2.2 Characterization .....	51
3.2.3 Catalytic Measurements .....	51
3.2.4 Density Functional Theory Calculations.....	52
3.3 Results and Discussion .....	53
3.3.1 Preparation of Bifunctional Ag-ZSM-5 Zeolite Catalyst.....	53

3.3.2 Kinetic Study on Ethylene Dehydroaromatization (DHA) Reaction...	56
3.3.3 Effect of Methane Coupling Reaction and DFT Studies.....	59
3.4 Summary.....	65
Chapter 4.....	67
4.1 Motivation .....	67
4.2 Experimental Methods.....	71
4.2.1 Material .....	71
4.2.2 Zeolite Catalyst Preparation .....	71
4.2.3 Characterization .....	73
4.2.4 Catalytic Measurements .....	75
4.2.5 Density Functional Theory Calculations.....	76
4.3 Results and Discussion .....	77
4.3.1 Preparation of Ga-ZSM-5 Zeolite Catalysts.....	77
4.3.2 Ethylene Dehydroaromatization (DHA) Reaction .....	83
4.3.3 Density Function Calculation.....	86
4.4 Summary.....	92
Chapter 5.....	94
5.1 Motivation .....	94
5.2 Experimental Methods.....	96
5.2.1 Materials.....	96
5.2.2 Zeolite Crystallization .....	97
5.2.3 Characterization .....	98
5.2.4 Catalytic Measurements .....	99
5.3 Results and Discussion .....	100
5.3.1 ZSM-5 Synthesis with Varied Sol Gel Si/Al Ratio.....	100
5.3.2 ZSM-5 synthesis at Higher Temperature. ....	108
5.3.3 Methanol to Hydrocarbons Reaction.....	110
5.4 Summary.....	115
Chapter 6.....	118
6.1 Current Research Summary .....	118
6.2 Future Outlook.....	119
6.2.1 Zeolite Structure Performance .....	119
6.2.2 Lewis Acid Sites.....	121

6.2.3 Alternative reactions to tune selectivity towards valuable aromatic..	122
References.....	124
Appendix A Supplementary Information for Chapter 2.....	152
Appendix B Supplementary Information for Chapter 3.....	160
Appendix C Supplementary Information for Chapter 4.....	164
Appendix D Supplementary Information for Chapter 5.....	171

## LIST OF TABLES

<b>Table 1.1.</b> Selected catalytic applications of metal-exchanged zeolite catalysts. ....	10
<b>Table 2.1.</b> Properties of MWW materials produced with and without CTA .....	32
<b>Table 2.2.</b> Relative peak areas of $^{27}\text{Al}$ MAS NMR spectra.....	37
<b>Table 2.3.</b> Summary of Al content and adsorbed probe (TMPO and TBPO) amounts in H-MWW samples .....	43
<b>Table 3.1.</b> Chemical composition and textural properties of MFI zeolites .....	54
<b>Table 3.2.</b> Activation barriers and binding energies (in parenthesis) for the activation of ethylene and methane on H-ZSM-5 and Ag-ZSM-5.....	62
<b>Table 4.1.</b> Elemental analysis of zeolite catalyst samples.....	79
<b>Table 4.2.</b> Best fits of the structural parameters obtained from of Ga K-edge EXAFS. ....	81
<b>Table 5.1.</b> Properties of ZSM-5 samples synthesized from different sol gel Si/Al ratios. ....	102
<b>Table A1.</b> Physicochemical Properties of MWW materials.....	152
<b>Table A2.</b> Elemental composition of as-synthesized MWW materials .....	152
<b>Table A3.</b> Solid-state $^{31}\text{P}$ NMR peaks ( $\pm 2$ ppm) and fraction of adsorbed TMPO and TBPO on MWW zeolites .....	153
<b>Table A4.</b> Catalytic results for the Friedel-Craft alkylation of benzene and benzyl alcohol.....	153
<b>Table B1.</b> Chemical compositions of Ag-ZSM-5 prepared using different $\text{AgNO}_3(\text{aq})$ concentrations.....	163
<b>Table B2.</b> Comparison of aromatic selectivity in the ETL reaction over ZSM-5 catalysts .....	163
<b>Table C1.</b> Chemical compositions of Ga-ZSM-5 prepared using different $\text{Ga}(\text{NO}_3)_3(\text{aq})$ concentrations.....	169
<b>Table C2.</b> Electronic energies from DFT calculations for all considered mechanisms for ethylene activation.....	169
<b>Table C3.</b> Binding energies in eV from DFT calculations .....	170
<b>Table C4.</b> Lewis/Brønsted acid site redistribution energies across all 12 T-site combinations in ZSM-5 .....	170

## LIST OF FIGURES

<b>Figure 1.1.</b> Zeolites with known 2D forms (yellow box with bold frame) and zeolites used industrially or those of commercial interest (red bold 3-letter code) This figure is adapted from previous work. <sup>65</sup> .....	6
<b>Figure 1.2.</b> Selectivity for the formation of methanol with different catalysts as a function of methane converted. This figure is adapted from previous work. <sup>109</sup> .....	11
<b>Figure 1.3.</b> Crude oil to chemical production routes. Crude oil to chemicals production routes. This figure is adapted from previous work. <sup>134</sup> .....	14
<b>Figure 1.4.</b> General mechanism for NOC and DHA where $M^{n+}$ represents a Lewis acid site and $H^+$ is a Brønsted acid site.....	16
<b>Figure 2.1.</b> PXRD patterns of MWW type materials (gel Si/Al: 15) prepared with (i) 0, (ii) 5.5, and (iii) 8 wt% CTA. The top (grey) lines are as-synthesized material, whereas the bottom (black) lines are the calcined (c) materials. ....	29
<b>Figure 2.2.</b> Scanning electron micrographs of calcined MWW type materials: (A and B) MCM-22; (C and D) d-MWW <sub>8.0</sub> . All scale bars are equal to 1 $\mu$ m.....	31
<b>Figure 2.3.</b> HRTEM images of disordered MWW (8 wt% CTA). (A) Bright field image (B-D) Magnified detail of panel A, scale bar of panel D equals 1 nm. (E) A fast Fourier transform (FFT) of a single crystalline portion of panel C.....	33
<b>Figure 2.4.</b> Histograms of layer thickness from HRTEM analysis of (A) MCM-22 and (B – D) d-MWW <sub>x</sub> samples prepared with the following CTA concentrations: (B) 5.5 wt%, (C) 7.5 wt%, and (D) 8.0 wt%.....	35
<b>Figure 2.5.</b> Two-dimensional <sup>27</sup> Al MQ MAS NMR spectra of H-form (A) MCM-22 and (B) d-MWW <sub>7.5</sub> samples (gel Si/Al: 15). Deconvolution of these two samples were performed on one-dimensional <sup>27</sup> Al MAS NMR spectra. ....	36
<b>Figure 2.6.</b> Parametric analysis of d-MWW synthesis at varying gel Si/Al ratios. The total BET surface area measured from N <sub>2</sub> sorption isotherms (Figure A4) is reported (solid symbols) for syntheses at varying CTA concentration.....	39
<b>Figure 2.7.</b> Putative roles of organic (HMI and CTA) and inorganic (Na <sup>+</sup> ) structure-directing agents during the one-pot synthesis of MWW type materials. The illustrations are adapted from schemes reported by Roth et al. <sup>65, 163</sup> .....	40
<b>Figure 2.8.</b> (A) Model reaction used to assess the performance of MWW-type catalysts. (B) Benzyl alcohol (BA) conversion (blue, left axis) and turnover number (yellow, right axis) for the four H-form MWW-type samples. ....	45
<b>Figure 3.1.</b> Powder XRD patterns and XPS spectra of (i) H-ZSM-5, (ii) as-prepared Ag <sub>25</sub> -ZSM-5, and (iii) calcined Ag <sub>25</sub> -ZSM-5 are shown in black, red, and blue, respectively. ....	55
<b>Figure 3.2.</b> (A) Solid-state UV-Vis spectrum of calcined Ag <sub>25</sub> -ZSM-5 (B) Schematic representation of Ag <sup>+</sup> (Lewis acid) and H <sup>+</sup> (Brønsted acid) species associated with framework Al sites in ZSM-5 (MFI type topology). ....	56

<b>Figure 3.3.</b> Effects of space velocity (x-axis) on product selectivity (left y-axis) and ethylene conversion (right y-axis) over (A) Ag-ZSM-5 and (B) H-ZSM-5. Data were acquired after 10 min time on stream. ....	57
<b>Figure 3.4.</b> Effects of Ag/Al ratio (x-axis) on product selectivity (left y-axis) and ethylene conversion (right y-axis) over various ZSM-5 catalysts (Ag <sub>25</sub> -, Ag <sub>15</sub> -, Ag <sub>8</sub> -, and H-ZSM-5) at 400 °C and 1 atm. ....	59
<b>Figure 3.5.</b> Performance of H-ZSM-5 (open squares) and Ag <sub>25</sub> -ZSM-5 (open circles) catalysts. Plots compare (A) methane and (B) ethylene conversion. ....	60
<b>Figure 3.6.</b> Effects of methane addition on the performance of ZSM-5 catalysts at 400 °C and 1 atm. Dashed lines are interpolations for improved visualization. ....	64
<b>Figure 3.7.</b> (A) Proposed mechanism of ethylene activation over an H <sup>+</sup> (Brønsted acid) site in a ZSM-5 pore (B) Generalized pathways of DHA reactions .....	65
<b>Figure 4.1.</b> (A) Normalized Ga K-edge XANES and (B) Magnitudes of k <sup>2</sup> -weighted Fourier-transformed EXAFS spectra for Ga-Z1 (direct synthesis) and Ga-Z2 (solution ion exchange). ....	80
<b>Figure 4.2.</b> <sup>71</sup> Ga MAS NMR spectra of hydrated Ga-ZSM-5 zeolites: (A) direct synthesis (Ga-Z1) and after H <sub>2</sub> treatment (Ga-Z1H); (B) Ga-Z2 (solution ion exchange), Ga-Z2H (Z2 after H <sub>2</sub> treatment), and Ga-Z3 (chemical vapor-phase exchange) .....	83
<b>Figure 4.3.</b> (A) Hydrocarbon product selectivity over various ZSM-5 catalysts. Data were acquired at 10 min time on stream. (B) Ethylene conversion for each catalyst as a function of time-on-stream (TOS). ....	85
<b>Figure 4.4.</b> Comparison of aromatics product selectivity (histogram, left y-axis) and ethylene conversions (square symbols, right y-axis) for six ZSM-5 catalysts. Data were acquired at 10 min time on stream. ....	86
<b>Figure 4.5.</b> (A) Potential energy diagram for ethylene activation and oligomerization at an H <sup>+</sup> site, and 1-butene at an GaH <sub>2</sub> <sup>+</sup> site. (B) Binding energies of unsaturated hydrocarbons at GaH <sub>2</sub> <sup>+</sup> and Ga <sup>+</sup> Lewis acid sites. ....	88
<b>Figure 4.6.</b> Brønsted (H <sup>+</sup> ) and Lewis ([GaH <sub>2</sub> ] <sup>+</sup> ) acid site exchange energies between framework Ga <sub>FW</sub> at T <sub>i</sub> sites and Al <sub>FW</sub> atoms at T <sub>j</sub> sites according to the reaction in Eq. 4-4. ....	91
<b>Figure 5.1.</b> Scanning electron micrographs of the following as-made ZSM-5 samples: (A) Z30, (B) Z50, (C) Z75, and (D) Z100. Scale bars are equal to 500 nm. Scale bars of the insets are equal to 100 nm. ....	103
<b>Figure 5.2.</b> (A) Ratio of surface Al content and bulk Al content as a function of the sol gel Si/Al ratio. (B) ΔSi/Al ratio = Si/Al (after acid treatment) – Si/Al (before acid treatment) as a function of the sol gel Si/Al ratio. ....	105
<b>Figure 5.3.</b> <sup>27</sup> Al MAS NMR spectra for the H-form samples: (i) Z30, (ii) Z50, (iii) Z75, and (iv) Z100. Vertical dashed lines represents: tetrahedral Al (55ppm), penta-coordinated Al (31 ppm), and octahedral Al (0 ppm). ....	106

<b>Figure 5.4.</b> Deconvolution of $^{27}\text{Al}$ MAS NMR spectra showing the curve fittings of (A) H-Z30 (as-made aluminous sample) and (B) H-Z30T (corresponding sample after mild acid treatment). .....	107
<b>Figure 5.5.</b> $^{27}\text{Al}$ MAS NMR spectra of (i) H-Z50, (ii) H-Z50H, and (iii) H-Z50HT. Dashed lines highlight peaks corresponding to FAI (55 ppm), penta-coordinated Al (31 ppm), and EFAI (0 ppm). .....	109
<b>Figure 5.6.</b> Methanol conversion as a function of time-on-stream (TOS) for five H-form ZSM-5 catalysts. Dashed lines are interpolated to guide the eye. ....	111
<b>Figure 5.7.</b> (A) Comparison of product selectivity in MTH reactions at sub-complete methanol conversion (left axis) and ethene-to-2MBu ratio (right axis) for each catalyst. (B) Comparison of the propene-to-ethene ( $C_3=C_2$ ) ratio. ....	114
<b>Scheme 1.1.</b> (A) MWW framework with its network of pores (B) Top down view of an external pocket with unique T sites for Al incorporation, and (C) side view along the a-direction (90 degrees relative to panel B). .....	7
<b>Scheme 1.2.</b> Possible MWW-type zeolite structures obtained via direct and post-synthetic treatment. The scheme is redrawn and adapted from previous work. <sup>65</sup> .....	8
<b>Scheme 1.3.</b> Possible metal-zeolite configuration via different preparation methods. The scheme is modified and adapted from previous literature. <sup>120</sup> .....	13
<b>Scheme 4.1.</b> (A). Possible zeolite Brønsted and Lewis acid sites generated from heteroatom framework (T = Al or Ga) and/or extra-framework species: (A) framework $\text{Ga}^{3+}$ ; (B) $\text{Ga}_2\text{O}_3$ ; (C) $\text{Ga}^+$ ; (D) $[\text{GaO}]^+$ ; (E) $[\text{GaH}_2]^+$ , $[\text{Ga}(\text{OH})_2]^+$ , or $[\text{GaH}(\text{OH})]^+$ ; and (F) $[\text{GaH}]^{2+}$ . .....	70
<b>Figure A1.</b> Powder XRD patterns of as-prepared MWW materials prepared with (i) 4, (ii) 5, (iii) 6, (iv) 7, (v). 8 wt%, (vi). 10wt% CTAB, and (vii). ITQ-2. MWW materials obtained in different gel Si/Al ratio: (A) 15, (B) 30, and (C) 45. ....	154
<b>Figure A2.</b> Example of sample thickness measurement for d-MWW <sub>8.0</sub> using Digital Micrograph. The line profile clearly shows the edge-on oriented MWW nanosheet is approximately 2 unit cells thick (~ 5 nm). .....	154
<b>Figure A3.</b> (A). Two-dimensional $^{27}\text{Al}$ MQMAS NMR spectrum of ITQ-2_15 (B). One-dimensional $^{27}\text{Al}$ MAS NMR spectrum of ITQ-2_15. ....	155
<b>Figure A4.</b> Nitrogen adsorption and desorption isotherms of calcined MWW materials. ....	156
<b>Figure A5.</b> Thermogravimetric analysis (TGA) of as-synthesized MWW materials. ....	157
<b>Figure A6.</b> Deconvolution solid-state $^{31}\text{P}$ NMR spectra of TMPO adsorption on MWW-type zeolites: (A) MCM-22; (B) d-MWW <sub>5.5</sub> ; (C) d-MWW <sub>8.0</sub> ; (D) ITQ-2_15; and (E) ITQ-2_45. ....	157
<b>Figure A7.</b> Deconvolution solid-state $^{31}\text{P}$ NMR spectra of TMPO adsorption on MWW-type zeolites: (A) MCM-22_15; (B) d-MWW <sub>5.5</sub> _15; (C) d-MWW <sub>8.0</sub> _15; (D) ITQ-2_15 and (E) ITQ-2_45. ....	158

<b>Figure A8.</b> (A) Benzyl alcohol conversion as a function of reaction time over MWW-type catalysts. (B) Benzyl alcohol (BA) conversion (left axis) and turnover number (right axis). The results are shown for a single time point (9 h).....	159
<b>Figure A9.</b> Scanning electron micrographs of calcined MWW type materials: (A and B) H-ITQ-2 (gel Si/Al = 15); (C and D) H-ITQ-2 (gel Si/Al = 45), and H-d-MWW <sub>5.5</sub> (gel Si/Al = 15). All scale bars are equal to 2 $\mu\text{m}$ .....	159
<b>Figure B1.</b> Solid-state UV-Vis spectrum of spent Ag <sub>25</sub> -ZSM-5 with an absorbance band at ca. 420 nm assigned to metallic Ag species.....	160
<b>Figure B2.</b> Product selectivity profile obtained in the NOC of methane and ethylene at over Ag <sub>25</sub> -ZSM-5. The space velocity was 2000 ml g <sup>-1</sup> h <sup>-1</sup> for both methane and ethylene. ....	160
<b>Figure B3.</b> Product selectivity profile obtained in the NOC of methane and ethylene at over H-ZSM-5. The space velocity was 2000 ml g <sup>-1</sup> h <sup>-1</sup> for both methane and ethylene. ....	161
<b>Figure B4.</b> Performance of Ag <sub>25</sub> -ZSM-5 catalyst in NOC of methane. The space velocity was 2000 ml g <sup>-1</sup> h <sup>-1</sup> for methane. Dashed lines are interpolations for improved visualization. ....	161
<b>Figure B5.</b> Product selectivity profile obtained in the ETL reaction over Ag <sub>25</sub> -ZSM-5. The space velocity was 2000 ml g <sup>-1</sup> h <sup>-1</sup> for ethylene.....	162
<b>Figure B6.</b> Product selectivity profile obtained in the ETL reaction over H-ZSM-5. The space velocity was 2000 ml g <sup>-1</sup> h <sup>-1</sup> for ethylene.....	162
<b>Figure C1.</b> Powder X-ray diffraction (XRD) patterns of calcined H-form ZSM-5 samples prepared with different methods (Ga-Z1, Ga-Z1H, Ga-Z2, Ga-Z2H, and Ga-Z3) and calcined commercial ZSM-5 (Z-ref).....	164
<b>Figure C2.</b> Powder X-ray diffraction (XRD) patterns of ZSM-5 samples prepared by ion exchange using different Ga(NO <sub>3</sub> ) <sub>3</sub> concentrations: (i) 5 mM; (ii) 10 mM; (iii) 20 mM; (iv) 30 mM; (v) 40 mM; and (vi) 50 mM. Peaks marked with asterisks refer to crystalline Ga <sub>2</sub> O <sub>3</sub> species. <sup>255-256</sup> .....	164
<b>Figure C3.</b> Scanning electron micrographs of the following as-synthesized samples: (A) Ga-Z1 and (B) Ga-Z2. Scale bars equal 1 $\mu\text{m}$ . Insets scale bars equal 500 nm. .	165
<b>Figure C4.</b> Magnitudes of k <sup>2</sup> -weighted Fourier-transformed Ga K-edge EXAFS spectra of the following ZSM-5 samples: (A) Ga-Z1 (direct synthesis) with k range = 2-12 $\text{\AA}^{-1}$ ; and (B) Ga-Z2 (ion exchange) with k-range = 2-13 $\text{\AA}^{-1}$ .....	165
<b>Figure C5.</b> <sup>27</sup> Al MAS NMR spectra of hydrated ZSM-5 materials: (A) Ga-Z1, (B) Ga-Z1H, (C) Ga-Z2, (D) Ga-Z2H, (E) Ga-Z3, (F) Z-ref, and (G) Z1 (obtained via the same approach of Ga-Z1 synthesis without the addition of Ga).....	166
<b>Figure C6.</b> <sup>71</sup> Ga MAS NMR spectra of hydrated ZSM-5 materials: Ga-Z1 (black), Ga-Z1H (red), Ga-Z2H (green), and Ga-Z3 (orange).....	167
<b>Figure C7.</b> Illustration of ethylene dimerization to 2-butene at a Brønsted acid site located at the T-12 position of H-ZSM-5 (MFI framework). ....	167

<b>Figure C8.</b> (A) Potential energy diagram for ethylene dimerization at Ga <sup>+</sup> and GaH <sub>2</sub> <sup>+</sup> Lewis acid sites (B) The corresponding atomic configurations.....	168
<b>Figure D1.</b> Powder X-ray diffraction (XRD) patterns of as-made ZSM-5 samples prepared with different sol gel Si/Al ratios: (A) Z20, (B) Z30, (C) Z50, (D) Z75, (E) Z100, (F) Z22-1, and (G) Z22-2.....	171
<b>Figure D2.</b> Nitrogen adsorption/desorption isotherms of calcined ZSM-5 samples.	171
<b>Figure D3.</b> The approximate mass (yield) of collected ZSM-5 solid products from syntheses of varying sol gel Si/Al ratio. The samples contain residual OSDA and water. ....	172
<b>Figure D4.</b> Deconvolution curve fittings of the <sup>27</sup> Al MAS NMR spectra of H-Z50, H-Z75, H-Z100, H-30T, H-50T, H-75T, H-100T, H-50H, H-50HT, Z22-1, and Z22-2. Each sample is labeled above the respective NMR data.....	172

## Chapter 1

### Prior Work on Zeolites as Catalysts: Rational Design and Aromatics Production

#### 1.1 Zeolite Catalysts: Synthesis Approaches and Nature of Active Sites

Zeolite is a crystalline, microporous material that is composed of tetrahedral units coordinated by O atoms,  $TO_4$  (T usually represents Si or Al atom).<sup>1</sup> Before the discoveries of industrial zeolite applications, over 40 naturally-occurring zeolites were found forming inside rocks.<sup>2</sup> After the discoveries of its commercial applications, researchers tried to mimic the geological condition to obtain synthetic zeolites. To optimize the physical and chemical properties of zeolites, different methods of preparation were developed, such as hydrothermal synthesis<sup>3</sup>, dry gel conversion synthesis<sup>4</sup>, and fluoride-medium synthesis<sup>5-6</sup>. Although zeolites are commonly considered to be aluminosilicates, other heteroatoms can replace Si atoms and incorporate into the framework structure, e.g.,  $P^{5+}$ ,  $Ge^{4+}$ ,  $Ti^{4+}$ ,  $Ga^{3+}$ ,  $B^{3+}$ ,  $Co^{2+}$ , or  $Zn^{2+}$ .<sup>7-</sup>

<sup>8</sup> Currently, there are over 248 frameworks that have been documented by the International Zeolite Association<sup>9</sup>, where each framework is given a three-letter code. Micropore size of most zeolites can be divided into three categories: small-pore (8 member-ring, ca. 4 Å), medium-pore (10 member-ring, ca. 5-6 Å), and large-pore (12 member-ring, ca. 7Å). Recently, ultra-large pore zeolites (14 member-ring to 18 member-ring) have been developed, which can be considered as potential catalysts in oil refining.<sup>10</sup> In general, zeolites have been widely used as ion exchangers, adsorbents, and catalysts,<sup>11-12</sup> while new applications have started to emerge that include (but are not limited to) drug delivery<sup>13</sup>, sensors<sup>14</sup>, fuel cells<sup>15</sup>, and imaging<sup>16</sup>.

In this dissertation, the major research focus is on the applications of zeolite catalysts. The widespread use of zeolites as heterogeneous catalysts in industrial

applications is attributed to their exceptionally high (hydro)thermal stability, tunable Brønsted acidity, and unique microporous topologies.<sup>17-19</sup> The incorporation of tetrahedral aluminum in the zeolite framework creates a negative charge that is counterbalanced by an extra-framework cation (e.g., Brønsted or Lewis acid site). One of the challenges associated with zeolite catalyst design is their propensity to rapidly deactivate due to internal diffusion limitations that result in coke formation. This is particularly problematic for small-pore zeolites ( $< 4 \text{ \AA}$  pore apertures), and has led to significant efforts within the zeolite synthesis community to design nano-sized materials with markedly reduced internal diffusion pathlength.<sup>20-23</sup> Indeed, there have been many notable advancements in the area of crystal engineering that has led to ultra-small zeolites,<sup>24-26</sup> 2-dimensional materials,<sup>27-31</sup> hierarchical zeolites,<sup>32-36</sup> and other types of unique architectures that have proven to effectively reduce diffusion limitations and improve the performance of zeolite catalysts.<sup>37-39</sup>

In select cases, a facile approach to prepare nano-sized zeolites involves the judicious adjustment of synthesis parameters, which includes (but is not limited to) gel composition, the source of reagents, and temperature. For example, the selection of silicon and/or aluminum sources can have a notable impact on the kinetics of crystallization.<sup>40</sup> Moreover, the intimate contact between these sources and alkali metals, which often serve as structure-directing agents (SDAs), can dramatically alter crystal growth as well as the final physicochemical properties of zeolites.<sup>41</sup> Among the various synthesis parameters that are available to control, the temperature is one that can have an appreciable effect on particle size. In particular, it is widely reported that low-temperature syntheses favor nucleation over crystal growth, thereby leading to an increase in the number of crystals with a concomitant reduction in average crystal size.<sup>42</sup> Examples include the work of Valtchev and coworkers<sup>43</sup> who systematically

examined the effect of temperature on zeolite A (LTA) crystallization and observed a monotonic decrease in crystal size with decreasing synthesis temperature. Rodríguez and coworkers showed for the case of ZSM-5 (MFI) synthesis that ultra-small crystals (10–20 nm) could be generated at low temperatures (70–90 °C).<sup>44</sup> Numerous studies of ZSM-5 size control can be found in the literature where the vast majority of cases examine the formation of nano-sized crystals with relatively low aluminum content (i.e., Si/Al > 25). In catalytic reactions, it is often desirable to prepare ZSM-5 with higher Al content; however, it is nontrivial to synthesize ZSM-5 with the dual conditions of high acid site density and small crystal size. Reported cases in the literature where such scenarios are achievable tend to involve nano-sized ZSM-5 synthesis at low temperature.<sup>45</sup>

The network of one- to three-dimensional micropores in zeolites provides confined regions for enhanced shape selectivity, and/or specific environments that direct the formation of certain products by stabilizing their associated transition state(s).<sup>46-52</sup> To further enhance the selectivity towards desired products, the introduction of extra-framework cations (i.e., Lewis acid sites) is attracting widespread interest, which is discussed in greater detail in the following section. An alternative approach to tailor product selectivity is to control the aluminum content inside the zeolite catalyst (i.e., framework Al that serve as Brønsted acid sites). Khare et al. recently argued that increasing aluminum content in ZSM-5 catalysts enhances the propagation of aromatics-based cycles for methanol to hydrocarbon (MTH) reaction using ethylene selectivity as an indicator.<sup>53</sup> They further related the effect of Al content with their previous findings on the crystallite size and argued that the average number of acid sites is as a general descriptor that strongly influences product selectivity.

To investigate the nature of an active site(s) in zeolite catalysts, it is often necessary to use multiple characterization techniques, such as diffraction, microscopy, and spectroscopy. Vibrational spectroscopy, especially infrared (IR), plays a key role in the characterization of zeolite catalysts.<sup>54</sup> Due to its acid-base properties, zeolites can be titrated with probe molecules (i.e., CO, NH<sub>3</sub>, and pyridine) to obtain quantitative information regarding the number, location, and strength of acid sites.<sup>55</sup> For example, pyridine has been widely used as a probe molecule to differentiate between Brønsted and Lewis acid site density.<sup>56</sup> On the other hand, substituted pyridines, such as 2,4,6-collidine, can only titrate the external active sites due to its limited access to the zeolite pores.<sup>57</sup> By comparing measurements using different probe molecules, internal and external active sites can be distinguished. Solid-state nuclear magnetic resonance (NMR) is another powerful technique to determine the local environment (both structure and dynamics).<sup>58</sup> Both <sup>27</sup>Al and <sup>29</sup>Si magic angle spinning (MAS) solid-state NMR are the most conventional measurements for zeolites. <sup>27</sup>Al MAS NMR can distinguish between framework Al (tetrahedral,  $\delta = 55$  ppm) and extra-framework Al (octahedral,  $\delta = 0$  ppm), which provides quantitative information regarding (extra)framework Al content. <sup>29</sup>Si MAS NMR spectra of zeolites usually exhibit as many as five signals in the SiO<sub>4</sub> units (Q4) region, Si(4Al), Si(3Al), Si(2Al), Si(1Al), and Si(0Al), where Si(nAl) (n = 0, 1, 2, 3, 4) represents the number of Al sites bound to the Si atom.<sup>59</sup> Therefore, framework Si/Al ratio can be determined from the <sup>29</sup>Si MAS NMR spectra. Recently, Xu et al. have explored metal active sites inside zeolite pores (host-guest interaction) and catalytic reaction intermediates via advanced solid-state NMR methods.<sup>60</sup>

## 1.2 Two-dimensional Zeolite Catalyst

As mentioned in the previous section, micropores of zeolitic materials provide confined environments for molecules during the course of reactions, which may direct the formation of certain products by stabilizing the associated transition state(s).<sup>46-49</sup> In addition to providing shape selectivity, small pore dimensions (4 ~ 7 Å) of typical zeolites often impose mass transport limitations, especially in applications that involve bulky molecules such as catalytic reforming.<sup>61-64</sup> Two-dimensional (2D) zeolites, on the other hand, have exhibited properties that can alleviate mass transport restrictions by providing accessible acid sites (and short diffusion path lengths) to molecules in reactions without significant diffusion into internal pore structures.<sup>65-67</sup>

Most zeolite can be obtained via conventional hydrothermal synthesis to directly form three-dimensional structures of interconnected TO<sub>4</sub> tetrahedral units; however, some zeolite frameworks are able to undergo a different pathway to form two-dimensional layered zeolite precursors (LZP) after the synthesis.<sup>65</sup> In the 2D LZP structure, each layer is connected via hydrogen bonding (i.e., weaker bonds) instead of covalent bonding. Due to its unique layer formation, many studies have focused on expanding different zeolite frameworks that can directly form LZP architectures. Figure 1.1 lists thirteen zeolite frameworks, such as FER<sup>68</sup>, SOD<sup>69</sup>, MFI<sup>29</sup>, NSI<sup>70</sup>, and PCR<sup>71</sup>, which are reportedly synthesized from a layered precursor.

MCM-22 (MWW type) is one of the most investigated 2D zeolites because of its unique crystallographic structure formed by stacking thin MWW layers (ca. 2.5 nm thick).<sup>72-73</sup> The MWW layers have thicknesses equal to a single unit cell dimension, and are aligned perpendicular to the c-axis (Scheme 1.1). The internal pores of MWW are comprised of supercages (boxed area of Scheme 1.1A) connected by 10-membered ring

(MR) apertures. These cages are surrounded by sinusoidal channels with narrower 10-MR openings located in close proximity to each corner of the supercage. The exterior surfaces of MWW layers are comprised of 12-MR pockets (or cups) equal to approximately one-half the volume of a supercage. Distinct from surface acid sites on many zeolite catalysts, the acid sites in the external cups of MWW-type zeolite exhibit strong acidity, similar to sites within the micropores,<sup>74</sup> which has generated interest for their use in catalytic reactions involving bulky molecules with steric restrictions for accessing interior cages/channels such as Friedel–Crafts alkylation<sup>75</sup>, hydrocracking<sup>27</sup>, and acetalization of aldehydes<sup>76</sup>. The MWW structure is comprised of eight unique tetrahedral (T) sites, which are illustrated in Scheme 1.1B and C.

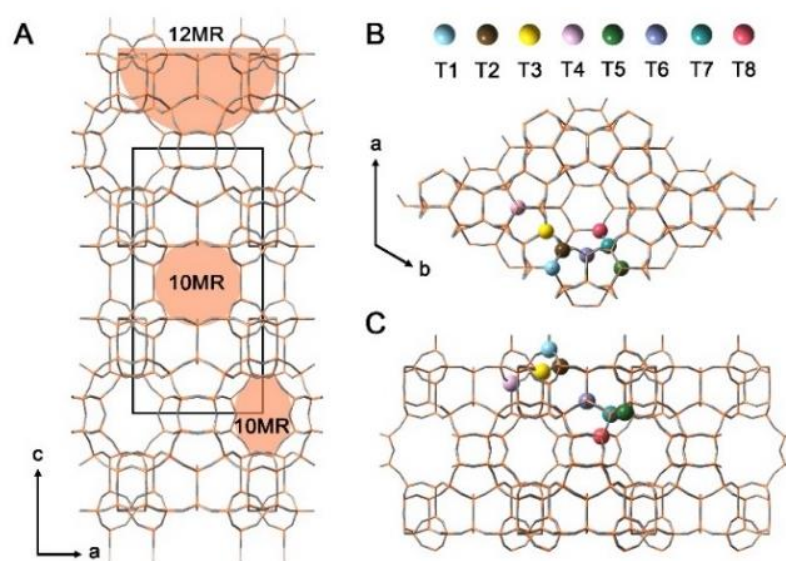
ABW	ACO	AEI	<b>AEL</b>	AEN	AET	AFG	AFI	AFN	<b>AFO</b>	AFR	AFS
AFT	AFX	AFY	AHT	ANA	APC	APD	AST	ASV	ATN	ATO	ATS
ATT	ATV	AWO	AWW	BCT	<b>*BEA</b>	BEC	BIK	BOF	BOG	BOZ	BPH
BRE	BSV	CAN	<b>CAS</b>	<b>CDO</b>	CFI	CGF	CGS	<b>CHA</b>	-CHI	-CLO	CON
CZP	DAC	DDR	DFO	DFT	DOH	DON	EAB	EDI	EMT	EON	EPI
ERI	ESV	ETR	<b>EUO</b>	EZT	FAR	<b>FAU</b>	<b>FER</b>	FRA	GIS	GIU	GME
GON	GOD	<b>HEU</b>	IFO	IFR	IHW	IMF	IRR	ISV	ITE	ITH	ITR
ITT	-ITV	ITW	IWR	IWS	IWV	IWW	JBW	JOZ	JRY	JSN	JSR
JST	JSW	KFI	LAU	LEV	LIO	-LIT	LOS	LOV	<b>LTA</b>	LTF	LTJ
<b>LTL</b>	LTN	MAR	MAZ	MEI	MEL	MEP	MER	<b>MFI</b>	MFS	MON	<b>MOR</b>
MOZ	<b>*MRE</b>	MSE	MSO	MTF	MTN	<b>MTT</b>	<b>MTW</b>	MVY	<b>MWW</b>	NAB	NAT
NES	NON	NPO	NPT	<b>NSI</b>	OBW	OFF	<b>OKO</b>	OSI	OSO	OWE	-PAR
PAU	<b>PCR</b>	PHI	PON	PUN	<b>RHO</b>	-RON	<b>RRO</b>	RSN	RTE	RTH	RUT
<b>RWR</b>	RWY	SAF	SAO	SAS	SAT	SAV	SBE	SBN	SBS	SBT	SEW
SFE	SFF	SFG	SFH	SFN	SFO	SFS	*SFV	SFW	SGT	SIV	<b>SOD</b>
SOF	SOS	SSF	SSY	STF	STI	*STO	STT	STW	-SVR	SVV	SZR
TER	THO	TOL	<b>TON</b>	TSC	TUN	UEI	UFI	UOS	UOZ	USI	UTL
UWY	VET	VFI	VNI	VSV	WEI	-WEN	YUG	ZON			<b>MCM-41</b>

16	<b>ZEO</b>	Synthetic used industrially or of commercial interest
13	<b>ZEO</b>	Layered or 2D form known
3	<b>ZEO</b>	Used commercially and layered or 2D form known

**Figure 1.1.** Zeolites with known 2D forms (yellow box with bold frame) and zeolites used industrially or those of commercial interest (red bold 3-letter code). This figure is adapted from previous work.<sup>65</sup>

As shown in Scheme 1.2, post-synthetic approaches have been developed to delaminate MCM-22P, where *P* is used to denote layered precursors that are not covalently connected. Calcination of the precursors leads to the direct condensation of MWW layers, which can be avoided via post-synthesis processes to exfoliate the layers, thereby producing disorder nanosheets with a high surface area exposing 12-MR

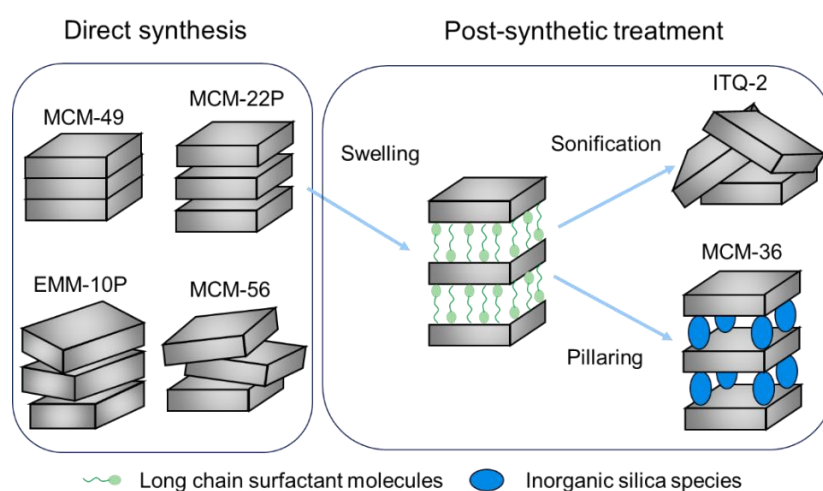
pockets. A notable example is ITQ-2 prepared by swelling MCM-22P with an exfoliating agent (e.g., surfactant) and subsequently delaminated via sonication.<sup>77</sup> Calcined ITQ-2 exhibits very high external surface area ( $\sim 700 \text{ m}^2/\text{g}$ ), indicating the material is composed of disordered MWW layers.<sup>78-79</sup> It has been reported that ITQ-2 shows the superior catalytic activity as compared to conventional MCM-22 zeolites in various applications, such as cracking of vacuum gas oil.<sup>77</sup> The original procedure and conditions used to prepare ITQ-2 involved the use of harsh conditions (i.e., high pH and temperature), leading to partial amorphization.<sup>80</sup> Several methods were established since the initial reports of ITQ-2 synthesis to overcome these problems. For example, the separation of MWW layers can be achieved without the use of sonication.<sup>81</sup>



**Scheme 1.1.** (A) MWW framework with its network of pores (B) Top down view of an external pocket with unique T sites for Al incorporation, and (C) side view along the a-direction (90 degrees relative to panel B).

Similarly, potential amorphization of MWW layers can be avoided when operating under pH 9 and via the use of tetraalkylammonium ions to avoid energy-intensive sonication.<sup>82</sup> Another worth-mentioning MWW-type material prepared via post-synthetic treatment is MCM-36, which is the first pillared zeolitic material developed by Mobil Research and Development Corporation.<sup>83</sup> Scheme 1.2 indicates

the swollen layers are intercalated by silica species, which is able to hold the layers apart. Similar to the synthesis of ITQ-2 material, the swelling step to obtain MCM-36 zeolite also requires severe conditions such as high temperature and pH, resulting the partial dissolution of framework silica. To resolve this challenge, Maheshwari et al. demonstrated the post-swelling step can be performed at room temperature (compared to conventional processes at 353 K) by extensive washing with water.<sup>84</sup> Interestingly, post-synthetic processes have been extended to borosilicates where single-step delamination along with isomorphous substitution of boron with aluminum has been demonstrated on ERB-1 (MWW type; borosilicate counterpart).<sup>85</sup> Delamination has also been used in somewhat related processes referred to as ADOR (assembly-disassembly-organization-reassembly) to construct new frameworks.<sup>71, 86-89</sup> In these processes, building units consisting of a chemical weakness (i.e., Ge heteroatoms) are used to delaminate (or disable) and then reassemble via silica bridges to construct new frameworks that are otherwise difficult to prepare directly. Moreover, layered zeolites can be used as seeds for the topotactic conversion between different 2D zeolitic precursors through a 3-dimensional germanosilicate intermediate.<sup>90</sup>



**Scheme 1.2.** Possible MWW-type zeolite structures obtained via direct and post-synthetic treatment. The scheme is redrawn and adapted from previous work.<sup>65</sup>

It is highly desirable from both an economic and practical standpoint to develop one-pot synthesis methods to yield zeolite MWW nanosheets with large external surface areas, while simultaneously avoiding loss of structure that is often the result of post-synthesis treatments. To our knowledge, there are few strategies reported in the literature to achieve disordered MWW-type materials with properties similar to ITQ-2. Several approaches that come close include the preparation of UZM-8,<sup>91</sup> MCM-56,<sup>92-93</sup> EMM-10,<sup>94</sup> and ITQ-30.<sup>95</sup> Despite the fact these materials exhibit some degree of disordered MWW layers, their relatively low mesoporosity indicates MWW layers are not highly separated with respect to a fully delaminated MWW-type zeolite. Multiple groups have reported<sup>31, 96-97</sup> the preparation of MWW-type materials with single layers using a one-step method; however, these methods required the use of custom organic structure-directing agents (OSDAs) that were not commercially available, and required multi-step synthesis. To this end, it has remained elusive to design a one-step synthesis of delaminated MWW type zeolite through more practical pathways.

### **1.3 Bifunctional Metal-exchanged Zeolite Catalyst**

Zeolites are shape-selective microporous catalysts that are widely used in refining and (petro)chemical processes. The incorporation of aluminum in the zeolite framework creates a negative charge that is counterbalanced by an extra-framework cation (either a Brønsted or Lewis acid site). The use of metal Lewis acids broadens the range of catalytic applications. Table 1.1 summarizes the use of metal-exchanged zeolite in selected key catalytic applications in the perspectives of natural gas and oil processing, pollutant treatment, fine chemical synthesis, and biomass conversion. However, in this dissertation, the major focus is to optimize the dehydroaromatization (DHA) catalytic performance of bifunctional metal-exchanged zeolites. Numerous research studies have established that with the addition of Lewis acid sites (i.e., Ag (I),

Ga (III), and Zn (II)), the combination of two types of active sites (Brønsted and/or Lewis acid sites) can enhance aromatics yield due to the dehydrogenation properties of the added acid sites.<sup>98-99</sup> In addition, among all zeolite frameworks, ZSM-5 (MFI topology) has been demonstrated to be a superb catalyst for BTX production from different feedstocks, including syngas<sup>100</sup>, methanol<sup>101-102</sup>, light alkanes<sup>103-104</sup>, and alkenes<sup>105-108</sup>, due to its unique medium pore (10-member ring) shape selectivity.

**Table 1.1.** Selected catalytic applications of metal-exchanged zeolite catalysts.

Selected applications <sup>a</sup>	Metals	ref
<b>Natural gas processing</b>		
Methane dehydroaromatization (DHA)	Mo, Re, Fe	103
Oxidation of methane to methanol	Cu, Fe	109
<b>Oil processing</b>		
Hydrocracking	Ni/Mo, Ni/W, Pt, Pd	110
Naphtha reforming	Pt	111
Light alkane/alkene dehydroaromatization (DHA)	Ga, Zn, Ag	99
<b>Environmental application</b>		
Selective catalytic reduction (SCR) of nitrogen oxides (deNO <sub>x</sub> )	Cu, Fe, Ag, Co	
(photo-)catalytic removal of volatile organic compounds (VOC)	Ti, Cu, Pt, Pd	112
Deep catalytic oxidation of water pollutants	Cu, Fe	113
Catalytic combustion of CO and hydrocarbons	Pd, Ni	114
<b>Synthesis of fine chemicals</b>		
Benzene to phenol oxidation with N <sub>2</sub> O	Fe, Ti	115
Selective hydrogenation of nitroarenes	Pd, Pt	116
Diels-Alder reactions	Zn, Cr, Ga, Cu, Zr	117
Baeyer-Villiger oxidation of ketones	Sn, Ti, Zr	118
<b>Biomass conversion</b>		
Conversion of carbohydrates to lactic acid	Sn, Ti, Zr	119

<sup>a</sup> The table is modified from the previous literature.<sup>120</sup>

Direct conversion from light alkenes (e.g., ethylene) to desired aromatics (BTX) has attracted much attention over the past few decades. In 1998, Qiu et al.<sup>106</sup> observed that aromatic selectivity over Ga-ZSM-5 can reach as high as 87% at the comparable ethylene conversion (95%) and the reaction conditions 1 atm and 793K; however, in 2017, Coqueblin et al.<sup>121</sup> investigated four metal-exchanged ZSM-5 catalysts (Mo, Ni, Ga, and Zn cations) over the same catalytic reaction (ethylene DHA) and observed that Zn-ZSM-5 shows the highest ethylene conversion (ca. 92%) and aromatics yield (ca. 60%) at atmospheric pressure and 773K. Moreover, studies of methane activation have increased in number over the last decade due to the recent surge in shale gas. Particularly, partial oxidation of methane to methanol is a promising route to further produce aromatics and holds interests for researchers worldwide.<sup>109</sup> As shown in Figure 1.2, Ravi et al. have summarized the direct methane-to-methanol conversion results over different metal loading solid catalysts. For all reported catalysts, a higher methanol selectivity at a lower methane conversion is observed. It is worth mentioning that Cu-ZSM-5 catalysts can achieve nearly 85% methanol selectivity at a relatively high methane conversion.

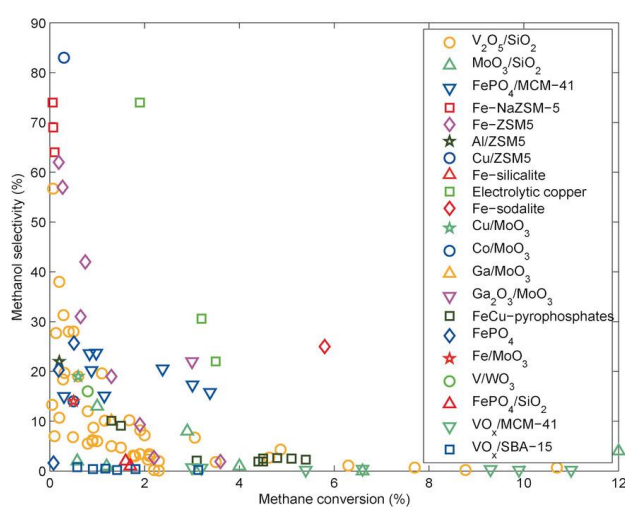
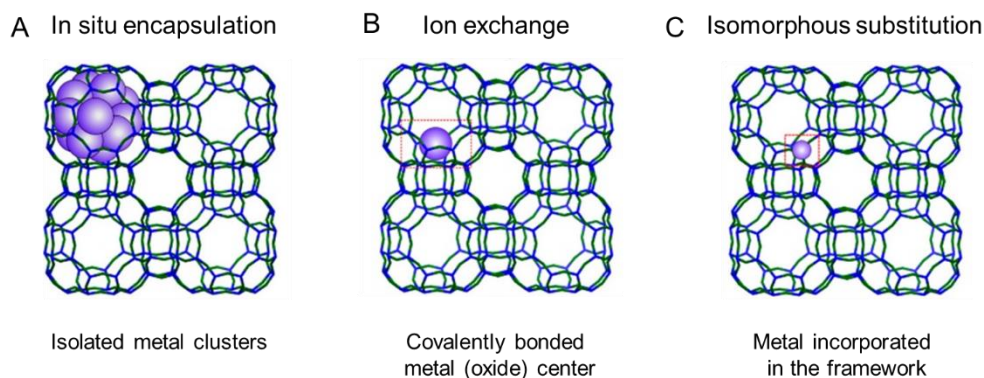


**Figure 1.2.** Selectivity for the formation of methanol with different catalysts as a function of methane converted. This figure is adapted from previous work.<sup>109</sup>

The incorporation of Al into the zeolite framework creates a negative charge that needs to be balanced by extra-framework cations, usually  $H^+$  (Brønsted acid site). Wetness impregnation is the most common method that has been widely used to introduce transition metals into zeolite matrix. Typically, zeolite host is mixed with a solution where the metal precursor is dissolved in. The volume of zeolite micropore should be equal to the solution volume. The metal-loaded zeolite can then be dried and calcined, leading to the removal of volatile components and deposition of active metal sites. However, in the presence of gas molecules inside the zeolite structure, previous literature suggests the metal precursor solution cannot fill the entire zeolite micropore volume hence leading to a non-uniform metal site distribution with aggregates on the external zeolite surface.<sup>122</sup> To achieve the homogeneous metal species distribution, a conventional ion exchange method is performed in an aqueous solution with an excessive amount of metal precursor and washing. Compared with the wetness impregnation method, the final metal loading is different from the amount of metal species dissolved in the solution. Factors such as metal precursor concentration, ion exchange temperature, and solution pH are all essential to influence the final metal loading amount. Although most monovalent cations (e.g.,  $Na^+$ ,  $K^+$ , and  $Ag^+$ ) can easily exchange with  $H^+$  and covalently bond with framework oxygen (Scheme 1.3B), multivalent cations usually have difficulty to interact with the zeolite host. Specifically, Ga-ZSM-5 prepared using a solution ion exchange method typically exhibits large fractions of  $Ga_xO_y$  deposits formed on the external zeolite surfaces due to the slow diffusion of hydrated  $Ga^{3+}$  ionic species into the micropores.<sup>123</sup> To obtain more dispersed Ga species, Ga-ZSM-5 could be reduced in  $H_2$  at high temperature ( $>700K$ ) and exchanged with Brønsted acid sites.<sup>123-125</sup> However, Ga cannot completely migrate into the zeolite micropore channels thus obtaining uniform dispersed Ga speciation is

challenging. Chemical vapor deposition is another approach to introduce isolated metal species into the zeolite micropore via reacting a volatile metal precursor (e.g., chloride, alkyl, etc.) with zeolite Brønsted acid sites under anhydrous conditions.<sup>120</sup> For example, Phadke et al. developed a novel vapor-phase exchange of H-ZSM-5 with GaCl<sub>3</sub> to obtain isolated Ga<sup>3+</sup> cations inside ZSM-5.<sup>123</sup>



**Scheme 1.3.** Possible metal-zeolite configuration via different preparation methods. The scheme is modified and adapted from previous literature.<sup>120</sup>

In situ encapsulation of metal clusters is a powerful technique to generate metals inside zeolite micropores (Scheme 1.3A). However, most metal cations have a propensity to precipitate when directly added into zeolite synthesis gel mixtures, leading the formation of separated phases between metal cluster and zeolite framework.<sup>122</sup> To overcome these challenges, Iglesia and coworkers demonstrated that metal cluster (Pt, Ru, Rh) can be incorporated via interzeolite transformation from a parent zeolite (BEA or FAU) to a daughter zeolite (e.g., MFI).<sup>126</sup> Moreover, utilizing the silica ligand precursor to stabilize the metal species is also able to encapsulate metal clusters inside zeolite pores. Jones and coworkers developed a method that creates Ga Lewis acid sites via this approach.<sup>127</sup> They reported that with the addition of 3-mercaptopropyl-trimethoxysilane (MPS), Ga can be encapsulated into the framework without directly forming the covalent bonds with the framework oxygen. As shown in Scheme 1.3C, isomorphous substitution leads to the formation of isolated framework

metal sites. Instead of Al atom, other trivalent elements such as Ga<sup>3+</sup>, Fe<sup>3+</sup>, and B<sup>3+</sup> can also be incorporated into the zeolite framework and exhibit different Brønsted acid strength.<sup>128</sup> In this dissertation, we aim to develop a novel metal-exchanged zeolite catalyst that can maximize aromatics yield. Moreover, we focus on the identification of metal active sites and the elucidation of their role(s) in alkene DHA reactions.

#### 1.4 Recent Development in Aromatics Production over Zeolites

Aromatic hydrocarbons (benzene, toluene, and xylene isomers referred to collectively as BTX) are essential precursors in the current petrochemical industry. BTX products can be commercially used as valuable materials such as fuel additives, raw materials for polymers, and other value-added aromatics-derived products.<sup>129-130</sup> As the industrial production of aromatics still heavily relies on catalytic reforming in oil refineries,<sup>131-132</sup> a supply gap is expected in the future. Therefore, alternative routes to produce aromatics are desirable given the limited supply of fossil fuels. The recent surge in shale gas has created opportunities to develop processes based on methane and light olefin feedstocks.<sup>133</sup> Recently, IHS Markit claimed that novel process technologies (Figure 1.3) could change the entire chemical industry by 2025, where the feedstock will gradually shift from conventional crude oil to light crude oil (< C4).<sup>134</sup>

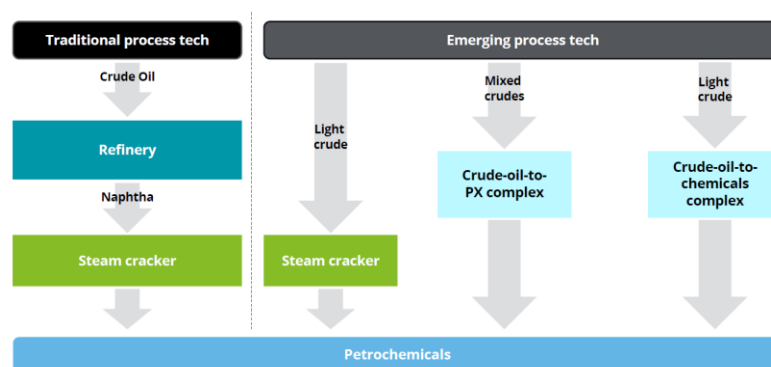


**Figure 1.3.** Crude oil to chemical production routes. Crude oil to chemicals production routes. This figure is adapted from previous work.<sup>134</sup>

One promising technology is the direct conversion of ethylene to aromatics (or ethylene dehydroaromatization, DHA).<sup>135</sup> This feedstock has received relatively little

attention compared to methane<sup>103, 136</sup> and propane.<sup>98</sup> There is a high degree of feedstock flexibility in ethylene DHA reactions owing to the availability of ethylene from steam cracking in refineries,<sup>137</sup> and its potential generation from ethane dehydrogenation.<sup>138-140</sup> Furthermore, the ethylene to liquids (ETL) reaction could be used in combination with the oxidative coupling of methane (OCM) to avoid costly separation of ethylene from OCM products.<sup>106, 141-142</sup> Alternatively, ethylene can be used in methane upgrading through non-oxidative coupling (NOC),<sup>108</sup> or in ethylene-to-propylene (ETP) reactions.<sup>143</sup> While prior literature has focused on ethylene upgrading over nickel-based catalysts,<sup>144-146</sup> there are disproportionately fewer studies of ethylene DHA reactions catalyzed by metal-containing zeolite catalysts.<sup>9, 107, 147-148</sup>

Motivated by recent high production of natural gas and light olefins, we aimed to develop structure-performance relationships of metal-containing zeolite catalysts in non-oxidative CH<sub>4</sub> and C<sub>2</sub>H<sub>4</sub> upgrading reactions. According to the literature on non-oxidative methane upgrading, methane conversion has not exceeded 20%, which is far from the practical level for industrial viability. Hence, elucidation of both NOC and DHA reaction mechanisms and corresponding active sites that include their locations in framework is a key step to enhance methane conversion. A general mechanism is shown in Figure 1.4 where methane activation, the rate-limited step, is proposed to occur at a Lewis acid site. In the presence of ethylene, C-C bond formation may occur at both Brønsted and Lewis acid sites via oligomerization and dehydrogenation. To improve methane conversion, screening Lewis acid sites using density functional theory (DFT) calculations is necessary to determine which metal promoter is the most promising one to activate methane. Moreover, methane or ethylene conversion is also strongly influenced by active site locations and co-feed reactants. Their effects can be elucidated with a fundamental understanding of the reaction mechanism.

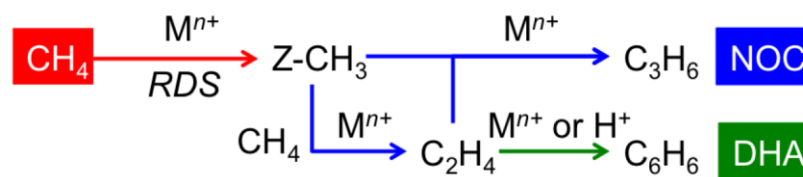


**Figure 1.4.** General mechanism for NOC and DHA where M<sup>n+</sup> represents a Lewis acid site and H<sup>+</sup> is a Brønsted acid site.

In addition to aromatics production from DHA, it is economically important to explore alternative pathways to produce aromatics and other value-added chemicals through processes such as hydrocarbon cracking (i.e., converting heavy polyaromatics to valuable BTX). These critical industrial processes commonly use zeolites as heterogeneous catalysts; however, it is challenging for the high-molecular-weight feed to diffuse into the microporous channels of zeolites.<sup>27</sup> High surface area 2D layered zeolites, such as MWW-type materials, can reduce internal mass transport limitations by providing more external acid sites and decreasing diffusion within pores. In addition, Friedel-Crafts alkylation involving aromatics is used widely in industry to produce fine chemicals, which can be further transformed into dyes and pharmaceuticals, among other products.<sup>30</sup> Layered MWW materials have become promising catalysts for the production of ethylbenzene and cumene from alkylation owing to their unique surface pockets that enhance selectivity due to the strong acid sites inside the 12 MR exterior cups (Scheme 1.1).

## 1.5 Dissertation Outline

This dissertation is divided into three parts. In chapter 2 and 3, we discuss structure-performance relationships of metal-containing (Ag, Ga) zeolite catalysts in non-oxidative CH<sub>4</sub> and C<sub>2</sub>H<sub>4</sub> dehydroaromatization (DHA) reactions. By using advanced *in situ* techniques and DFT calculations, the nature of active sites and reaction mechanisms can be elucidated. In chapter 4, we demonstrate a novel one-step synthesis approach to produce ultrathin 2D nanosheets. In this study, we selected a common

layered zeolite, the MWW framework, to explore methods of preparing 2D nanosheets via a one-pot synthesis in the absence of complex organic structure-directing agents. Using a combination of high-resolution microscopy and spectroscopy, we show that it is possible to generate 2D MWW-type layers with an average thickness of 3.5 nm (ca. 1.5-unit cells). In chapter 5, we highlight the challenges associated with synthesizing ZSM-5 at low temperature (ca. 100°C), which is often necessary to generate small crystals (< 200 nm) with an appreciable quantity of acid sites (i.e., Si/Al < 25). By using solid-state  $^{27}\text{Al}$  NMR technique, we observe the existence of extra-framework (octahedral) Al and penta-coordinated Al from ZSM-5 via low-temperature synthesis. Although these three parts have different objectives, all of them require rational design of zeolite catalysts to maximize their reaction performance (i.e., activity, selectivity, and stability).

## Chapter 2

### Enhanced Surface Activity of MWW Zeolite Nanosheets Prepared By a One-Step Synthesis Method

The material discussed in this chapter has been published. Figure and table numbers have been changed for dissertation consistency. The work was in collaboration with Yanyu Mu, Dr. Bernd Kabius, Dr. Carlos Pacheco, Dr. Carol Bator and Dr. Robert M Rioux from the Pennsylvania State University.

#### 2.1 Motivation

Zeolites with small-to-medium sized pores (3 ~ 7 Å) often encounter mass transport limitations with limited access of bulky molecules.<sup>62-64, 149</sup> In comparison, two-dimensional (2D) zeolites possess properties that enhance mass transport within pores while providing accessible acid sites on external surfaces for molecules sterically restricted from accessing internal sites.<sup>65-67</sup> MCM-22 (MWW type) is one of the most investigated 2D zeolites because of its unique crystallographic structure formed by stacking thin MWW layers (ca. 2.5 nm thick).<sup>72-73</sup> The MWW framework has a hexagonal crystal structure (*P6/mmm*) with unit cell parameters  $a = 1.421$ ,  $b = 1.421$ , and  $c = 2.495$  nm.<sup>150</sup> These MWW layers are perpendicular with respect to each layer along the *c*-axis, in which half of the 12-MR cage (referred to as semi 12-MR cups, boxed area of Scheme 1.1A) is located on the exterior of MWW layers. Different from normal surface acid sites, these acid sites in the semi cups still exhibit strong acidity similar to ones in micropores., hence leading MWW-type zeolites to become very promising catalysts for reactions involving large molecules that cannot diffuse into zeolite microporous channels.<sup>74</sup>

In addition, conventional layered MCM-22 precursors, referred to as MCM-22(P), result in direct condensation of MWW layers during calcination, sacrificing significant accessibility to surface acid sites. Post-synthetic approaches have been

developed to expose semi 12-MR cups by preventing direct condensation of MWW layers. As mentioned in Chapter 1, a notable example is ITQ-2 (high external surface area  $\sim 700 \text{ m}^2/\text{g}$ ) prepared by swelling MCM-22(P) with long chain surfactant molecules and subsequently delaminated via sonication.<sup>27, 78-79</sup> However, the original procedure and conditions used to prepare ITQ-2 appear to be limited to certain Al content and are also relatively harsh for zeolitic materials, leading to partial amorphization.<sup>151</sup> Several methods were established to overcome these problems. For example, the swelling treatment can be performed at room temperature compared to the original temperature (353 K).<sup>152</sup> Additionally, separation of MWW layers can be achieved without sonication.<sup>81</sup> Potential amorphization of MWW layers can be avoided when using media under pH  $\sim 9$  and through the use of long-chain surfactants without energy-intensive sonication.<sup>151</sup> Roth et al. obtained the first pillared zeolitic material, MCM-36, where swollen layers are intercalated by silica species.<sup>83</sup> Recently, Liu et al. developed a novel vapor-phase pillarization (VPP) process to produce pillared 2D zeolite materials with  $\sim 100\%$  efficiency.<sup>153</sup> While various post-synthetic treatments have been established, it is still highly desirable to develop one-step synthesis methods to expose semi 12-MR cups. However, most of the reported one-step strategies have not been successful in achieving properties that are comparable to MWW type zeolites prepared using multi-step post-synthetic treatments. Several examples include MCM-56,<sup>93, 154</sup> EMM-10,<sup>94</sup> and ITQ-30.<sup>95</sup> Despite the fact that these materials exhibit disordered MWW layers along *c*-axis based on the X-ray diffraction (XRD) patterns, the relatively low mesoporosity indicates that the MWW layers are not well separated with respect to delaminated MWW type zeolites. More recently, two research groups co-currently developed methods to prepare separated MWW layers in one-step approaches,<sup>31, 96</sup> which require specially designed organic structure-directing agents

(OSDAs) that are costly and commercially unavailable. To this end, it is still challenging to develop a one-step synthesis of delaminated MWW type zeolites using economic reagents.

In this chapter, we report a one-pot synthesis of disordered MWW zeolite using a conventional route that is modified through the addition of a commercial surfactant, cetyltrimethylammonium (CTA). Our findings reveal that CTA acts as a secondary OSDA to alter Al siting without impacting the overall Si/Al ratio of the final product. Parametric studies of growth conditions identify regions of growth solution composition resulting in disordered MWW. Textural analysis reveals the final product exhibits a degree of disorder and corresponding external surface area comparable to ITQ-2, while solid-state  $^{27}\text{Al}$  NMR reveals materials prepared by direct synthesis contains fewer Al defect sites. We also report the catalytic performance of these materials relative to 3D MWW (MCM-22) using a model reaction to verify that higher surface area leads to greater access to external acid sites (i.e., greater initial conversion), while the intrinsic activity (when normalized by the number of external acid sites) of the disordered MWW is identical to MCM-22. Collectively, these studies highlight a potentially new, facile route to generate 2D zeolites from naturally layered frameworks that may prove relevant to a broader class of microporous materials.

## **2.2 Experimental Methods**

### **2.2.1 Material**

The following reagents were purchased from Sigma-Aldrich: benzene (99.9%), benzyl alcohol (anhydrous, 99.8%), isopropylamine (99%), hexamethyleneimine (HMI, 99%), hexadecyltrimethylammonium bromide (CTAB, 99.9%), hydrochloric acid solution (HCl, 1.0N) and sodium hydroxide (NaOH, 98%). Sodium aluminate

(technical grade), tetrapropylammonium hydroxide (TPAOH, 40%) and trimethylphosphineoxide (99%) was purchased from Alfa Aesar. Tributylphosphineoxide (90%) was purchased from Tokyo Chemical Industry (TCI). Fumed silica (Cab-o-Sil, M-5, scintillation grade) was purchased from Spectrum Chemical. Anhydrous dichloromethane (99.9%) was purchased from Fisher Scientific. Deionized (DI) water was produced with an Aqua Solutions RODI-C-12A purification system (18.2 MΩ). All reagents were used as received without further purification.

### 2.2.2 Synthesis of MWW Materials

Synthesis of MWW type zeolite was performed based on a reported protocol in literature with slight modifications.<sup>72</sup> MCM-22 zeolites (gel Si/Al = 15, 30, and 45) were synthesized using growth solution with a nominal composition of 0.49 HMI : 0.09 Na<sub>2</sub>O : 1 SiO<sub>2</sub> :  $x$  Al<sub>2</sub>O<sub>3</sub> : 43.9 H<sub>2</sub>O, where  $x = 0.033, 0.017, \text{ or } 0.011$ . The initial procedure involved the addition of sodium aluminate to a solution of HMI, NaOH and DI water. The mixture was aged at room temperature overnight under continuous stirring. Fumed silica was then added and the growth solution was heated at 150 °C for 7d in a Teflon-lined autoclave (Parr Instruments) with rotation. The solution was then removed from the oven and immediately cooled to room temperature.

Disordered MWW material was prepared by modifying the MCM-22 synthesis to include the addition of cetyltrimethylammonium bromide (CTAB). A small quantity of CTAB (0.55 – 1.38 g, or 4 – 10 wt%) was added in a mixture of 1M sodium hydroxide solution (2.41 g), DI water (9.55 g), sodium aluminate (0.03 – 0.09 g), and 0.74 g of organic structure-directing agent, hexamethyleneimine (HMI). After stirring this mixture overnight at room temperature, 0.9 g of fume silica was added to give a gel molar composition of 0.49 HMI : 0.09 Na<sub>2</sub>O : 1 SiO<sub>2</sub> :  $x$  Al<sub>2</sub>O<sub>3</sub> :  $y$  CTA : 43.9 H<sub>2</sub>O, where  $x = 0.033, 0.017, \text{ or } 0.011$  and  $y = 0.10 - 0.25$ . The solution was heated at 150 °C

for 7d in a Teflon-lined autoclave with rotation. The solid product (zeolite crystals) was collected by vacuum filtration, washed thoroughly with DI water, and dried at 60 °C. Samples were calcined in a Thermo Fisher Lindberg Blue furnace under a constant flow of dried air (Matheson Tri-Gas) at 550 °C for 10 h with a temperature ramp/cooling rate of 1 °C/min.

ITQ-2 was synthesized by delamination of MCM-22P using a method reported in literature,<sup>155</sup> with minor modifications to increase the Al content of the final product. The procedure involved the mixing of MCM-22P (1g) with DI water (25 g), CTAB (1.42 g), and TPAOH (3.75 g of 40 wt% reagent) to achieve a starting gel Si/Al ratio of 15. The mixture was stirred at 80 °C under reflux for 16 h. After cooling to room temperature, the mixture was sonicated (110 W, 40 kHz) for 2 h. The pH of the mixture was dropped below 2 by the addition of stock HCl solution, and subsequently, the mixture was centrifuged to recover the solids. The delaminated product was dried in air and calcined at 550 °C for 8 h. A second ITQ-2 sample synthesized from a starting gel of Si/Al ratio of 45 was prepared according to the same procedure with the following modifications: 1g MCM-22P (gel Si/Al = 45) was added into a mixture containing 12.22 g DI water, 1.13 g CTAB, and 2.50 g TPAOH (40wt% reagent).

Samples for catalytic testing were converted to their H<sup>+</sup> forms by ion exchange wherein calcined zeolite was mixed with 1.0 M ammonium nitrate solution to obtain a 2 wt % suspension. This mixture was heated to 80 °C for 2 h to allow the exchange of Na<sup>+</sup> with NH<sub>4</sub><sup>+</sup>. This process was performed three times with centrifugation/washing between each ion exchange cycle, using a Beckman Coulter Avanti J-E centrifuge at 5 °C and 13000 rpm for 10 min per cycle. The final NH<sub>4</sub>-zeolite samples were washed thrice with DI water before they were calcined once again at 550 °C for 5 h with a

temperature ramping/cooling rate of 1 °C/min (leading to the generation of H-form zeolites).

### 2.2.3 Characterization

MWW type zeolite samples were characterized by powder X-ray diffraction (PXRD), nitrogen adsorption/desorption, scanning electron microscopy (SEM), thermogravimetric analysis (TGA), cryo-transmission electron microscopy (cryo-TEM), inductively coupled plasma–optical emission spectroscopy (ICP-OES), and solid-state NMR. PXRD patterns were acquired from 5 to 50° 2 $\theta$  with a step size of 0.02° at 40 kV and 44 mA using a Rigaku Smartlab X-ray Diffractometer. Analysis of surface area by the BET method was performed on N<sub>2</sub> adsorption/desorption isotherms obtained using a Micrometrics ASAP 2020 instrument. Crystal morphology and size were measured by a FEI Nova NanoSEM 230 instrument after Pt coating (ca. 5 nm thickness). Thermogravimetric analysis (TGA) was performed in flowing air (20 mL min<sup>-1</sup>) on a TG 209 F3 Tarsus instrument with a heating rate of 10 °C min<sup>-1</sup>. The temperature was ramped up to 850 °C to assess the weight percentage of occluded organics in MWW type materials.

A Thermo Fisher Krios G3 Cryo-TEM with an image aberration corrector and customized Gatan BioQuantum electron-energy loss spectrometer was used for all measurements. The samples were cooled to liquid nitrogen temperature. During the entire TEM investigation, no contamination or radiation damage effects were observed. Images were detected with a Falcon 3EC direct electron detector in counting mode. An acceleration voltage of 300 kV was used for all imaging. The system is capable of a spatial resolution of better than 0.14 nm.

In order to prepare Cryo-TEM sample, zeolite dispersions (~3 mg/mL) in water were drop-cast (~1.5  $\mu$ L volume) onto Quantifoil grids (1.2/1.3/300 mesh Cu) (Ted Pella) which were subjected to glow discharge (PELCO easiGlow™ Glow Discharge Cleaning System) in air (0.3 mbar) at 20 mA for 40 s. For the grids, 1.2 refers to the hole sizes on the Quantifoil grid in  $\mu$ m, while 1.3 refers to the average hole size in carbon support in  $\mu$ m. The glow discharge ensured the TEM grids were hydrophilic. Prior to drop-casting, suspensions were sonicated in a water bath to ensure zeolite particles were fully suspended since they tended to settle out without agitation. After allowing the grids to dry by evaporation in the atmosphere, the Quantifoil grids were clipped into autoloader cartridges and loaded into the Krios autoloader at room temperature. Grids were cooled inside the Krios to liquid nitrogen temperature and maintained at cryogenic temperature throughout screening and data collection.

In order to measure the thickness of nanosheets whose surface normal ((001) direction) are perpendicular to the electron beam, we processed images (which contained one or more of these edge-on oriented sheets) with Digital Micrograph. A sufficient number of crystals in this orientation could be identified over numerous micrographs allowing for the collection of substantial statistics (150-500 individual measurements). We chose vertically oriented crystals over flat-lying crystals since the latter had uniform thickness and minimum intensity at the boundaries enabling more accurate measurement of thickness. Thickness for each vertical crystal was determined from the distance between two positions of intensity minima in the line profile (

Figure **A2**). Nanosheets were only included into the data pool if they are visualized edge-on. Measurements on sheets tilted away from this condition are subject to projection effects falsifying the thickness value. The following criteria were used to identify edge-on sheets: (i) crystal structure has to be visible when the sheet extension

in beam was small enough ( $< 50$  nm); (ii) lattice planes have to be visible when the sheet extension in beam was smaller than 150 nm and (iii) image contrast parallel to sheet normal has to be homogeneous for thicker sample (up to micron level). The line-scan in

Figure A2 across a nanosheet shows the thickness measurement procedure. The white fringes at the surface of the sheets are an image artifact caused by Fresnel diffraction. All thickness measurements were done from where the contrast turns dark to where the dark contrast ends on the other side of the sheet. This turning point is equivalent to the average electron count surrounding the sheet. Measurement error is related to image resolution which depends on sample thickness and ranges from 0.2 nm up to about one nanometer. This lower limit of 0.2 nm measurement error is inconsequential because there are crystallographic limitations to the allowed thickness values. From images of the crystal structure, the sheets are always terminated by (001) or (002) lattice planes. Therefore, the sheet thickness has to be a multiple of 2.52 nm. The upper limit of about one nanometer is valid for crystals which are about 20-40 nm thick, resulting in a measurement error of only a few percent.

Solid-state  $^{27}\text{Al}$  NMR experiments were performed at 11.7 T on a JEOL ECA-500 spectrometer, equipped with a 3.2mm Magic Angle Spinning Probe.  $^{27}\text{Al}$  MAS NMR spectra were obtained at a spinning frequency of 12.5 kHz with a  $\pi/12$  pulse width of 1.25  $\mu\text{s}$  and a recycle delay of 0.8 s. The number of scans was 4096 for all measurements.  $^{27}\text{Al}$  MQMAS measurements were performed using the same instrument, where the experiment details can be found elsewhere.<sup>156</sup> The percentages of framework and extra-framework Al species (FAI and EFAI, respectively) were determined using the Dmfit program. The broad peak (ca. 56 ppm) in  $^{27}\text{Al}$  MAS NMR spectra was deconvoluted into three peaks at 50, 56, and 61 ppm (represented as Al<sub>(A)</sub>,

Al<sub>(B)</sub>, and Al<sub>(C)</sub>, respectively). The <sup>27</sup>Al chemical shift was referenced using 1M Al(NO<sub>3</sub>)<sub>3</sub> aqueous solution. Solid-state <sup>31</sup>P NMR experiments were carried out on a Bruker AVANCE III HD solid-state 500 MHz NMR with a quadruple tuned 4 mm CPMAS probe or a Bruker AVANCE solid-state 300 MHz NMR with a double-resonance 4 mm HX probe spectrometers at room temperature (298 K). <sup>31</sup>P NMR spectra were acquired at the frequency of 202.5 MHz using a single-pulse sequence with a pulse width of 1 μs, a recycle delay of 5 s in AVANCE III HD solid-state 500 MHz NMR and a pulse width of 2.5 μs, a recycle delay of 10 s in Bruker AVANCE solid-state 300 MHz NMR. The sample spinning frequency is 12 kHz with 2-10 k scans. CaHPO<sub>4</sub>·2H<sub>2</sub>O was used as an external reference.

Prior to the adsorption of phosphine oxides onto zeolites, MWW samples were dried at 473 K for 2 h in N<sub>2</sub> (UHP, Praxair) and transferred into the N<sub>2</sub>-purged glovebox. A known amount of TMPO or TBPO dissolved in anhydrous CH<sub>2</sub>Cl<sub>2</sub> was added into a flask containing the dried sample in a glovebox at room temperature. The P-loaded sample was sonicated for 5 h and then stirred at 500 rpm for over 24 h at room temperature. Removal of CH<sub>2</sub>Cl<sub>2</sub> was achieved on a Schlenk line at 313 K. This procedure is a modified version of the preparation approach of Zhao et al<sup>157</sup>. The sample was then transferred into the N<sub>2</sub> glovebox where the sample was transferred into a ZrO<sub>2</sub> MAS rotor and then sealed by a gastight Kel-F cap. The concentration of total (internal + external) acid sites were quantified by TMPO adsorption, while external active sites were determined by TBPO. The nature of the phosphine oxide was characterized by characteristic <sup>31</sup>P shifts. The concentration of acid sites was quantified from area ratio from NMR and the total P content determined by ICP-OES.

Inductively coupled plasma-optical emission spectrometry (Agilent ICP-OES 700) was used to determine the total P content of the zeolite after being titrated by

TMPO or TBPO. Typically, 40 mg of the P-loaded MWW sample was dissolved in a mixture of 2 mL of UA-1 solution (Inorganic Ventures), 0.2 mL of 70% nitric acid (BDH) and 10 mL UNS-1 solution (Inorganic Ventures). After visual confirmation, all of the solid dissolved, DI water was added to adjust the final solution volume to 100 mL. The concentration of P, Si and Al elements were determined using commercial standards (High-purity standards). Three scans were obtained for each element (Si, Al, P) and averaged to determine the concentration of each element from established calibration curves.

#### 2.2.4 Catalytic Measurements

Friedel-Crafts alkylation of benzene with benzyl alcohol reactions were carried out in septum-sealed, round-bottom flask with magnetic stirring. A fixed quantity of catalyst (30 mg) was added in a mixture of 0.54 g benzyl alcohol and 8.32 g benzene. Both reactants and catalyst were sealed into the flask and placed in an oil bath at 80 °C. Reaction mixtures were collected at a certain time period after cooling the flask to room temperature. The solution was evaluated using a gas chromatograph (Agilent 7890B) equipped with an FID detector and an Agilent HP-5 capillary column. Benzene was used as an internal standard. Both reactants, benzene and benzyl alcohol (BA), and products, diphenylmethane (DPM) and dibenzyl ether (DE), were calibrated, and their response factors were obtained. Benzyl alcohol is considered as a reactant with the conversion ( $X_{BA}$ ) defined as

$$X_{BA} = \frac{N_{BA,o} - N_{BA}}{N_{BA,o}} = \frac{N_{DPM} + N_{DE}}{N_{BA} + N_{DPM} + N_{DE}}, \quad (2-1)$$

where  $N_{BA,o}$  is the mole amount of benzyl alcohol in the feed and  $N_{BA}$ ,  $N_{DPM}$ , and  $N_{DE}$  are the mole amount of benzyl alcohol, diphenylmethane, and dibenzyl ether in the reaction mixture. The yield ( $Y_i$ ) of product,  $i$ , is defined as

$$Y_i = \frac{N_i}{N_{BA} + N_{DPM} + N_{DE}}, \quad (2-2)$$

where  $N_i$  is the mole amount of product in the reaction mixture.

## 2.3 Results and Discussion

### 2.3.1 Preparation of Disordered MWW-type Nanosheets

In this study, we use a modified protocol for conventional MCM-22 synthesis that employs hexamethyleneimine (HMI) as an OSDA. To the growth mixture, we add a commercially available quaternary ammonium surfactant, cetyltrimethylammonium (CTA). Established post-synthesis methods (top-down approaches) of MCM-22 delamination employ CTA as an exfoliating (or swelling) agent, where it is presumed that the hydrophobic tails of the surfactant aid in the separation of layers. Here, we use a bottom-up approach where the surfactant, with its positively-charged head group, has the ability to associate with negatively-charged aluminates in solution and/or Al tetrahedral sites within the MWW framework, thus creating opportunities for CTA to act as a secondary OSDA. The primary OSDA (HMI) is neutral in alkaline growth mixtures, but prior studies have indicated HMI can adopt a positive charge in confined channels of MWW zeolite, thereby acting as an extra-framework cation to counterbalance the negative charge of Al framework sites.<sup>158</sup> Through parametric analysis of synthesis mixtures prepared with a combination of HMI and CTA, we explore the putative role of the latter as a cooperative OSDA and dual exfoliating agent in the synthesis of MWW type materials.

Powder X-ray diffraction (PXRD) patterns were used to validate the successful synthesis of MWW type materials and qualitatively assess differences in the degree of layer disorder, which was specifically evaluated within the range  $2\theta = 6 - 10^\circ$  based on the common practice in literature<sup>94</sup> to differentiate interlayer distances along the  $c$

direction. As-synthesized MCM-22 (Figure 2.1, *i*) contains four peaks in this range. The position of the (002) inter-layer reflection, purely related to the layer thickness in the *c* direction, is located at  $6.5^\circ$ . Due to the presence of inter-layer reflections, (101) and (102), two discrete peaks appear at  $7.8^\circ$  and  $9.6^\circ$ , respectively. After calcination, the (002) reflection of the MCM-22 sample (Figure 2.1, *i-c*) shifts to  $7.0^\circ$  and overlaps with the (100) reflection due to the condensation of individual layers. As the CTA concentration in the growth mixture is increased to 5.5 wt% (Figure 2.1, *ii*) and 8.0 wt% (Figure 2.1, *iii*), the intensity of the (002) peak correspondingly decreases and the bands assigned for the (101) and (102) peaks gradually coalesce into a single broad peak. Both changes reflect the loss of long-range order in the *c* direction. When the quantity of CTA is further increased (e.g., 10 wt%), the PXRD pattern reveals a purely amorphous phase (Figure A1), thus indicating an upper limit of CTA that seemingly disrupts the nucleation of the MWW zeolite. For calcined samples prepared with CTA concentrations below this threshold (Figure 2.1, *ii-c* and *iii-c*), the single broad band at  $2\theta = 7.8 - 9.6^\circ$  is preserved, which confirms the disordered layer arrangement of CTA-derived materials (herein referred to as *d-MWW<sub>x</sub>* where *x* = weight percentage of CTA).

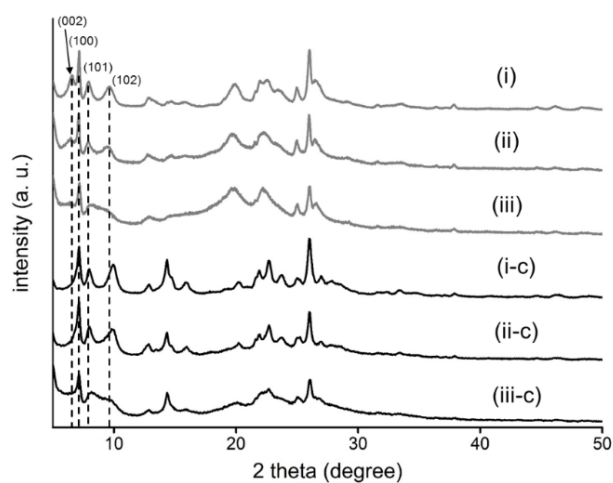


**Figure 2.1.** PXRD patterns of MWW type materials (gel Si/Al: 15) prepared with (i) 0, (ii) 5.5, and (iii) 8 wt% CTA. The top (grey) lines are as-synthesized material, whereas the bottom (black) lines are the calcined (*c*) materials.

To further investigate the degree of disorder of MWW type materials, Scanning Electron microscopy (SEM) and nitrogen adsorption/desorption measurements were performed. Electron micrographs of MCM-22 (Figure 2.2A and B) show aggregates of plate-like crystals. In comparison, the disordered material d-MWW (Figure 2.2C and D) is an interpenetrating network of nanosheets with apparent uniform thickness, consistent with PXRD patterns indicating CTA alters crystal morphology. Textural analysis (Table 2.1) can be used to quantify the degree of disorder for which we define a *disorder index* as the ratio between the external and total surface areas. We introduce this parameter as an approximate measure of MWW layer delamination. The addition of CTA from 0 to 8 wt% increases the disorder index from 0.2 to 0.6, respectively, thus indicating CTA quantitatively improves the separation of layers in MWW type materials. Nitrogen physisorption on calcined MCM-22 reveals a type I isotherm (Figure A4) whereas d-MWW samples exhibit a type IV isotherm. At the highest concentration of CTA (8 wt%), the isotherm is characteristic of a mesoporous material with a sharp increase in N<sub>2</sub> uptake at higher relative pressures and a large hysteresis loop, indicating the presence of high external surface area and mesoporosity (consistent with SEM images in Figure 2.2). At low relative pressure in the isotherms (i.e., the micropore filling region), the d-MWW materials prepared with 5.5 and 8 wt% CTA exhibit lower N<sub>2</sub> uptake compared to MCM-22. This is expected due to the loss of 10-membered ring (MR) channels and 12-MR supercages along the *c* direction (see Scheme 1.1) with an increasing percentage of disordered layers.

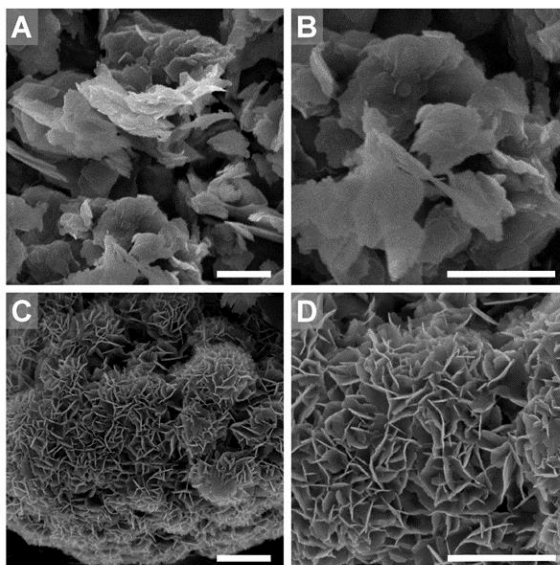


**Figure 2.2.** Scanning electron micrographs of calcined MWW type materials: (A and B) MCM-22; (C and D) d-MWW<sub>8.0</sub>. All scale bars are equal to 1  $\mu\text{m}$ .

Textural details and statistically-relevant measurements of the thickness of MCM-22 and d-MWW were assessed with cryogenic transmission electron microscopy (cryo-TEM). The collection of TEM images with the MWW samples cooled to liquid nitrogen temperatures enabled high-resolution imaging and long-time imaging of single samples to collect data over hundreds of nanosheets to quantify average thickness statistics. Contamination and radiation damage were suppressed significantly due to the low temperature and the use of the Falcon 3 direct electron detector, which allowed observation at low electron dose. Figure 2.3 is a summary of images collected with cryo-TEM for the d-MWW<sub>8.0</sub> sample. Figure 2.3A is a bright field high-resolution TEM (HRTEM) image collected at liquid nitrogen (LN2) temperature of d-MWW<sub>8.0</sub> zeolite sheets randomly oriented. The sheets, which are visualized “edge-on” ([001] direction perpendicular to the electron beam), appear dark and narrow. Figure 2.3B shows two of these sheets at higher magnification. The one on the left-hand side is a single unit cell thick, while the sheet on the right is two unit cells thick. Both high-resolution images of the zeolite crystal structure in Figure 2.3B are along a low indexed zone axis, type  $(xy0)$ . A small deviation ( $\sim 1^\circ$ ) from the observed zone axis would destroy the high-

resolution pattern. Therefore, these sheets are oriented nearly edge-on, which makes thickness measurements of the sheets accurate. The brightest areas in Figure 2.3A are “flat” sheets where the (001) normal is oriented parallel to the electron beam. A flat area at higher magnification (Figure 2.3C) shows a high-resolution image of the crystal structure of MWW zeolite in the (001) orientation. In Figure 2.3D, a model of the zeolite structure is superimposed on detail from Figure 2.3C under the conventional assumption that the bright areas are identical with the cages in the zeolite. A fast Fourier transform (FFT) of a single crystalline portion of the sample (Figure 2.3E) shows information transfer better than 0.2 nm.

**Table 2.1.** Properties of MWW materials produced with and without CTA

sample	DI <sup>a</sup>	BET S <sub>A</sub> <sup>b</sup> (m <sup>2</sup> /g)	External S <sub>A</sub> <sup>b</sup> (m <sup>2</sup> /g)	V <sub>micro</sub> <sup>b</sup> (ml/g)
MCM-22	0.2	634	149	0.19
d-MWW <sub>5.5</sub>	0.3	558	164	0.16
d-MWW <sub>8.0</sub>	0.6	557	359	0.09

<sup>a</sup>DI (disorder index) defined as the ratio between external and total surface areas, which are calculated using the BET method; <sup>b</sup> BET S<sub>A</sub> (surface area), External S<sub>A</sub> (external surface area) and V<sub>micro</sub> (micropore volume) calculated from N<sub>2</sub> adsorption isotherms.

Detailed analysis of HRTEM images was performed to quantify the average thickness of d-MWW nanosheets and to ascertain the statistical distribution of sizes among samples prepared with varying CTA concentration. Measurement of the thickness of MWW nanosheets as a function of sample treatment (wt% CTA) requires a substantial number of measurements to be statistically significant, since the spread in thickness for each sample is rather high. Selection of the sample area investigated had to be done without bias. A possible bias from a TEM study is to select the thinnest area(s) where image quality (contrast and resolution) is at an optimum. This bias ultimately excludes sheets thicker than a few unit cells. To avoid this situation, we employed two methods to measure nanosheet thickness: (i) electron energy loss

spectroscopy (EELS) based thickness measurement using the mean free path of electrons  $\lambda$  in the sample and (ii) measuring the thickness of sheets whose (001) basal surface is oriented perpendicular to the electron beam, as observed in a number of micrographs (see Figure 2.3A). The latter method is equivalent to edge-on imaging of the sheets and measurement of sheet thickness does not require high resolution, enabling quantification of thicker areas. Method (ii) resulted in a greater number of measurements than method (i), which requires high resolution to detect areas where multiple nanosheets are in line-of-sight. These areas have to be excluded because the thickness measurement results from more than one sheet; therefore, method (i) is limited to very thin areas, excluding thicker sheets and thus creating a biased selection of results. All thickness data presented here have been obtained with method (ii).

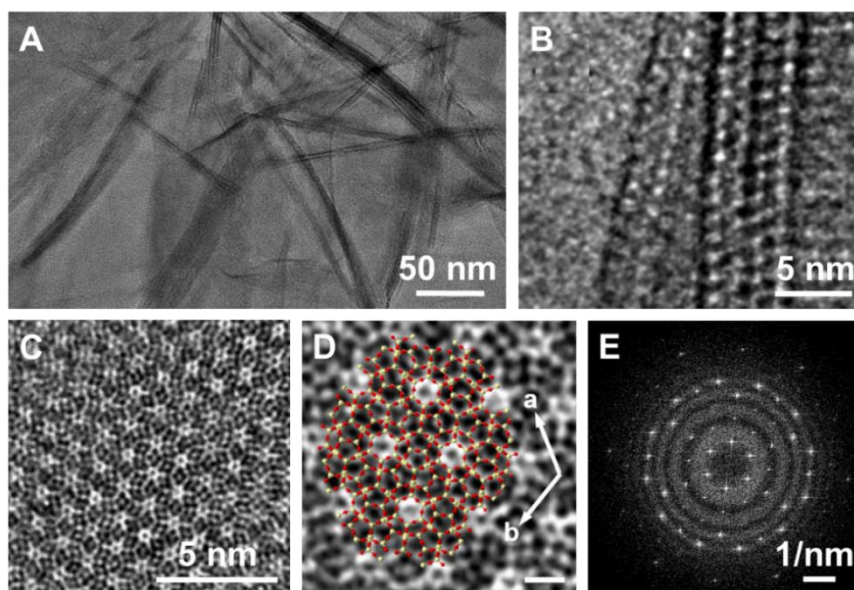


**Figure 2.3.** HRTEM images of disordered MWW (8 wt% CTA). (A) Bright field image (B-D) Magnified detail of panel A, scale bar of panel D equals 1 nm. (E) A fast Fourier transform (FFT) of a single crystalline portion of panel C.

Figure 2.4 represents the histograms of sheet thickness for MCM-22 and all d-MWW<sub>x</sub> samples. Each histogram is composed of at least 150 independent measurements. For each sample, the mean thickness (in nm) is 23.3 (MCM-22), 13.0

(d-MWW<sub>5.5</sub>), 7.5 (d-MWW<sub>7.5</sub>), and 3.5 (d-MWW<sub>8.0</sub>). A histogram consisting of more than 700 individual thickness measurements of d-MWW<sub>8.0</sub> is plotted in

Figure A2, where it is apparent that neither the skewed left nature of the histogram nor the average thickness change with an increased number of measurements. It is apparent from the images the spread of measured thicknesses is skewed to the left (i.e., a skewness parameter<sup>159</sup> ranging from 2.3 to 4.8). Skewness describes an asymmetry from the mean of the thickness distribution, where left skewness represents an imbalance with most of the data shifted to values smaller than the mean. We plotted histograms using a bin size of 2.5 nm, which represents a thickness equal to a single unit cell (*c*) of MCM-22. Therefore, the thickness is discretized and any reported value deviating from multiples of 2 nm are likely errors associated with the measurement of edge-on oriented particles due to edge effects and orientation of the nanosheets relative to the beam, which is not perfectly parallel (i.e., the orientation is off from the [001] zone axis). On this basis, the mean thickness should be interpreted as ca. 6 (MCM-22), 3 – 4 (d-MWW<sub>5.5</sub>), 2 (d-MWW<sub>7.5</sub>), and 1 (d-MWW<sub>8.0</sub>) unit cell dimensions. Further analysis of the histogram demonstrates the mode (thickness value encountered most often in data set) of each sample is 5 (MCM-22), 8 (d-MWW<sub>5.5</sub>), 1 – 1.5 (d-MWW<sub>7.5</sub>), and 0.5 – 1 (d-MWW<sub>8.0</sub>) unit cells. The data (obtained from a large sample number) demonstrate single unit cell nanosheets form in all syntheses (including MCM-22), but the distribution is skewed more heavily to a single unit cell or a few unit cell thick nanosheets with the addition of CTA. Indeed, the statistics demonstrate for d-MWW<sub>8.0</sub> that out of the 186 nanosheets measured, 85% are 1-2 unit cells thick. For the remaining samples, the corresponding percentages are 25% (MCM-22), 42% (d-MWW<sub>5.5</sub>), and 67% (d-MWW<sub>7.5</sub>).

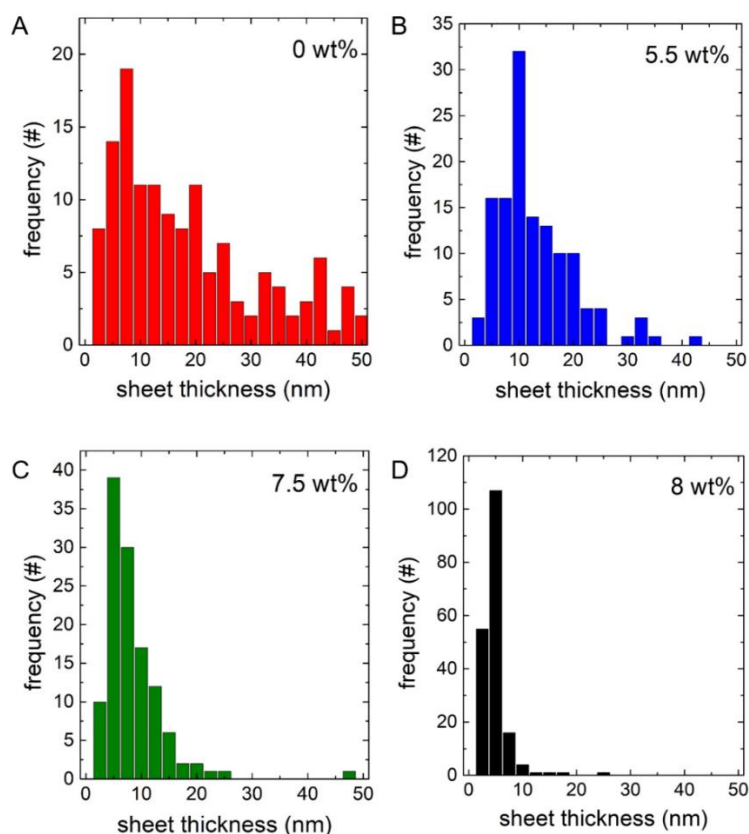


**Figure 2.4.** Histograms of layer thickness from HRTEM analysis of (A) MCM-22 and (B – D) d-MWW<sub>x</sub> samples prepared with the following CTA concentrations: (B) 5.5 wt%, (C) 7.5 wt%, and (D) 8.0 wt%.

### 2.3.2 Putative Role of CTA as an OSDA

Here we first examine the impact of CTA on Al siting using solid-state  $^{27}\text{Al}$  NMR measurements of MCM-22 and d-MWW samples. Elemental analysis of samples prepared with identical gel Si/Al ratio reveals CTA addition has a marginal effect on the product (solid) Si/Al ratio (Table 2.3). To discern potential differences in the spatial distribution of Al sites among samples, the local environments of Al(III) atoms were investigated by  $^{27}\text{Al}$  Multi-Quantum Magic Angle Spinning (MQMAS) NMR spectroscopy. The MWW framework consists of eight unique tetrahedral sites for Al occupancy (Scheme 1.1). Prior studies<sup>160-161</sup> have shown high-field (17.6 T)  $^{27}\text{Al}$  MAS is capable of distinguishing between three groups of tetrahedral (T) sites occupied by framework Al (FAI) at specific chemical shifts: Group A ( $\delta = 50$  ppm) refers to T<sub>6</sub> +

T<sub>7</sub>; Group B ( $\delta = 56$  ppm) refers to T<sub>1</sub> + T<sub>3</sub> + T<sub>4</sub> + T<sub>5</sub> + T<sub>8</sub>; and Group C ( $\delta = 61$  ppm) refers to T<sub>2</sub>. A fourth species detected at  $\delta = 0$  ppm (Group D) is octahedral-coordinated Al, which is often considered as extra-framework Al (EFAI). With known chemical shifts corresponding to different Al species, the deconvolution and curve fitting of 1-dimensional <sup>27</sup>Al NMR spectra were performed on both ordered MCM-22 (Figure 2.5A) and disordered d-MWW<sub>7.5</sub> (Figure 2.5B) using the previous assignments of FAI species.

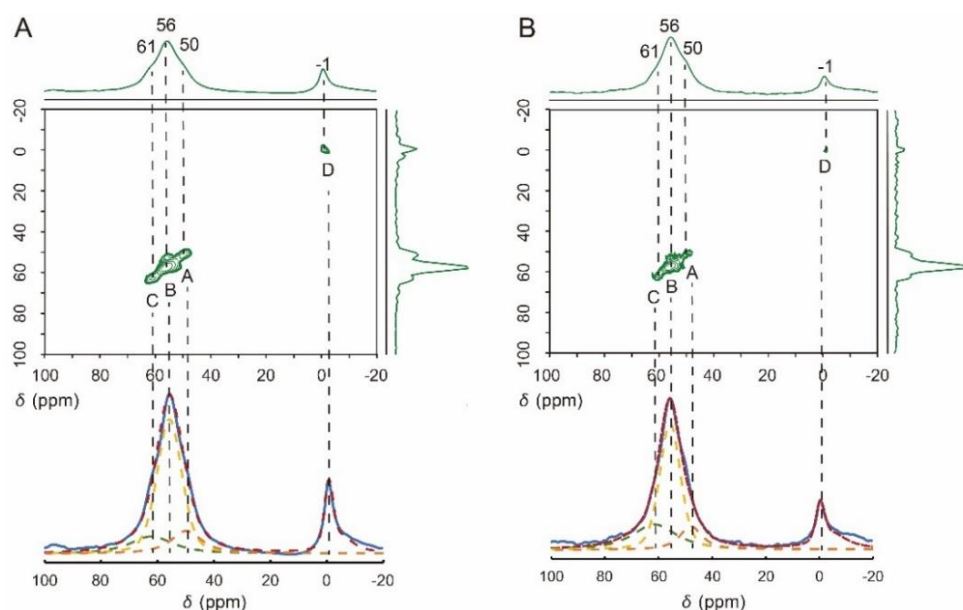


**Figure 2.5.** Two-dimensional <sup>27</sup>Al MQ MAS NMR spectra of H-form (A) MCM-22 and (B) d-MWW<sub>7.5</sub> samples (gel Si/Al: 15). Deconvolution of these two samples were performed on one-dimensional <sup>27</sup>Al MAS NMR spectra.

The integrated areas of deconvoluted peaks in Figure 2.5 are presented in Table 2.2 for MCM-22 and d-MWW<sub>7.5</sub> samples after ion exchange with NH<sub>4</sub><sup>+</sup> and calcination to generate H-form zeolites (i.e., catalysts used for studies discussed later). Similar measurements were performed on H-ITQ-2; however, the post-synthesis method involving delamination at high pH and temperature leads to the dissolution of framework Si, which generates defective FAI that renders NMR spectra too noisy for analysis (Figure A3A), consistent with prior reports indicating a loss of crystallinity during post-synthesis exfoliation.<sup>84</sup> Comparing the results of NMR analysis in Table 2.2, we observe the fraction of Al sites in Groups A, B, and D is similar for both ordered

and disordered materials. Interestingly, the quantity of Al in Group C (assigned to the T<sub>2</sub> site) increases from 15 to 25% with CTA addition. According to the distribution of T sites in Scheme 1.1, the T<sub>2</sub> site is located on the exterior surface of 2D nanosheets close to the outer rim of the 12-MR cup. The appreciable increase in T<sub>2</sub> content of d-MWW suggests CTA acts as an OSDA to alter the distribution of Al sites, and specifically place FAI species on the exterior surfaces where they are more accessible to bulky adsorbates. Although T<sub>1</sub> and T<sub>3</sub> (part of Group B) are also located at the exterior surface, Ivanova et al.<sup>162</sup> argued that the substitution of Al atom in eight T sites of MCM-22 took place in the order of T<sub>4</sub>  $\approx$  T<sub>2</sub> > T<sub>6</sub>  $\approx$  T<sub>8</sub>  $\approx$  T<sub>3</sub> > T<sub>7</sub> > T<sub>5</sub> > T<sub>1</sub>. Thus, the 5% reduction of Al content in Group B can be attributed to the loss of T<sub>4</sub> site. We also observe the one-pot process using combinations of CTA and HMI does not alter the occlusion of FAI species (i.e., both have similar Si/Al ratios; see Table 2.3), and both samples contain approximately the same quantity of EFAl species (Al<sub>(D)</sub> in Table 2.2).

**Table 2.2.** Relative peak areas of <sup>27</sup>Al MAS NMR spectra.

$\delta$ (ppm)	Al <sub>(A)</sub>	Al <sub>(B)</sub>	Al <sub>(C)</sub>	Al <sub>(D)</sub>
	50	56	61	-1
MCM-22 <sup>a</sup>	14%	54%	15%	17%
d-MWW <sub>7.5</sub> <sup>a,b</sup>	12%	48%	25%	15%

<sup>a</sup> H-form samples; <sup>b</sup> prepared with 7.5 wt% CTA

We performed a parametric analysis of synthesis conditions to determine the compositional range where d-MWW<sub>x</sub> can be prepared without appreciable loss of crystallinity. Syntheses were first performed in the absence of CTA at varying gel Si/Al ratios where we observed a systematic reduction in the disorder index of MCM-22 with increasing silicon content (Table A1). The quantification of percent crystallinity is difficult to extract from PXRD patterns owing to the broad peaks that overlap the region of amorphous product. To this end, we used textural analysis to evaluate changes in

both total BET surface area and micropore volume (Table A1). The disorder index increases with CTA concentration, irrespective of the gel Si/Al ratio; however, in more siliceous growth solutions the presence of CTA appears to stabilize an amorphous product. This is evident in syntheses using a gel Si/Al ratio of 45 where the PXRD patterns clearly show the presence of an amorphous peak (Figure A1); and the micropore volume correspondingly decreases well below 0.1 ml/g (Table A1) while the overall BET surface area monotonically decreases with increasing CTA concentration (Figure 2.6). At the lowest gel Si/Al ratio of 15, it is possible to prepare d-MWW over a relatively broad range of CTA concentration without a significant reduction in total BET surface area. Under these conditions, we observe an anticipated reduction in micropore volume (from 0.2 to 0.1 ml/g) and increasing disorder index (from 0.2 to 0.6) owing to the loss of supercages and channels with the formation of 2D nanosheets. For syntheses at intermediate silica content (gel Si/Al of 30), the determination of d-MWW formation is more convoluted. Based on the trend in total BET surface area (Figure 2.6), it appears d-MWW with a disorder index of 0.3 can be prepared with 4 wt% CTA, while higher surfactant concentration leads to lower total surface area and micropore volume less than 0.1 ml/g (Table A1). From these studies, it is evident that the ability of CTA to generate d-MWW is influenced by the Al content of the growth medium wherein it is possible to prepare disordered nanosheets with gel Si/Al ratios spanning from 15 to 30, outside the range of ITQ-2 (gel Si/Al = 50) reported in the literature. We posit the upper limit is attributed to the need for a sufficient number of Al sites occupying the surface of disordered layers to electrostatically interact with adsorbed CTA molecules. This would imply a minimum coverage of adsorbed CTA is required for disoriented layers along the *c*-axis and concomitant stabilization of surface Al species, which is favored at low Si/Al ratios.

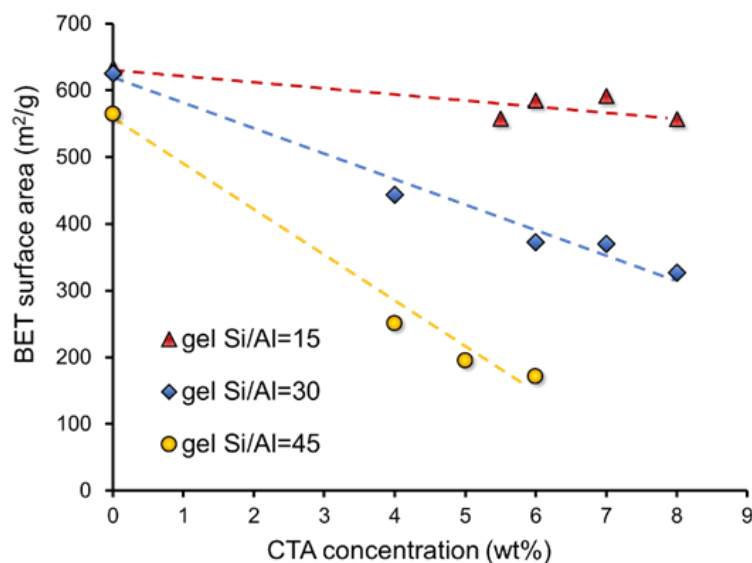


**Figure 2.6.** Parametric analysis of d-MWW synthesis at varying gel Si/Al ratios. The total BET surface area measured from N<sub>2</sub> sorption isotherms (Figure A4) is reported (solid symbols) for syntheses at varying CTA concentration.

Here we hypothesize the role of CTA in the synthesis of d-MWW (Figure 2.7).

For the preparation of ordered layered precursors at a high gel Si/Al ratio, it has been postulated<sup>61</sup> that neighboring layers interact via hydrogen bonding between opposing silanol groups and interstitial HMI molecules (Figure 2.7A). As the gel Si/Al ratio decreases, there is an increased probability of Al atoms becoming incorporated at surface sites on the layers. A higher surface density of Al sites leads to enhanced electrostatic interactions between the negative charges of framework Al and Na<sup>+</sup> counterions, which act as an inorganic structure-directing agent (Figure 2.7B). As the gel Si/Al ratio decreases from 45 to 15, the disorder index concomitantly increases from 0.13 to 0.24 (in the absence of CTA), suggesting the presence of Na<sup>+</sup> ions on layer surfaces impede layer alignment. In the presence of CTA, the positively-charged head group of the surfactant can also act as a counterion to balance framework Al atoms, which is consistent with the results of NMR analysis (Table 2.2) showing the ability of CTA to act as an OSDA (i.e., alter Al siting). Residual CTA in extracted solids after multiple steps of isolation involving extensive washing with water was confirmed by

thermogravimetric analysis (TGA) where we observe two different peaks (Figure A5), which we attribute to surface species and those occluded within pores (or between the interstitial regions of neighboring nanosheets). Moreover, we observe an appreciable reduction in the quantity of occluded HMI that accompanies an increased amount of CTA and  $\text{Na}^+$  (Table A2) measured from TGA and elemental analysis (ICP), respectively. This trend agrees with prior studies showing MCM-56 (partially disordered MWW) contains a higher content of  $\text{Na}^+$  and a lower amount of HMI compared to conventional MCM-22P.<sup>163</sup> For syntheses with CTA, we posit the long hydrocarbon tail of the surfactant can separate layers (Figure 2.7C), similar to the proposed mechanism of post-synthesis exfoliation.<sup>27</sup> The accumulation of CTA at exterior surfaces may impede layer-layer interactions, thus maximizing layer separation along the *c*-direction to generate disordered materials that are maintained even after the removal of organics by calcination.

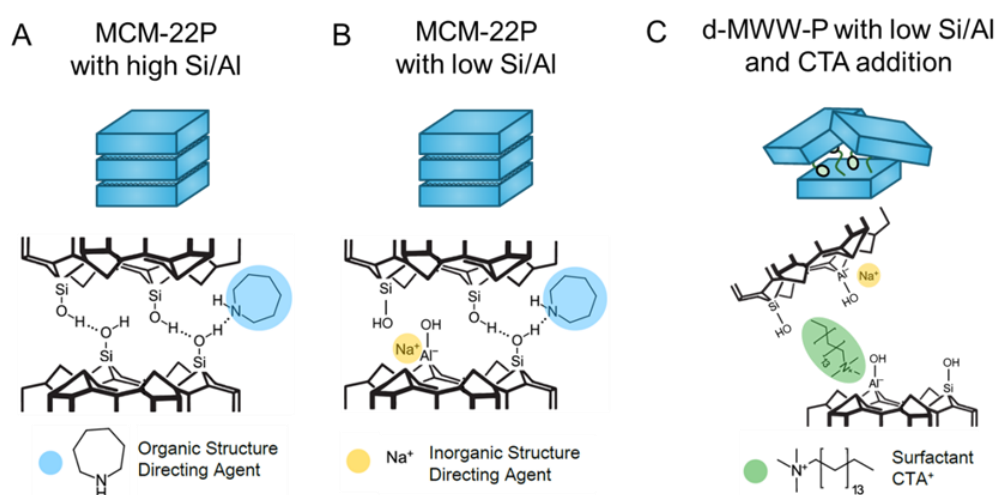


**Figure 2.7.** Putative roles of organic (HMI and CTA) and inorganic ( $\text{Na}^+$ ) structure-directing agents during the one-pot synthesis of MWW type materials. The illustrations are adapted from schemes reported by Roth et al.<sup>65, 163</sup>

### 2.3.3 Enhanced surface catalytic activity

A comparison of MWW type materials was performed using a model reaction to assess differences in catalyst lifetime and selectivity with increasing degree of layer

disorder. For comparison, we tested our material against a conventional disordered MWW material. The two most commonly reported disordered MWW type materials, MCM-56 and ITQ-2, have surface areas of ca. 211 and  $\geq 700$  m<sup>2</sup>/g, respectively.<sup>27, 93</sup> Given the higher degree of disorder in ITQ-2, we used this material as a reference and we prepared a sample following a reported post-synthesis delamination protocol<sup>27</sup> (with the Si/Al gel ratio reduced to match the Al content of d-MWW). All as-synthesized samples were converted to H-form by standard NH<sub>4</sub><sup>+</sup> ion exchange and calcination. The internal and external acidity of H-MCM-22, H-d-MWW<sub>x</sub>, and H-ITQ-2 was determined by a method reported in the literature for MWW-type materials based on the adsorption of two molecules, a less bulky trimethylphosphine oxide (TMPO) and a more bulky tributylphosphine oxide (TBPO), using solid-state <sup>31</sup>P NMR spectroscopy. The <sup>31</sup>P NMR spectra for TMPO and TBPO adsorption on MWW type samples reveal complex spectra composed of a number of distinct species (deconvoluted spectra for TMPO and TBPO can be found in Figure A6 and Figure A7, respectively). Prior studies discussed the sites accessible by each of the phosphine oxide probe molecules used in this study. Zhao and co-workers<sup>157</sup> stated TMPO can access acid sites in both the 10-MR channels (internal acid sites) as well as the external acid sites present in the 12-MR pockets. Therefore, the total amount of titrated TMPO represents the total number of acid sites accessible on MWW-type zeolites. More recently, Luo and co-workers<sup>31</sup> have utilized the same probe molecules to probe internal and external acid sites on MIT-1; their assignments agreed with those used by Zhao. TBPO is presumed to only access the 12-MR pockets on the exterior surfaces.<sup>164</sup> Here, like the previous groups, we posit TMPO is capable of accessing the same sites as TBPO given that its size is less restricted; therefore, it can be assumed that the amount of adsorbed TMPO constitutes the total number of H<sup>+</sup> sites, while the amount of adsorbed TBPO is a measure of external active

sites. Luo conducted DFT calculations to confirm the  $^{31}\text{P}$  chemical shifts at 85, 72, 68 and 63 ppm are associated with Brønsted acid sites present in the 10-MR and 12-MR channels of MCM-22.<sup>31</sup> Luo also suggested the peak at 53 ppm is associated with Lewis acid sites; which appears to be a controversial assignment. Since the fraction of TMPO assigned to a 53 ppm chemical shift is small and no peak at 53 ppm was observed for any sample using TBPO, we opt not to make any definitive statement regarding the presence of Lewis acid sites on the MWW-type zeolites.

Table 2.3 summarizes the measured TMPO and TBPO adsorbed concentrations for all catalysts. A total of ten resonance peaks at chemical shifts of  $\delta = 82, 78, 69, 66, 58, 53, 48, 42, 36,$  and 33 ppm (Table A3) were identified for samples with adsorbed TMPO. The peaks at  $\delta = 82, 78, 69, 66, 58,$  and 53 ppm correspond internal acid sites present in the 12-MR pockets and 10-MR pores; and the peaks at 48 and 42 correspond to physisorbed TMPO and the peaks at 36 and 33 ppm correspond to crystalline TMPO (not associated with the zeolite).<sup>31</sup> Six resonances at chemical shifts  $\delta = 75, 71, 62, 57, 50,$  and 46 ppm (Table A3) were identified for adsorbed TBPO. Peaks at  $\delta = 75, 71,$  and 62 ppm correspond to TBPO bound to external acid sites, whereas the peak at 57 ppm corresponds to physisorbed TBPO and the peaks at 50 and 46 ppm correspond to crystalline TBPO. The total quantity of acid sites (both internal and external) was measured using spectra integration coupled with ICP-OES elemental analysis of P.<sup>31</sup>

157

**Table 2.3.** Summary of Al content and adsorbed probe (TMPO and TBPO) amounts in H-MWW samples

Sample	Si/Al <sup>c</sup>	[Al] (mmol g <sup>-1</sup> )	[TMPO] (mmol g <sup>-1</sup> ) <sup>d</sup>	[TBPO] or [H <sup>+</sup> ] <sub>ext</sub> (mmol g <sup>-1</sup> ) <sup>d</sup>	[H <sup>+</sup> ] <sub>int</sub> (mmol g <sup>-1</sup> )
H-MCM-22 <sup>a</sup>	11.2	0.76	0.43	0.05	0.38
H-d-MWW <sub>5.5</sub> <sup>a</sup>	12.7	0.68	0.18	0.07	0.11
H-d-MWW <sub>8.0</sub> <sup>a</sup>	12.7	0.67	0.44	0.06	0.38
H-ITQ-2 <sup>a</sup>	20.3	0.48	0.19	0.10	0.09
H-ITQ-2 <sup>b</sup>	45.0	0.20	0.11	0.06	0.05

a. samples prepared with gel Si/Al = 15; b. samples prepared with gel Si/Al = 45; c. determined by ICP-OES; d. determined from ICP-OES and <sup>31</sup>P NMR spectroscopy.

A comparison of acid site densities in Table 2.3 reveals discrepancies between the total amount of Al sites measurement by ICP-OES, labeled as [Al], and that of TMPO adsorption that presumably represents the total number of Al sites. The comparison of <sup>27</sup>Al MAS NMR spectra for all samples indicates an average 15 – 20% extra-framework Al ( Table 2.2), which likely accounts for some (but not all) of these differences. Additional considerations may include steric constraints that limit the number of accessible sites for TMPO adsorption. For example, Al sites located at the bottom of 12-MR pockets on the external surfaces may be too confined for TMPO adsorption. This would also be true for the bulkier TBPO probe molecule, which may be unable to efficiently bind to Al sites in external pockets. The latter hypothesis may explain why the number of external acid sites, [H<sup>+</sup>]<sub>ext</sub>, does not appreciably increase with higher CTA concentration (counter to the increased external surface area from BET analysis in Table 2.1). Collectively, our data seems to highlight inherent problems with the conventional use of TMPO and TBPO as probe molecules and has prompted ongoing studies in our groups to identify alternative methods of acid site titration (outside the scope of this study).

Another interesting observation is that H-d-MWW<sub>5.5</sub> and H-ITQ-2 exhibit markedly lower acid density than the other samples. The H-ITQ-2 sample has a notably higher Si/Al ratio than other samples, which partially explains this observation; however, <sup>27</sup>Al MAS NMR analysis reveals defective Al in this material (Figure A3), which may influence the measurements in Table 2.3. For the case of H-d-MWW<sub>5.5</sub>, the reasoning for low acid site density is less intuitive. It seems as though intermediate concentrations of CTA, which correspond to the transition between ordered and disordered MWW-type materials, has an apparent impact on Al siting that is not well understood. This suggests an optimal CTA concentration (ca. 6 – 8 wt%) where values below this range lead to seemingly defective materials, while values above this range result in an amorphous product. The exact mechanism for this effect remains elusive.

To assess the catalytic performance of our materials, we selected the Friedel-Crafts alkylation of benzyl alcohol (BA) with benzene as a model reaction<sup>28, 31, 165</sup> employing bulky molecules (Figure 2.8A) that can only access external sites on MWW-type catalysts. Liquid-phase batch reaction was performed at 80°C using a large excess of benzene. Aliquots of the reaction mixture were removed at periodic times to analyze the products by gas chromatography (Figure A8). A comparison of BA conversion at fixed reaction time (9 h) is shown in Figure 2.8B (left axis) based on an equivalent mass of catalyst. As shown in Table 2.3, the Si/Al ratios of H-MCM-22 and H-d-MWW<sub>x</sub> (with  $x = 5.5$  and 8 wt% CTA) are approximately equal, whereas H-ITQ-2 has a slightly higher Si/Al ratio. At equivalent mass, the H-d-MWW<sub>8.0</sub> catalyst exhibits much higher conversion among these four catalysts owing to its larger external surface area and the increased density of Al sites in external 12-MR pockets (as inferred from Table 2.2). Notably, the conversion for H-d-MWW<sub>8.0</sub> catalyst is ca. 30% higher than that of H-MCM-22. Normalization of reacted BA by the total number of external acid sites

reveals H-MCM-22 and H-d-MWW<sub>8.0</sub> have a comparable turnover number (TON) (Figure 2.8B, right axis), and similar activity evaluated after 9 h (Figure A8). Conversely, the TON of H-d-MWW<sub>5.5</sub> and H-ITQ-2 are markedly lower, reflecting a lower activity. For H-ITQ-2, we attribute this observation to its high percentage of defective (or non-framework) Al sites, which is evident in <sup>27</sup>Al MQMAS NMR spectra (Figure A3). To confirm that the preparation of ITQ-2 with increased Al content did not impact its structural integrity, we also prepared a sample according to the original recipe (with a higher gel Si/Al ratio of 45)<sup>155</sup> and observed a similar, albeit slightly lower, turnover number as the ITQ-2 sample prepared with a gel Si/Al ratio of 15 (Figure A8). For H-d-MWW<sub>5.5</sub>, the lower catalytic activity is more difficult to rationalize. As previously discussed, the incorporation of Al in d-MWW at intermediate CTA concentrations is less effective, which correlates with decreased BA conversion.

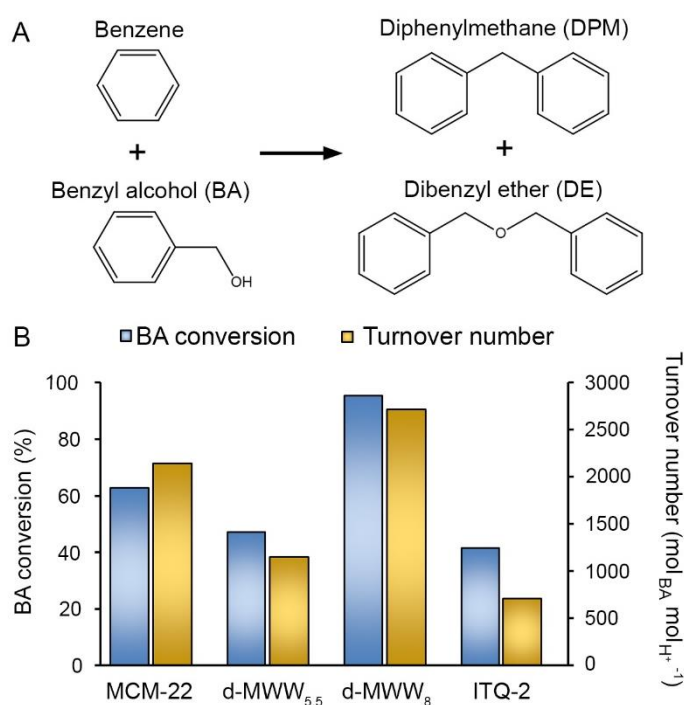


**Figure 2.8.** (A) Model reaction used to assess the performance of MWW-type catalysts. (B) Benzyl alcohol (BA) conversion (blue, left axis) and turnover number (yellow, right axis) for the four H-form MWW-type samples.

## 2.4 Summary

In summary, we present a direct route to prepare disordered MWW type nanosheets (d-MWW) without the need for post-synthesis exfoliation or the use of elaborate organic structure-directing agents. The one-step approach is accomplished through the addition of a commercial surfactant, cetyltrimethylammonium, to a conventional MCM-22 growth mixture. A combination of powder X-ray diffraction and N<sub>2</sub> desorption/adsorption analyses reveal high surface area nanosheets are generated within a narrow range of growth mixture composition (Si/Al = 15 – 30) and quantity of added surfactant (6 – 8 wt% CTA). These studies indicate CTA behaves as an *in situ* exfoliating agent wherein we posit that the positively-charged amine groups of the surfactant associate with negatively-charged Al sites on the surfaces of d-MWW nanosheets; however, solid-state <sup>27</sup>Al NMR spectra of d-MWW reveals that CTA also behaves as a structure-directing agent by virtue of its ability to alter Al siting, placing additional acid sites within the 12-membered ring pockets lining the exterior surfaces. The number of Brønsted acid sites within the interior and exterior of MWW type materials was scrutinized through a combination of elemental analysis and <sup>31</sup>P MAS NMR using two acid titrant: trimethylphosphine oxide and tributylphosphine oxide. The size disparity between these molecules allowed for the former to access both internal and external sites, whereas the latter is only able to access external sites owing to its large size relative to the 10-membered ring pores granting access to the interior supercages and sinusoidal channels.

A combination of high surface area and increased number of external Brønsted acids for d-MWW compared to its 3-dimensional analogue, MCM-22, results in greater access to surface sites for reactions involving bulky organic molecules. To this end, we tested the catalytic performance of several MWW type materials using Friedel-Crafts

alkylation of benzyl alcohol with benzene as a model reaction. Our findings reveal the conversion of benzyl alcohol is markedly faster. Comparisons of turnover number reveal that d-MWW exhibits similar activity as MCM-22; however, preparation of 2D nanosheets through post-synthesis exfoliation reveals that the resulting catalyst, ITQ-2, is highly defective (e.g., extra-framework or distorted Al sites) and exhibits poor catalytic performance in the Friedel-Crafts alkylation reaction. Collectively, our findings indicate the direct incorporation of long-chain surfactant into syntheses of MWW type materials can lead to disordered 2D materials. It remains to be determined if this approach can be used as a generalized methodology for other layered zeolites to generate high surface area nanosheets. It is evident, however, the success along these lines could have practical implications for the rational design of zeolite catalysts for a broad range of applications.

## Chapter 3

### Silver-Promoted Dehydroaromatization of Ethylene over ZSM-5 Catalysts

The majority of material discussed in this chapter has been published. Figure and table numbers have been changed for dissertation consistency. The work was in collaboration with Dr. Hari Thirumalai and Prof. Lars C. Grabow from the University of Houston.

#### 3.1 Motivation

Aromatic hydrocarbons (e.g., benzene, toluene, and xylene isomers) are essential precursors in the chemical industry, such as fuel additives, raw materials for polymers, and other value-added aromatics-derived products.<sup>129-130</sup> Developing alternative routes for aromatics production is desirable due to the limited supply of fossil fuels, which are the main feedstocks for producing aromatics.<sup>131-132</sup> Due to the recent rapid growth of methane and light olefin feedstocks<sup>133</sup>, one promising route is directly converting methane/ethylene to aromatics. Numerous studies have done regarding methane<sup>103, 136</sup> and propane<sup>98</sup> dehydroaromatization (DHA) reactions. In comparison, ethylene to aromatics attracted relatively little attention,<sup>135</sup> although new technologies, such as ethane dehydrogenation<sup>138-140</sup>, have been developed for ethylene production. In addition, ethylene, as a feedstock, can be coupled with methane to form propylene with/without the presence of oxygen.<sup>108, 143</sup> While prior literature has focused on ethylene upgrading over nickel-based catalysts,<sup>144-146</sup> there are disproportionately fewer studies of ETL reactions catalyzed by metal-containing zeolite catalysts.<sup>9, 107, 147-148</sup>

Zeolites are shape-selective microporous catalysts that are widely used in refining and (petro)chemical processes owing to their unique porous topologies, high thermal stability, and tunable acidity.<sup>17-19</sup> The incorporation of aluminum in the zeolite framework creates a negative charge that is counterbalanced by an extra-

framework cation (either a Brønsted or Lewis acid site). The use of metal Lewis acids broadens the range of catalytic applications, e.g., hydroisomerization reactions,<sup>166-168</sup> selective catalytic reduction (SCR) in catalytic converters,<sup>169-171</sup> and the production of fine chemicals,<sup>172-175</sup> among others. Herein, we examine Ag-exchanged MFI (Ag-ZSM-5), which has proven to be an active catalyst for SCR,<sup>176-178</sup> CO oxidation,<sup>179-180</sup> and alkane aromatization<sup>181</sup> reactions. The activity of Ag-ZSM-5 catalysts is attributed, in part, to the redox and acidic properties of Ag species.<sup>108, 182</sup> For example, Ag-ZSM-5 exhibits superior selectivity to aromatics in isobutane aromatization than Ga-ZSM-5 (a common catalyst for alkane aromatization).<sup>105</sup> Interestingly, Ag-ZSM-5 has been proposed as an alternative catalyst for NOC of methane (or methane/ethylene co-feed) at moderate temperatures (e.g., 400 °C).<sup>108</sup> Such reaction conditions are less severe than those required for direct non-oxidative methane upgrading via dehydroaromatization (DHA) at temperatures of 700 °C or higher.<sup>103, 136</sup> Despite prior studies of Ag-ZSM-5 performance in NOC reactions,<sup>108</sup> the mechanism of methane activation over Ag sites in NOC (in the absence or presence of ethylene) is a topic of debate.<sup>183</sup> Specifically, it has been suggested that Ag species catalyze the rate-determining the C-H bond activation of methane via two possible pathways: the formation of silver hydride species (i.e., Ag-H)<sup>184-185</sup> or silver-methyl complexes (i.e., Ag-CH<sub>3</sub>).<sup>186</sup>

In this chapter, motivated by the lack of ethylene dehydroaromatization work in the literature and the ambiguous role of Ag-ZSM-5 in ETL reactions, we investigated the role of Ag species in NOC of ethylene with and without methane co-feed. Our findings reveal that Ag-ZSM-5 promotes the formation of aromatics in ETL, whereas H-ZSM-5 preferentially yields light olefins and other aliphatic hydrocarbons. We observe that methane co-feed is activated over Ag-ZSM-5 catalysts with smaller conversion than previously reported, whereas H-ZSM-5 is an inactive catalyst for

methane upgrading under identical reaction conditions. In an effort to rationalize these observations, we studied the adsorption and activation of methane and ethylene on H-ZSM-5 and Ag-ZSM-5 using periodic, van der Waals corrected density functional theory (DFT). Our results show that on H-ZSM-5 ethylene reacts with a moderate activation barrier, while methane is for practical purposes inert. On Ag-ZSM-5, however, methane activation requires a lower energy barrier than ethylene, but ethylene binds strongly to the  $\text{Ag}^+$  active site and blocks access to methane. These findings are consistent with our catalytic studies showing that  $\text{Ag}^+$  species promote aromatization and exhibit much lower activity for methane upgrading.

## **3.2 Experimental Methods**

### **3.2.1 Zeolite Catalyst Preparation**

$\text{NH}_4$ -ZSM-5 catalyst was purchased from Zeolyst International (product number 2314). Introduction of silver extraframework cations (Ag-ZSM-5) was accomplished by solution Ag ion exchange at room temperature in the absence of light for 24 h. Solutions for ion exchange were prepared with 100 mL  $\text{AgNO}_{3(\text{aq})}$ /g of  $\text{NH}_4$ -ZSM-5, where the  $\text{AgNO}_{3(\text{aq})}$  concentration was adjusted by dissolving  $\text{AgNO}_{3(\text{s})}$  ( $\geq 99\%$ , Sigma-Aldrich) to reach the targeted Ag loading in the final product. Detailed information is provided in the Appendix (Table B1). Following ion exchange, Ag-ZSM-5 samples were dried in air at room temperature overnight and calcined under flowing air (ultra-zero grade, Matheson Tri-gas Inc.). Calcination was performed by increasing the temperature from 25 to 120°C at a rate of 1°C/min, held at 120°C for 2 h, and then a second ramping to 500°C at 1°C/min and held for an additional 2 h. Following this dwell time at 500°C, the temperature was cooled to room temperature.

The same calcination profile was applied to as-received samples to convert extra-framework  $\text{NH}_4^+$  to  $\text{H}^+$  Brønsted acid sites.

### 3.2.2 Characterization

Ag-ZSM-5 catalysts were characterized by powder X-ray diffraction (XRD), energy dispersive X-ray spectroscopy (EDX), solid-state UV-Vis spectroscopy, and X-ray photoelectron spectroscopy (XPS). Powder XRD patterns were acquired from 5 to  $50^\circ 2\theta$  with a step size of  $0.02^\circ$  at 40 kV and 44 mA using a Rigaku Smartlab X-ray Diffractometer. EDX analyses were performed using a JEOL JSM 6330F Field Emission scanning electron microscope (SEM). Solid-state UV-Vis spectra were obtained at wavelengths 200 – 800 nm with a step size of 1 nm using an Aglient Cary 5000 UV/VIS/NIR spectrometer. The UV-Vis reference spectrum was collected using polytetrafluoroethylene fine powder, and the Kubelka-Munk function,  $F(R)$ , was selected as the measuring mode. XPS spectra were collected from a Physical Electronics Model 5700 XPS instrument. A monochromatic  $\text{Al-K}\alpha$  X-ray source (1486.6 eV) was used with the power at 350 W. All spectra were obtained once reaching a vacuum of  $5 \times 10^{-9}$  torr or better. The binding energy was calibrated with the C 1s peak at 284.8 eV. Micropore volume was measured by  $\text{N}_2$  adsorption using a Micromeritics ASAP 2020 instrument. Samples were degassed at  $350^\circ\text{C}$  for 4 h before  $\text{N}_2$  adsorption.

### 3.2.3 Catalytic Measurements

Prior to reaction tests, catalysts were pelletized, crushed, and sieved to generate aggregates of size 250 to 400  $\mu\text{m}$  (i.e., 40 – 60 mesh). For each catalytic measurement, pelletized catalyst (6 – 120 mg) was diluted with 500 – 550 mg of quartz sand (50 – 70 mesh, Sigma-Aldrich) to avoid temperature gradients in the catalyst bed. For time-on-stream studies,  $\text{Ag}_{25}$ - and H-ZSM-5 catalysts (~150 mg) were used without inert quartz

sand. This catalyst bed was supported between quartz wool in a tubular, single-pass fixed bed reactor. Temperature was regulated with a ThermoScientific Lindberg Blue M furnace using a K-type thermocouple inserted at the bottom of the quartz wool bed (on the effluent side). All catalysts were pretreated *in situ* under the flow of 24 ml/min N<sub>2</sub> (99.999%, Praxair) and 6 ml/min O<sub>2</sub> (99.993%, Praxair). During pretreatment, the temperature was increased to 250°C at a rate of 1°C/min and then was further ramped to 500°C in 2 h and held for 3 h. After pretreatment, the temperature was decreased to 400°C under flowing Ar (99.999%, Praxair) and was held for at least 1 h before catalytic measurements. The inlet gas containing methane (99.99%, Praxair) and/or ethylene (99.999%, Matheson Tri-gas Inc.) was diluted with Ar (99.999 %, Praxair) to the desired reactant partial pressure. Various space velocities were achieved by changing the amount of catalyst and/or gas flow rate. Effluent gas was analyzed using an on-stream mass spectroscopy/gas chromatography instrument (Agilent MSD 5977A/GC 7890B). Reactant conversion and product selectivities were calculated on a carbon mole basis.

### 3.2.4 Density Functional Theory Calculations

Density functional theory (DFT) calculations were carried out using the Vienna Ab-initio Simulation Package (VASP) in combination with the Atomic Simulation Environment (ASE).<sup>187-190</sup> The projector augmented wave (PAW) method<sup>191</sup> and the Bayesian error estimation functional with van der Waals correction (BEEF-vdW)<sup>192</sup> were used to solve the Kohn–Sham equations. This functionality has been shown to quantitatively describe van der Waals interactions as well as reaction kinetics in zeolite pores.<sup>193</sup> All calculations were performed with a cutoff energy of 540 eV, Gaussian smearing of  $k_B T = 0.1$  eV<sup>194</sup> and  $\Gamma$ -point sampling was used to sample the Brillouin-zone. All calculations were run such that the residual force on each atom did not exceed

0.05 eV/Å. Transition state energies and structures were obtained from the climbing image nudged elastic band method and subsequently refined using the Dimer method.<sup>195-196</sup>

The ZSM-5 periodic unit cell was optimized for use with the BEEF-vdW functional, and lattice constants were found to be  $a = 20.26 \text{ \AA}$ ,  $b = 19.91 \text{ \AA}$  and  $c = 13.26 \text{ \AA}$ . These lattice parameters correspond to an error of less than 1% from those obtained experimentally.<sup>197</sup> The activation and subsequent dissociation of methane and ethylene were modeled to occur at the intersection of straight [010] and tortuous sinusoidal channels [100], specifically at the T12 site. The Si atom at this tetrahedral (T) site was replaced with Al and the resulting negative charge was balanced by  $\text{Ag}^+$  or  $\text{H}^+$ , thus forming charge-neutral models for Ag-ZSM-5 and H-ZSM-5, respectively. The binding energies are reported with reference to  $\text{CH}_4$  and  $\text{C}_2\text{H}_4$  centered in a  $12 \times 12 \times 12 \text{ \AA}$  box and otherwise the same settings as used for the zeolite calculations, but with  $k_B T = 0.01 \text{ eV}$ .

### 3.3 Results and Discussion

#### 3.3.1 Preparation of Bifunctional Ag-ZSM-5 Zeolite Catalyst

$\text{Ag}_n$ -ZSM-5 catalysts with different Ag loadings were prepared by conventional solution Ag ion exchange to achieve loadings of  $n = 8, 15,$  and  $25$  (where  $n$  is the percentage of Al sites occupied by Ag). Details of this procedure are provided in the Experimental Section and Table B1 of the Appendix. Powder X-ray diffraction (XRD) patterns confirm the structural integrity of ZSM-5 (MFI framework, Figure 3.1A, *i*) and the absence of impurities after Ag ion exchange (Figure 3.1A, *ii*). For instance, common impurities may include large metallic Ag particles that would be visible in the XRD patterns at  $2\theta = 38.3$  and  $44.2^\circ$ ,<sup>198</sup> if present at appreciable weight percentage. The long-range ordering of Ag-ZSM-5 samples remains intact after calcination (Figure 3.1A, *iii*),

as revealed by the nearly identical XRD patterns. Furthermore, textural analysis of Ag<sub>25</sub>-ZSM-5 (Table 3.1) reveals a micropore volume (0.12 ml/g) that is similar to its parent H-ZSM-5 (0.14 ml/g), suggesting the presence of Ag species does not significantly reduce accessible pore volume.

**Table 3.1.** Chemical composition and textural properties of MFI zeolites

Sample	Si/Al <sup>[a]</sup>	Ag/Al <sup>[a]</sup>	Si/Al <sup>[b]</sup>	Ag/Al <sup>[b]</sup>	Pore volume (ml/g) <sup>[c]</sup>
H-ZSM-5	10.0 ± 0.6	-----	10.2	N/A	0.14
Ag <sub>25</sub> -ZSM-5	10.3 ± 0.8	0.24 ± 0.07	10.8	0.52	0.12

[a] Measured by EDX; [b] Measured by XPS; [c] Determined by t-plot

Metal species with different oxidation states and clusters thereof can significantly influence the performance of microporous catalysts.<sup>199-206</sup> To assess the oxidation state(s) of extra-framework Lewis acid sites in Ag-ZSM-5, we used X-ray photoelectron spectroscopy (XPS) to characterize as-prepared and calcined Ag<sub>25</sub>-ZSM-5. XPS spectra (Figure 3.1B) reveal two bands at 375.3 and 369.3 eV separated by 6 eV, which are assigned to Ag 3d<sub>3/2</sub> and Ag 3d<sub>5/2</sub>, respectively. These two characteristic bands are consistent with literature values of Ag-ZSM-5 and AgNO<sub>3</sub>,<sup>207-208</sup> indicating that both as-prepared and calcined Ag<sub>25</sub>-ZSM-5 are predominantly comprised of Ag<sup>+</sup> species. Interestingly, XPS surface analysis of as-prepared Ag<sub>25</sub>-ZSM-5 indicates an Ag/Al ratio that is nearly two-fold higher than the value measured by EDX (0.24 ± 0.07). XPS has a short penetration depth (ca. 5 nm)<sup>209</sup> in the sample, and thus elemental analysis by this technique is biased to the exterior region of zeolite particles. Conversely, EDX has a much longer penetration depth capable of assessing the catalyst interior. Differences between XPS and EDX are indicative of spatial gradients in composition throughout the zeolite sample. Similar comparisons of the Si/Al ratio for H-ZSM-5 and Ag<sub>25</sub>-ZSM-5 (Table 3.1) reveal the absence of Al zoning – meaning that Al is uniformly

distributed throughout the zeolite particle. As such, Ag zoning (i.e., a higher percentage of Ag located at the exterior region of zeolite particles) is uncorrelated with the spatial distribution of Al sites. The exact origin of Ag zoning in Ag<sub>25</sub>-ZSM-5 is not well understood and is the subject of an ongoing investigation.

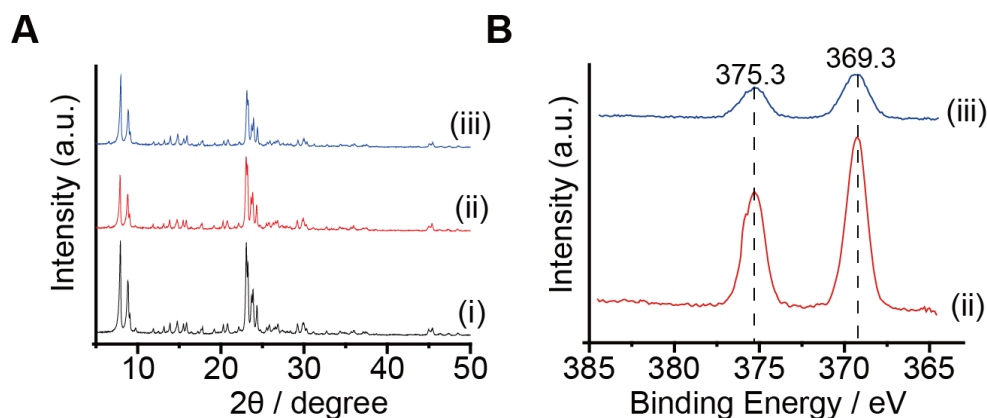


**Figure 3.1.** Powder XRD patterns and XPS spectra of (i) H-ZSM-5, (ii) as-prepared Ag<sub>25</sub>-ZSM-5, and (iii) calcined Ag<sub>25</sub>-ZSM-5 are shown in black, red, and blue, respectively.

XPS surface analysis confirmed that as-prepared and calcined Ag<sub>25</sub>-ZSM-5 samples contain Ag<sup>+</sup> ions as primary Lewis acid sites. This finding is consistent with solid-state UV-Vis spectroscopy measurements of Ag species. Notably, Figure 3.2A shows the UV-Vis spectrum of calcined Ag<sub>25</sub>-ZSM-5 with an absorption band at ca. 220 nm. This band, which has been observed in other Ag-exchanged zeolite catalysts,<sup>198, 208</sup> has been assigned to the intra-ionic electronic transition (*i.e.*, [Kr]4d<sup>10</sup> → [Kr]4d<sup>9</sup>5s<sup>1</sup>) on isolated Ag<sup>+</sup> ions. In addition, there is a broad absorption band spanning from 260 to 330 nm that is likely attributed to Ag clusters.<sup>210-212</sup> It is unlikely that metallic Ag is present given the absence of an absorption band at 405 nm.<sup>213</sup> In summary, a combination of XRD, XPS, and UV-Vis measurements collectively reveal that Ag<sup>+</sup> is the dominant Lewis acid site in Ag<sub>25</sub>-ZSM-5 (as illustrated in Figure 3.2B).

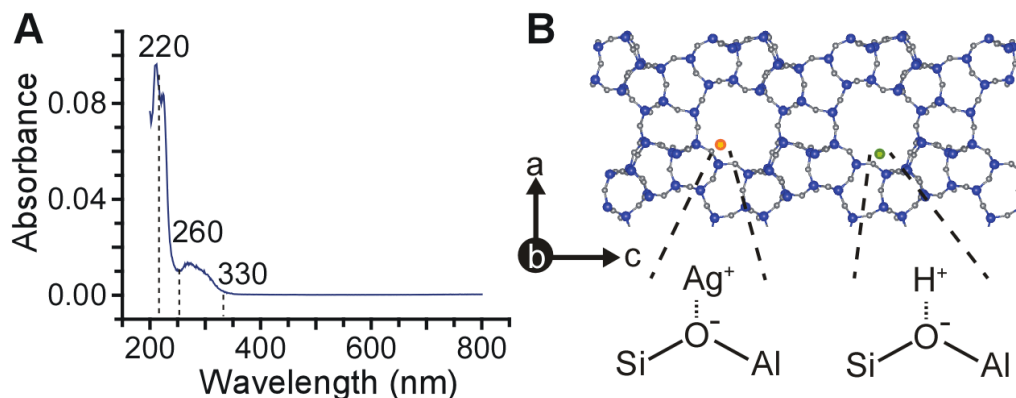


**Figure 3.2.** (A) Solid-state UV-Vis spectrum of calcined Ag<sub>25</sub>-ZSM-5 (B) Schematic representation of Ag<sup>+</sup> (Lewis acid) and H<sup>+</sup> (Brønsted acid) species associated with framework Al sites in ZSM-5 (MFI type topology).

### 3.3.2 Kinetic Study on Ethylene Dehydroaromatization (DHA) Reaction

It has been suggested in prior studies<sup>108, 214</sup> that Ag-ZSM-5 is a promising catalyst for paraffin and natural gas upgrading. Motivated by these studies, we aimed to understand the catalytic behavior of Ag-ZSM-5 in the ethylene-to-liquids (ETL) reaction with the objective of converting ethylene directly to aromatics – notably benzene, toluene, and xylene isomers (BTX). To avoid secondary reactions that may interfere with the evaluation of catalyst performance, ethylene conversion was kept less than 50% for both Ag<sub>25</sub>-ZSM-5 and H-ZSM-5 (this was achieved by adjusting the space velocity). Figure 3.3A and B show product selectivity for Ag<sub>25</sub>-ZSM-5 and H-ZSM-5, respectively, as a function of ethylene conversion. Our findings reveal that the Brønsted acid sites in H-ZSM-5 are more active for ethylene conversion (i.e., high ethylene conversion over Ag<sub>25</sub>-ZSM-5 requires substantially lower space velocity than that of H-ZSM-5). For example, a comparison of ethylene conversion at the same space velocity (5000 ml g<sup>-1</sup> h<sup>-1</sup>) reveals a significant difference between Ag<sub>25</sub>-ZSM-5 (33% ethylene conversion) and H-ZSM-5 (90% ethylene conversion). On the contrary, Ag<sub>25</sub>-ZSM-5 exhibits higher selectivity towards aromatics irrespective of the space velocity. Comparison at 90% ethylene conversion reveals that Ag<sub>25</sub>-ZSM-5 exhibits twice the

aromatics selectivity as that of H-ZSM-5. This suggests that the initial activation of ethylene occurs at Brønsted acid sites, while Ag<sup>+</sup> sites promote the formation of aromatics. This finding qualitatively agrees with prior studies of different reactions (e.g., methanol to hydrocarbons) showing enhanced aromatics formation over Ag-zeolites.<sup>203</sup>

As shown in Figure 3.3, the selectivity to aromatics decreases by ca. 50% with decreased ethylene conversion for both H-ZSM-5 and Ag<sub>25</sub>-ZSM-5. At the lowest ethylene conversion (30%), the selectivity to aromatics is much higher for Ag<sub>25</sub>-ZSM-5 (27%) compared to H-ZSM-5 (5%). Over the full range of ethylene conversion, the selectivity to aromatics for H-ZSM-5 never exceeds that of Ag<sub>25</sub>-ZSM-5. Indeed, Ag-ZSM-5 catalysts increase BTX production by at least a factor of three relative to H-ZSM-5, consistent with our observation that Ag<sup>+</sup> acts as a promoter of dehydroaromatization (DHA) reactions.

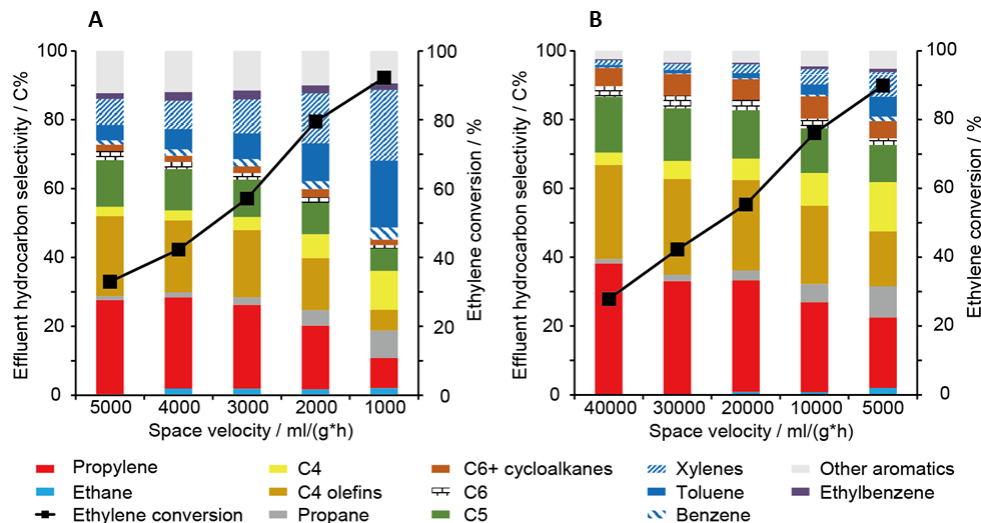


**Figure 3.3.** Effects of space velocity (x-axis) on product selectivity (left y-axis) and ethylene conversion (right y-axis) over (A) Ag-ZSM-5 and (B) H-ZSM-5. Data were acquired after 10 min time on stream.

To further explore the effect of Brønsted acid sites in the ETL reaction, we prepared a homologous series of Ag-exchanged H-ZSM-5 catalysts where the Ag/Al ratio was varied while keeping the Si/Al ratio constant. Figure 3.4 shows the changes

in product selectivity and ethylene conversion as a function of Ag/Al ratio. Under identical reaction conditions (400 °C and 5000 ml g<sup>-1</sup> h<sup>-1</sup>), ethylene conversion increases from 33 to 90% as the Ag/Al ratio monotonically decreases. The reason for the ca. 60% reduction in ethylene conversion with only 25% loss of Brønsted acid sites is unknown. There may be an intrinsic loss of activity, which is consistent with previous solid-state <sup>2</sup>H NMR studies<sup>184</sup> showing that ethylene forms stable  $\pi$  complexes on Ag species that likely reduce ethylene activity. Conversely, Ag<sup>+</sup> promotes DHA that, in turn, could lead to more rapid coking; however, visual comparison of as prepared and spent catalyst after 10 min time on stream indicates very little coking, as inferred from the nearly consistent color of the catalyst (i.e., there is no change from white to gray/black that is characteristic of coked zeolite catalysts). Another possible cause of decreased conversion is related to mass transport limitations imposed by ethylene adsorption to Ag<sup>+</sup> sites disproportionately populated on the exterior of Ag-ZSM-5 particles. A high coverage of adsorbed ethylene on the catalyst exterior due to Ag zoning may limit ethylene and/or other hydrocarbon access to internal acid sites. A third possibility is the potential migration of Ag<sup>+</sup> ions during the reaction to form clusters that block reactant access to pores. For instance, we characterized the spent catalyst after a long time on stream and observed the presence of Ag metal (see Table B1). This preliminary data is suggestive of ion migration, but further studies are required to confirm this hypothesis and the nature of rapid deactivation in Ag-ZSM-5 catalysts at higher metal loading.

Interestingly, the lowest Ag loading (Ag<sub>8</sub>-ZSM-5) has minimal impact on ethylene conversion (i.e., 5% reduction compared to H-ZSM-5), while this small quantity of Ag also leads to a 20% increase in aromatic selectivity. The ability of Ag to stabilize  $\pi$  complexes can explain the increased selectivity to aromatics (see Table B2

in the Appendix). Selectivity comparisons, however, may be complicated by secondary reactions when reactant conversion is high.<sup>215</sup> Nevertheless, these results highlight the relative contribution of Brønsted and Lewis acid sites in Ag-exchanged zeolites on the ETL reaction.

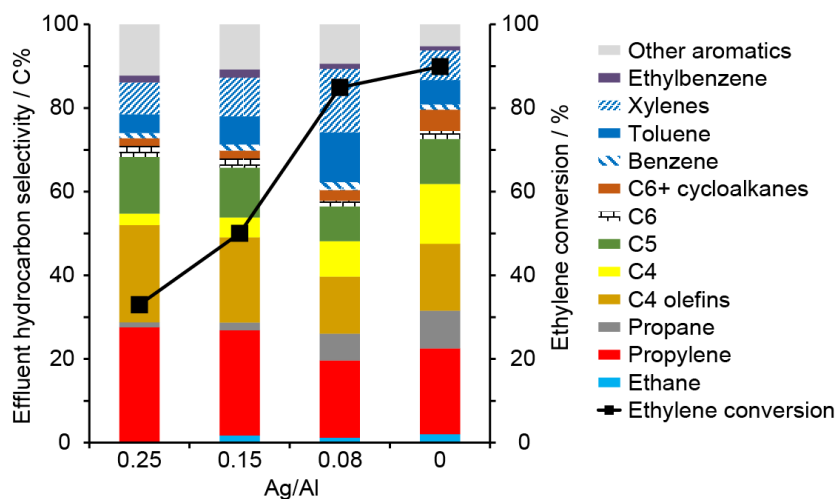


**Figure 3.4.** Effects of Ag/Al ratio (x-axis) on product selectivity (left y-axis) and ethylene conversion (right y-axis) over various ZSM-5 catalysts (Ag<sub>25</sub>-, Ag<sub>15</sub>-, Ag<sub>8</sub>-, and H-ZSM-5) at 400 °C and 1 atm.

### 3.3.3 Effect of Methane Coupling Reaction and DFT Studies

Here, we explore the role of Brønsted and Lewis acid sites in the NOC of methane and ethylene. The use of methane and ethylene co-feed was motivated by previous studies suggesting Ag-ZSM-5 promotes methane C-H bond breakage and coupling with ethylene to produce propylene,<sup>108, 214</sup> a value-added chemical with high market demand.<sup>216</sup> Figure 3.5A shows methane conversion over Ag<sub>25</sub>-ZSM-5 and H-ZSM-5 catalysts with time-on-stream (TOS). Ag<sub>25</sub>-ZSM-5 exhibits an induction period within the first 90 min TOS wherein methane conversion is  $\leq 1\%$ . Methane conversion subsequently increases to ca. 3.5% after 1.5 h TOS and eventually reaches a maximum of 5%. The maximum methane conversion is lower than previously reported values (ca. 13%) for NOC reactions at 400 °C.<sup>214</sup> It is well known that methane C-H bond activation in metal-exchanged zeolites requires high temperatures (e.g., > 600 °C).<sup>199,</sup>

<sup>217-218</sup> The disparity between our methane conversion and those of prior studies may be attributed to variations in sample preparation. For instance, Ag-ZSM-5 catalysts in our studies were prepared by solution ion exchange, whereas Baba and coworkers<sup>214</sup> prepared Ag-ZSM-5 through wetness impregnation (a technique that is more susceptible to the generation of Ag clusters and/or oxides). Different methods of metal loading could impact Ag speciation and/or the spatial distribution of Lewis acid sites throughout zeolite particles, thereby leading to differences in catalytic performance.

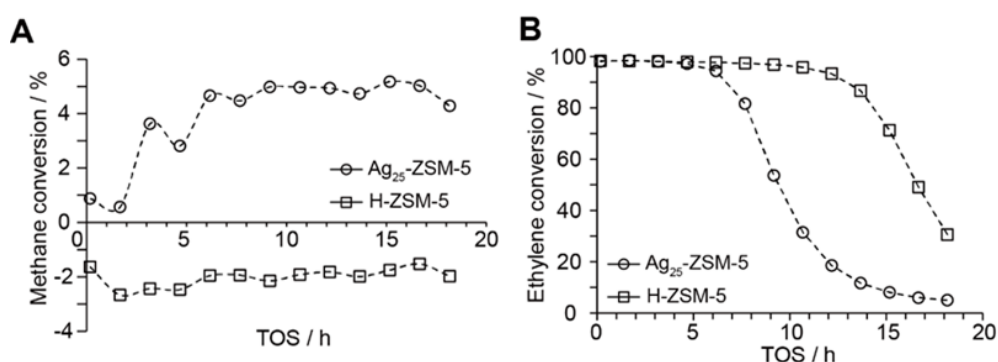


**Figure 3.5.** Performance of H-ZSM-5 (open squares) and Ag<sub>25</sub>-ZSM-5 (open circles) catalysts. Plots compare (A) methane and (B) ethylene conversion.

NOC of methane and ethylene over H-ZSM-5 under the same reaction conditions as above resulted in higher outlet methane concentration than that of the feed (i.e., negative methane conversion). This observation can be attributed to two factors: (i) the inability of Brønsted acid sites to activate the C-H bond of methane at low temperature, and (ii) the generation of methane from hydrocarbon cracking during the NOC reaction. Comparison of Ag- and H-ZSM-5 catalytic data indicates that Ag<sup>+</sup> promotes methane C-H bond activation, while the latter outperforms Ag<sub>25</sub>-ZSM-5 with respect to on-stream lifetime (on the basis of ethylene conversion). As shown in Figure 3.5B, ethylene conversion is maintained at 100% for the first 4.6 h TOS for both Ag<sub>25</sub>-ZSM-5 and H-ZSM-5. The latter exhibits longer lifetime (i.e.,  $\geq 95\%$  ethylene conversion for 14 h TOS) compared to that of Ag<sub>25</sub>-ZSM-5 where ethylene conversion rapidly declines around 7 h TOS.

Product selectivity profiles for Ag<sub>25</sub>-ZSM-5 and H-ZSM-5 are significantly different during the first 8 h TOS (see Figure B2 and Figure B3 of Appendix A, respectively). Notably, Ag<sub>25</sub>-ZSM-5 exhibits 66 % selectivity to aromatics compared to 32 % for H-ZSM-5 after 10 min TOS. The relatively short lifetime of Ag-ZSM-5, however, results in decreased aromatic selectivity to 18 % around 8 h TOS and  $\leq 10\%$  at later times. Conversely, H-ZSM-5 aromatics selectivity increases to ca. 44 % during the first 8 h TOS, followed by a monotonic decrease to 10 % around 18 h TOS. It is expected that higher aromatics yield for the Ag<sub>25</sub>-ZSM-5 catalyst would lead to coking and pore blockage at shorter TOS, resulting in more rapid catalyst deactivation. Such behavior is consistent with aromatization reactions in zeolites where coking is the primary cause of reduced activity.<sup>219-220</sup> Coke formation reduces internal pore volume and available active sites for various hydrocarbons during the course of the reaction, which can have an appreciable impact on product selectivity.

Table 3.2 summarizes the DFT calculations of the activation barriers and binding energies of ethylene and methane on H-ZSM-5 and Ag-ZSM-5. The energy barrier for ethylene activation at the Brønsted acid site of H-ZSM-5 is  $E_a = 1.37$  eV, and is substantially lower than on the Lewis acid site of Ag-ZSM-5 ( $E_a = 1.94$  eV). The energy barrier for methane activation at the Brønsted acid site of H-ZSM-5 ( $E_a = 5.06$  eV) is significantly higher than on the Lewis acid site of Ag-ZSM-5 ( $E_a = 1.62$  eV). Methane and ethylene both exhibit stronger binding energies on Lewis acid sites. Collectively, these findings support the conclusions that ethylene preferentially activates on Brønsted acid sites, whereas methane is unreactive over H-ZSM-5 but does exhibit marginal activity on Lewis acid sites. The differences between ethylene and methane on Ag-ZSM-5 are less pronounced and require a brief discussion. In terms of activation barriers only, methane is in fact easier to activate on Ag-ZSM-5 than ethylene

by approximately 0.3 eV. We attribute the stark contrast between the Brønsted ( $Z-H^+$ ) and Lewis ( $Z-Ag^+$ ) acid sites for ethylene and methane activation to mechanistic features. Over Brønsted acid sites ethylene is able to accept the proton and forms a  $Z-C_2H_5^+$  intermediate. An equivalent pathway for methane would require the formation of a  $Z-CH_5^+$  species, which is not stable. The only accessible pathway for methane activation at a  $Z-H^+$  site is the highly activated formation of  $Z-CH_3^+$  and  $H_2$ . On the Lewis acid site of Ag-ZSM-5 the C-H bond activation in methane and ethylene proceeds via a similar pathway resulting in a  $Z-H^+$  site and an Ag-CH<sub>3</sub> or Ag-C<sub>2</sub>H<sub>3</sub> species, respectively. Alternative pathways for methane activation on Ag-ZSM-5 would involve the formation of Z-OCH<sub>3</sub> (methoxy) intermediates, which have previously been identified in NMR studies.<sup>185</sup> While our calculations suggest that this alternative pathway is thermodynamically less favorable, the presence of these intermediates cannot be ruled out without a more in-depth investigation into active sites and mechanisms of activation of methane and ethylene on H-ZSM-5 and Ag-ZSM-5.

**Table 3.2.** Activation barriers and binding energies (in parenthesis) for the activation of ethylene and methane on H-ZSM-5 and Ag-ZSM-5.

Species	H-ZSM-5 [a]	Ag-ZSM-5 [a]
C <sub>2</sub> H <sub>4</sub>	1.37 (-0.75)	1.94 (-1.17)
CH <sub>4</sub>	5.06 (-0.35)	1.62 (-0.44)

[a] All values are reported in eV (see also Table A6)

Low methane conversion (5% maximum) in the NOC of methane and ethylene over Ag-ZSM-5 may be due to (i) competing effects of methane and ethylene adsorption on Ag sites and/or (ii) poor activation of the methane C-H bond on Ag sites. DFT calculations indicate that ethylene activation is energetically favorable on Brønsted acid sites, which is consistent with our catalytic studies showing high ethylene conversion over H-ZSM-5. The higher barrier for ethylene activation compared to

methane activation over Ag-ZSM-5 may in part be attributed to the high stability of the  $\pi$ -bonded ethylene complex at the  $\text{Ag}^+$  site, which represents the initial state of the activation step. This stable and less reactive ethylene  $\pi$ -complex is also likely to occupy  $\text{Ag}^+$  Lewis acid sites when methane is present and ultimately impair methane conversion. Perhaps more importantly, DFT calculations indicate a large activation barrier for methane. To confirm the low activity of Ag-ZSM-5, we performed catalytic studies using only methane as feed and observed less than 4% conversion (see Figure B4). This suggests that low methane conversion is limited by the prohibitively large barrier of methane C-H bond activation (and to a lesser extent on competitive adsorption in reactions employing a co-feed).

Based on these findings, it is expected that the presence of methane in an ethylene feed would have minimal influence on the performance of ZSM-5 catalysts. This was confirmed in Figure 3.6 by the comparison of ethylene conversion over  $\text{Ag}_{25}$ -ZSM-5 and H-ZSM-5 catalysts in the absence of methane (solid circles and solid squares, respectively). Ethylene conversion profiles for  $\text{Ag}_{25}$ -ZSM-5 and H-ZSM-5 are nearly identical with and without methane addition (illustrated by open and solid symbols, respectively). It should also be noted that the selectivity profiles in the absence of methane for  $\text{Ag}_{25}$ -ZSM-5 and H-ZSM-5 (Figure B5 and Figure B6) of the Appendix, respectively) are nearly identical to similar measurements in the presence of methane (Figure B2 and Figure B3 of the Appendix, respectively). These findings indicate that methane is primarily a spectator and that ethylene dominates the NOC reaction for all catalysts tested.

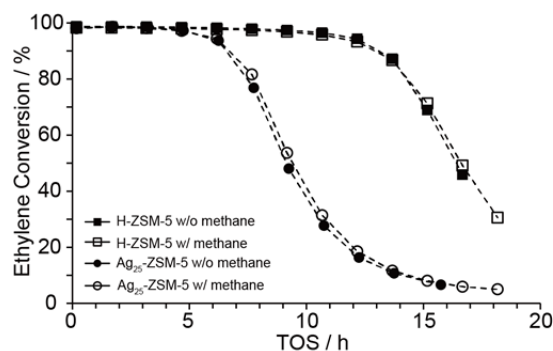


**Figure 3.6.** Effects of methane addition on the performance of ZSM-5 catalysts at 400 °C and 1 atm. Dashed lines are interpolations for improved visualization.

Based on the results of reaction tests and DFT, we propose a generalized mechanism (Figure 3.7) to describe the conversion of ethylene to various hydrocarbon products. It is evident that the first step involves ethylene activation on a Brønsted acid site (Figure 3.7A, *i*), followed by the transformation of the activated ethylene species via nonoxidative coupling with ethylene and/or other hydrocarbon species (Figure 3.7A, *ii* and *iii*). As highlighted in Figure 3.7B, Brønsted acid sites preferentially direct the formation of alkanes and olefins.<sup>221-223</sup> The formation of aromatics is promoted by Ag species, which has been observed in aromatization reactions catalyzed by Ag-exchanged zeolites.<sup>105, 203-204</sup> It is also possible that catalytic cracking (facilitated by long residence times in zeolite pores) could contribute to the production of light olefins, analogous to acid-catalyzed pathways in methanol to hydrocarbon reactions.<sup>38</sup> A more detailed understanding of the ETL reaction pathway is elusive owing to the inherent complexity of these reactions in zeolite frameworks.

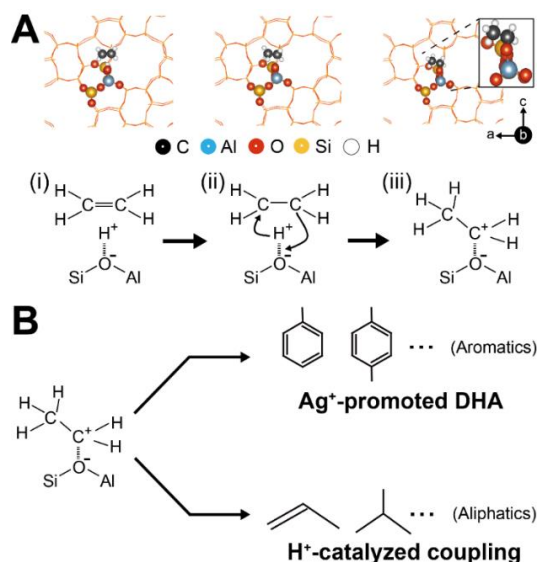


**Figure 3.7.** (A) Proposed mechanism of ethylene activation over an H<sup>+</sup> (Brønsted acid) site in a ZSM-5 pore (B) Generalized pathways of DHA reactions

### 3.4 Summary

In summary, we have shown that Ag<sup>+</sup> Lewis acid sites in ZSM-5 promote the formation of aromatics with selectivity as high as 60% relative to H-ZSM-5 where the maximum BTX selectivity is 20%. Catalytic measurements reveal enhanced dehydroaromatization on Ag-ZSM-5, which is qualitatively consistent with DFT calculations showing that π complexes between ethylene and the zeolite framework are stabilized by Ag<sup>+</sup> extra-framework cations. Interestingly, DFT calculations reveal that the binding energy of ethylene on Ag<sup>+</sup> sites is more favorable (i.e., lower enthalpy of adsorption), whereas the barrier for ethylene activation is lower on H<sup>+</sup> sites. Collectively, experimental and computational studies suggest the first step in the ETL reaction is ethylene activation on Brønsted acid sites. The extent to which there is a synergistic effect, if any, between Lewis and Brønsted acid sites in subsequent coupling reactions is unknown, and remains a subject of the ongoing investigation.

Systematic studies of Ag-ZSM-5 catalysts with varying Ag loading reveal that a small quantity of metal (e.g., 8% exchanged Ag) is capable of doubling BTX selectivity while sacrificing little of the catalyst activity. Ethylene conversion decreases

disproportionately at higher Ag loadings (upwards of 25% exchange). This relatively sharp decrease in catalyst activity with increased Ag<sup>+</sup> exchange of H<sup>+</sup> sites is not well understood. This phenomenon may be attributed to Ag zoning wherein the exterior of ZSM-5 particles contains a higher density of Ag sites relative to its interior. It does not appear that the decrease in activity at higher Ag loadings is associated with more rapid coking, which is often correlated with increased production of aromatics. Alternatively, it is possible that the binding of ethylene to Ag<sup>+</sup> sites on the catalyst exterior may generate mass transport limitations by restricted access of ethylene and/or other hydrocarbons to the interior of the zeolite comprised of a higher density of H<sup>+</sup> sites. This hypothesis is consistent with catalytic studies showing that a 5-fold reduction in the space velocity is required for ETL on Ag-ZSM-5 in order to achieve a conversion that is equivalent to H-ZSM-5 under similar reaction conditions.

Studies of methane co-feed confirmed that Ag<sup>+</sup> sites are capable of activating C-H bond breakage, but to a lesser extent than what has been reported in the literature. There is an approximate 5 h induction period where methane conversion monotonically increases to a maximum of 5%; however, the presence of methane has little effect on the performance (i.e., conversion, selectivity, and on-stream lifetime) of Ag- and H-ZSM-5 catalysts. Moreover, such low methane conversion is insufficient to justify the use of Ag-ZSM-5 as a catalyst for direct methane upgrading or as co-feed in ETL reactions. On the contrary, we show that Ag-ZSM-5 promotes DHA reactions and may prove to be a promising catalyst for low-temperature NOC reactions compared to other metal-exchanged zeolites.

## Chapter 4

### Dehydroaromatization of Ethylene over Gallium-Modified ZSM-5 Catalysts

The work is in collaboration with Dr. Hari Thirumalai, Dr. Scott Smith and Prof. Lars Grabow from the University of Houston; Prof. Kenton Whitmire from Rice University; Prof. Jing Liu from Manhattan College; and Prof. Anatoly Frenkel from Brookhaven National Laboratory. The manuscript of this research work is submitted.

#### 4.1 Motivation

Benzene, toluene, and xylene (BTX) are important precursors in the petrochemical industry for the production of polymers, fuel additives, and other value-added aromatics-derived products.<sup>129-130</sup> The previous chapter explored the influence of Ag ions on the dehydroaromatization (DHA) of ethylene and showed that the combination of Brønsted and Lewis acid sites can enhance aromatics yield. Ga-modified H-ZSM-5 zeolite catalysts are investigated owing to the reported exceptional properties of Ga species for dehydrogenation reactions.<sup>98, 127, 224-225</sup> For example, Ga-ZSM-5 has been used commercially in the UOP/BP Cyclar process, which converts light alkanes to aromatics.<sup>226</sup> Despite numerous studies of Ga-zeolites, a general understanding of the active sites in Ga-ZSM-5 and the potential synergism between Lewis and Brønsted acid sites is lacking. In this chapter, we compare a series of Ga-ZSM-5 catalysts where Ga is selectively incorporated at (non)framework sites to quantify the effect of Ga speciation on DHA performance. Here, we use a combination of zeolite synthesis, state-of-the-art characterization, catalytic testing, and computational calculations to investigate the mechanism of ethylene DHA over Ga-ZSM-5, and elucidate the specific role(s) of Ga species in promoting aromatics.

In addition to Ga-ZSM-5, prior studies have also characterized structure-performance relationships for Ga-exchanged chabazite (CHA) and beta (\*BEA) catalysts.<sup>227-228</sup> There are two conventional post-synthetic approaches to prepare Ga-

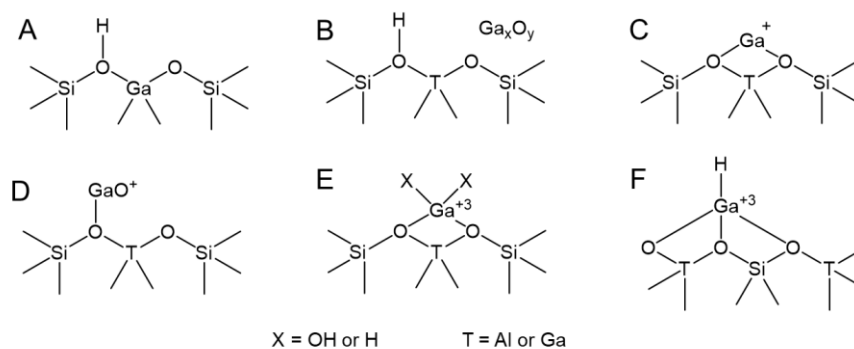
modified zeolites: (1) aqueous ion exchange with a gallium salt (e.g.  $\text{Ga}(\text{NO}_3)_3$ ); and (2) incipient-wetness impregnation.<sup>98</sup> Characterization of Ga-zeolites prepared by these methods often reveals large fractions of  $\text{Ga}_x\text{O}_y$  deposits on external surfaces of zeolite particles owing to the slow diffusion of hydrated Ga ionic species into the micropores.<sup>229</sup> To obtain more dispersed Ga species within zeolites pores, it has been shown that  $\text{Ga}_x\text{O}_y$  can be reduced under  $\text{H}_2$  at high temperature ( $>700$  K) to facilitate Ga migration into pores and ion exchange with Brønsted acid sites.<sup>123-125</sup> Price et al. investigated the effects of various treatment methods on the state of Ga (in ZSM-5 catalysts) and the aromatization activity in DHA reactions.<sup>124, 230</sup> They observed that the optimal catalyst was prepared by reduction of  $\text{Ga}_x\text{O}_y$  to dispersed Ga species and re-oxidation to obtain  $\text{Ga}^{3+}$  sites within the 3-dimensional pores of ZSM-5; however, it has been hypothesized that achieving uniform dispersion of  $\text{Ga}^{3+}$  sites by this method is challenging.<sup>229</sup> Bell and coworkers prepared isolated  $\text{Ga}^{3+}$  cations inside H-ZSM-5 using vapor-phase exchange with  $\text{GaCl}_3$ ,<sup>123, 225</sup> and investigated the mechanism and kinetics of  $\text{C}_3\text{H}_8$  dehydrogenation over Ga-ZSM-5 catalysts. They report  $[\text{GaH}]^{2+}$  is the active site for both propane dehydrogenation and cracking reactions.<sup>225</sup> Lercher and coworkers used conventional wetness impregnation to prepare well-characterized Ga-ZSM-5 catalysts for propane dehydrogenation wherein they reported Lewis-Brønsted acid pairs are essential to catalyze the reaction.<sup>231</sup> They proposed the existence of  $\text{Ga}^+$  sites that can be protonated by proximal Brønsted acids to form  $[\text{GaH}]^{2+}$ . Bell and Lercher both claim  $[\text{GaH}]^{2+}$  is the active species for propane dehydrogenation (despite differences in their proposed reaction mechanisms).

Ga-ZSM-5 catalysts prepared via direct hydrothermal synthesis have been shown to enhance aromatics selectivity in alkane dehydrogenation reactions.<sup>125, 232-234</sup> Jones and coworkers developed a method to generate Ga Lewis acid sites using

synthesis mixtures with 3-mercaptopropyl-trimethoxysilane (MPS),<sup>127</sup> which facilitates the occlusion of extra-framework Ga species into zeolite pores without directly forming covalent bonds with framework oxygens. The resulting gallosilicate catalyst (i.e. Ga-MFI in the absence of Al) enhanced rates of propane dehydrogenation compared to gallosilicates prepared by conventional methods. Shu and coworkers evaluated several Ga-ZSM-5 catalysts obtained via different methods (i.e. hydrothermal synthesis, ion exchange, impregnation, and physical mixing) on n-heptane aromatization.<sup>235</sup> They reported the Ga-ZSM-5 catalyst synthesized via direct hydrothermal synthesis exhibited the highest BTX selectivity, which they attribute to enhanced Lewis acidity and the presumed mesoporosity incurred by the incorporation of framework Ga. Moreover, they hypothesized that both liquid-phase ion exchange and direct hydrothermal synthesis lead to Ga substitution in framework sites. On the contrary, Hsieh et al.<sup>236</sup> argued that Ga is less prone to be incorporated into the zeolite framework (compared to Al) based on their analysis of [Ga, Al]-ZSM-5 catalysts obtained via seeded hydrothermal synthesis.

Ga species supported on microporous materials can be difficult to characterize due to the complexity of zeolite topology and interactions with strong Brønsted acid sites. To this end, Scott and coworkers systematically examined nonporous catalysts (e.g. Ga(i-Bu)<sub>3</sub> grafted onto  $\gamma$ -alumina and silica) wherein they showed that mononuclear alumina-supported Ga sites exhibit higher activity (in propane dehydrogenation) than silica-supported Ga sites.<sup>237</sup> Using a combination of high-field solid-state NMR and X-ray absorption spectroscopy (XAS), they resolved the structure of Ga species. For Ga-zeolites, the number of potential Ga species reported in the literature (as illustrated in Scheme 4.1) includes the following: Ga<sub>2</sub>O<sub>3</sub>, Ga<sup>+</sup>, [GaO]<sup>+</sup>, [GaH<sub>2</sub>]<sup>+</sup>, [Ga(OH)<sub>2</sub>]<sup>+</sup>, [GaH(OH)]<sup>+</sup>, and [GaH]<sup>2+</sup>.<sup>124, 225, 238-242</sup> The majority of these

species contain Ga in its +3 oxidation state. For direct hydrothermal synthesis, Ga incorporated in framework sites (Scheme 4.1A) may also lead to the generation of Brønsted acid sites.<sup>128</sup>



**Scheme 4.1.** (A). Possible zeolite Brønsted and Lewis acid sites generated from heteroatom framework (T = Al or Ga) and/or extra-framework species: (A) framework  $\text{Ga}^{3+}$ ; (B)  $\text{Ga}_2\text{O}_3$ ; (C)  $\text{Ga}^+$ ; (D)  $[\text{GaO}]^+$ ; (E)  $[\text{GaH}_2]^+$ ,  $[\text{Ga}(\text{OH})_2]^+$ , or  $[\text{GaH}(\text{OH})]^+$ ; and (F)  $[\text{GaH}]^{2+}$ .

In this chapter, we investigate the speciation and siting of Ga in ZSM-5 catalysts, and correlate the synergy of Brønsted and Lewis acid sites on the ethylene DHA reaction. We systematically examine five Ga-ZSM-5 zeolite catalysts prepared via different treatments, including both direct synthesis and post-synthesis exchange. Using a combination of experimental techniques, including X-ray absorption (XAS) and solid-state  $^{27}\text{Al}$  and  $^{71}\text{Ga}$  magic angle spinning (MAS) nuclear magnetic resonance (NMR) spectroscopy, we have distinguished Ga species with different oxidation states and coordination numbers. The catalytic performance of various Ga-ZSM-5 catalysts helps distinguish the roles of different (extra)framework Ga species. Experimental characterization and catalytic studies were coupled with density functional theory (DFT) calculations to assess the relative activities of different Ga and Al sites. Collectively, these findings highlight the challenges of elucidating Ga speciation, and the impact of Ga-ZSM-5 preparation on enhanced activity for the promotion of aromatics (BTX) products.

## 4.2 Experimental Methods

### 4.2.1 Material

The following reagents were purchased from Sigma-Aldrich: tetraethylorthosilicate (TEOS, 98%), sodium hydroxide (NaOH, 98%), pyridine (anhydrous, 99.8%) and silica gel (Davisol Grade 636, 35-60 mesh size). Tetrapropylammonium hydroxide (TPAOH, 40%), gallium chloride (ultra dry, 99.999%), gallium nitrate hydrate (99.999%, metals basis) and sodium aluminate (technical grade) were purchased from Alfa Aesar. Materials for catalyst preparation and reaction testing included argon, oxygen and nitrogen gases (Praxair, UHP grade, 99.999%) and ethylene (99.999%, Matheson Tri-gas Inc.). All reagents were used as received without further purification. The commercial zeolite NH<sub>4</sub>-ZSM-5 was purchased from Zeolyst (CBV 5524G). Deionized (DI) water was produced with an Aqua Solutions RODI-C-12A purification system (18.2 MΩ).

### 4.2.2 Zeolite Catalyst Preparation

The zeolite Ga-Z1 was obtained via direct hydrothermal synthesis from a growth mixture with the molar composition 5.25 TPAOH:1.25 Na<sub>2</sub>O:25 SiO<sub>2</sub>:0.63 Al<sub>2</sub>O<sub>3</sub>:0.41 Ga<sub>2</sub>O<sub>3</sub>:1000 H<sub>2</sub>O. To a solution of 1.28 g TPAOH (40 wt%), 1.25 g NaOH (1 M), and 7.14 g DI water was added 2.50 g TEOS, 0.05 g sodium aluminate, and 0.10 g gallium nitrate. The mixture was aged at room temperature for 24 h under continuous stirring. The growth solution was then placed in a Teflon-lined stainless steel acid digestion bomb (Parr Instruments) and heated at 170°C under rotation (~30 rpm) and autogenous pressure in a Thermo-Fisher Precision Premium 3050 Series gravity oven. The autoclave was removed from the oven after 3 days and immediately cooled to room temperature by quenching. The solid was isolated from the supernatant by three cycles

of centrifugation (13,000 rpm) and washing using a Beckman Coulter Avanti® J-E series high-speed centrifuge. The solid product was then dried at room temperature in air. The Ga-ZSM-5 sample was calcined in flowing dried air ( $100 \text{ mL min}^{-1}$ ) at  $550^\circ\text{C}$  using heating and cooling rates of  $1 \text{ }^\circ\text{C min}^{-1}$  for a total of 5 h to remove occluded organics. Ion exchange for catalyst preparation was performed three times using a 1 M  $\text{NH}_4\text{NO}_3$  solution containing 2wt% of calcined zeolite sample. This solution was heated at  $80^\circ\text{C}$  under continuous stirring for 2 h. The exchanged samples were dried and calcined using the same procedure to obtain the H-form zeolite (H-Ga-Z1).

The sample Ga-Z2 was prepared by conventional aqueous ion exchange using a commercial  $\text{NH}_4$ -ZSM-5 material purchased from Zeolyst International (CBV 5524G). Introduction of extra-framework gallium species was accomplished by solution Ga ion exchange at  $80^\circ\text{C}$  in the oil bath for 24 h under continuous stirring. The Ga ion exchange was performed using  $\text{Ga}(\text{NO}_3)_3$  solution containing 1wt% of commercial  $\text{NH}_4$ -ZSM-5 sample, where  $\text{Ga}(\text{NO}_3)_{3(\text{aq})}$  concentration was adjusted by dissolving  $\text{Ga}(\text{NO}_3)_3$  in DI water to reach the targeted Ga loading in the final product. Detailed information is provided in Table C1. Following ion exchange, the sample was dried in air at room temperature overnight and calcined. Pretreatment with  $\text{H}_2$  via reduction and re-oxidation according to a protocol reported by Dooley et al.<sup>124</sup>. In a fixed bed, the sample was heated to  $575 \text{ }^\circ\text{C}$  at  $1 \text{ }^\circ\text{C min}^{-1}$ , held for 2 h, and then cooled to  $350 \text{ }^\circ\text{C}$  under the flow of  $\text{H}_2$  and He ( $\text{H}_2 = 2 \text{ ml/min}$  and  $\text{He} = 26 \text{ ml/min}$ ). At the set point temperature, the system was flushed with pure He ( $30 \text{ ml/min}$ ) for 30 min. A subsequent oxidation under flow of dried air was performed at  $550 \text{ }^\circ\text{C}$  (using a heating rate of  $1 \text{ }^\circ\text{C min}^{-1}$ ) for 5 h, and then cooled to ambient temperature (resulting in sample Ga-Z2H). The same procedure was used to generate sample Ga-Z1H.

The sample Ga-Z3 was prepared by vapor-phase exchange following the procedure reported by Bell and coworkers<sup>123</sup>. Here, commercial NH<sub>4</sub>-ZSM-5 (CBV 5524G) was again used as the parent zeolite. To achieve the comparable Ga elemental composition, 0.13 g anhydrous GaCl<sub>3</sub> was physically mixed with 2 g calcined H-ZSM-5 (dehydrated, CBV 5524G) inside an N<sub>2</sub>-purged glovebox (i.e., inert atmosphere) to achieve a mole ratio of Ga/Al = 0.5. The mixture was then loaded into a glass ampule, taken out of the glovebox, evacuated and flame-sealed under dynamic vacuum. The ampule containing a mixture of GaCl<sub>3</sub> and zeolite sample was heated to 200 °C at 5 °C min<sup>-1</sup>, held for 2 h, and then cooled room temperature. After the vapor phase exchange of Brønsted acid O–H group with GaCl<sub>3</sub>, the material inside the ampule was transferred into a fixed bed. The sample was heated to 500 °C at 2 °C min<sup>-1</sup>, held for 1 h, and then cooled to 100 °C under the flow of synthetic air (30 ml/min). At the set point temperature, the system was flushed with pure He (30 ml/min) for 30 min. The sample was then heated to 550 °C at 5 °C min<sup>-1</sup>, held for 2 h, and then cooled to 350 °C under the flow of H<sub>2</sub> and He (H<sub>2</sub> = 2 ml/min and He = 26 ml/min). At this temperature, the system was flushed with pure He (30 ml/min) for 30 min. A subsequent oxidation under flow of dried air (30 ml/min) was performed at 500 °C (using a heating rate of 5 °C min<sup>-1</sup>) for 1 h, and then cooled to ambient temperature (resulting in sample Ga-Z3). For the reference sample Z-ref, the commercial NH<sub>4</sub>-ZSM-5 zeolite was calcined using the aforementioned procedure.

### 4.2.3 Characterization

Powder X-ray diffraction (XRD) patterns were acquired from  $2\theta = 5$  to  $50^\circ$  with a step size of  $0.02^\circ$  at 40 kV and 44 mA using a Rigaku Smartlab X-ray Diffractometer. Analysis of surface area by the BET method was performed on N<sub>2</sub> adsorption/desorption isotherms obtained with a Micrometrics ASAP 2020 instrument.

Crystal morphology and size were measured by a FEI Nova NanoSEM 230 instrument after Pt coating (ca. 5 nm thickness). Energy-dispersive X-ray spectroscopy (EDX) was performed using a JEOL SM-31010/METEK EDAX system at 15 kV and 15 mm working distance. The molar ratios Si/Al and Si/Ga of zeolite samples were measured by inductively coupled plasma analysis in combination with optical emission spectroscopy (ICP-OES). Before analysis, a Katanax X-300 Fusion Fluxer instrument was used to conduct the fusion of samples (approximately 50 mg) prepared by first dissolving with LiBO<sub>2</sub> (98.5 wt% lithium metaborate and 1.5 wt% LiBr). The mixture was heated to 1000 °C for 15 min. Then 50 mL 2 N HNO<sub>3</sub> was added to the molten mixture and stirred for 10 min. The elemental components of the samples were analyzed using an Agilent 725 instrument.

Solid-state NMR experiments were performed at 11.7 T on a JEOL ECA-500 spectrometer equipped with a 3.2mm Magic Angle Spinning Probe. The <sup>27</sup>Al MAS NMR spectra were obtained at a spinning frequency of 12.5 kHz with a  $\pi/12$  pulse width of 1.25  $\mu$ s and a recycle delay of 0.8 s. The number of scans was 4096 for all measurements. The <sup>27</sup>Al chemical shift was referenced using a 1 M Al(NO<sub>3</sub>)<sub>3</sub> aqueous solution. <sup>71</sup>Ga MAS NMR spectra were obtained at a spinning frequency of 12.5 kHz with a  $\pi/12$  pulse width of 1  $\mu$ s, a relaxation delay of 0.5 s. The number of scans ranged from 9746 to 55296 for all measurements. The <sup>71</sup>Ga chemical shift was referenced using a 1 M Ga(NO<sub>3</sub>)<sub>3</sub> aqueous solution.

The Ga K-edge X-ray absorption spectra of the samples were measured in transmission mode. The data were obtained at the National Synchrotron Light Source-II (NSLS-II) at the QAS (7-BM) beamline. XAFS data processing and analysis were done using Athena and Artemis software within the IFEFFIT package. EXAFS fittings were performed using FEFF code and model structures obtained from Ga<sub>2</sub>O<sub>3</sub>

structure.<sup>243-244</sup> One Ga-O path was used to fit the first shell of Ga-Z1. Two Ga-O paths (Ga-O1 and Ga-O2) with different bond lengths and one Ga-Ga path were included to obtain the best fit of Ga-Z2 sample. The k-range for fit of Ga-Z1 was 2-12 Å<sup>-1</sup> for Ga-Z1 and for the fit of Ga-Z2 was 2-13 Å<sup>-1</sup>. The fits were performed in r-space, using k<sup>2</sup>-weighing. The k-ranges were 2-12 Å<sup>-1</sup>. The amplitude factor ( $S_0^2$ ) was set at 0.99 when performing EXAFS fits for Ga-Z1 and Ga-Z2 samples. The fraction of tetrahedral Ga sites in sample Ga-Z2 was estimated by the following equation<sup>245</sup>,

$$\frac{N(\text{Ga}-\text{O}_1)/4}{N(\text{Ga}-\text{O}_1)/4+N(\text{Ga}-\text{O}_2)/6} \quad (4-1)$$

where  $N$  is the coordination number of Ga-O<sub>x</sub> bonds listed in Table 4.2.

#### 4.2.4 Catalytic Measurements

Prior to each catalytic test, the zeolite powder (H-form) was pelletized, crushed, and sieved to generate aggregates of size 250 to 400 μm (i.e., 40 – 60 mesh). For each catalytic measurement, pelletized catalyst (40 mg) was diluted with 110 mg of quartz sand (50 – 70 mesh, Sigma-Aldrich) to avoid temperature gradients in the catalyst bed. The catalyst bed was supported between quartz wool in a tubular, single-pass fixed bed reactor. The temperature was regulated with a ThermoScientific Lindberg Blue M furnace using a K-type thermocouple inserted at the bottom of the quartz wool bed (on the effluent side). All catalysts were pretreated *in situ* under the flow of 24 ml/min N<sub>2</sub> (99.999 %) and 6 ml/min O<sub>2</sub> (99.999 %). During pretreatment, the temperature was increased to 250°C at a rate of 1°C/min and then was further ramped to 500°C in 2 h and held for 3 h. After pretreatment, the temperature was decreased to 400°C under flowing Ar (99.999%) and was held for at least 1 h before catalytic measurements. The inlet gas consisted of ethylene (2 ml/min, 99.999%) diluted with Ar (14 ml/min, 99.999 %) to achieve the desired reactant partial pressure. The effluent gas was

analyzed using an on-stream mass spectroscopy/gas chromatography instrument (Agilent MSD 5977A/GC 7890B). Reactant conversion and product selectivity were calculated on a carbon mole basis.

#### 4.2.5 Density Functional Theory Calculations

Density functional theory calculations investigating the Brønsted and Lewis acid sites and associated mechanisms of ethylene activation were performed using the Vienna ab-initio simulation package (VASP).<sup>189, 246-247</sup> The setup and post-processing of the calculations were done using the atomic simulation environment (ASE).<sup>248</sup> The Kohn-Sham equations were solved using the projector-augmented wave (PAW) method and the exchange and correlation energy were computed by the Bayesian error-estimation functional with van der Waals correlation (BEEF-vdW).<sup>191-192, 249</sup> This functional has been shown to adequately describe interactions of molecules within zeolite pores that are dominated by long range vdW forces.<sup>8</sup> Hard pseudopotentials that include the 3*d* electrons of gallium were used along with an energy cutoff of 540 eV and a Gaussian smearing ( $k_B T$ ) of 0.1 eV to ensure electronic convergence. The Brillouin zone was sampled at the  $\Gamma$ -point. Calculation geometries were relaxed until the maximum force on any atom was below 0.02 eV/Å. Transition state structures and energies were calculated using the climbing image nudged-elastic-band method and subsequently refined using the Dimer method to a force convergence criterion of 0.05 eV/Å.<sup>196, 250</sup>

The MFI zeolite unit cell was obtained from the International Zeolite Association (IZA) database<sup>251</sup> and was initially optimized for use with the calculation parameters chosen for this study. An optimized unit cell with lattice constants  $a = 20.41$  Å,  $b = 20.05$  Å, and  $c = 13.35$  Å was obtained, differing from experimental lattice constants by less than 1%.<sup>197</sup> A framework anionic defect at a T-site was created by

replacing a silicon with an aluminum atom, therefore, requiring an extra-framework monovalent Lewis or Brønsted acid site to compensate for the negative charge on the framework. The stability of the smaller Brønsted acid hydrogen atom ( $H^+$ ) was explored as a function of T-site as well as the oxygen atoms bound to that particular T-site. Stabilities of extra-framework Lewis acid sites ( $GaH_2^+$  and  $Ga^+$ ) were explored at all 12 T-sites. All initial, transition and final states for ethylene activation and oligomerization were modeled at the T-12 site to allow for sufficient void space to sample larger transition states.

## 4.3 Results and Discussion

### 4.3.1 Preparation of Ga-ZSM-5 Zeolite Catalysts

In this chapter, we investigate Ga-ZSM-5 catalysts prepared by three distinct methods of gallium occlusion. The first method is a hydrothermal synthesis adapted from a previous study<sup>127</sup> that places Ga in either extra-framework or framework sites. Inductively coupled plasma analysis in combination with optical emission spectroscopy (ICP-OES) reveals the product of direct synthesis contains a molar composition of Si:Al:Ga = 57:2.4:1.0. This sample is referred to herein as Ga-Z1. The second and third methods are post-synthesis modifications to a commercial ZSM-5 (Zeolyst CBV 5524G, referred to as Z-ref) with nearly identical molar Si/Al ratio as that of Ga-Z1 (Table 4.1). In one approach we use aqueous phase ion-exchange with  $Ga(NO_3)_3$  to produce a product, referred to as Ga-Z2. In the second approach, we use vapor-phase exchange with  $GaCl_3$  according to a protocol reported by Bell and coworkers<sup>123</sup> (referred to as sample Ga-Z3). The molar compositions of samples Ga-Z2 and Ga-Z3 are both equal to Si:Al:Ga = 54:1.8:1.0.

The liquid-phase ion exchange method reportedly leads to a large fraction of  $\text{Ga}_x\text{O}_y$  species deposited on the external surfaces of ZSM-5.<sup>229, 252</sup> Using a reported approach<sup>238</sup> to obtain more dispersed Ga species, samples Ga-Z2 and Ga-Z1 were treated in  $\text{H}_2$  at high temperature ( $>700\text{K}$ ) and are referred to herein as Ga-Z2H and Ga-Z1H, respectively (note that the protocol for Ga-Z3 also involves  $\text{H}_2$  treatment). The aluminum speciation for each sample was quantified using solid-state NMR (Figure C5) where peaks at 55 ppm and 0 ppm in  $^{27}\text{Al}$  MAS NMR spectra correspond to tetrahedral Al (framework Al, *FAI*) and octahedral Al (extra-framework Al, *EFAI*), respectively.<sup>253</sup> The percentages of Al species for each sample are listed in Table 4.1, showing that Al speciation is not altered by either liquid ion-exchange or  $\text{H}_2$  treatment; however, there is a 9% reduction in FAI (with a concomitant increase in EFAI) during Ga impregnation by chemical vapor-phase exchange, as observed for Ga-Z3 (compared to Z-ref). This is likely due to the release of HCl during the decomposition of  $\text{GaCl}_3$ , which could facilitate dealumination of the zeolite framework.

Powder X-ray diffraction (XRD) patterns confirmed the structural integrity (MFI framework) of all calcined Ga-ZSM-5 catalysts (Figure C1) and the absence of impurities in Ga-Z1. It has been reported<sup>229</sup> that liquid phase ion exchange can lead to the formation of crystalline  $\text{Ga}_x\text{O}_y$  that is not visible in XRD patterns of Ga-Z2; however, samples prepared by ion exchange with higher Ga concentrations clearly show the presence of crystalline  $\text{Ga}_2\text{O}_3$  by XRD (i.e. peaks at  $2\theta = 21.6$  and  $37.1^\circ$ <sup>254-255</sup>, Figure C2). It has also been reported<sup>236</sup> that powder XRD patterns can provide evidence of Ga incorporation in framework sites based on shifts in two characteristic MFI peaks, (501) and (303), when a larger Ga atom replaces a smaller Al atom. For all Ga-ZSM-5 samples in this study, these two peaks ( $2\theta = 23.0$  and  $23.8^\circ$ , respectively)

exhibit no observable shifts compared to commercial zeolite, Z-ref. This suggests the majority of Ga are extra-framework species.

**Table 4.1.** Elemental analysis of zeolite catalyst samples.

Sample <sup>d</sup>	Sample Preparation	Composition <sup>a</sup>		Al content (%) <sup>b</sup>	
		Si/Al	Si/Ga	Al (55 ppm)	Al (0 ppm)
Ga-Z1	Direct synthesis	24	57	89	11
Ga-Z2	Solution ion exchange	30	54	94	6
Ga-Z3	Vapor phase exchange	30	54	85	15
Ga-Z1H	Z1 with H <sub>2</sub> treatment	24	57	91	9
Ga-Z2H	Z2 with H <sub>2</sub> treatment	31	54	94	6
Z-ref	Commercial zeolite	29 <sup>c</sup>	----	94	6

(a) Determined by ICP-OES; (b) Measured by <sup>27</sup>Al MAS NMR spectra of hydrated zeolite materials (Figure C5); (c) Value of commercial zeolite CBV 5524G (Zeolyst) reported by Phadke et al.<sup>256</sup>; (d) SEM images of samples reveal a spheroidal morphology with average particle sizes in the range of 300 – 500 nm (Figure C3).

X-ray absorption fine structure (XAFS) spectroscopy was used to characterize the changes in the local structure and electronic states of Ga between the Ga-Z1 and Ga-Z2 samples (a similar analysis of Ga-Z3 is reported by Phadke et al.<sup>123</sup>). X-ray absorption near edge structure (XANES) at the Ga K-edge (Figure 4.1A) shows that the absorption edge energy is very similar between Ga-Z1 and Ga-Z2 while the peak region is more broadened for Ga-Z2. The absorption edge energy is defined here at the first inflection point of the XANES spectrum and is related to the charge state of the probed atoms. The charge state of Ga atoms in both samples is, effectively, +3 since the position of the absorption edge energy is at ~10376 eV for both samples, similar to the value of the reported standard Ga<sup>3+</sup> species.<sup>123</sup> The variation between XANES features in these two Ga-ZSM-5 samples is evidence of differences in their local environments.

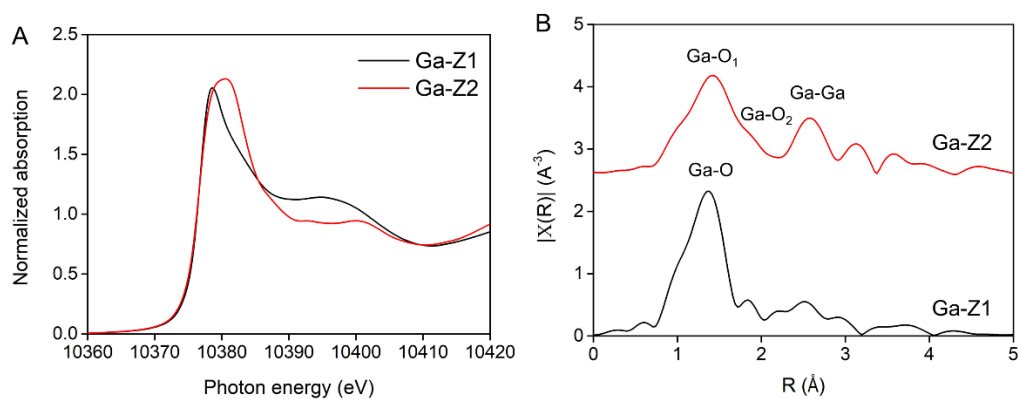


**Figure 4.1.** (A) Normalized Ga K-edge XANES and (B) Magnitudes of  $k^2$ -weighted Fourier-transformed EXAFS spectra for Ga-Z1 (direct synthesis) and Ga-Z2 (solution ion exchange).

Fourier transform magnitudes of the  $k^2$ -weighted extended X-ray absorption fine structure (EXAFS) spectrum (Figure 4.1B) of Ga-Z2 features a shoulder near the 2 Å distance that is absent for the Ga-Z1 sample. Moreover, the first main peak between 1 and 2 Å in the spectrum of Ga-Z2 is slightly shifted to a higher distance compared to that of Ga-Z1. These observations, together with the large signal in the region of 2- 4 Å in the spectrum of Ga-Z2, indicate the local environments around Ga atoms in these two zeolites are different – namely, we observe a greater degree of order in sample Ga-Z2. To extract detailed local structure information from EXAFS, quantitative analysis was carried out for samples Ga-Z1 and Ga-Z2. The fitting results (Table 4.2 and Figure C4) highlight distinct differences in the local environments around Ga atoms in these samples, in agreement with visual observations of XANES and EXAFS data (*vide supra*). The coordination number of the Ga-O bond in Ga-Z1 is close to four, consistent with a tetrahedral-coordination of Ga atoms with an effective Ga-O distance of  $1.81 \pm 0.01$  Å. This value falls within the range of 1.73 – 1.93 Å reported for Ga-Z3.<sup>123</sup> The best fit for Ga-Z2 involves two distinct Ga-O shells with interatomic distances of  $1.90 \pm 0.02$  Å and  $2.13 \pm 0.08$  Å. Such a split in the Ga-O distances is likely due to the distribution of Ga atoms between tetrahedral and octahedral sites.<sup>245, 257</sup> We estimate the fraction of tetrahedral Ga sites in Ga-Z2 to be 82% (refer to the Supporting

Information for detailed calculations). The peak at about 2.96 Å is attributed to Ga-Ga pairs.

**Table 4.2.** Best fits of the structural parameters obtained from of Ga K-edge EXAFS.

Sample	Bond	N	R (Å)	$\sigma^2$ (Å <sup>2</sup> )
Ga-Z1	Ga-O	4.2 ± 0.3	1.81 ± 0.01	0.005 ± 0.001
Ga-Z2	Ga-O <sub>1</sub>	3.6 ± 0.8	1.90 ± 0.02	0.008 ± 0.003
	Ga-O <sub>2</sub>	1.2 ± 0.7	2.13 ± 0.08	0.008 ± 0.003
	Ga-Ga	8 ± 2	2.96 ± 0.02	0.015 ± 0.003

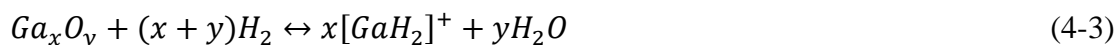
The effect of Ga-ZSM-5 sample preparation on the coordination (or local environment) of Ga species was assessed by solid-state NMR. Previous studies of <sup>71</sup>Ga MAS NMR spectra generally assign peaks in the ranges 150-160 ppm and -7-12 ppm to tetrahedral (framework) Ga and octahedral (extra-framework) Ga (i.e. Ga<sub>2</sub>O<sub>3</sub>), respectively.<sup>258-260</sup> However, an alternative interpretation from Dai et al.<sup>261</sup> is the signal at 150-160 ppm is tetrahedral coordination attributed to either framework Ga cations or extra-framework Ga species such as Ga<sup>3+</sup>, [Ga(OH)<sub>2</sub>]<sup>+</sup>, or [GaO(OH)]. Moreover, Gao et al.<sup>101</sup> assigned the peak at 58 ppm to highly dispersed Ga<sub>2</sub>O<sub>3</sub> particles, and the peak at 190 ppm to cationic [GaO]<sup>+</sup> or its hydrous state [Ga(OH)<sub>2</sub>]<sup>+</sup>. The <sup>71</sup>Ga NMR spectra of all Ga-ZSM-5 samples in this study are shown in Figure 4.2. Samples Ga-Z1 and Ga-Z1H exhibit a single peak around 159 ppm (Figure 4.2A), indicating the majority of Ga species have tetrahedral coordination. For the remaining samples (Figure 4.2B), the signal-to-noise ratio of spectra is relatively low due to the strong broadening effect on the oxidic extra-framework Ga species.<sup>260</sup> The Ga-Z2 spectrum contains two bands located at 159 and 102 ppm, respectively. Since EXAFS suggests 82% of the Ga sites in Ga-Z2 are tetrahedrally coordinated, the peak at 102 ppm could be assigned to distorted tetrahedral sites of extra-framework Ga or amorphous Ga<sub>2</sub>O<sub>3</sub>. After H<sub>2</sub> treatment, the peak located at 102 ppm disappears due to the formation of dispersed

tetrahedral  $[\text{Ga}(\text{X})_2]^+$  ( $\text{X} = \text{OH}$  or  $\text{H}$ ) species that can exchange with Brønsted acid sites. Indeed, the NMR spectrum for Ga-Z2H (Figure 4.2B) is similar to that of Ga-Z3 (i.e. single peak around 147 ppm), which is consistent with tetrahedrally-coordinated Ga reported by Bell.<sup>123</sup> Direct comparison of these two spectra with that of Ga-Z1 provides evidence for the presence of framework Ga in the latter (although the exact percentage cannot be quantified). The presence of framework Ga in sample Ga-Z1 (and Ga-Z1H) is inferred from the large difference in signal-to-noise ratio compared to Ga-Z2 and Ga-Z3, despite all samples having nearly identical Ga concentration (Table 4.1). The presence of tetrahedrally-coordinated Ga in framework sites leads to higher symmetry (i.e. higher peak intensity), consistent with previous  $^{71}\text{Ga}$  NMR spectra of gallosilicates,<sup>258, 262</sup> whereas the asymmetrical environment of tetrahedral  $[\text{Ga}(\text{X})_2]^+$  species leads to lower signal-to-noise ratios.

The  $^{71}\text{Ga}$  MAS NMR spectra of samples Ga-Z1, -Z1H, -Z2H, and -Z3 indicate a predominance of tetrahedral Ga species, which could be either  $[\text{GaX}_2]^+$  (Scheme 4.1E) or  $[\text{GaH}]^{2+}$  (Scheme 4.1F). The relatively high Si/Al ratio of ZSM-5 samples suggests there are few paired Al sites, which would limit the number of  $[\text{GaH}]^{2+}$  species; thus, we propose the majority of extra-framework sites are  $[\text{GaX}_2]^+$ . Direct synthesis of Ga-Z1 generates  $[\text{Ga}(\text{OH})_2]^+$  in the as-synthesized product. Hydrogen treatment of sample Ga-Z1H results in hydrogen exchange via the reaction



Treatment of Ga-Z2 with  $\text{H}_2$  mobilizes  $\text{Ga}_x\text{O}_y$  to generate dispersed  $[\text{GaH}_2]^+$  sites via a similar reaction,



The final step of treatment involves exposure to O<sub>2</sub> at high temperature, which reoxidizes sites to [Ga(OH)<sub>2</sub>]<sup>+</sup>. During catalyst testing, non-oxidative DHA of ethylene produces H<sub>2</sub> to regenerate [GaH<sub>2</sub>]<sup>+</sup> species *in situ*, which we presume herein to be the active site for Lewis acid catalysis.

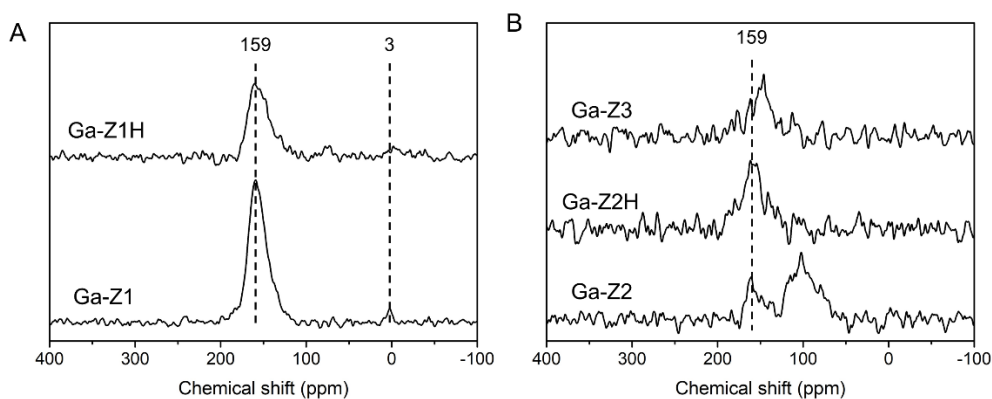


**Figure 4.2.** <sup>71</sup>Ga MAS NMR spectra of hydrated Ga-ZSM-5 zeolites: (A) direct synthesis (Ga-Z1) and after H<sub>2</sub> treatment (Ga-Z1H); (B) Ga-Z2 (solution ion exchange), Ga-Z2H (Z2 after H<sub>2</sub> treatment), and Ga-Z3 (chemical vapor-phase exchange)

### 4.3.2 Ethylene Dehydroaromatization (DHA) Reaction

The catalytic performance of all H-form Ga-ZSM-5 catalysts was compared in the ethylene DHA reaction using a packed bed reactor with a fixed space velocity (3000 ml g<sup>-1</sup> h<sup>-1</sup>) and ethylene partial pressure (12.7 kPa). Reactions were performed at sub-complete ethylene conversion (ca. 80%) to assess catalyst deactivation and selectivity towards light olefins and aromatics. As shown in Figure 4.3A, isoconversion comparison reveals the following order of aromatic selectivity: Ga-Z1H > Ga-Z1 ≈ Ga-Z2H > Ga-Z3 > Ga-Z2 > Z-ref. Commercial ZSM-5 (Z-ref), which lacks Ga Lewis acid sites, exhibits the least aromatic selectivity (16%) owing to the presence of Brønsted acid sites that preferentially direct the formation of alkanes (e.g. 19% butane) and olefins (e.g. 23% propylene). Among Ga-ZSM-5 catalysts, Ga-Z2 has the lowest aromatics selectivity owing to the presence of Ga<sub>x</sub>O<sub>y</sub> species on the zeolite surface, which are reportedly inert sites for aromatic formation.<sup>229</sup> The Ga-Z3 catalyst obtained

via chemical vapor phase exchange produced an appreciable amount of aromatics (45%), suggesting the existence of well-dispersed extra-framework Ga species (i.e. isolated Ga<sup>3+</sup> sites substituting Brønsted acids as illustrated in Scheme 4.1E with T = Al)<sup>123</sup>. The catalyst prepared via direct hydrothermal synthesis (Ga-Z1) exhibits the highest aromatics selectivity (52%), which can be explained by the presence of tetrahedrally-coordinated Ga<sup>3+</sup> species. Analyses by XAS and <sup>71</sup>Ga MAS NMR cannot distinguish the fraction of Ga occupying framework and extra-framework sites, which is illustrated in Scheme 4.1A and E, respectively. One differentiating factor between samples Ga-Z3 and Ga-Z1 is that extra-framework Ga in the latter can be associated with either Al or Ga in the framework. Another factor that must be considered is the potential impact of framework Ga on the acidity of Brønsted acid sites. Investigation of both scenarios by DFT modeling is described later.

Figure 4.3A compares product selectivities for specific light paraffins and olefins where the most notable differences observed among the catalysts are with respect to propylene and C<sub>4</sub> olefins. Comparisons were made at a fixed space velocity, where we observe nearly identical ethylene conversion at initial time on stream (Figure 4.3B), indicating all six catalysts have similar activity. Comparison of the rates of catalyst deactivation reveal two groups of similar stability: those with lower rates of deactivation (Ga-Z2, Ga-Z2H, and Z-ref) and those with 3.4-fold higher rates of deactivation (Ga-Z1, Ga-Z1H, and Ga-Z3). In general, the stability of the catalyst decreases with increased aromatics selectivity (Figure 4.3B), presumably due to the generation of heavier coke species. Interestingly, the only catalyst that deviates from this trend is Ga-Z2H, which has the second highest aromatics selectivity, yet exhibits one of the lowest rates of deactivation. The exact reason for its enhanced stability is unknown. It is seemingly not attributed to difference in aromatics selectivity at

isoconversion, which is highlighted in Figure 4.4. For all catalysts, their relative fractions of BTX products are similar.

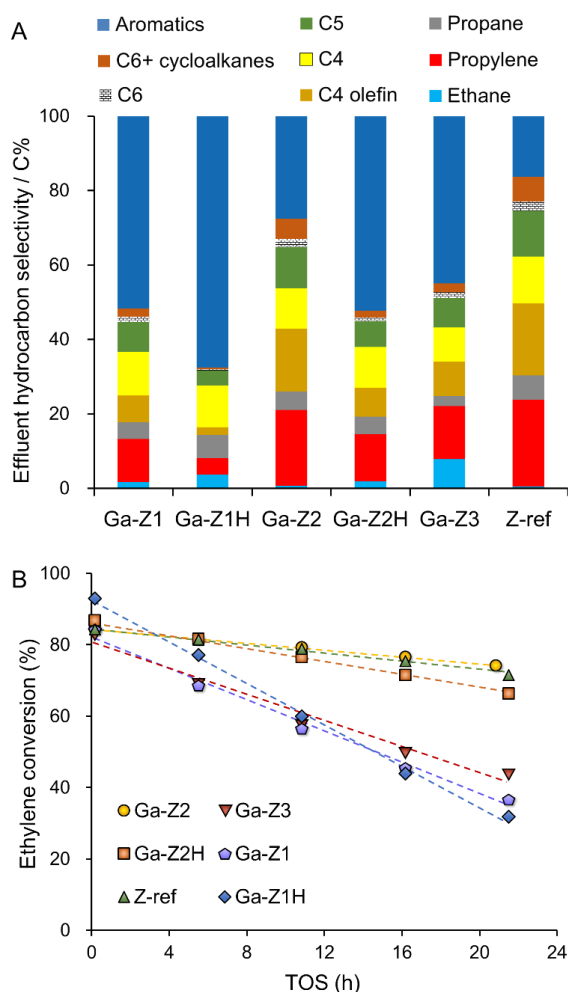


**Figure 4.3.** (A) Hydrocarbon product selectivity over various ZSM-5 catalysts. Data were acquired at 10 min time on stream. (B) Ethylene conversion for each catalyst as a function of time-on-stream (TOS).

The effect of H<sub>2</sub> treatment leads to significant increases in aromatics production for both Ga-Z1 and Ga-Z2. Prior studies have shown that the reduction of Ga-zeolites in H<sub>2</sub> at high temperature is essential to reduce Ga<sub>x</sub>O<sub>y</sub> (Eq. 4-3) to more dispersed Ga species.<sup>124, 230</sup> It has also been reported that reoxidation to the Ga<sup>3+</sup> phase after dispersion can further enhance aromatic selectivity, indicating reoxidized Ga differs from the initial Ga<sub>x</sub>O<sub>y</sub> species. This is consistent with the observation of Ga-Z2 (containing Ga<sub>x</sub>O<sub>y</sub> species) producing fewer aromatics than Ga-Z2H (after H<sub>2</sub>

treatment). Indeed, the BTX selectivity increases from 28 to 52% (Figure 4.4), indicating a large shift to well-dispersed  $\text{Ga}^{3+}$  species, consistent with its NMR spectrum (Figure 4.2B). It was anticipated that Ga-Z3, which also contains  $\text{Ga}^{3+}$  species and was treated with  $\text{H}_2$ , would perform similarly to Ga-Z2H; however, we observe the former produces 8% less BTX. This may be attributed, in part, to the loss of framework Al in Ga-Z3 during chemical vapor phase exchange. An even more unexpected observation was the fact that  $\text{H}_2$  treatment of Ga-Z1 raises its BTX selectivity from 52 to 68% (Figure 4.4, sample Ga-Z1H), the highest among all samples tested. The  $^{71}\text{Ga}$  MAS NMR spectra for samples before and after treatment are identical (Figure 4.2A). Moreover,  $^{27}\text{Al}$  MAS NMR reveals no loss of framework Al species with  $\text{H}_2$  treatment, and only a small (ca. 2%) reduction in the amount of extra-framework Al (Table 4.1). The exact reasoning for the large increase in aromatics yield is not fully understood, but herein we put forth a hypothesis based on DFT calculations that provide a molecular level analysis of Ga speciation and its impact on ethylene DHA.

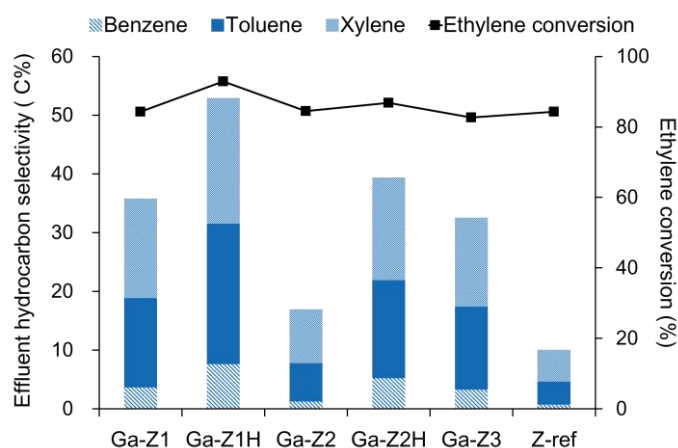


**Figure 4.4.** Comparison of aromatics product selectivity (histogram, left y-axis) and ethylene conversions (square symbols, right y-axis) for six ZSM-5 catalysts. Data were acquired at 10 min time on stream.

### 4.3.3 Density Function Calculation

Ethylene can potentially be activated on BASs or LASs<sup>263</sup>, but after exploring the pathways compiled in Table C2 we were only able to identify a mechanism with

realistic barriers on BASs. DFT calculations<sup>264</sup> of heteroatom substitution in ZSM-5 revealed that pyridine binding energy (i.e., measure of acidity) is stronger for framework Al compared to Ga; therefore, the presence of framework Ga in sample Ga-Z1 is expected to weaken the intrinsic strength of BASs, which can impact the catalytic mechanisms underlying DHA of ethylene. To examine differences among heteroatom sites, we explored the activation and oligomerization of ethylene to butene (a characteristic product of the DHA reaction) by means of periodic DFT calculations with van der Waals (vdW) corrections. To this end, we selected the T-12 site of ZSM-5 as a representative BAS (and one of the most frequently studied in literature), located at the intersection of straight and sinusoidal channels in the MFI structure.<sup>265</sup> The potential energy diagram depicting the energies of reaction and activation barriers for each intermediate step for Al<sub>FW</sub> in orange and Ga<sub>FW</sub> in blue, are shown in Figure 4.5A. Visualizations of the initial, transition, and final states along the reaction coordinate are provided in Figure C7.

Ethylene is stabilized at the vicinity of the BAS through vdW forces and  $\pi$ -bonds with a total binding energy of -1.83 eV for Al<sub>FW</sub> and -1.88 eV for Ga<sub>FW</sub>. The activation of ethylene at a BAS proceeds with the formation of a positively-charged ethyl (C<sub>2</sub>H<sub>5</sub><sup>+</sup>) species (Figure C7, top) with activation barriers of 1.46 eV (Al<sub>FW</sub>) and 1.56 eV (Ga<sub>FW</sub>). Next, a second ethylene molecule attacks the unsaturated carbon atom of the ethyl group and proceeds through the formation of a  $\pi$ -bonded transition state, forming a butyl (C<sub>4</sub>H<sub>9</sub><sup>+</sup>) complex (Figure C7, middle). The activation barrier for this step was calculated to be 1.38 eV (Al<sub>FW</sub>) and 1.65 eV (Ga<sub>FW</sub>) and is followed by a mildly exothermic internal hydrogen transfer step. The formation of 2-butene and restoration of the BAS occurs by  $\beta$ -hydrogen elimination with an activation barrier of 0.23 and 0.25 eV for Al<sub>FW</sub> and Ga<sub>FW</sub>, respectively (Figure C7, bottom). We also considered the

formation of 1-butene with Al<sub>FW</sub>, which was only marginally more activated. Overall, each BAS provides an accessible pathway to the activation and oligomerization of ethylene to butene; however, the barriers of all elementary steps are somewhat lower when the framework heteroatom is Al instead of Ga, suggesting that the BAS bound to Al<sub>FW</sub> is more amenable to oligomerization or hydrocarbon upgrade reactions. This result is consistent with the higher intrinsic acidity of H-(Al)-ZSM-5 compared to H-(Ga)-ZSM-5.<sup>266</sup>

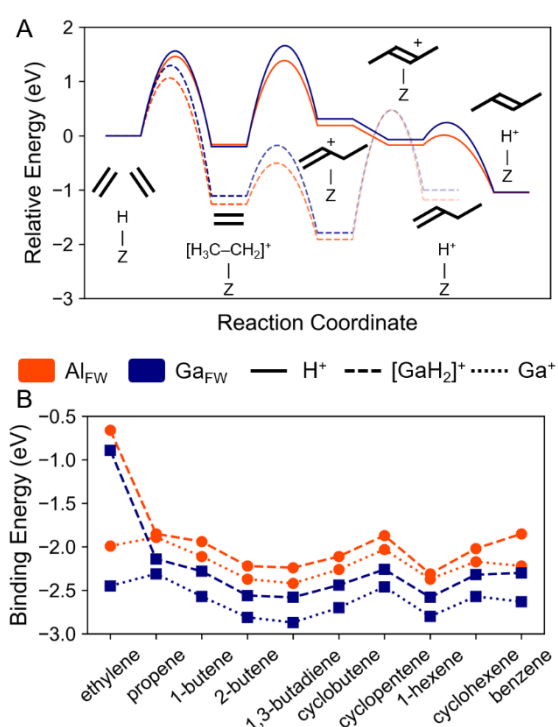


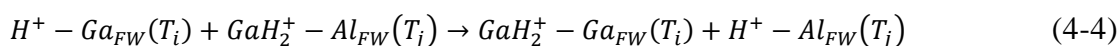
**Figure 4.5.** (A) Potential energy diagram for ethylene activation and oligomerization at an H<sup>+</sup> site, and 1-butene at an GaH<sub>2</sub><sup>+</sup> site. (B) Binding energies of unsaturated hydrocarbons at GaH<sub>2</sub><sup>+</sup> and Ga<sup>+</sup> Lewis acid sites.

Zeolite samples Ga-Z1, -Z2, and -Z3 all contain Ga<sub>EFW</sub> sites with Lewis acidity that affects the overall catalytic activity and product selectivity. To examine the role of Ga<sub>EFW</sub> we built on the work by Bell and coworkers<sup>242</sup> to study the oligomerization of ethylene to 1-butene over [GaH<sub>2</sub>]<sup>+</sup> sites bound to framework Al<sub>FW</sub> and Ga<sub>FW</sub> anionic sites. The reaction energies and activation barriers of the accessible pathway for ethylene oligomerization for [GaH<sub>2</sub>]<sup>+</sup> (dotted line) are visualized in Figure 4.5A. For

comparison we also include an analysis of  $\text{Ga}^+$  species, as well as various other inaccessible pathways we considered for the activation of ethylene in the Supporting Information (Figure C8, Table C2). The activation of ethylene on  $[\text{GaH}_2]^+$  results in a  $[\text{C}_2\text{H}_5\text{-GaH}]^+$  intermediate, resembling the activation mechanism on the BAS, but with a lower ethylene activation barrier on the  $[\text{GaH}_2]^+$  LAS. For instance, calculations with  $\text{Al}_{\text{FW}}$  reveal an activation barrier of 0.97 eV at the LAS compared to 1.46 eV at the BAS. In the case of  $\text{Ga}_{\text{FW}}$ , the barrier at the LAS is only 1.22 eV, but 1.56 eV at the BAS. For both heteroatoms, the coupling to a second ethylene molecule to form  $[\text{C}_4\text{H}_9\text{-GaH}]^+$  is exothermic and fast. Despite the existence of this low energy pathway to C-C coupling on  $[\text{GaH}_2]^+$ , we were unable to identify a feasible mechanism for the desorption of 1-butene. The lowest desorption barriers we found were 2.37 eV for  $\text{Al}_{\text{FW}}$  and 2.24 eV for  $\text{Ga}_{\text{FW}}$ . Thus, the oligomerization of ethylene on  $[\text{GaH}_2]^+$  sites is desorption limited.

If the role of extra-framework  $\text{Ga}_{\text{EFW}}$  is not to accelerate the oligomerization of ethylene, it may play a critical role in increasing the selectivity to aromatics.<sup>263</sup> Since complete aromatization pathways are complex and highly branched, it is not possible to rigorously examine them with DFT. Instead, we have calculated the binding energy of various olefins and aromatics to  $\text{Ga}^+$  and  $[\text{GaH}_2]^+$  extra-framework sites located at  $\text{Al}_{\text{FW}}$  and  $\text{Ga}_{\text{FW}}$  heteroatoms in the T-12 position. These unsaturated hydrocarbons shown in Figure 4.5B (numerical values in Table C3) have been detected in catalytic experiments (Figure 4.3) and we postulate that stabilizing these products has a positive effect on their yield. Notably, the  $\text{Ga}_{\text{EFW}}\text{-Ga}_{\text{FW}}$  sites in blue exhibit significantly stronger binding to all tested olefins and aromatics, suggesting selectivity improvements for samples containing framework and extra-framework Ga.

During H<sub>2</sub> treatment we noted that extra-framework Ga<sub>EFW</sub> becomes mobile and can be atomically dispersed to increase reactivity.<sup>123-125</sup> One of the unexplained observations in Figure 4.4 is the dramatic enhancement of Ga-Z1 with H<sub>2</sub> treatment. Here we hypothesize that the enhanced BTX selectivity is due to a redistribution of extra-framework [GaH<sub>2</sub>]<sup>+</sup> among available framework Al and Ga sites. Based on our DFT results we have assigned ethylene oligomerization primarily to strong BAS associated with Al<sub>FW</sub>, and attribute selectivity improvements to the stronger binding of higher olefins and aromatics at LAS near Ga<sub>FW</sub>. To rationalize the substantial selectivity improvement observed for Ga-Z1H, we have calculated the energies associated with swapping a proton at a Ga<sub>FW</sub> framework site (labelled as T<sub>i</sub>) with [GaH<sub>2</sub>]<sup>+</sup> at an Al site (labelled as T<sub>j</sub>), which is expressed in the following reaction



Here, we considered [GaH<sub>2</sub>]<sup>+</sup> to be the more likely Ga<sub>EFW</sub> species under hydrogen treatment conditions. The ion-exchange energies for all possible T-site combinations are summarized in Figure 4.6, where blue rectangles indicate a preference for [GaH<sub>2</sub>]<sup>+</sup> LAS located near framework Ga<sub>FW</sub> and a strong BAS near Al<sub>FW</sub>. The calculated values are provided in Table C4. A cursory inspection shows that blue is more prevalent among all possible combinations, suggesting that H<sub>2</sub> treatment can indeed alter the BAS/LAS site distribution and favor a desirable BAS/Al<sub>FW</sub> and LAS/Ga<sub>FW</sub> combination. If Ga<sub>FW</sub> heteroatoms are located at the T-4 site, then the BAS/Al<sub>FW</sub> and LAS/Ga<sub>FW</sub> configuration is always preferred. In contrast, if Al<sub>FW</sub> heteroatoms are located at either T-4 or T-8 sites, the BAS/LAS distribution is reversed. Without knowledge of the exact distribution of framework Al<sub>FW</sub> and Ga<sub>FW</sub> sites in sample Ga-Z1, it is not possible to draw a firm conclusion regarding the BAS/LAS distribution; however, our computational results support the hypothesis that H<sub>2</sub>

treatment of Ga-Z1 leads to a redistribution of BAS/LAS sites that benefits ethylene conversion and selectivity to aromatics as demonstrated for the Ga-Z1H sample. It should also be noted that this is fully consistent with  $^{71}\text{Ga}$  MAS NMR data showing no apparent change in spectra before and after  $\text{H}_2$  treatment (Figure 4.2A), which suggests that LAS speciation remains the same.

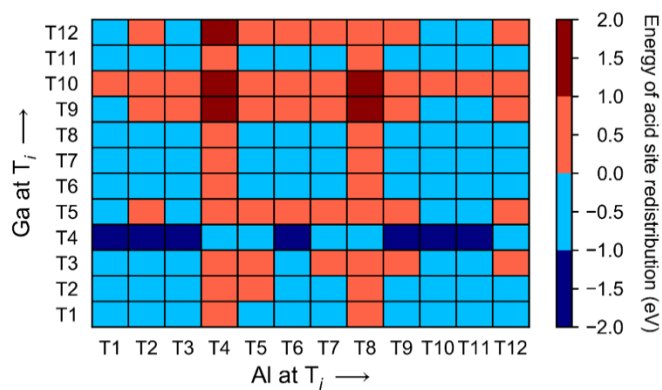


**Figure 4.6.** Brønsted ( $\text{H}^+$ ) and Lewis ( $[\text{GaH}_2]^+$ ) acid site exchange energies between framework  $\text{Ga}_{\text{FW}}$  at  $T_i$  sites and  $\text{Al}_{\text{FW}}$  atoms at  $T_j$  sites according to the reaction in Eq. 4-4.

An underlying characteristic of catalysts Ga-Z1, -Z2H, and -Z3 is the presence of  $[\text{GaH}_2]^+$  extra-framework LAS species, which is a likely explanation for their nearly identical performance in DHA of ethylene. DFT calculations predict enhanced aromatics selectivity for  $\text{GaH}_2^+ - \text{Ga}_{\text{FW}}$  combinations, which can only be achieved in Ga-Z1 (the direct synthesis method) given its distinguishing attribute of having  $\text{Ga}_{\text{FW}}$  heteroatoms substituted at framework sites. The notable improvement of Ga-Z1 performance after  $\text{H}_2$  treatment (sample Ga-Z1H) can be rationalized from DFT calculations revealing a preferential exchange of  $[\text{GaH}_2]^+$  LAS between framework  $\text{Al}_{\text{FW}}$  and  $\text{Ga}_{\text{FW}}$  sites (Eq. 4-4), leading to an increase in  $\text{GaH}_2^+ - \text{Ga}_{\text{FW}}$  sites that enhances BTX selectivity and a concomitant increase in  $\text{H}^+ - \text{Al}_{\text{FW}}$  sites that enhances ethylene activation. It is feasible that the high temperature of  $\text{H}_2$  treatment coupled with the mobility of  $[\text{GaH}_2]^+$  species can lead to this exchange of sites; however, in order for

this to be true, it implies that direct synthesis of Ga-Z1 places an appreciable fraction of extra-framework Ga<sub>EFW</sub> at framework Al<sub>FW</sub> sites ( $GaH_2^+ - Al_{FW}$ ), which on average are less energetically favorable. Although the exact location and quantity of framework and extra-framework Ga sites cannot easily be resolved, it is frequently reported that zeolite synthesis produces metastable, or kinetically trapped, structures; and with sufficiently high temperature it is possible to promote interzeolite transformations from the initial structure to one that is more thermodynamically stable.<sup>267</sup> A similar phenomenon may occur for Ga<sub>EFW</sub> species during H<sub>2</sub> treatment to result in a more energetically favorable distribution of sites. This hypothesis, although unverifiable by the techniques used in this study, is consistent with experimental and modeling results, and thus is a viable explanation for the superior performance of Ga-Z1H.

#### 4.4 Summary

In summary, we present a direct synthesis method to introduce well-dispersed extra-framework Ga<sup>3+</sup> Lewis acid sites without the need for additional post-synthetic treatments (i.e. solution ion exchange or chemical vapor deposition). A combination of advanced characterization techniques such as XAS and solid-state NMR spectroscopy indicates that framework Ga<sub>FW</sub> and tetrahedrally-coordinated extra-framework Ga<sub>EFW</sub> sites can be simultaneously generated via this direct synthesis method. We also investigate the roles of Ga speciation in ZSM-5 prepared by three distinct methods, direct synthesis (Ga-Z1), solution ion exchange (Ga-Z2), and chemical vapor-phase exchange (Ga-Z3), to identify the structure and catalytic function of different Ga sites. We have shown that any type of Ga<sub>EFW</sub> Lewis site can promote the formation of BTX with a total selectivity as high as 57%, whereas the aromatics selectivity is only 16% for commercial H-ZSM-5 at comparable ethylene conversion. Isoconversion comparisons further reveal the following order of aromatic selectivity: Ga-Z1 > Ga-Z3 >

Ga-Z2, indicating the Ga Lewis sites and the existence of framework  $\text{Ga}_{\text{FW}}$  species in Ga-Z1 catalyst lead to superior catalytic performance and promote aromatics formations. XAS and NMR measurements both indicate Ga-Z2 prepared via solution ion exchange contains a large amount of  $\text{Ga}_x\text{O}_y$  species on the external zeolite surface, suggesting that  $\text{Ga}_x\text{O}_y$  species are not the most active Lewis sites for aromatics promotion.

We further explore the effect of  $\text{H}_2$  treatment on Ga-Z1 and Ga-Z2 and directly compare their selectivity with Ga-Z3, which was obtained via chemical vapor-phase exchange involving  $\text{H}_2$  treatment. For both treated Ga-Z1H and Ga-Z2H catalysts, we observed increased BTX selectivity, but the improvement was attributed to two different phenomena: For Ga-Z2 the  $\text{H}_2$  treatment disperses inactive  $\text{Ga}_x\text{O}_y$  to active  $[\text{GaH}_2]^+$  species, while for Ga-Z1 the  $\text{H}_2$  treatment is believed to redistribute Brønsted acid protons to  $\text{Al}_{\text{FW}}$  and  $[\text{GaH}_2]^+$  to  $\text{Ga}_{\text{FW}}$  sites. The Brønsted and Lewis acid site redistribution is supported by DFT simulations, which also suggest that ethylene activation is preferred on strong  $\text{H}^+/\text{Al}_{\text{FW}}$  sites, whereas  $\text{Ga}_{\text{EFW}}/\text{Ga}_{\text{FW}}$  exhibits the strongest affinity to aromatics. This would explain the exceptional activity and selectivity to aromatics observed for the Ga-Z1H sample. To our knowledge, few studies have considered the possibility of directing Lewis acid siting in zeolites (i.e. the majority focus on  $\text{Al}_{\text{FW}}$  siting and distribution<sup>268-270</sup>). Our findings indicate that if heteroatoms (such as Ga) can be selectively placed at specific T sites within zeolites, this would afford the opportunity to direct the spatial distribution of Lewis acid sites for bifunctional catalysis.

## Chapter 5

### Deleterious Effects of Non-framework Al Species on the Catalytic Performance of ZSM-5 Crystals Synthesized at Low Temperature

The material discussed in this chapter has been published. Figure and table numbers have been changed for dissertation consistency. This work is initiated by former group member, Dr. Wei Qin.

#### 5.1 Motivation

One of the challenges associated with zeolite catalyst is their propensity to rapidly deactivate due to internal diffusion limitations that result in coke formation. This is particularly problematic for small-pore zeolites ( $< 4 \text{ \AA}$  pore apertures), and has led to significant efforts within the zeolite synthesis community to design nano-sized materials with markedly reduced internal diffusion pathlength.<sup>20-23</sup> Indeed, there have been many notable advancements in the area of crystal engineering that has led to ultrasmall zeolites,<sup>24-26</sup> 2-dimensional materials,<sup>27-31</sup> hierarchical zeolites,<sup>32-36</sup> and other types of unique architectures that have proven to reduce diffusion limitations and improve the performance of zeolite catalysts.<sup>37-39</sup>

In select cases, a facile approach to prepare nano-sized zeolites is the judicious adjustment of synthesis parameters, which include (but are not limited to) gel composition, the source of reagents, and temperature. For example, the selection of silicon and/or aluminum sources can have a notable impact on the kinetics of crystallization.<sup>40</sup> Moreover, the intimate contact between these sources and alkali metals, which often serve as structure-directing agents, can dramatically alter crystal growth as well as the final physicochemical properties of zeolites.<sup>261</sup> Among the various synthesis parameters that are available to control, temperature is one that can have a notable impact on particle size. In particular, it is widely reported that low-temperature syntheses favor nucleation over crystal growth, thereby leading to an increase in the

number of crystals with a concomitant reduction in average crystal size.<sup>42</sup> Examples include the work of Valtchev and coworkers<sup>43</sup> who systematically examined the effect of temperature on zeolite A (LTA) crystallization and observed a monotonic decrease in crystal size with decreasing synthesis temperature. Rodríguez and coworkers showed for the case of ZSM-5 (MFI) synthesis that ultrasmall crystals (10–20 nm) could be generated at low temperatures (70–90 °C).<sup>44</sup> Numerous studies of ZSM-5 size control can be found in the literature where the vast majority of cases examine the formation of nano-sized crystals with relatively low aluminum content (i.e., Si/Al > 25). In catalytic reactions, it is often desirable to prepare ZSM-5 with higher Al content; however, it is nontrivial to synthesize ZSM-5 with the dual conditions of high acid site density and small crystal size. Reported cases in the literature where such scenarios are achievable tend to involve nano-sized ZSM-5 synthesis at low temperature.<sup>45</sup> One potential pitfall of low-temperature conditions is a higher probability of sacrificing the percent crystallinity of the final product, particularly when trying to synthesize materials within a reasonable time period (i.e., on the order of days).

In this chapter, we focus on the deleterious effect of ZSM-5 synthesis at low temperature, and the challenges associated with achieving Al-rich (Si/Al < 25) nanomaterials for applications in catalysis. Using a combination of experimental techniques, including <sup>29</sup>Al MAS NMR, we show that low temperature favors the incorporation of non-framework Al. These species include extra-framework (octahedral) Al as well as penta-coordinated Al. Moreover, the ZSM-5 catalysts prepared under these conditions are susceptible to Al zoning, which is a well-known phenomenon in zeolite synthesis (most notably for ZSM-5)<sup>271-272</sup> where a disproportionate number of Al sites in the exterior rim of the crystals leads to a spatial gradient in acid site density. The formation of Al-zoned zeolites could be due to delayed

incorporation of Al into the zeolite during crystallization; however, some Al-zoned ZSM-5 crystals exhibit a relatively sharp boundary in Si/Al ratio between the exterior Al-rich rim and the interior Si-rich core, which has been explained by the deposition of Al on zeolite surfaces during quenching.<sup>273-274</sup> Analysis of Al speciation by solid-state NMR reveals that many of the Al species associated with low-temperature synthesis of ZSM-5 are not fully incorporated within the zeolite framework; and given that the Brønsted acidity of zeolites for catalysis applications is attributed to framework (tetrahedral) Al sites,<sup>275</sup> the presence of non-framework species reduces the total acidity, and can adversely affect catalyst activity. Typical methods of dealumination include steam and acid treatments.<sup>253, 276-281</sup> Mild applications of the latter are used in this study to remove extra-framework Al. Here we examine a series of as-made and acid-treated ZSM-5 materials that were prepared with a range of sol gel Si/Al ratios at low temperature (100°C). Our findings highlight the challenges associated with synthesizing “defect-free” ZSM-5 crystals, and the impact of non-framework Al species on the methanol to hydrocarbons (MTH) reaction, which was used as a benchmark to compare the performance of various H-ZSM-5 catalysts.

## **5.2 Experimental Methods**

### **5.2.1 Materials**

The following reagents were purchased from Sigma-Aldrich: tetraethylorthosilicate (TEOS, 98%), aluminum isopropoxide (AIP, 98%), aluminum-tri-sec-butoxide (97%), sodium hydroxide (NaOH, 98%), hydrochloric acid solution (HCl, 1 N), and silica gel (Davisol Grade 636, 35-60 mesh size). Tetrapropylammonium hydroxide (TPAOH, 40%) and sodium aluminate (technical grade) were purchased from Alfa Aesar. Deionized (DI) water was produced with an Aqua Solutions RODI-C-12A purification system (18.2 MΩ). All reagents were used as received without

further purification. For reaction studies, methanol was purchased from J.T. Baker (99.8%) and the argon, oxygen, and nitrogen gases were purchased from Praxair with UHP grade (99.999%).

### 5.2.2 Zeolite Crystallization

ZSM-5 zeolites (gel Si/Al = 20, 30, 50, 75, and 100) were synthesized from growth solutions with a nominal molar composition of 6 TPAOH:0.1 $x$  Na<sub>2</sub>O:25 SiO<sub>2</sub>:0.25 $x$  Al<sub>2</sub>O<sub>3</sub>:480 H<sub>2</sub>O:100 EtOH, where  $x$  = 0.5, 0.67, 1.0, 1.67, or 2.5. TEOS was added to a solution of TPAOH, NaOH and DI water. The mixture was aged at room temperature for 24 h under continuous stirring. AIP was added and the mixture was aged for an additional 24 h at room temperature. The growth solution was then placed in a Teflon-lined stainless steel acid digestion bomb (Parr Instruments) and heated at either 100 or 170°C under autogenous pressure for 3 days. The solution was then removed from the oven and immediately cooled to room temperature. The preparation of ZSM-5 with gel Si/Al = 22 (sample Z22-2) was performed according to a protocol reported by Palčić et al.<sup>282</sup> whereby sodium aluminate and TPAOH were combined in DI water with continuous stirring until the solution was clear. To this mixture was added TEOS to yield a molar composition of 1.23 Na<sub>2</sub>O:9.74 TPAOH:1.0 Al<sub>2</sub>O<sub>3</sub>:43.2 SiO<sub>2</sub>:806 H<sub>2</sub>O. This growth mixture was aged at 80°C for 24 h, and then placed in an acid digestion bomb and heated at 100°C for 7 days. This same procedure was repeated to prepare sample Z22-1 with identical molar composition using a different Al source (AIP), room temperature aging for 24 h, and heating at 100°C for 3 days.

Solid products were isolated from the supernatant by three cycles of centrifugation (13,000 rpm) and washing, and then dried in air under ambient conditions. A fraction of the synthesized ZSM-5 samples were acid treated in 0.1 M

HCl (3 g sample per 100 g of solution) at room temperature for 5 h. After drying, both the treated and untreated samples were calcined in flowing dried air (100 mL min<sup>-1</sup>, Matherson Tri-Gas) at 550°C (using heating and cooling rates of 1 °C min<sup>-1</sup>) for 5 h to removed occluded organic structure-directing agent. To prepare catalysts, ion-exchange was performed three times using a 1 M NH<sub>4</sub>NO<sub>3</sub> solution containing 2 wt% of calcined zeolite samples, which was heated at 80°C under continuous stirring for 2 h. The exchanged samples were dried and calcined again to obtain protonated (H-form) zeolites.

### 5.2.3 Characterization

Powder X-ray diffraction (XRD) patterns were collected on a Rigaku diffractometer using Cu K $\alpha$  radiation (40kV, 40 mA). Scanning electron microscopy (SEM) was conducted at the Methodist Hospital Research Institute in the Department of Nanomedicine SEM Core using a Nova NanoSEM 230 instrument with ultrahigh resolution FESEM (operated at 15 kV and a 5mm working distance). Energy dispersive X-ray spectroscopy (EDX) was performed using a JEOL SM-31010/METEK EDAX system at 15 kV and 15 mm working distance. X-ray photoelectron spectroscopy (XPS) analysis of samples was performed using a PHI 5800 ESCA (Physical Electronics) multi-technique system equipped with a standard achromatic Al K $\alpha$  X-ray source (1486.6 eV) operating at 300 W (15 kV and 20 mA) and a concentric hemispherical analyzer. The equipment neutralizer component was utilized to prevent charging effects. All data were collected at a 45° takeoff angle. Solid-state NMR experiments were performed at 11.7 T on a JEOL ECA-500 spectrometer, equipped with a 3.2mm Magic Angle Spinning Probe. <sup>27</sup>Al MAS NMR spectra were obtained at a spinning frequency of 12.5 kHz, pulse of  $\pi/12$ , relaxation delay of 0.8 s and 4 k scans. The <sup>27</sup>Al chemical

shift was referenced using 1M Al(NO<sub>3</sub>)<sub>3</sub> aqueous solution. The BET surface area was measured by N<sub>2</sub> adsorption using a Micromeritics ASAP2020 instrument.

#### 5.2.4 Catalytic Measurements

Methanol-to-hydrocarbon (MTH) reaction was carried out in a ¼ inch stainless steel tube installed in a Thermo Scientific Lindberg Blue M furnace. All catalysts beds of ZSM-5 (36.9 mg, 40-60 mesh size) were mixed with silica gel (113.1 mg, 35-60 mesh size) and held between two plugs of quartz wool. A K-type thermocouple (Omega Engineering) was inserted into the stainless tube to measure the temperature of the catalyst bed. Prior to the reaction, the catalyst bed was pretreated *in situ* at 550°C for 3 h under flow of dried air (6 cm<sup>3</sup> min<sup>-1</sup> of O<sub>2</sub>, 24 cm<sup>3</sup> min<sup>-1</sup> of N<sub>2</sub>). The catalyst bed was then cooled to the reaction temperature, 350°C. Methanol was fed by a syringe pump (Harvard Apparatus) at 7 µL min<sup>-1</sup> into a heated inert gas stream of Ar (Matheson, 30 cm<sup>3</sup> min<sup>-1</sup>), which resulted in a reactant flow with a weight hourly space velocity (WHSV) of 9 h<sup>-1</sup>. Reaction effluent was evaluated using an on-stream gas chromatograph (Agilent 7890B) equipped with a FID detector and an Agilent DB-1 capillary column. Methanol and dimethyl ether (DME) are considered as reactant with the conversion (*X*) defined as

$$X = [1 - C_{eff}/C_{feed}] \times 100\%, \quad (5-1)$$

where *C<sub>eff</sub>* is the concentration of both methanol and DME in the effluent and *C<sub>feed</sub>* is the concentration of methanol in the feed. The selectivity (*S<sub>i</sub>*) of hydrocarbon product *i* is defined as

$$S_i = [C_i/C_{t,eff}] \times 100\%, \quad (5-2)$$

where  $C_i$  is the concentration of hydrocarbon  $i$  in the effluent and  $C_{t,eff}$  is the total concentration of hydrocarbons in the effluent.

## 5.3 Results and Discussion

### 5.3.1 ZSM-5 Synthesis with Varied Sol Gel Si/Al Ratio

The protocol for ZSM-5 (MFI) synthesis was adapted from a previous study by Persson and workers<sup>283</sup> that reported nano-sized (ca. 150 nm) crystals prepared at low synthesis temperature (100°C). The use of low temperature to produce small ZSM-5 crystallites is common in literature.<sup>42, 44, 284</sup> In this study, our original intent was to assess whether the nominal aluminum content of the crystalline product could be increased. For instance, Persson et al. expressed difficulties with incorporating additional Al into ZSM-5 beyond their reported value of Si/Al = 50. This is consistent with a broader survey of literature wherein it is difficult to find reports of ultrasmall ZSM-5 crystals (<200 nm) prepared with high Al content (i.e., Si/Al  $\leq$  25). Valtchev and coworkers<sup>282</sup> recently reported the synthesis of ZSM-5 crystals with sizes of 100 – 150 nm with Si/Al ratios of 25 to 35. Their study revealed that lower temperature resulted in less crystalline ZSM-5 (i.e., reduced framework Al) and a higher percentage of amorphous (extra-framework) species and defects (e.g., silanol nests).

Here, we examined Al incorporation at fixed temperature of 100°C by adjusting the sol gel Si/Al ratio. The ZSM-5 samples are denoted as ZX, where X is the Si/Al ratio of the original sol gel mixture. We varied X from 20 to 100 (Table 5.1) by adjusting the quantity of aluminum source while keeping the silica content fixed. Aluminum incorporation into the zeolite framework requires a structure-directing agent (SDA) to facilitate the formation of the 3-dimensional porous network and also to compensate for the negative charge of tetrahedral Al sites within the MFI framework. To this end,

we used a combination of tetrapropylammonium ( $\text{TPA}^+$ ) and  $\text{Na}^+$  ions as organic and inorganic SDAs, respectively. For each synthesis, we adjusted the NaOH content in order to maintain a constant sodium-to-aluminum ( $\text{Na}^+/\text{Al}$ ) ratio. Powder X-ray diffraction (XRD) patterns of as-made ZSM-5 samples (Figure D1) confirm that syntheses with  $X \geq 30$  result in ZSM-5 without noticeable impurities or residual amorphous material, whereas higher Al content ( $X = 20$ ) leads to an amorphous product. The latter can be avoided when using higher  $\text{Na}^+$  concentration, analogous to the protocol reported by Palčić et al.,<sup>282</sup> which leads to a crystalline product (sample Z22-1). Although there is no apparent amorphous material in its powder XRD pattern (Figure D1), it is evident this sample is not fully crystalline by virtue of its  $^{27}\text{Al}$  MAS NMR spectrum (Figure D3) revealing an abnormally low framework Al content (Table 5.1). Indeed, samples Z22-1 and Z30 both have <60% framework Al (i.e., as denoted by the 55 ppm peak in the NMR spectra); however, longer synthesis time used to prepare sample Z22-2 appears to facilitate Al incorporation, as denoted by an increase to >70% framework Al. Textural analysis by nitrogen adsorption/desorption (Figure D2) reveals a monotonic reduction in BET surface area from 547 to 470  $\text{m}^2/\text{g}$  with increasing sol gel Si/Al ratio (samples Z30 to Z100), with only minor differences in micropore volume (Table 5.1). Elemental analysis by energy-dispersive X-ray spectroscopy (EDX) shows a linear increase in the Si/Al ratio of ZSM-5 crystals (spanning from 17 to 57) with increasing sol gel Si/Al ratio. For samples with gel Si/Al  $\geq 30$ , the zeolite (solid) contains a disproportionately larger amount of Al compared to the starting sol gel mixture (i.e.,  $\text{Si}/\text{Al}_{(\text{gel})} > \text{Si}/\text{Al}_{(\text{solid})}$ ).

**Table 5.1.** Properties of ZSM-5 samples synthesized from different sol gel Si/Al ratios.

Sample <sup>a</sup>	Si/Al (gel)	Si/Al (solid)		Al content (%) <sup>b</sup>			Textural analysis	
		EDX	XPS	Al (55 ppm)	Al (31 ppm)	Al (0 ppm)	S <sub>BET</sub> (m <sup>2</sup> /g)	V <sub>micro</sub> (cm <sup>3</sup> /g)
Z20 <sup>c</sup>	20	----	----	----	----	----	----	----
Z30	30	16.8	15.0	58.5	23.8	17.7	547	0.16
Z50	50	26.5	19.0	84.5	4.7	10.8	517	0.15
Z75	75	39.4	24.0	83.9	3.6	12.5	475	0.14
Z100	100	57.4	25.4	88.6	2.7	8.7	470	0.14
Z30T	30	45.6	49.8	85.1	3.9	11.0	498	0.14
Z50T	50	52.4	65.2	90.7	2.6	6.7	476	0.16
Z75T	75	52.6	56.1	85.9	4.5	9.6	475	0.16
Z100T	100	54.8	48.4	90.8	2.2	7.1	488	0.16
Z50H	50	30.5	20.7	91.4	1.7	6.9	460	0.14
Z50HT	50	34.8	25.3	97.1	0.1	2.8	465	0.13
Z22-1 <sup>d</sup>	22	24.5	14.1	52.7	26.1	21.2	359	0.12
Z22-2 <sup>e</sup>	22	25.4	13.5	70.4	12.4	17.3	435	0.15

(a) Samples nomenclature: Z = ZSM-5, numbers refer to sol gel Si/Al ratio, T = samples treated with mild acid, and H = samples synthesized at higher temperature; (b) Deconvoluted peaks in <sup>27</sup>Al MAS NMR spectra (Figure 5.4 and Figure D3); (c) Determined to be amorphous from its XRD pattern (Figure D1A); (d) Sample Z22-1 was prepared with increased NaOH content (0.73 Na<sub>2</sub>O:26 SiO<sub>2</sub>); (e) Z22-2 was prepared using a modified procedure reported by Palčić et al.<sup>282</sup> (see the Experimental section for details).

ZSM-5 samples exhibit a spheroidal morphology with crystal sizes in the range of 100 – 200 nm (Figure 5.1). There was no apparent change in crystal size with decreasing sol gel Si/Al ratio. The average size (diameter) of crystals measured from at least 30 particles within a single batch is 198 ± 26 nm, 182 ± 15 nm, 169 ± 15 nm, and 167 ± 11 nm for Z30, Z50, Z75, and Z100 samples, respectively. Likewise, the crystals all exhibit some degree of surface roughness (Figure 5.1, inset images), which is reflected in N<sub>2</sub> adsorption/desorption profiles (Figure D2) showing hysteresis at P/P<sub>0</sub> > 0.75 that is attributed to interparticle porosity. Comparison of SEM images does not indicate a systematic change in surface roughness with Al content. This is seemingly inconsistent with the trend proposed by Stucky and coworkers<sup>285</sup> who reported that

rough and smooth ZSM-5 crystals are formed in Al-rich and Al-deficient synthesis gels, respectively. They attributed the rough surface features of ZSM-5 crystals to a branching epitaxial growth of Al-rich MFI nanocrystals near the end of zeolite crystallization due to Al zoning. While spatial gradients in the elemental composition of zeolite ZSM-5 are widely reported, the synthesis conditions and processes leading to Al zoning are not well understood.

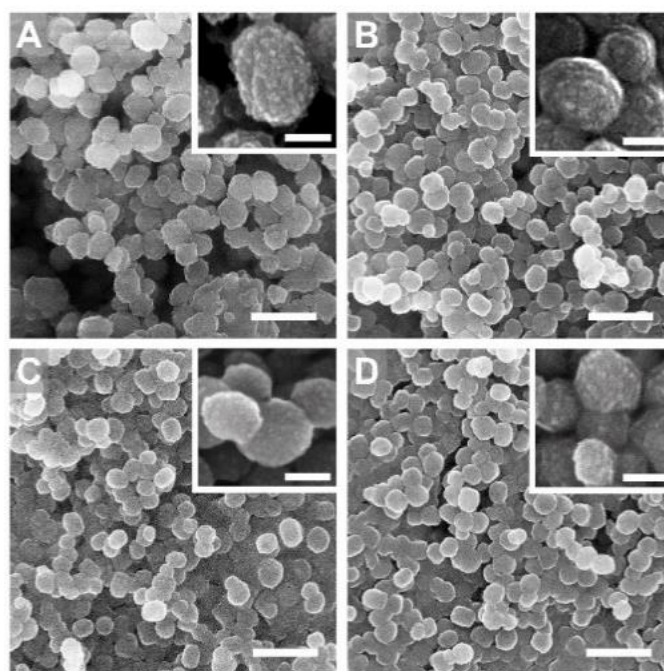


**Figure 5.1.** Scanning electron micrographs of the following as-made ZSM-5 samples: (A) Z30, (B) Z50, (C) Z75, and (D) Z100. Scale bars are equal to 500 nm. Scale bars of the insets are equal to 100 nm.

To determine if as-made ZSM-5 samples are Al-zoned, we compared the Si/Al ratios of solids measured by EDX and X-ray photoelectron spectroscopy (XPS). EDX has a sampling depth around two micrometers and was used to obtain the bulk chemical composition of each sample. XPS is a surface-sensitive technique with a sampling depth of only a few nanometers that was used to obtain the surface (or outer rim) chemical composition. The results of elemental analysis are summarized in Table 5.1. Interestingly, the sample prepared with the highest quantity of Al (Z30), which also has the highest degree of surface roughness (Figure 5.1A, inset), exhibits negligible Al

zoning. This is counter to the correlation reported by Stucky and coworkers linking Al zoning with enhanced surface roughness. Here, we find that the ZSM-5 sample prepared with the least Al content (Z100) exhibits the highest degree of Al zoning. When comparing the entire series of samples, we observe a linear dependence of the  $\text{Al}_{(\text{surface})}/\text{Al}_{(\text{bulk})}$  ratio (or the degree of Al zoning) of extracted solids on the Si/Al ratio of the sol gel synthesis mixture (Figure 5.2A, triangles).

Prior studies have suggested different types of Al coordination in Al-zoned ZSM-5. For instance, it is reported that Al in the exterior rim is crystalline (i.e., framework Al, denoted as *FAI*).<sup>285</sup> Alternatively, it has been posited that Al zoning may be attributed to Al deposition on the zeolite surface during the quenching (cooling) step when solids are extracted from the mother liquor.<sup>271</sup> The latter hypothesis indicates that the formation of an Al-rich exterior could be attributed to extra-framework Al (denoted as *EFAl*). To determine the chemical nature of Al zoning in our ZSM-5 samples, we performed a common method of removing EFAl via mild acid treatment. Notably, as-made zeolites were treated with 0.1 M HCl at room temperature, which is reported to exclusively remove EFAl without extracting FAI.<sup>286</sup> We refer to the acid-treated samples herein as ZXT (where T = treated). After acid treatment, the physicochemical properties of each sample were evaluated. Mild acid treatment removes Al from the zeolites, resulting in two observed effects. First, acid-treated samples lack any evidence of Al zoning, i.e.,  $\text{Al}_{(\text{surface})}/\text{Al}_{(\text{bulk})} \approx 1$  (Figure 5.2A, circles). As also shown in Table 5.1, we observe by EDX that irrespective of the original sol gel composition, all Si/Al ratios of acid-treated samples converge to  $\text{Si}/\text{Al} \approx 50$  (i.e., the nominal sol gel Si/Al ratio reported by Persson and coworkers<sup>283</sup>). Comparison of EDX and XPS data also reveal negligible Al zoning in all acid-treated samples. Moreover, we observe that the total loss of Al during acid treatment monotonically decreases with increasing sol gel

Si/Al (Figure 5.2B). It should be noted that the most significant reduction in zoning occurs for zeolites with a higher Si/Al ratio (Figure 5.2A, Z100); however, the net change in solid Si/Al is minimal (Figure 5.2B) owing to the reduced quantity of Al throughout the framework. Conversely, samples with low Si/Al ratio (e.g., Z30) show no evidence of Al zoning, but acid treatment results in the most significant loss of Al and the most notable change in solid Si/Al ratio.

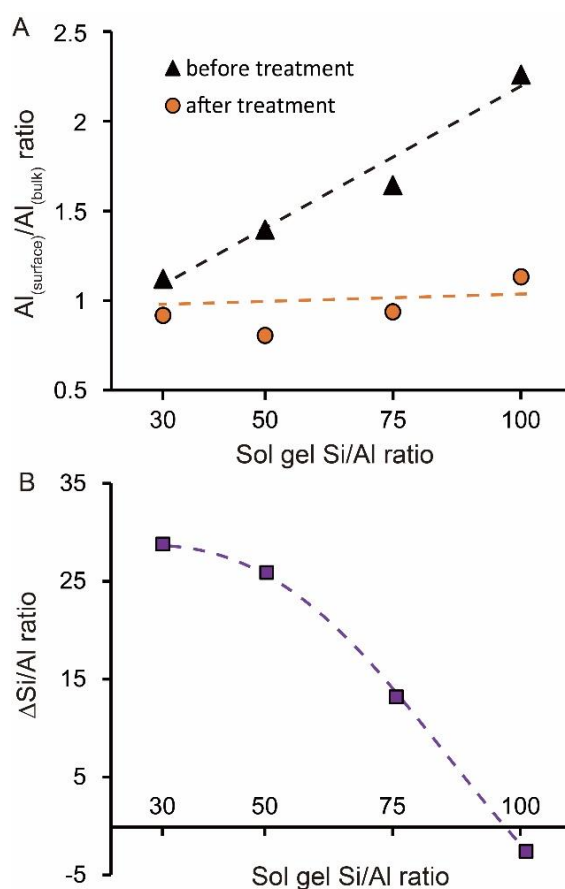


**Figure 5.2.** (A) Ratio of surface Al content and bulk Al content as a function of the sol gel Si/Al ratio. (B)  $\Delta$ Si/Al ratio = Si/Al (after acid treatment) – Si/Al (before acid treatment) as a function of the sol gel Si/Al ratio.

Significant shifts in Al content with acid treatment is evidence for the presence of non-framework Al. In order to gain a better understanding of Al speciation, we used  $^{27}$ Al MAS NMR to distinguish between framework and extra-framework species. Figure 5.3 contains the  $^{27}$ Al MAS NMR spectra of H-ZSM-5 samples prepared with sol gel Si/Al ratios spanning from 30 to 75. The peaks at 55 ppm and 0 ppm in  $^{27}$ Al MAS

NMR spectra correspond to tetrahedral Al (FAI) and octahedral Al (EFAI), respectively.<sup>253</sup> As previously discussed, samples prepared at higher Al content (e.g., Z30) have < 60% FAI, whereas the samples prepared at lower Al content have  $85 \pm 2\%$  FAI (Table 5.1). Inspection of NMR spectra reveals a peak around 31 ppm that increases in relative intensity with higher Al content in the sol gel mixture. This peak has been assigned to either penta-coordinated or distorted tetrahedral Al and is frequently observed in amorphous aluminosilicates.<sup>287-288</sup> In Table 5.1, we report the percentages of each Al species estimated from the deconvolution of NMR spectra at resonances  $\delta = 0, 31,$  and 55 ppm corresponding to octa-, penta-, and tetra-coordinated Al, respectively. An example of peak deconvolution is shown in Figure 5.4, while analogous plots for all samples are provided in Figure D3 of the Appendix.

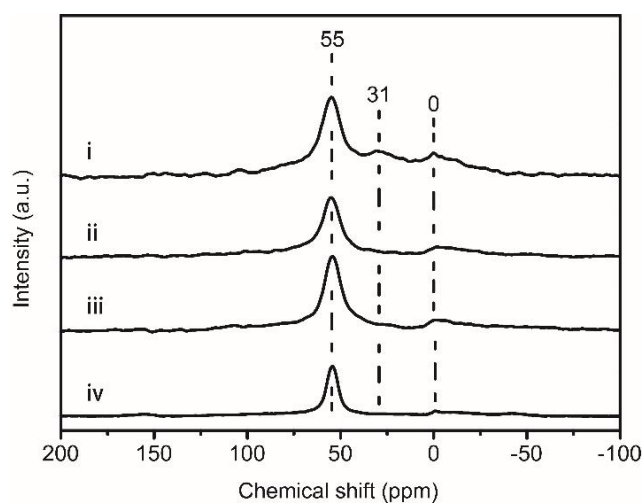


**Figure 5.3.** <sup>27</sup>Al MAS NMR spectra for the H-form samples: (i) Z30, (ii) Z50, (iii) Z75, and (iv) Z100. Vertical dashed lines represents: tetrahedral Al (55ppm), penta-coordinated Al (31 ppm), and octahedral Al (0 ppm).

The presence of a third Al species in ZSM-5 samples (at  $\delta = 31$  ppm) has long been identified in zeolites and nonporous aluminosilicates<sup>289-293</sup>; however, it is being recognized more frequently in studies of zeolites, although the molecular details of its incorporation within the ZSM-5 framework are not well understood. The Z30 sample has the largest percentage of penta-coordinated Al, but lacks evidence of Al zoning,

which suggests the latter is not uniquely correlated with this Al species. Indeed, samples with a higher degree of zoning exhibit much less penta-coordinated Al (< 7%), suggesting that EFAl may be responsible for non-framework Al in the outer rim of zeolites. Solid-state NMR analysis of the most aluminous H-form sample before (Figure 5.4A, Z30) and after (Figure 5.4B, Z30T) acid treatment reveals a significant reduction in the resonance at  $\delta = 31$  ppm with a concomitant reduction in the intensity of the 0 ppm peak. The partial removal of EFAl is an expected outcome of mild acid treatment, whereas the nearly complete removal of penta-coordinated Al (or distorted tetrahedral Al) indicates the facile removal of this species during post-synthesis treatment.

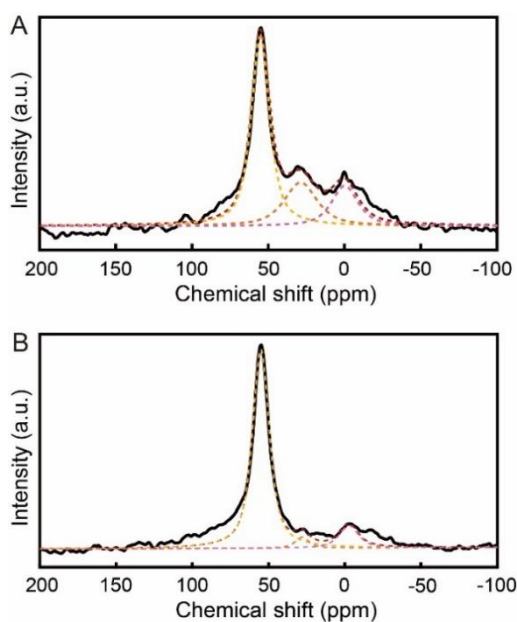


**Figure 5.4.** Deconvolution of  $^{27}\text{Al}$  MAS NMR spectra showing the curve fittings of (A) H-Z30 (as-made aluminous sample) and (B) H-Z30T (corresponding sample after mild acid treatment).

It is not fully evident whether the penta-coordinated Al reported here should be classified as distorted FAI species or as EFAl. Here we simply refer to these species as non-framework Al, placing it in the same category as EFAl. This is consistent with previous studies indicating that signals in the  $^{27}\text{Al}$  MAS NMR spectra around  $\delta = 30$  ppm are extra-framework moieties,<sup>282, 289, 291</sup> whereas resonances at higher chemical

shifts (ca.  $\delta=40$  ppm) are attributed to less-ordered (or distorted) FAI species.<sup>294</sup> Chen et al.<sup>290</sup> came to a similar conclusion when characterizing dealuminated zeolite omega and showed that distorted tetrahedral Al and penta-coordinated Al are generated by steam treatment at low and high temperature, respectively. Similar Al speciation was noted by Park et al.<sup>292</sup> when synthesizing a CHA-type  $\text{AlPO}_4$  molecular sieve. Moreover, Pidko et al.<sup>291</sup> investigated the catalytic role of extra-framework Al species in FAU zeolites, introduced by chemical vapor deposition of trimethylaluminum (TMA) followed by its decomposition. Their analysis of these samples by  $^{27}\text{Al}$  MAS NMR revealed both penta-coordinated and octahedral Al species in modified FAU catalysts, which reportedly exhibited a much higher propane cracking rate than commercial USY zeolite.

### 5.3.2 ZSM-5 synthesis at Higher Temperature.

The synthesis conditions for Z50 that were adopted from a previous protocol<sup>283</sup> were also used in our previous study to generate nano-sized ZSM-5 crystals as seeds for the formation of ZSM-5@silicalite-1 coreshell particles.<sup>295</sup> The epitaxial growth of purely siliceous MFI (silicalite-1) over Z50 seeds was accomplished by first annealing the ZSM-5 particles at high temperature to remove any residual amorphous material from the surface of zeolite particles, and also to remove EFAl or transform it to FAI. An unreported observation in this study was that ZSM-5 crystals without the high-temperature annealing step performed poorly in catalytic studies. Motivated by this observation as well as a general survey of literature showing that ZSM-5 is commonly crystallized at higher temperatures, we investigated Al zoning as a function of synthesis temperature. There are numerous effects that temperature can impose on zeolite formation, such as altering the solubility of Si and Al sources as well as the crystallization kinetics. It is generally expected that elevated synthesis temperature

increases the rate of crystal growth. Moreover, it is anticipated that a higher temperature can facilitate Al incorporation in the MFI framework, thus resulting in a more homogeneous distribution of acid sites. This, in turn, would minimize Al zoning that is the byproduct of Al incorporation (or deposition) at later stages of crystallization or during sample quenching. To our knowledge, thermodynamic data of aluminosilicate speciation at synthesis conditions (100 – 170°C) is unknown, and thus the premise of a more homogeneous distribution of Al throughout the zeolite particle with increasing temperature is based on a hypothesis that barriers for Si-O-Al bond formation are lowered at these conditions, which would facilitate FAI formation. An additional point of concern when preparing ZSM-5 is its molar composition – notably disproportionate ratios of Na<sup>+</sup>/Al given that Na<sup>+</sup> serves as an inorganic SDA and counterion to negatively-charged FAI sites. To offset the potential deleterious effects of low inorganic SDA concentration, we also tested modified synthesis mixtures containing additional Na<sup>+</sup> (see the Experimental section for details).

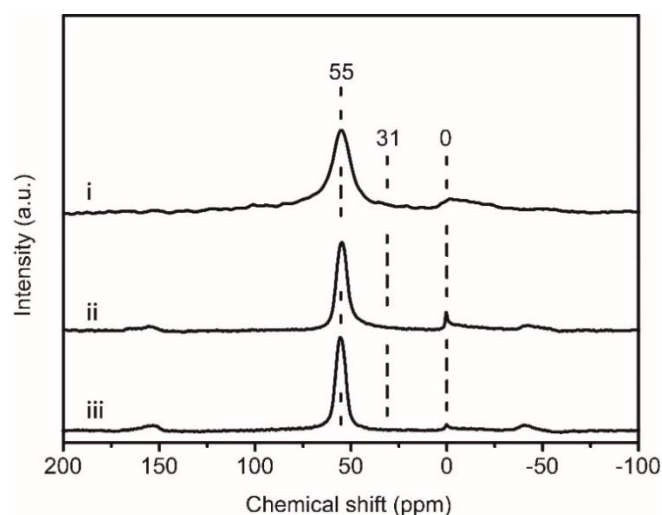


**Figure 5.5.** <sup>27</sup>Al MAS NMR spectra of (i) H-Z50, (ii) H-Z50H, and (iii) H-Z50HT. Dashed lines highlight peaks corresponding to FAI (55 ppm), penta-coordinated Al (31 ppm), and EFAI (0 ppm).

To test the effect of higher temperature, we repeated the synthesis of Z50 at 170°C (referred to as sample Z50H) and compared its <sup>27</sup>Al MAS NMR spectrum

(Figure 5.5ii) with the corresponding sample after mild acid treatment, Z50HT (Figure 5.5iii). The higher temperature of ZSM-5 synthesis gives rise to sharper NMR peaks, counter to the broad and asymmetric peaks of Z50 synthesized at 100°C (Figure 5.5i). It has been suggested<sup>282</sup> that lower peak intensity for ZSM-5 prepared at low temperature may be attributed to so-called *NMR invisible Al species*, which broadens the signal and renders their detection more challenging (particularly for dehydrated Al sites).<sup>296-297</sup> Deconvolution of the NMR data shows that the penta-coordinated Al ( $\delta = 31$  ppm) in Z50H is nearly one-third that of Z50 (Table 5.1), whereas the quantity of EFAI (0 ppm) is 36% less than its counterpart prepared at low temperature. Higher synthesis temperature, however, does not fully eliminate non-framework Al from the final product (consistent with the previous findings<sup>282</sup>). This is evident when comparing samples before (Z50H) and after (Z50HT) acid treatment, where the latter has the highest fraction of FAI (ca. 97%) and the lowest fraction of penta-coordinated Al (ca. 0.1%) among all zeolites analyzed in Table 5.1. We also observed that higher synthesis temperature does not eliminate Al zoning. Moreover, acid treatment had little effect on the removal of exterior Al from Z50H, as verified by elemental analysis of samples before and after acid treatment that shows no difference in zoning, i.e.,  $\text{Al}_{(\text{surface})}/\text{Al}_{(\text{bulk})} \approx 1.4$  for both Z50H and Z50HT.

### 5.3.3 Methanol to Hydrocarbons Reaction

Here we compare the catalytic performance of several as-made and acid-treated ZSM-5 samples in the methanol-to-hydrocarbons (MTH) reaction to assess differences in the lifetime and selectivity of catalysts with varying Al speciation and zoning. All zeolites were ion-exchanged to their acid form (HZSM-5) to introduce Brønsted acid sites. The catalysts were tested in a packed bed reactor with a fixed weight hourly space velocity (WHSV). MTH reactions were performed at sub-complete methanol

conversion to assess catalyst deactivation and selectivities to light olefins and aromatics. We first assessed the performance of H-Z30 (Figure 5.6, purple triangles), which has high amounts of EFAl and penta-coordinated Al, a low percentage of FAI, and no apparent Al zoning. The initial methanol conversion over this catalyst is relatively low (ca. 18%) and rapidly decreases to ca. 3 % in less than 1 h time on stream (TOS). We next tested the corresponding acid-treated sample, H-Z30T (Figure 5.6, red squares), which resulted in significant removal of Al, leading to a dramatic increase in FAI (from 59 to 85%), a marked reduction in penta-coordinated Al (from 24 to 4%), and a more moderate reduction in EFAl (from 18 to 11%). The initial methanol conversion over H-Z30T is 41% and it exhibits a slow rate of deactivation with TOS. Interestingly, the performance of H-Z30T is similar to that of H-Z75 (Figure 5.6, yellow circles), which has nearly identical percentages of FAI, EFAl, and penta-coordinated Al as well as similar bulk Si/Al ratio (measured by EDX). The primary difference between these two catalysts is that H-Z75 is slightly Al zoned, yet this does not appear to affect catalyst lifetime, but does have an appreciable impact on selectivity (as discussed below).

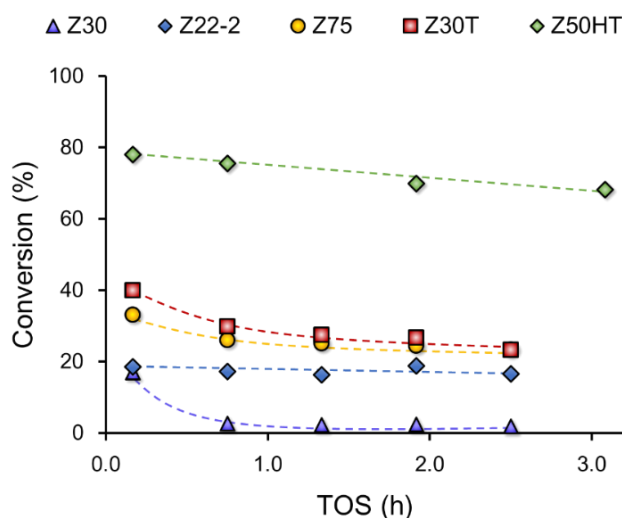


**Figure 5.6.** Methanol conversion as a function of time-on-stream (TOS) for five H-form ZSM-5 catalysts. Dashed lines are interpolated to guide the eye.

Palčić et al. recently reported that H-Z22-2 with an approximate size of 100 nm exhibits superior MTH performance relative to an industrial ZSM-5 catalyst (1 – 3  $\mu\text{m}$  in size) supplied by Süd-Chemie.<sup>282</sup> The unique properties of H-Z22-2 were attributed in part to its synthesis at 100°C, which resulted in a 70% crystalline product with markedly lower Brønsted acidity (79  $\mu\text{mol g}^{-1}$ ) compared to the commercial catalyst (582  $\mu\text{mol g}^{-1}$ ). The conditions they selected for catalytic testing were WHSV = 1  $\text{h}^{-1}$  and 450°C, which resulted in H-Z22-2 having a longer lifetime at 100% methanol conversion, and also produced a 6.3-fold higher propene-to-ethene ratio ( $\text{C}_3=/\text{C}_2=$ ) compared to commercial ZSM-5. Here, we performed catalytic testing at a different set of reaction conditions (WHSV = 9  $\text{h}^{-1}$  and 350°C) to ensure sub-complete methanol conversion. As shown in Figure 5.6, we observe that H-Z22-2 exhibits a low methanol conversion (ca. 20%), nearly identical to H-Z30 with a much slower rate of deactivation. The lower reaction temperature and shorter contact time used in our experiments likely explain the disparity in catalyst performance. Indeed, the catalysts in Figure 5.6 that were prepared at low synthesis temperature all exhibit poor activity. It is apparent that the significant quantities of non-framework Al in ZSM-5 synthesized at 100°C has a negative impact on catalyst performance. Moreover, we show that acid treatment to remove a large percentage of non-framework Al leads to only marginal improvement in performance, suggesting there is something inherently defective in these materials that cannot easily be corrected with post-synthesis treatment. To test this hypothesis, we performed the MTH reaction using the sample prepared at 170°C after acid treatment, H-Z50HT (Figure 5.6, green diamonds). As previously noted, this sample had the highest percentage of FAI and lowest percentages of non-framework Al among all zeolites. As shown in Figure 5.6, the initial methanol conversion using this catalyst (ca. 80%) is nearly double those of the other catalysts, including H-Z75 (a material with

approximately the same bulk Si/Al ratio). This suggests that higher synthesis temperature produces ZSM-5 crystals with fewer defects; however, beyond the relative amounts of EFAl and penta-coordinated Al, or the degree of Al zoning, it is difficult to elucidate the exact cause of unexpectedly low catalyst activity. To this end, there may exist several factors beyond what is considered in this study that contributes to suboptimal catalytic performance, which would require more detailed characterization and modeling to fully rationalize these observations.

In addition to probing catalyst activity, we also compared MTH selectivities for several ZSM-5 samples prepared at low temperature (Figure 5.7A). The catalysts selected for this study exhibit similar initial methanol conversion (20 – 40%); and the data presented here was taken from the initial time point in Figure 5.6. There are subtle differences in the product distribution among all catalysts studied; however, a signature feature of all samples is the relatively high percentage of methane (10 – 20%) in the effluent. We attribute this to the large percentages of non-framework Al species. For instance, Lercher and coworkers<sup>298-300</sup> have proposed that EFAl promotes the formation of formaldehyde and enhances the aromatics-based cycle of the hydrocarbon pool (HCP) mechanism for MTH reactions.<sup>301-303</sup> Moreover, Hwang et al. have proposed that formaldehyde and methane are generated simultaneously via methanol disproportionation.<sup>304</sup> Arora et al.<sup>301</sup> have investigated the effect of formaldehyde co-feed with methanol on the  $C_{3=}/C_{2=}$  ratio. They found that the ratio decreases from 24.7 in the absence of formaldehyde to 0.8 in the case of 20 Pa formaldehyde co-feed, thus indicating the presence of formaldehyde enhances the aromatics cycle. This is consistent with the higher EFAl content of untreated ZSM-5 catalysts, which exhibit relatively low  $C_{3=}/C_{2=}$  ratios (Figure 5.7B) compared to values for ZSM-5 reported in the literature. Comparison of as-made samples with the one subjected to acid treatment

reveals a noticeable difference in selectivity. The results for H-Z30T reveal that the removal of EFAl by mild acid treatment leads to a concomitant reduction in methane selectivity (ca. 5%). In addition, the acid-treated catalyst exhibits a higher  $C_{3=}/C_{2=}$  ratio (Figure 5.7B), which indicates the promotion of the olefins-based cycle of the HCP mechanism. Conversely, the lower  $C_{3=}/C_{2=}$  ratios for untreated samples are consistent with EFAl promotion of the aromatic-based cycle of the HCP mechanism. Additional evidence is gleaned from the reduced ethylene-to-2MBu ratio in Figure 5.7A (where 2-MBu refers to the sum of 2-methylbutane and 2-methyl-2-butene). This ratio is conventionally used in literature as an indicator of the relative propagation of the two cycles in the HCP mechanism.<sup>38, 53</sup>

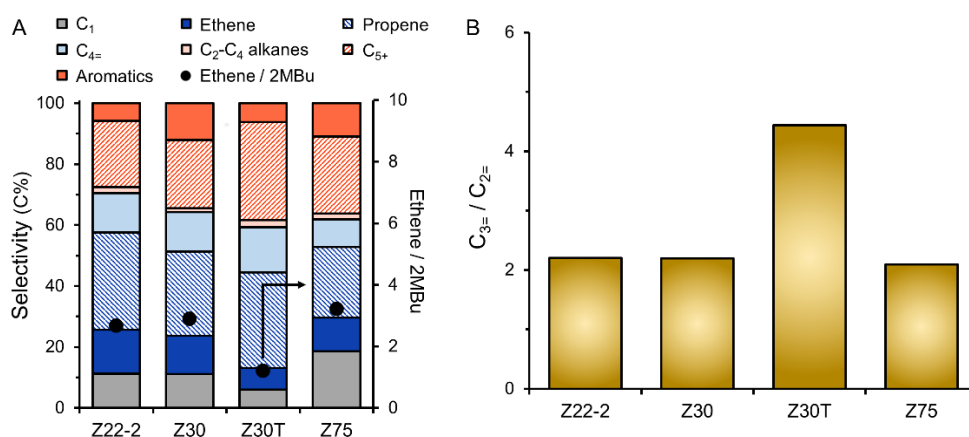


**Figure 5.7.** (A) Comparison of product selectivity in MTH reactions at sub-complete methanol conversion (left axis) and ethene-to-2MBu ratio (right axis) for each catalyst. (B) Comparison of the propene-to-ethene ( $C_{3=}/C_{2=}$ ) ratio.

Brønsted acidity can have a significant effect on product selectivity. This was highlighted in a review by Weckhuysen and coworkers who reported a linear relationship between propylene selectivity and Si/Al ratio (or reduced Brønsted acidity).<sup>305</sup> As proof of concept, the same group also reported a study in which they showed that propylene yield can be increased as high as 53% over HZSM-5 by reducing Brønsted acid sites via calcium exchange.<sup>306</sup> Another study of MTH over HZSM-5 by Khare et al.<sup>53</sup> found that the ethylene-to-2MBu ratio increased from 0.8 to 2.4 with

decreasing Si/Al ratio (from 1580 to 55), suggesting that the propagation rate of aromatics-based cycle is enhanced with higher aluminum content. A study by Wang et al.<sup>287</sup> characterized proton-exchanged tetrahedral and penta-coordinated Al in amorphous silica-alumina (ASA) and reported similar Brønsted acidity; however, the data in Figure 5.7B suggest that variations similar behavior does not apply to aluminosilicate zeolites given that the quantity of non-framework Al has little impact on the  $C_{3=}/C_{2=}$  ratio. Indeed, samples H-Z22-2, H-Z30, and H-Z75 all have varying quantities of Al species (and bulk Si/Al ratios), but similar activity and selectivities. The removal of non-framework Al species leads to improved lifetime and higher  $C_{3=}/C_{2=}$  ratio (e.g., sample H-Z30T), which is seemingly consistent with the trends reported in literature for changes in the Si/Al ratio; however, it is also evident that the presence of non-framework Al renders such trends among the entire set of samples convoluted. Thus, particular care should be taken when evaluating the performance of ZSM-5 catalysts containing high percentages of octahedral and penta-coordinated Al. The acid strength of each species (relative to FAI sites) in HZSM-5 and their putative role(s) in the catalytic reaction remain to be determined.

#### **5.4 Summary**

In summary, we have demonstrated that the incorporation of Al into ZSM-5 is often incomplete, leading to non-framework sites that result in poor catalytic performance. This is particularly true for low temperature syntheses, which are ostensibly necessary to prepare ZSM-5 materials with small crystal size (i.e., less than 200 nm) and high Al content (i.e., Si/Al < 25). Our findings seem to indicate that higher synthesis temperature leads to improved catalyst performance, presumably by facilitating Al incorporation into framework sites; however, the materials prepared at high temperature in this study still possess defects, many of which may not be obvious

from common characterization techniques. In general, comparisons between zeolites of comparable physicochemical properties where the synthetic material of choice exhibits inferior catalytic performance to a benchmark (e.g., commercial catalyst) are rarely reported. While zeolites prepared in the laboratory may be prone to underperform relative to commercial catalysts, such outcomes are less likely to be found in the open literature.

One intent of this study was to highlight the challenges of ZSM-5 synthesis that often get overlooked – particularly considering it is one of the most synthesized, characterized, tested, and commercially used materials among the ca. 248 known zeolites. While ZSM-5 is arguably much easier to synthesize compared to the vast majority of framework types, this does not necessarily imply the ease of preparing ZSM-5 with few defects. The presence of defects can be difficult to extract from published studies of ZSM-5 catalysis owing to the expectation that these studies only report materials with exceptional performance relative to either commercial catalysts or some high-performance reference material. Moreover, the variability in reaction conditions makes it difficult to draw comparisons among different studies, which is critical for the broader development of structure-performance relationships. In light of the growing impact of data analytics and machine learning, it would be beneficial to populate databases with information on synthesis failures, which is sparsely available, but can be equally important as data on successful syntheses.

The library of ZSM-5 materials synthesized and tested here are a relatively small fraction of examples that highlight the impact of reaction conditions on the generation of defects. In this study, we focus solely on non-framework Al and the phenomenon of zoning; however, it is important to state that there are potentially other factors that contribute to the unexpectedly low activity of these zeolites in MTH reactions.

Examples may include (but are not limited to) the blocking of pores, the presence of silanol pockets, and/or residual amorphous material that is undetected in powder X-ray diffraction patterns. Moreover, it is evident from a survey of the literature that the presence of non-framework Al, under certain circumstances, can have a positive impact on catalyst performance depending on the reaction, zeolite framework type, and reaction conditions (e.g., temperature and space velocity). There is an increasing number of studies that report penta-coordinated Al, although it is not well understood how these species are incorporated in zeolites, and to what extent they influence catalytic performance. More detailed investigations, both experimental and computational, are needed to better understand the role of various Al species and their impact (either positive or negative) on catalytic reactions.

## Chapter 6

### Summary and Future Outlook

#### 6.1 Current Research Summary

In this dissertation, we explored methods of preparing 2D nanosheets via a one-pot synthesis since prior studies of 2D zeolite catalysts demonstrate enhanced mass transport with a concomitant improvement in catalyst lifetime and selectivity. We selected a common layered zeolite, the MWW framework, and demonstrated a novel commercially-viable one-step synthesis approach to produce MWW-type nanosheets with an average thickness of 3.5 nm (ca. 1.5 unit cells). We observed that the surfactant cetyltrimethylammonium (CTA) can operate as a dual OSDA and exfoliating agent to affect Al siting and eliminate the need for post-synthesis delamination. A model reaction was also tested to assess external (surface) Brønsted acid sites. The catalytic performance of our 2D material showed a remarkable increase in the conversion relative to 3-dimensional MWW (MCM-22) and 2D layers prepared from post-synthesis exfoliation (ITQ-2). Furthermore, we have developed structure-performance relationships of metal-containing zeolite catalysts in ethylene DHA reactions. Using a combination of experiments and DFT modeling (collaboration with Dr. Hari Thirumalai and Prof. Lars C. Grabow from the University of Houston) we first investigated the effect of  $\text{Ag}^+$  (Lewis acid) addition on DHA reactions. Our findings revealed that ethylene activation on  $\text{H}^+$  (Brønsted acid) sites is more energetically favorable, and likely constitutes the first mechanistic step in the DHA reaction. On the other hand,  $\text{Ag}^+$  sites could further promote dehydroaromatization with enhanced selectivity towards toluene and xylenes. We also investigated the roles of (extra)framework Ga species and explored the locations and structures of different Ga species prepared via distinct synthesis approaches. Using a combination of advanced

techniques, including X-ray absorption (XAS) and solid-state  $^{27}\text{Al}$  and  $^{71}\text{Ga}$  magic angle spinning (MAS) Nuclear Magnetic Resonance (NMR) spectroscopy and DFT calculations, we believe the most effective Lewis sites to promote aromatics are highly dispersed  $[\text{Ga}(\text{X})_2]^+$  ( $\text{X} = \text{OH}$  or  $\text{H}$ ) species that can exchange with Brønsted acid sites. We further observed the presence of framework Ga can facilitate and stabilize strong Ga Lewis acid sites. Lastly, we studied the challenges associated with synthesizing ZSM-5 at low temperature (ca.  $100^\circ\text{C}$ ), which is often necessary to generate small crystals ( $< 200$  nm) with markedly reduced internal diffusion path length for enhanced catalyst stability. Our findings revealed that synthesis at low temperature results in the incomplete incorporation of Al (e.g., penta-coordinated Al species) in ZSM-5 that can be partially removed through post-synthesis mild acid treatment.

## **6.2 Future Outlook**

### **6.2.1 Zeolite Structure Performance**

One of my research projects aims to develop a fundamental understanding of elementary steps in both non-oxidative methane and ethylene upgrading over metal-exchanged zeolite catalysts, as well as to optimize reaction performance by designing novel zeolites for these applications. Tuning zeolite framework compositions will be the future approach to enhance reaction performance (BTX selectivity and catalyst lifetime). As such, three routes, a) number and location of acid sites, b) metal-ZSM-5/silicate-1 core-shell catalyst, and c) mesoporosity will be explored to improve the performance.

Khare et al. recently argued that increasing aluminum content in ZSM-5 catalysts enhances the propagation of aromatics-based cycles for the methanol to hydrocarbon (MTH) reactions using ethylene selectivity as an indicator.<sup>53</sup> They further related the

Al content effect with their previous finding on crystallite size and argued an average number of acid sites, a general parameter, strongly influences product selectivity. A similar trend is also found in our ethylene DHA reactions over ZSM-5 catalysts with different SARs. When time on stream is 10min, BTX selectivity over Ag<sub>25</sub>-ZSM-5 (SAR = 12) is 15% higher than the one over Ag<sub>26</sub>-ZSM-5 (SAR = 23). In order to further investigate the effect of aluminum, we could synthesize ZSM-5 with different Al locations (channel and intersection) by using organic structure-directing agents.<sup>49</sup> Selectivity towards aromatics could be tuned with different Al amount and locations, and the results we obtained may also give us insights on dehydroaromatization mechanism. With the addition of Lewis acid sites, different metal ions may have different oxidation state and preferred locations in zeolite catalysts. Effects of Lewis acid amount and location are the other approach to tune product selectivity. Metal zoning (more metal on the exterior surface) was often observed during our ion exchange process. In order to investigate the effect of metal zoning on reaction performance, zoning degree needs to be controlled, which could be related to ion exchange solution concentration and zeolite size.

In addition, Miyake et al. claimed that they have successfully designed Zn-exchanged ZSM-5@silicate-1 catalysts, which show high para-xylene selectivity (99% based on xylene production, 40% based on total products) over MTH reaction.<sup>307</sup> ZSM-5 with the medium pore size is known for para-xylene production in the industrial level. Removing active sites on the exterior surface by coating silicate-1 can prevent further condensation among aromatics on the external surface, which increases selectivity to p-xylene and catalyst lifetime. Thus, core-shell catalysts with different metal promoters are another future approach to maximize desired product selectivity.

Current reaction results all indicate faster deactivation occurs with the addition of Lewis acid sites compared to the case of Brønsted sites only. Finding a solution that enhances lifetime without loss of aromatic selectivity is worth further investigation. Problem could be solved by elucidating the deactivation mechanism that has been typically attributed to the coke species (ca. 8 Å) at the channel intersections.<sup>308</sup> However, using recent advanced in-situ single crystal UV-Vis and confocal fluorescence microspectroscopy, Weckhuysen argues that rapid deactivation for methanol to hydrocarbon reaction is due to the fast formation of aromatics at the exterior surface of zeolite catalysts.<sup>220</sup> These aromatics are further transformed into heavy aromatic coke species, preventing the diffusion of hydrocarbons through catalysts. If the latter deactivation mechanism occurs in our case, metal-ZSM-5@silicate-1 core-shell zeolite mentioned earlier could impede the deactivation rate because of the inactive silicate-1 shell.

Due to the sinusoidal channels for the MFI framework, the diffusion path of aromatics could be more complicated than the one along the straight channel (MEL framework). Difficulties for aromatics to get out of the zeolite pores may cause rapid deactivation as well. Metal exchanged ZSM-11 could also be investigated and tested for the lifetime comparison. Creating mesopores or preparing hierarchical pore structures in microporous metal-ZSM-5 also can assist the incorporation and diffusion of aromatic molecules formed during DHA reaction.<sup>309-312</sup>

### **6.2.2 Lewis Acid Sites**

Lewis acid sites generally can both tune product selectivity and facilitate reactant activation. Investigation on different types of Lewis acid will be performed on ethylene DHA reaction. We found Lewis acid sites can improve aromatic selectivity than Brønsted acid sites for ethylene DHA reaction. Screening metal promoters that have the

best selectivity towards valuable aromatics, especially benzene, toluene, and xylenes (BTX), is another future objective of our research. As mentioned before, Epron and co-workers found Zn-ZSM-5 shows the highest ethylene conversion (ca. 92%) and aromatics in yield (ca. 60%) at atmospheric pressure and 773K.<sup>147</sup> But Qiu et al. observed aromatic selectivity over Ga-ZSM-5 can reach as high as 87% at the comparable ethylene conversion (95%) and the reaction conditions (1 atm and 793K).<sup>106</sup> This disparity may come from the different metal loading contents, preparation methods, and reactor setups. Thus, in order to improve selectivity towards aromatics, a systematic study to explore the selectivity distribution as a function of metal promoters and loading concentration at the same reaction conditions needs to be performed. On the other hand, methane activation is another interesting subject to explore over metal-containing zeolite catalysts. Based on literature search, while Mo-ZSM-5 showed the highest methane conversion (9.5%), Zn showed the highest selectivity to aromatics (70%) at low methane conversion (1%).<sup>313-314</sup> With a combination of Mo and Zn species in zeolite catalyst, Mo Lewis site is responsible for methane activation, and Zn Lewis site can facilitate to increase aromatic selectivity. Therefore, bimetallic zeolite catalyst (e.g., Mo-Zn-ZSM-5) theoretically is able to improve methane activity and aromatic selectivity at the same time.

### **6.2.3 Alternative reactions to tune selectivity towards valuable aromatic**

Besides yielding aromatic production from the ethylene DHA route, it is economically important to explore alternative pathways to produce aromatic, such as hydrocarbon cracking. Hydrocarbon cracking, i.e., converting heavy polyaromatics to valuable BTX, is a critical industrial process, where zeolite catalysts are commonly used. However, it is challenging for the high-molecular-weight feed to diffuse into the microporous channel of zeolite.<sup>27</sup> 2D layered zeolite (e.g., MWW) and nanosized

zeolite (e.g., MFI) can reduce the diffusion-related issue by providing more external acid sites on the surface. In Chapter 2, we reported a novel approach to synthesize disordered MWW-type material via a single step. Using the newly developed MWW material, cracking reaction from vacuum gas oil can be explored. With reduced diffusion path length, it is expected to exhibit a higher cracking rate and slower formation rate of coke species.

## References

1. Barrer, R. M., Zeolites and their synthesis. *Zeolites* **1981**, *1* (3), 130-140.
2. Bernal, M. P.; Lopez-Real, J. M., Natural zeolites and sepiolite as ammonium and ammonia adsorbent materials. *Bioresource Technology* **1993**, *43* (1), 27-33.
3. Morris, R. E., Ionothermal Synthesis of Zeolites and Other Porous Materials. *Zeolites and Catalysis* **2010**, 87-105.
4. Strohmaier, K. G., Synthesis Approaches. *Zeolites and Catalysis* **2010**, 57-86.
5. A. Cambor, M.; Corma, A.; Valencia, S., Synthesis in fluoride media and characterisation of aluminosilicate zeolite beta. *Journal of Materials Chemistry* **1998**, *8* (9), 2137-2145.
6. Zones, S. I.; Darton, R. J.; Morris, R.; Hwang, S.-J., Studies on the Role of Fluoride Ion vs Reaction Concentration in Zeolite Synthesis. *The Journal of Physical Chemistry B* **2005**, *109* (1), 652-661.
7. Chu, C. T. W.; Chang, C. D., Isomorphous substitution in zeolite frameworks. 1. Acidity of surface hydroxyls in [B]-, [Fe]-, [Ga]-, and [Al]-ZSM-5. *The Journal of Physical Chemistry* **1985**, *89* (9), 1569-1571.
8. Dusselier, M.; Davis, M. E., Small-Pore Zeolites: Synthesis and Catalysis. *Chemical Reviews* **2018**, *118* (11), 5265-5329.
9. Chen, X.; Dong, M.; Niu, X.; Wang, K.; Chen, G.; Fan, W.; Wang, J.; Qin, Z., Influence of Zn species in HZSM-5 on ethylene aromatization. *Chinese Journal of Catalysis* **2015**, *36* (6), 880-888.
10. Paillaud, J.-L.; Harbuzaru, B.; Patarin, J.; Bats, N., Extra-Large-Pore Zeolites with Two-Dimensional Channels Formed by 14 and 12 Rings. *Science* **2004**, *304* (5673), 990.
11. Cundy, C. S.; Cox, P. A., The hydrothermal synthesis of zeolites: Precursors, intermediates and reaction mechanism. *Microporous and Mesoporous Materials* **2005**, *82* (1), 1-78.
12. Bellussi, G.; Carati, A.; Millini, R., Industrial Potential of Zeolites. *Zeolites and Catalysis* **2010**, 449-491.
13. Hsu, H.-L.; Selvin, R.; Cao, J.-W.; Roselin, L. S.; Bououdina, M., Facile Synthesis of Magnetically Separable Nanozeolites for Bio-Applications. *Science of Advanced Materials* **2011**, *3* (6), 939-943.
14. Simon, U.; Franke, M. E., Electrical properties of nanoscaled host/guest compounds. *Microporous and Mesoporous Materials* **2000**, *41* (1), 1-36.

15. Yeung, K. L.; Han, W., Zeolites and Molecular Sieves in Fuel Cell Applications. *Zeolites and Catalysis* **2010**, 827-861.
16. Grandjean, D.; Coutiño-Gonzalez, E.; Cuong, N. T.; Fron, E.; Baekelant, W.; Aghakhani, S.; Schlexer, P.; D'Acapito, F.; Banerjee, D.; Roeffaers, M. B. J.; Nguyen, M. T.; Hofkens, J.; Lievens, P., Origin of the bright photoluminescence of few-atom silver clusters confined in LTA zeolites. *Science* **2018**, 361 (6403), 686.
17. Davis, M. E., Ordered porous materials for emerging applications. *Nature* **2002**, 417, 813.
18. Martínez, C.; Corma, A., Inorganic molecular sieves: Preparation, modification and industrial application in catalytic processes. *Coordination Chemistry Reviews* **2011**, 255 (13-14), 1558-1580.
19. Primo, A.; Garcia, H., Zeolites as catalysts in oil refining. *Chemical Society Reviews* **2014**, 43 (22), 7548-7561.
20. Lupulescu, A. I.; Qin, W.; Rimer, J. D., Tuning Zeolite Precursor Interactions by Switching the Valence of Polyamine Modifiers. *Langmuir* **2016**, 32 (45), 11888-11898.
21. Olafson, K. N.; Li, R.; Alamani, B. G.; Rimer, J. D., Engineering Crystal Modifiers: Bridging Classical and Nonclassical Crystallization. *Chemistry of Materials* **2016**, 28 (23), 8453-8465.
22. Rimer, J. D.; Chawla, A.; Le, T. T., Crystal Engineering for Catalysis. *Annual Review of Chemical and Biomolecular Engineering* **2018**, 9 (1), 283-309.
23. Qin, W.; Agarwal, A.; Choudhary, M. K.; Palmer, J. C.; Rimer, J. D., Molecular Modifiers Suppress Nonclassical Pathways of Zeolite Crystallization. *Chemistry of Materials* **2019**, 31 (9), 3228-3238.
24. Schmidt, I.; Madsen, C.; Jacobsen, C. J. H., Confined Space Synthesis. A Novel Route to Nanosized Zeolites. *Inorganic Chemistry* **2000**, 39 (11), 2279-2283.
25. Tosheva, L.; Valtchev, V. P., Nanozeolites: Synthesis, Crystallization Mechanism, and Applications. *Chemistry of Materials* **2005**, 17 (10), 2494-2513.
26. Awala, H.; Gilson, J.-P.; Retoux, R.; Boullay, P.; Goupil, J.-M.; Valtchev, V.; Mintova, S., Template-free nanosized faujasite-type zeolites. *Nature Materials* **2015**, 14, 447.
27. Corma, A.; Fornes, V.; Pergher, S. B.; Maesen, T. L. M.; Buglass, J. G., Delaminated zeolite precursors as selective acidic catalysts. *Nature* **1998**, 396 (6709), 353-356.
28. Choi, M.; Na, K.; Kim, J.; Sakamoto, Y.; Terasaki, O.; Ryoo, R., Stable single-unit-cell nanosheets of zeolite MFI as active and long-lived catalysts. *Nature* **2009**, 461 (7261), 246-249.

29. Zhang, X.; Liu, D.; Xu, D.; Asahina, S.; Cychosz, K. A.; Agrawal, K. V.; Wahedi, Y. A.; Bhan, A.; Hashimi, S. A.; Terasaki, O.; Thommes, M.; Tsapatsis, M., Synthesis of Self-Pillared Zeolite Nanosheets by Repetitive Branching. *Science* **2012**, *336* (6089), 1684-1687.
30. Roth, W. J.; Nachtigall, P.; Morris, R. E.; Čejka, J., Two-Dimensional Zeolites: Current Status and Perspectives. *Chemical Reviews* **2014**, *114* (9), 4807-4837.
31. Luo, H. Y.; Michaelis, V. K.; Hodges, S.; Griffin, R. G.; Roman-Leshkov, Y., One-pot synthesis of MWW zeolite nanosheets using a rationally designed organic structure-directing agent. *Chemical Science* **2015**, *6* (11), 6320-6324.
32. Egeblad, K.; Christensen, C. H.; Kustova, M.; Christensen, C. H., Templating Mesoporous Zeolites. *Chemistry of Materials* **2008**, *20* (3), 946-960.
33. Chal, R.; Gérardin, C.; Bulut, M.; van Donk, S., Overview and Industrial Assessment of Synthesis Strategies towards Zeolites with Mesopores. *ChemCatChem* **2011**, *3* (1), 67-81.
34. Verboekend, D.; Pérez-Ramírez, J., Design of hierarchical zeolite catalysts by desilication. *Catalysis Science & Technology* **2011**, *1* (6), 879-890.
35. Serrano, D. P.; Escola, J. M.; Pizarro, P., Synthesis strategies in the search for hierarchical zeolites. *Chemical Society Reviews* **2013**, *42* (9), 4004-4035.
36. Sachse, A.; Grau-Atienza, A.; Jardim, E. O.; Linares, N.; Thommes, M.; García-Martínez, J., Development of Intracrystalline Mesoporosity in Zeolites through Surfactant-Templating. *Crystal Growth & Design* **2017**, *17* (8), 4289-4305.
37. Dai, W.; Wu, G.; Li, L.; Guan, N.; Hunger, M., Mechanisms of the Deactivation of SAPO-34 Materials with Different Crystal Sizes Applied as MTO Catalysts. *ACS Catalysis* **2013**, *3* (4), 588-596.
38. Khare, R.; Millar, D.; Bhan, A., A mechanistic basis for the effects of crystallite size on light olefin selectivity in methanol-to-hydrocarbons conversion on MFI. *Journal of Catalysis* **2015**, *321*, 23-31.
39. Shen, Y.; Le, T. T.; Fu, D.; Schmidt, J. E.; Filez, M.; Weckhuysen, B. M.; Rimer, J. D., Deconvoluting the Competing Effects of Zeolite Framework Topology and Diffusion Path Length on Methanol to Hydrocarbons Reaction. *ACS Catalysis* **2018**, *8* (12), 11042-11053.
40. Liu, H.; Liu, G.; Zhang, X.; Zhao, D.; Wang, L., Effects of aluminum sources on synthesis and catalytic performance of b-oriented ZSM-5 coatings. *Microporous and Mesoporous Materials* **2017**, *244*, 164-170.

41. Li, R.; Linares, N.; Sutjipto, J. G.; Chawla, A.; Garcia-Martinez, J.; Rimer, J. D., Ultrasmall Zeolite L Crystals Prepared from Highly Interdispersed Alkali-Silicate Precursors. *Angewandte Chemie International Edition* **2018**, *57* (35), 11283-11288.
42. Valtchev, V.; Tosheva, L., Porous Nanosized Particles: Preparation, Properties, and Applications. *Chemical Reviews* **2013**, *113* (8), 6734-6760.
43. Dimitrov, L.; Valtchev, V.; Nihitjanova, D.; Kalvachev, Y., Submicrometer Zeolite A Crystals Formation: Low-Temperature Crystallization Versus Vapor Phase Gel Transformation. *Crystal Growth & Design* **2011**, *11* (11), 4958-4962.
44. Aguado, J.; Serrano, D. P.; Escola, J. M.; Rodríguez, J. M., Low temperature synthesis and properties of ZSM-5 aggregates formed by ultra-small nanocrystals. *Microporous and Mesoporous Materials* **2004**, *75* (1), 41-49.
45. Triantafyllidis, K. S.; Nalbandian, L.; Trikalitis, P. N.; Ladavos, A. K.; Mavromoustakos, T.; Nicolaides, C. P., Structural, compositional and acidic characteristics of nanosized amorphous or partially crystalline ZSM-5 zeolite-based materials. *Microporous and Mesoporous Materials* **2004**, *75* (1), 89-100.
46. Chen, N. Y.; Degnan, T. F.; Smith, C. M., *Molecular Transport and Reaction in Zeolites: Design and Application of Shape Selective Catalysis*. Wiley: 1994; p 328-328.
47. Degnan, T. F., The implications of the fundamentals of shape selectivity for the development of catalysts for the petroleum and petrochemical industries. *Journal of Catalysis* **2003**, *216* (1), 32-46.
48. Gounder, R.; Iglesia, E., The catalytic diversity of zeolites: confinement and solvation effects within voids of molecular dimensions. *Chemical communications (Cambridge, England)* **2013**, *49* (34), 3491-509.
49. Gallego, E. M.; Portilla, M. T.; Paris, C.; León-Escamilla, A.; Boronat, M.; Moliner, M.; Corma, A., "Ab initio" synthesis of zeolites for preestablished catalytic reactions. *Science* **2017**, *355* (6329), 1051.
50. Li, C.; Paris, C.; Martínez-Triguero, J.; Boronat, M.; Moliner, M.; Corma, A., Synthesis of reaction - adapted zeolites as methanol-to-olefins catalysts with mimics of reaction intermediates as organic structure - directing agents. *Nature Catalysis* **2018**, *1* (7), 547-554.
51. Rimer, J. D., Rational design of zeolite catalysts. *Nature Catalysis* **2018**, *1* (7), 488-489.

52. Kang, J. H.; Alshafei, F. H.; Zones, S. I.; Davis, M. E., Cage-defining Ring: A Molecular Sieve Structural Indicator for Light Olefin Product Distribution from the Methanol-to-Olefins Reaction. *ACS Catalysis* **2019**.
53. Khare, R.; Liu, Z.; Han, Y.; Bhan, A., A mechanistic basis for the effect of aluminum content on ethene selectivity in methanol-to-hydrocarbons conversion on HZSM-5. *Journal of Catalysis* **2017**, *348*, 300-305.
54. Bordiga, S.; Lamberti, C.; Bonino, F.; Travert, A.; Thibault-Starzyk, F., Probing zeolites by vibrational spectroscopies. *Chemical Society Reviews* **2015**, *44* (20), 7262-7341.
55. Stavitski, E.; Weckhuysen, B. M., Vibrational Spectroscopy and Related In situ Studies of Catalytic Reactions within Molecular Sieves. *Zeolites and Catalysis* **2010**, 209-236.
56. Thibault-Starzyk, F.; Gil, B.; Aiello, S.; Chevreau, T.; Gilson, J.-P., In situ thermogravimetry in an infrared spectrometer: an answer to quantitative spectroscopy of adsorbed species on heterogeneous catalysts. *Microporous and Mesoporous Materials* **2004**, *67* (1), 107-112.
57. Thibault-Starzyk, F.; Vimont, A.; Gilson, J.-P., 2D-COS IR study of coking in xylene isomerisation on H-MFI zeolite. *Catalysis Today* **2001**, *70* (1), 227-241.
58. Koller, H., New developments of NMR spectroscopy applied to zeolite catalysts. In *Studies in Surface Science and Catalysis*, Ocelli, M., Ed. Elsevier: 2004; Vol. 149, pp 105-122.
59. Stepanov, A. G., Chapter 4 - Basics of Solid-State NMR for Application in Zeolite Science: Material and Reaction Characterization. In *Zeolites and Zeolite-Like Materials*, Sels, B. F.; Kustov, L. M., Eds. Elsevier: Amsterdam, 2016; pp 137-188.
60. Xu, J.; Wang, Q.; Deng, F., Metal Active Sites and Their Catalytic Functions in Zeolites: Insights from Solid-State NMR Spectroscopy. *Accounts of Chemical Research* **2019**, *52* (8), 2179-2189.
61. Položij, M.; Thang, H. V.; Rubeš, M.; Eliášová, P.; Čejka, J.; Nachtigall, P., Theoretical investigation of layered zeolites with MWW topology: MCM-22P vs. MCM-56. *Dalton Transactions* **2014**, *43* (27), 10443-10450.
62. Valtchev, V.; Mintova, S., Hierarchical zeolites. *MRS Bulletin* **2016**, *41* (9), 689-693.
63. Verboekend, D.; Nuttens, N.; Locus, R.; Van Aelst, J.; Verolme, P.; Groen, J. C.; Perez-Ramirez, J.; Sels, B. F., Synthesis, characterisation, and catalytic evaluation of hierarchical faujasite zeolites: milestones, challenges, and future directions. *Chemical Society Review* **2016**.

64. García-Martínez, J.; Johnson, M.; Valla, J.; Li, K.; Ying, J. Y., Mesostructured zeolite Y—high hydrothermal stability and superior FCC catalytic performance. *Catalysis Science & Technology* **2012**, *2* (5), 987-987.
65. Roth, W. J.; Nachtigall, P.; Morris, R. E.; Cejka, J., Two-Dimensional Zeolites: Current Status and Perspectives. *Chem Rev* **2014**, *114*, 4807-4837.
66. Xu, L.; Wu, P., Diversity of layered zeolites: from synthesis to structural modifications. *New Journal of Chemistry* **2016**.
67. Xu, L.; Sun, J., Recent Advances in the Synthesis and Application of Two-Dimensional Zeolites. *Advanced Energy Materials* **2016**, *6* (17), 1600441-n/a.
68. Schreyeck, L.; Caullet, P.; Mougénel, J.-C.; Guth, J.-L.; Marler, B., A layered microporous aluminosilicate precursor of FER-type zeolite. *Journal of the Chemical Society, Chemical Communications* **1995**, (21), 2187-2188.
69. Moteki, T.; Chaikittisilp, W.; Shimojima, A.; Okubo, T., Silica Sodalite without Occluded Organic Matters by Topotactic Conversion of Lamellar Precursor. *Journal of the American Chemical Society* **2008**, *130* (47), 15780-15781.
70. Zanardi, S.; Alberti, A.; Cruciani, G.; Corma, A.; Fornés, V.; Brunelli, M., Crystal Structure Determination of Zeolite Nu-6(2) and Its Layered Precursor Nu-6(1). *Angewandte Chemie International Edition* **2004**, *43* (37), 4933-4937.
71. Roth, W. J.; Nachtigall, P.; Morris, R. E.; Wheatley, P. S.; Seymour, V. R.; Ashbrook, S. E.; Chlubná, P.; Grajciar, L.; Položij, M.; Zukal, A.; Shvets, O.; Čejka, J., A family of zeolites with controlled pore size prepared using a top-down method. *Nature Chemistry* **2013**, *5*, 628.
72. Corma, A.; Corell, C.; Pérez-Pariente, J., Synthesis and characterization of the MCM-22 zeolite. *Zeolites* **1995**, *15* (1), 2-8.
73. Leonowicz, M. E.; Lawton, J. A.; Lawton, S. L.; Rubin, M. K., MCM-22: A Molecular Sieve with Two Independent Multidimensional Channel Systems. *Science* **1994**, *264* (5167), 1910.
74. Corma, A.; Martínez-Soria, V.; Schnoefeld, E., Alkylation of Benzene with Short-Chain Olefins over MCM-22 Zeolite: Catalytic Behaviour and Kinetic Mechanism. *Journal of Catalysis* **2000**, *192* (1), 163-173.
75. Bejblová, M.; Procházková, D.; Čejka, J., Acylation Reactions over Zeolites and Mesoporous Catalysts. *ChemSusChem* **2009**, *2* (6), 486-499.

76. Rodriguez, I.; Climent, M. J.; Iborra, S.; Fornés, V.; Corma, A., Use of delaminated zeolites (ITQ-2) and mesoporous molecular sieves in the production of fine chemicals: Preparation of dimethylacetals and tetrahydropyranylation of alcohols and phenols. *Journal of Catalysis* **2000**, *192* (2), 441-447.
77. Corma, A.; Fornes, V.; Pergher, S. B.; Maesen, T. L. M.; Buglass, J. G., Delaminated zeolite precursors as selective acidic catalysts. *Nature* **1998**, *396*, 353-356.
78. Corma, A.; Diaz, U.; Guil, J. M.; Martinez-Triguero, J.; Creightonb, E. J., Characterization and Catalytic Activity of MCM-22 and MCM-56 Compared with ITQ-2. *Journal of Catalysis* **2000**, *191* (1), 218-224.
79. Corma, A.; Fornes, V.; Guil, J. M.; Pergher, S. B.; Maesen, T. L. M.; Buglass, J. G., Preparation , characterisation and catalytic activity of ITQ-2 , a delaminated zeolite. *Microporous and Mesoporous Materials* **2000**, *38*, 301-309.
80. Frontera, P.; Testa, F.; Aiello, R.; Candamano, S.; Nagy, J. B., Transformation of MCM-22(P) into ITQ-2: The role of framework aluminium. *Microporous and Mesoporous Materials* **2007**, *106* (1), 107-114.
81. Maluangnont, T.; Yamauchi, Y.; Sasaki, T.; Roth, W. J.; Cejka, J.; Kubu, M., The aqueous colloidal suspension of ultrathin 2D MCM-22P crystallites. *Chemical communications (Cambridge, England)* **2014**, *50* (55), 7378-7381.
82. Ogino, I.; Nigra, M. M.; Hwang, S.-J.; Ha, J.-M.; Rea, T.; Zones, S. I.; Katz, A., Delamination of Layered Zeolite Precursors under Mild Conditions: Synthesis of UCB-1 via Fluoride/Chloride Anion-Promoted Exfoliation. *Journal of the American Chemical Society* **2011**, *133* (10), 3288-3291.
83. Roth, W. J.; Kresge, C. T.; Vartuli, J. C.; Leonowicz, M. E.; Fung, A. S.; McCullen, S. B., MCM-36: The first pillared molecular sieve with zeoliteproperties. In *Studies in Surface Science and Catalysis*, Beyer, H. K.; Karge, H. G.; Kiricsi, I.; Nagy, J. B., Eds. Elsevier: 1995; Vol. 94, pp 301-308.
84. Maheshwari, S.; Jordan, E.; Kumar, S.; Bates, F. S.; Penn, R. L.; Shantz, D. F.; Tsapatsis, M., Layer Structure Preservation during Swelling, Pillaring, and Exfoliation of a Zeolite Precursor. *Journal of the American Chemical Society* **2008**, *130* (4), 1507-1516.
85. Ouyang, X.; Hwang, S.-J.; Runnebaum, R. C.; Xie, D.; Wanglee, Y.-J.; Rea, T.; Zones, S. I.; Katz, A., Single-Step Delamination of a MWW Borosilicate Layered Zeolite Precursor under Mild Conditions without Surfactant and Sonication. *J Am Chem Soc* **2014**, *57* (136), 1449–1461-1449–1461.

86. Eliášová, P.; Opanasenko, M.; Wheatley, P. S.; Shamzhy, M.; Mazur, M.; Nachtigall, P.; Roth, W. J.; Morris, R. E.; Čejka, J., The ADOR mechanism for the synthesis of new zeolites. *Chemical Society Reviews* **2015**, *44* (20), 7177-7206.
87. Morris, S. A.; Bignami, G. P. M.; Tian, Y.; Navarro-Rojas, M.; Firth, D. S.; Čejka, J.; Wheatley, P. S.; Dawson, D. M.; Slawinski, W. A.; Wragg, D. S.; Morris, R. E.; Ashbrook, S. E., In situ solid-state NMR and XRD studies of the ADOR process and the unusual structure of zeolite IPC-6. *Nature Chemistry* **2017**, *9* (10), 1012-1018.
88. Kasneryk, V.; Shamzhy, M.; Opanasenko, M.; Wheatley, P. S.; Morris, S. A.; Russell, S. E.; Mayoral, A.; Trachta, M.; Čejka, J.; Morris, R. E., Expansion of the ADOR Strategy for the Synthesis of Zeolites: The Synthesis of IPC-12 from Zeolite UOV. *Angewandte Chemie International Edition* **2017**, *56* (15), 4324-4327.
89. Smith, R. L.; Eliášová, P.; Mazur, M.; Attfield, M. P.; Čejka, J.; Anderson, M. W., Atomic Force Microscopy of Novel Zeolitic Materials Prepared by Top-Down Synthesis and ADOR Mechanism. *Chemistry – A European Journal* **2014**, *20* (33), 10446-10450.
90. Xu, L.; Choudhary, M. K.; Muraoka, K.; Chaikittisilp, W.; Wakihara, T.; Rimer, J. D.; Okubo, T., Bridging the Gap between Structurally Distinct 2D Lamellar Zeolitic Precursors through a 3D Germanosilicate Intermediate. *Angewandte Chemie International Edition* **2019**, *58* (41), 14529-14533.
91. Rohde, L. M.; Lewis, G. J.; Miller, M. A.; Moscoso, J. G.; Gisselquist, J. L.; Patton, R. L.; Wilson, S. T.; Jan, D. Y. Crystalline aluminosilicate zeolitic composition: UZM-8. 2004.
92. Song, J. W.; Dai, L.; Ji, Y. Y.; Xiao, F. S., Organic template free synthesis of aluminosilicate zeolite ECR-1. *Chemistry of Materials* **2006**, *18* (12), 2775-2777.
93. Juttu, G. G.; Lobo, R. F., Characterization and catalytic properties of MCM-56 and MCM-22 zeolites. *Microporous and Mesoporous Materials* **2000**, *40* (1), 9-23.
94. Roth, W. J.; Dorset, D. L.; Kennedy, G. J., Discovery of new MWW family zeolite EMM-10: Identification of EMM-10P as the missing MWW precursor with disordered layers. *Microporous and Mesoporous Materials* **2011**, *142* (1), 168-177.
95. Corma, A.; Diazcaban, M.; Moliner, M.; Martinez, C., Discovery of a new catalytically active and selective zeolite (ITQ-30) by high-throughput synthesis techniques. *Journal of Catalysis* **2006**, *241* (2), 312-318.

96. Margarit, V. J.; Martínez-Armero, M. E.; Navarro, M. T.; Martínez, C.; Corma, A., Direct Dual-Template Synthesis of MWW Zeolite Monolayers. *Angewandte Chemie International Edition* **2015**, *54* (46), 13724-13728.
97. Grzybek, J.; Roth, W. J.; Gil, B.; Korzeniowska, A.; Mazur, M.; Cejka, J.; Morris, R. E., A new layered MWW zeolite synthesized with the bifunctional surfactant template and the updated classification of layered zeolite forms obtained by direct synthesis. *J. Mater. Chem. A* **2019**, *7* (13), 7701-7709.
98. Bhan, A.; Nicholas Delgass, W., Propane Aromatization over HZSM - 5 and Ga/HZSM - 5 Catalysts. *Catalysis Reviews* **2008**, *50* (1), 19-151.
99. Caeiro, G.; Carvalho, R. H.; Wang, X.; Lemos, M. A. N. D. A.; Lemos, F.; Guisnet, M.; Ramôa Ribeiro, F., Activation of C<sub>2</sub>-C<sub>4</sub> alkanes over acid and bifunctional zeolite catalysts. *Journal of Molecular Catalysis A: Chemical* **2006**, *255* (1), 131-158.
100. Yang, X.; Su, X.; Chen, D.; Zhang, T.; Huang, Y., Direct conversion of syngas to aromatics: A review of recent studies. *Chinese Journal of Catalysis* **2020**, *41* (4), 561-573.
101. Gao, P.; Wang, Q.; Xu, J.; Qi, G.; Wang, C.; Zhou, X.; Zhao, X.; Feng, N.; Liu, X.; Deng, F., Brønsted/Lewis Acid Synergy in Methanol-to-Aromatics Conversion on Ga-Modified ZSM-5 Zeolites, As Studied by Solid-State NMR Spectroscopy. *ACS Catalysis* **2018**, *8* (1), 69-74.
102. Gao, P.; Xu, J.; Qi, G.; Wang, C.; Wang, Q.; Zhao, Y.; Zhang, Y.; Feng, N.; Zhao, X.; Li, J.; Deng, F., A Mechanistic Study of Methanol-to-Aromatics Reaction over Ga-Modified ZSM-5 Zeolites: Understanding the Dehydrogenation Process. *ACS Catalysis* **2018**, *8* (10), 9809-9820.
103. Ma, S.; Guo, X.; Zhao, L.; Scott, S.; Bao, X., Recent progress in methane dehydroaromatization: From laboratory curiosities to promising technology. *Journal of Energy Chemistry* **2013**, *22* (1), 1-20.
104. Schwach, P.; Pan, X.; Bao, X., Direct Conversion of Methane to Value-Added Chemicals over Heterogeneous Catalysts: Challenges and Prospects. *Chemical Reviews* **2017**, *117* (13), 8497-8520.
105. Ono, Y.; Osako, K.; Kim, G. J.; Inoue, Y., Ag-ZSM-5 as a Catalyst for Aromatization of Alkanes, Alkenes, and Methanol. In *Studies in Surface Science and Catalysis*, J. Weitkamp, H. G. K. H. P.; Hölderich, W., Eds. Elsevier: 1994; Vol. Volume 84, pp 1773-1780.
106. Qiu, P.; Lunsford, J. H.; Rosynek, M. P., Characterization of Ga/ZSM-5 for the catalytic aromatization of dilute ethylene streams. *Catalysis Letters* **1998**, *52* (1), 37-42.

107. Choudhary, V. R.; Devadas, P.; Banerjee, S.; Kinage, A. K., Aromatization of dilute ethylene over Ga-modified ZSM-5 type zeolite catalysts. *Microporous and Mesoporous Materials* **2001**, *47* (2–3), 253-267.
108. Ono, Y.; Baba, T., Unique properties of silver cations in solid-acid catalysis by zeolites and heteropolyacids. *Phys Chem Chem Phys* **2015**, *17* (24), 15637-15654.
109. Ravi, M.; Ranocchiari, M.; van Bokhoven, J. A., The Direct Catalytic Oxidation of Methane to Methanol—A Critical Assessment. *Angewandte Chemie International Edition* **2017**, *56* (52), 16464-16483.
110. Primo, A.; Garcia, H., Zeolites as catalysts in oil refining. *Chem Soc Rev* **2014**, *43* (22), 7548-7561.
111. Perego, C.; Calemma, V.; Pollesel, P., Naphtha Reforming and Upgrading of Diesel Fractions. *Zeolites and Catalysis* **2010**, 585-621.
112. Zhang, L.; Peng, Y.; Zhang, J.; Chen, L.; Meng, X.; Xiao, F.-S., Adsorptive and catalytic properties in the removal of volatile organic compounds over zeolite-based materials. *Chinese Journal of Catalysis* **2016**, *37* (6), 800-809.
113. Shahidi, D.; Roy, R.; Azzouz, A., Advances in catalytic oxidation of organic pollutants – Prospects for thorough mineralization by natural clay catalysts. *Applied Catalysis B: Environmental* **2015**, *174-175*, 277-292.
114. Centi, G.; Perathoner, S., Environmental Catalysis over Zeolites. *Zeolites and Catalysis* **2010**, 745-774.
115. Fukuzumi, S.; Ohkubo, K., One-Step Selective Hydroxylation of Benzene to Phenol. *Asian Journal of Organic Chemistry* **2015**, *4* (9), 836-845.
116. Cui, T.-L.; Ke, W.-Y.; Zhang, W.-B.; Wang, H.-H.; Li, X.-H.; Chen, J.-S., Encapsulating Palladium Nanoparticles Inside Mesoporous MFI Zeolite Nanocrystals for Shape-Selective Catalysis. *Angewandte Chemie International Edition* **2016**, *55* (32), 9178-9182.
117. Van de Vyver, S.; Román-Leshkov, Y., Metalloenzyme-Like Zeolites as Lewis Acid Catalysts for C–C Bond Formation. *Angewandte Chemie International Edition* **2015**, *54* (43), 12554-12561.
118. Moliner, M., State of the art of Lewis acid-containing zeolites: lessons from fine chemistry to new biomass transformation processes. *Dalton Transactions* **2014**, *43* (11), 4197-4208.

119. Taarning, E.; Osmundsen, C. M.; Yang, X.; Voss, B.; Andersen, S. I.; Christensen, C. H., Zeolite-catalyzed biomass conversion to fuels and chemicals. *Energy & Environmental Science* **2011**, *4* (3), 793-804.
120. Kosinov, N.; Liu, C.; Hensen, E. J. M.; Pidko, E. A., Engineering of Transition Metal Catalysts Confined in Zeolites. *Chemistry of Materials* **2018**, *30* (10), 3177-3198.
121. Coqueblin, H.; Richard, A.; Uzio, D.; Pinard, L.; Pouilloux, Y.; Epron, F., Effect of the metal promoter on the performances of H-ZSM5 in ethylene aromatization. *Catalysis Today* **2017**, *289*, 62-69.
122. Wang, N.; Sun, Q.; Yu, J., Ultrasmall Metal Nanoparticles Confined within Crystalline Nanoporous Materials: A Fascinating Class of Nanocatalysts. *Advanced Materials* **2019**, *31* (1), 1803966.
123. Phadke, N. M.; Van der Mynsbrugge, J.; Mansoor, E.; Getsoian, A. B.; Head-Gordon, M.; Bell, A. T., Characterization of Isolated Ga<sup>3+</sup> Cations in Ga/H-MFI Prepared by Vapor-Phase Exchange of H-MFI Zeolite with GaCl<sub>3</sub>. *ACS Catalysis* **2018**, *8* (7), 6106-6126.
124. Dooley, K. M.; Chang, C.; Price, G. L., Effects of pretreatments on state of gallium and aromatization activity of gallium/ZSM-5 catalysts. *Applied Catalysis A: General* **1992**, *84* (1), 17-30.
125. Choudhary, V. R.; Kinage, A. K.; Sivadinarayana, C.; Sansare, S. D.; Guisnet, M., Initial activity/selectivity of H-gallosilicate (MFI) in propane aromatization: influence of H<sup>+</sup> exchange and thermal/hydrothermal pretreatments. *Catalysis Letters* **1995**, *33* (3), 401-412.
126. Goel, S.; Zones, S. I.; Iglesia, E., Encapsulation of Metal Clusters within MFI via Interzeolite Transformations and Direct Hydrothermal Syntheses and Catalytic Consequences of Their Confinement. *Journal of the American Chemical Society* **2014**, *136* (43), 15280-15290.
127. Choi, S.-W.; Kim, W.-G.; So, J.-S.; Moore, J. S.; Liu, Y.; Dixit, R. S.; Pendergast, J. G.; Sievers, C.; Sholl, D. S.; Nair, S.; Jones, C. W., Propane dehydrogenation catalyzed by gallosilicate MFI zeolites with perturbed acidity. *Journal of Catalysis* **2017**, *345*, 113-123.
128. Meng, L.; Zhu, X.; Mezari, B.; Pestman, R.; Wannapakdee, W.; Hensen, E. J. M., On the Role of Acidity in Bulk and Nanosheet [T]MFI (T=Al<sup>3+</sup>, Ga<sup>3+</sup>, Fe<sup>3+</sup>, B<sup>3+</sup>) Zeolites in the Methanol-to-Hydrocarbons Reaction. *ChemCatChem* **2017**, *9* (20), 3942-3954.
129. Franck, H.-G.; Stadelhofer, J. W., *Industrial Aromatic Chemistry*. Springer: 1988.
130. Arpe, K. W. H.-J., *Industrial Organic Chemistry, Fourth Edition*. 28 MAY 2008.
131. Little, D. M., *Catalytic Reforming*. Pennwell Books, Tulsa, OK: United States, 1985.

132. Antos, G. J.; Aitani, A. M., *Catalytic Naphtha Reforming, Revised and Expanded*. CRC Press: 2004.
133. Guisnet, M.; Gnep, N. S.; Alario, F., Aromatization of short chain alkanes on zeolite catalysts. *Applied Catalysis A: General* **1992**, *89* (1), 1-30.
134. Deloitte *The Future of Petrochemicals: Growth Surrounded by Uncertainty*; 2020.
135. Dufresne, L. A.; Le Van Mao, R., Hydrogen back-spillover effects in the aromatization of ethylene on hybrid ZSM-5 catalysts. *Catalysis Letters* **1994**, *25* (3), 371-383.
136. Majhi, S.; Mohanty, P.; Wang, H.; Pant, K. K., Direct conversion of natural gas to higher hydrocarbons: A review. *Journal of Energy Chemistry* **2013**, *22* (4), 543-554.
137. Ren, T.; Patel, M.; Blok, K., Olefins from conventional and heavy feedstocks: Energy use in steam cracking and alternative processes. *Energy* **2006**, *31* (4), 425-451.
138. Cavani, F.; Trifirò, F., The oxidative dehydrogenation of ethane and propane as an alternative way for the production of light olefins. *Catalysis Today* **1995**, *24* (3), 307-313.
139. Cavani, F.; Ballarini, N.; Cericola, A., Oxidative dehydrogenation of ethane and propane: How far from commercial implementation? *Catalysis Today* **2007**, *127* (1-4), 113-131.
140. Bañares, M. A., Supported metal oxide and other catalysts for ethane conversion: a review. *Catalysis Today* **1999**, *51* (2), 319-348.
141. Jiang, Y.; Yentekakis, I. V.; Vayenas, C. G., Methane to Ethylene with 85 Percent Yield in a Gas Recycle Electrocatalytic Reactor-Separator. *Science* **1994**, *264* (5165), 1563.
142. Machocki, A., Methane oxidative coupling in an undiluted reaction mixture in a reactor-adsorber system with gas recirculation. *Applied Catalysis A: General* **1996**, *146* (2), 391-400.
143. Andrei, R. D.; Popa, M. I.; Fajula, F.; Cammarano, C.; Khudhair, A. A.; Bouchmella, K.; Mutin, P. H.; Hulea, V., Ethylene to Propylene by One-Pot Catalytic Cascade Reactions. *ACS Catalysis* **2015**, *5* (5), 2774-2777.
144. Iwamoto, M.; Kosugi, Y., Highly Selective Conversion of Ethene to Propene and Butenes on Nickel Ion-Loaded Mesoporous Silica Catalysts. *The Journal of Physical Chemistry C* **2007**, *111* (1), 13-15.
145. Alvarado Perea, L.; Wolff, T.; Veit, P.; Hilfert, L.; Edelman, F. T.; Hamel, C.; Seidel-Morgenstern, A., Alumino-mesostructured Ni catalysts for the direct conversion of ethene to propene. *Journal of Catalysis* **2013**, *305*, 154-168.

146. Ikeda, K.; Kawamura, Y.; Yamamoto, T.; Iwamoto, M., Effectiveness of the template-ion exchange method for appearance of catalytic activity of Ni-MCM-41 for the ethene to propene reaction. *Catalysis Communications* **2008**, *9* (1), 106-110.
147. Coqueblin, H.; Richard, A.; Uzio, D.; Pinard, L.; Pouilloux, Y.; Epron, F., Effect of the metal promoter on the performances of H-ZSM5 in ethylene aromatization. *Catalysis Today* **2016**.
148. Heemsoth, J.; Tegeler, E.; Roessner, F.; Hagen, A., Generation of active sites for ethane aromatization in ZSM-5 zeolites by a solid-state reaction of zinc metal with Brønsted acid sites of the zeolite. *Microporous and Mesoporous Materials* **2001**, *46* (2-3), 185-190.
149. Li, K.; Valla, J.; Garcia-Martinez, J., Realizing the Commercial Potential of Hierarchical Zeolites: New Opportunities in Catalytic Cracking. *ChemCatChem* **2014**, *6* (1), 46-66.
150. Association, I. Z.
151. Ogino, I.; Nigra, M. M.; Hwang, S.-j.; Ha, J.-m.; Rea, T.; Zones, S. I.; Katz, A., Delamination of Layered Zeolite Precursors under Mild Conditions: Synthesis of UCB-1 via Fluoride/Chloride Anion-Promoted Exfoliation. *Journal of the American Chemical Society* **2011**, *133*, 3288-3291.
152. Maheshwari, S.; Jordan, E.; Kumar, S.; Bates, F. S.; Penn, R. L.; Shantz, D. F.; Tsapatsis, M., Layer Structure Preservation during Swelling, Pillaring, and Exfoliation of a Zeolite Precursor. **2008**, *4* (1), 1507-1516.
153. Wei, L.; Song, K.; Wu, W.; Holdren, S.; Zhu, G.; Shulman, E.; Shang, W.; Chen, H.; Zachariah, M. R.; Liu, D., Vapor-Phase Strategy to Pillaring of Two-Dimensional Zeolite. *Journal of the American Chemical Society* **2019**, *141* (22), 8712-8716.
154. Fung, A. S.; Lawton, S. L.; Roth, W. J. Synthetic Layered MCM-56, Its Synthesis and Use. US005362697A, 1994.
155. Corma, A.; Fornés, V.; Martínez-Triguero, J.; Pergher, S. B., Delaminated Zeolites: Combining the Benefits of Zeolites and Mesoporous Materials for Catalytic Uses. *Journal of Catalysis* **1999**, *186* (1), 57-63.
156. Fernandez, C.; Amoureux, J. P.; Dumazy, Y.; Delevoye, L. In *Multiquantum (3Q and 5Q) MAS NMR Spectroscopy of Aluminium-27 in Solids*, Nuclear Magnetic Resonance Spectroscopy of Cement-Based Materials, Berlin, Heidelberg, 1998//; Colombet, P.; Zanni, H.; Grimmer, A.-R.; Sozzani, P., Eds. Springer Berlin Heidelberg: Berlin, Heidelberg, 1998; pp 79-88.

157. Zhao, Q.; Chen, W.-H.; Huang, S.-J.; Wu, Y.-C.; Lee, H.-K.; Liu, S.-B., Discernment and Quantification of Internal and External Acid Sites on Zeolites. *The Journal of Physical Chemistry B* **2002**, *106* (17), 4462-4469.
158. Palin, L.; Croce, G.; Viterbo, D.; Milanesio, M., Monitoring the Formation of H-MCM-22 by a Combined XRPD and Computational Study of the Decomposition of the Structure Directing Agent. *Chemistry of Materials* **2011**, *23* (22), 4900-4909.
159. Doane, D. P.; Seward, L. E., Measuring Skewness: A Forgotten Statistic? *Journal of Statistics Education* **2011**, *19* (2), null-null.
160. Lawton, S. L.; Fung, A. S.; Kennedy, G. J.; Alemany, L. B.; Chang, C. D.; Hatzikos, G. H.; Lissy, D. N.; Rubin, M. K.; Timken, H.-K. C.; Steuernagel, S.; Woessner, D. E., Zeolite MCM-49: A Three-Dimensional MCM-22 Analogue Synthesized by in Situ Crystallization. *The Journal of Physical Chemistry* **1996**, *100* (9), 3788-3798.
161. Kennedy, G. J.; Lawton, S. L.; Fung, A. S.; Rubin, M. K.; Steuernagel, S., Multinuclear MAS NMR studies of zeolites MCM-22 and MCM-49. *Catalysis Today* **1999**, *49* (4), 385-399.
162. Knyazeva, E. E.; Dobryakova, I. V.; Shkuropatov, A. V.; Ponomareva, O. A.; Kolyagin, Y. G.; Ivanova, I. I., Influence of Synthesis Conditions on Properties of MWW Zeolites. *Russian Journal of Applied Chemistry* **2018**, *91* (11), 1821-1829.
163. Roth, W. J.; Čejka, J.; Millini, R.; Montanari, E.; Gil, B.; Kubu, M., Swelling and Interlayer Chemistry of Layered MWW Zeolites MCM-22 and MCM-56 with High Al Content. *Chemistry of Materials* **2015**, *27* (13), 4620-4629.
164. Seo, Y.; Cho, K.; Jung, Y.; Ryoo, R., Characterization of the Surface Acidity of MFI Zeolite Nanosheets by <sup>31</sup>P NMR of Adsorbed Phosphine Oxides and Catalytic Cracking of Decalin. *ACS Catalysis* **2013**, *3* (4), 713-720.
165. Opanasenko, M. V.; Roth, W. J.; Čejka, J., Two-dimensional zeolites in catalysis: current status and perspectives. *Catalysis Science & Technology* **2016**, *6* (8), 2467-2484.
166. Chica, A.; Corma, A., Hydroisomerization of Pentane, Hexane, and Heptane for Improving the Octane Number of Gasoline. *Journal of Catalysis* **1999**, *187* (1), 167-176.
167. Park, K.-C.; Ihm, S.-K., Comparison of Pt/zeolite catalysts for n-hexadecane hydroisomerization. *Applied Catalysis A: General* **2000**, *203* (2), 201-209.

168. Deldari, H., Suitable catalysts for hydroisomerization of long-chain normal paraffins. *Applied Catalysis A: General* **2005**, *293*, 1-10.
169. Brandenberger, S.; Kröcher, O.; Tissler, A.; Althoff, R., The State of the Art in Selective Catalytic Reduction of NO<sub>x</sub> by Ammonia Using Metal - Exchanged Zeolite Catalysts. *Catalysis Reviews* **2008**, *50* (4), 492-531.
170. Cant, N. W.; Liu, I. O. Y., The mechanism of the selective reduction of nitrogen oxides by hydrocarbons on zeolite catalysts. *Catalysis Today* **2000**, *63* (2-4), 133-146.
171. Li, J.; Chang, H.; Ma, L.; Hao, J.; Yang, R. T., Low-temperature selective catalytic reduction of NO<sub>x</sub> with NH<sub>3</sub> over metal oxide and zeolite catalysts—A review. *Catalysis Today* **2011**, *175* (1), 147-156.
172. Davis, R. J., New perspectives on basic zeolites as catalysts and catalyst supports. *Journal of Catalysis* **2003**, *216* (1-2), 396-405.
173. Moliner, M., State of the art of Lewis acid-containing zeolites: lessons from fine chemistry to new biomass transformation processes. *Dalton Trans* **2014**, *43* (11), 4197-4208.
174. Ono, Y., Solid base catalysts for the synthesis of fine chemicals. *Journal of Catalysis* **2003**, *216* (1-2), 406-415.
175. Barthomeuf, D., Basic Zeolites: Characterization and Uses in Adsorption and Catalysis. *Catalysis Reviews - Science and Engineering* **1996**, *38* (4), 521-612.
176. Li, Z.; Flytzani-Stephanopoulos, M., On the Promotion of Ag-ZSM-5 by Cerium for the SCR of NO by Methane. *Journal of Catalysis* **1998**, *182* (2), 313-327.
177. Martens, J. A.; Cauvel, A.; Francis, A.; Hermans, C.; Jayat, F.; Remy, M.; Keung, M.; Lievens, J.; Jacobs, P. A., NO<sub>x</sub> Abatement in Exhaust from Lean - Burn Combustion Engines by Reduction of NO<sub>2</sub> over Silver - Containing Zeolite Catalysts. *Angewandte Chemie International Edition* **1998**, *37* (13 - 14), 1901-1903.
178. Shibata, J.; Shimizu, K.-i.; Takada, Y.; Shichi, A.; Yoshida, H.; Satokawa, S.; Satsuma, A.; Hattori, T., Structure of active Ag clusters in Ag zeolites for SCR of NO by propane in the presence of hydrogen. *Journal of Catalysis* **2004**, *227* (2), 367-374.
179. Kolobova, E.; Pestryakov, A.; Mamontov, G.; Kotolevich, Y.; Bogdanchikova, N.; Farias, M.; Vosmerikov, A.; Vosmerikova, L.; Cortes Corberan, V., Low-temperature CO oxidation on Ag/ZSM-5

- catalysts: Influence of Si/Al ratio and redox pretreatments on formation of silver active sites. *Fuel* **2017**, *188*, 121-131.
180. Kolobova, E.; Pestryakov, A.; Shemeryankina, A.; Kotolevich, Y.; Martynyuk, O.; Tiznado Vazquez, H. J.; Bogdanchikova, N., Formation of silver active states in Ag/ZSM-5 catalysts for CO oxidation. *Fuel* **2014**, *138*, 65-71.
181. Ono, Y.; Kanae, K., Transformation of butanes over ZSM-5 zeolites. Part 2.-Formation of aromatic hydrocarbons over Zn-ZSM-5 and Ga-ZSM-5. *Journal of the Chemical Society, Faraday Transactions* **1991**, *87* (4), 669-675.
182. Ono, Y., Transformation of Lower Alkanes into Aromatic Hydrocarbons over ZSM-5 Zeolites. *Catalysis Reviews* **1992**, *34* (3), 179-226.
183. Baba, T.; Iwase, Y.; Inazu, K.; Masih, D.; Matsumoto, A., Catalytic properties of silver-exchanged zeolites for propene production by conversion of methane in the presence of ethene. *Microporous and Mesoporous Materials* **2007**, *101* (1-2), 142-147.
184. Arzumanov, S. S.; Kolokolov, D. I.; Freude, D.; Stepanov, A. G., Methane Mobility in Ag/H-ZSM-5 Zeolite in the Presence of Ethene: A View Based on PFG <sup>1</sup>H MAS NMR Analysis of Methane Diffusivity. *The Journal of Physical Chemistry C* **2015**, *119* (32), 18481-18486.
185. Gabrienko, A. A.; Arzumanov, S. S.; Moroz, I. B.; Toktarev, A. V.; Wang, W.; Stepanov, A. G., Methane Activation and Transformation on Ag/H-ZSM-5 Zeolite Studied with Solid-State NMR. *The Journal of Physical Chemistry C* **2013**, *117* (15), 7690-7702.
186. Ding, B.; Huang, S.; Wang, W., Methane activation over Ag-exchanged ZSM-5 zeolites: A theoretical study. *Applied Surface Science* **2008**, *254* (16), 4944-4948.
187. Kresse, G.; Hafner, J., *Ab initio* molecular dynamics for liquid metals. *Physical Review B* **1993**, *47* (1), 558-561.
188. Kresse, G.; Hafner, J., *Ab initio* molecular-dynamics simulation of the liquid-metal<sup>21</sup>amorphous-semiconductor transition in germanium. *Physical Review B* **1994**, *49* (20), 14251-14269.
189. Kresse, G.; Furthmüller, J., Efficient iterative schemes for *ab initio* total-energy calculations using a plane-wave basis set. *Physical Review B* **1996**, *54* (16), 11169-11186.
190. Bahn, S. R.; Jacobsen, K. W., An object-oriented scripting interface to a legacy electronic structure code. *Computing in Science & Engineering* **2002**, *4* (3), 56-66.

191. Blöchl, P. E., Projector augmented-wave method. *Physical Review B* **1994**, *50* (24), 17953-17979.
192. Wellendorff, J.; Lundgaard, K. T.; Møgelhøj, A.; Petzold, V.; Landis, D. D.; Nørskov, J. K.; Bligaard, T.; Jacobsen, K. W., Density functionals for surface science: Exchange-correlation model development with Bayesian error estimation. *Physical Review B* **2012**, *85* (23), 235149.
193. Brogaard, R. Y.; Moses, P. G.; Nørskov, J. K., Modeling van der Waals Interactions in Zeolites with Periodic DFT: Physisorption of n-Alkanes in ZSM-22. *Catalysis Letters* **2012**, *142* (9), 1057-1060.
194. Stevens, E. D.; Rys, J.; Coppens, P., Quantitative comparison of theoretical calculations with the experimentally determined electron density distribution of formamide. *Journal of the American Chemical Society* **1978**, *100* (8), 2324-2328.
195. Sheppard, D.; Xiao, P.; Chemelewski, W.; Johnson, D. D.; Henkelman, G., A generalized solid-state nudged elastic band method. *The Journal of Chemical Physics* **2012**, *136* (7), 074103.
196. Henkelman, G.; Jónsson, H., A dimer method for finding saddle points on high dimensional potential surfaces using only first derivatives. *The Journal of Chemical Physics* **1999**, *111* (15), 7010-7022.
197. Olson, D. H.; Kokotailo, G. T.; Lawton, S. L.; Meier, W. M., Crystal structure and structure-related properties of ZSM-5. *The Journal of Physical Chemistry* **1981**, *85* (15), 2238-2243.
198. Miao, S.; Wang, Y.; Ma, D.; Zhu, Q.; Zhou, S.; Su, L.; Tan, D.; Bao, X., Effect of Ag<sup>+</sup> Cations on Nonoxidative Activation of Methane to C<sub>2</sub>-Hydrocarbons. *The Journal of Physical Chemistry B* **2004**, *108* (46), 17866-17871.
199. Lezcano-González, I.; Oord, R.; Rovezzi, M.; Glatzel, P.; Botchway, S. W.; Weckhuysen, B. M.; Beale, A. M., Molybdenum Speciation and its Impact on Catalytic Activity during Methane Dehydroaromatization in Zeolite ZSM-5 as Revealed by Operando X-Ray Methods. *Angewandte Chemie International Edition* **2016**, *55* (17), 5215-5219.
200. Paolucci, C.; Parekh, A. A.; Khurana, I.; Di Iorio, J. R.; Li, H.; Albarracín Caballero, J. D.; Shih, A. J.; Anggara, T.; Delgass, W. N.; Miller, J. T.; Ribeiro, F. H.; Gounder, R.; Schneider, W. F., Catalysis in a Cage: Condition-Dependent Speciation and Dynamics of Exchanged Cu Cations in SSZ-13 Zeolites. *J Am Chem Soc* **2016**, *138* (18), 6028-6048.

201. Narsimhan, K.; Michaelis, V. K.; Mathies, G.; Gunther, W. R.; Griffin, R. G.; Román-Leshkov, Y., Methane to Acetic Acid over Cu-Exchanged Zeolites: Mechanistic Insights from a Site-Specific Carbonylation Reaction. *J Am Chem Soc* **2015**, *137* (5), 1825-1832.
202. Almutairi, S. M. T.; Mezari, B.; Magusin, P. C. M. M.; Pidko, E. A.; Hensen, E. J. M., Structure and Reactivity of Zn-Modified ZSM-5 Zeolites: The Importance of Clustered Cationic Zn Complexes. *ACS Catalysis* **2012**, *2* (1), 71-83.
203. Inoue, Y.; Nakashiro, K.; Ono, Y., Selective conversion of methanol into aromatic hydrocarbons over silver-exchanged ZSM-5 zeolites. *Microporous Materials* **1995**, *4* (5), 379-383.
204. Ausavasukhi, A.; Suwannaran, S.; Limtrakul, J.; Sooknoi, T., Reversible interconversion behavior of Ag species in AgHZSM-5: XRD, 1H MAS NMR, TPR, TPHE, and catalytic studies. *Applied Catalysis A: General* **2008**, *345* (1), 89-96.
205. Shimizu, K.-i.; Sugino, K.; Kato, K.; Yokota, S.; Okumura, K.; Satsuma, A., Formation and Redispersion of Silver Clusters in Ag-MFI Zeolite as Investigated by Time-Resolved QXAFS and UV-Vis. *The Journal of Physical Chemistry C* **2007**, *111* (4), 1683-1688.
206. He, X.; Huang, X.; Wang, Z.; Yan, Y., The role of silver species on the hydrothermal stability of zeolite catalysts. *Microporous and Mesoporous Materials* **2011**, *142* (1), 398-403.
207. Ju, W.-S.; Matsuoka, M.; Iino, K.; Yamashita, H.; Anpo, M., The Local Structures of Silver(I) Ion Catalysts Anchored within Zeolite Cavities and Their Photocatalytic Reactivities for the Elimination of N<sub>2</sub>O into N<sub>2</sub> and O<sub>2</sub>. *The Journal of Physical Chemistry B* **2004**, *108* (7), 2128-2133.
208. Aspromonte, S. G.; Mizrahi, M. D.; Schneeberger, F. A.; López, J. M. R.; Boix, A. V., Study of the Nature and Location of Silver in Ag-Exchanged Mordenite Catalysts. Characterization by Spectroscopic Techniques. *The Journal of Physical Chemistry C* **2013**, *117* (48), 25433-25442.
209. Briggs, D.; Seah, M. P. Practical surface analysis : by auger and x-ray photoelectron spectroscopy. <http://books.google.com/books?id=MtITAAAAMAAJ>.
210. Shibata, J.; Takada, Y.; Shichi, A.; Satokawa, S.; Satsuma, A.; Hattori, T., Ag cluster as active species for SCR of NO by propane in the presence of hydrogen over Ag-MFI. *Journal of Catalysis* **2004**, *222* (2), 368-376.
211. Shibata, J.; Takada, Y.; Shichi, A.; Satokawa, S.; Satsuma, A.; Hattori, T., Influence of zeolite support on activity enhancement by addition of hydrogen for SCR of NO by propane over Ag-zeolites. *Applied Catalysis B: Environmental* **2004**, *54* (3), 137-144.

212. Bartolomeu, R.; Mendes, A. N.; Fernandes, A.; Henriques, C.; da Costa, P.; Ribeiro, M. F., NO<sub>x</sub> SCR with decane using Ag-MFI catalysts: on the effect of silver content and co-cation presence. *Catalysis Science & Technology* **2016**, *6* (9), 3038-3048.
213. Besson, S.; Gacoin, T.; Ricolleau, C.; Boilot, J.-P., Silver nanoparticle growth in 3D-hexagonal mesoporous silica films. *Chem Commun (Camb)* **2003**, (3), 360-361.
214. Baba, T.; Abe, Y., Metal cation–acidic proton bifunctional catalyst for methane activation: conversion of 13CH<sub>4</sub> in the presence of ethylene over metal cations-loaded H-ZSM-5. *Applied Catalysis A: General* **2003**, *250* (2), 265-270.
215. Khare, R.; Bhan, A., Mechanistic studies of methanol-to-hydrocarbons conversion on diffusion-free MFI samples. *Journal of Catalysis* **2015**, *329*, 218-228.
216. Plotkin, J. S. The Propylene Gap: How Can It Be Filled? <https://www.acs.org/content/acs/en/pressroom/cutting-edge-chemistry/the-propylene-gap-how-can-it-be-filled.html>.
217. Gao, J.; Zheng, Y.; Jehng, J. M.; Tang, Y.; Wachs, I. E.; Podkolzin, S. G., Identification of molybdenum oxide nanostructures on zeolites for natural gas conversion. *Science* **2015**, *348* (6235), 686-690.
218. Borry, R. W.; Kim, Y.-H.; Huffsmith, A.; Reimer, J. A.; Iglesia, E., Structure and Density of Mo and Acid Sites in Mo-Exchanged H-ZSM5 Catalysts for Nonoxidative Methane Conversion. *Journal of Physical Chemistry B* **1999**, *103* (28), 5787-5796.
219. Ma, D.; Wang, D.; Su, L.; Shu, Y.; Xu, Y.; Bao, X., Carbonaceous Deposition on Mo/HMCM-22 Catalysts for Methane Aromatization: A TP Technique Investigation. *Journal of Catalysis* **2002**, *208* (2), 260-269.
220. Nordvang, E. C.; Borodina, E.; Ruiz-Martínez, J.; Fehrmann, R.; Weckhuysen, B. M., Effects of Coke Deposits on the Catalytic Performance of Large Zeolite H-ZSM-5 Crystals during Alcohol-to-Hydrocarbon Reactions as Investigated by a Combination of Optical Spectroscopy and Microscopy. *Chemistry – A European Journal* **2015**, *21* (48), 17324-17335.
221. Buchanan, J. S.; Santiesteban, J. G.; Haag, W. O., Mechanistic Considerations in Acid-Catalyzed Cracking of Olefins. *Journal of Catalysis* **1996**, *158* (1), 279-287.
222. Corma, A.; Orchillés, A. V., Current views on the mechanism of catalytic cracking. *Microporous and Mesoporous Materials* **2000**, *35–36*, 21-30.

223. Rahimi, N.; Karimzadeh, R., Catalytic cracking of hydrocarbons over modified ZSM-5 zeolites to produce light olefins: A review. *Applied Catalysis A: General* **2011**, *398* (1–2), 1-17.
224. Schreiber, M. W.; Plaisance, C. P.; Baumgärtl, M.; Reuter, K.; Jentys, A.; Bermejo-Deval, R.; Lercher, J. A., Lewis–Brønsted Acid Pairs in Ga/H-ZSM-5 To Catalyze Dehydrogenation of Light Alkanes. *Journal of the American Chemical Society* **2018**, *140* (14), 4849-4859.
225. Phadke, N. M.; Mansoor, E.; Bondil, M.; Head-Gordon, M.; Bell, A. T., Mechanism and Kinetics of Propane Dehydrogenation and Cracking over Ga/H-MFI Prepared via Vapor-Phase Exchange of H-MFI with GaCl<sub>3</sub>. *Journal of the American Chemical Society* **2019**, *141* (4), 1614-1627.
226. Gosling, C. D.; Hamm, D. A. Process for the production of benzene from light hydrocarbons 1992.
227. Gabrienko, A. A.; Arzumanov, S. S.; Toktarev, A. V.; Freude, D.; Haase, J.; Stepanov, A. G., Hydrogen H/D Exchange and Activation of C<sub>1</sub>–C<sub>4</sub> Alkanes on Ga-Modified Zeolite BEA Studied with <sup>1</sup>H Magic Angle Spinning Nuclear Magnetic Resonance in Situ. *The Journal of Physical Chemistry C* **2011**, *115* (28), 13877-13886.
228. Yasumura, S.; Huang, M.; Wu, X.; Liu, C.; Toyao, T.; Maeno, Z.; Shimizu, K.-i., A CHA zeolite supported Ga-oxo cluster for partial oxidation of CH<sub>4</sub> at room temperature. *Catalysis Today* **2019**.
229. Joly, J. F.; Ajot, H.; Merlen, E.; Raatz, F.; Alario, F., Parameters affecting the dispersion of the gallium phase of gallium H-MFI aromatization catalysts. *Applied Catalysis A: General* **1991**, *79* (2), 249-263.
230. Price, G. L.; Kanazirev, V., Ga<sub>2</sub>O<sub>3</sub>/HZSM-5 propane aromatization catalysts: Formation of active centers via solid-state reaction. *Journal of Catalysis* **1990**, *126* (1), 267-278.
231. Schreiber, M. W.; Plaisance, C. P.; Baumgärtl, M.; Reuter, K.; Jentys, A.; Bermejo-Deval, R.; Lercher, J. A., Lewis–Brønsted Acid Pairs in Ga/H-ZSM-5 To Catalyze Dehydrogenation of Light Alkanes. *Journal of the American Chemical Society* **2018**.
232. Al-Yassir, N.; Akhtar, M. N.; Al-Khattaf, S., Physicochemical properties and catalytic performance of galloaluminosilicate in aromatization of lower alkanes: a comparative study with Ga/HZSM-5. *Journal of Porous Materials* **2012**, *19* (6), 943-960.
233. Choudhary, V. R.; Mulla, S. A. R.; Banerjee, S., Aromatization of n-heptane over H-AlMFI, Ga/H-AlMFI, H-GaMFI and H-GaAlMFI zeolite catalysts: influence of zeolitic acidity and non-framework gallium. *Microporous and Mesoporous Materials* **2003**, *57* (3), 317-322.

234. Choudhary, V. R.; Devadas, P., Influence of Space Velocity on Product Selectivity and Distribution of Aromatics and Xylenes in Propane Aromatization over H-GaMFI Zeolite. *Journal of Catalysis* **1997**, *172* (2), 475-478.
235. Xin, M.; Xing, E.; Gao, X.; Wang, Y.; Ouyang, Y.; Xu, G.; Luo, Y.; Shu, X., Ga Substitution during Modification of ZSM-5 and Its Influences on Catalytic Aromatization Performance. *Industrial & Engineering Chemistry Research* **2019**, *58* (17), 6970-6981.
236. Hsieh, C.-Y.; Chen, Y.-Y.; Lin, Y.-C., Ga-Substituted Nanoscale HZSM-5 in Methanol Aromatization: The Cooperative Action of the Brønsted Acid and the Extra-Framework Ga Species. *Industrial & Engineering Chemistry Research* **2018**, *57* (23), 7742-7751.
237. Szeto, K. C.; Jones, Z. R.; Merle, N.; Rios, C.; Gallo, A.; Le Quemener, F.; Delevoye, L.; Gauvin, R. M.; Scott, S. L.; Taoufik, M., A Strong Support Effect in Selective Propane Dehydrogenation Catalyzed by Ga(i-Bu)<sub>3</sub> Grafted onto  $\gamma$ -Alumina and Silica. *ACS Catalysis* **2018**, *8* (8), 7566-7577.
238. Meitzner, G. D.; Iglesia, E.; Baumgartner, J. E.; Huang, E. S., The Chemical State of Gallium in Working Alkane Dehydrocyclodimerization Catalysts. In situ Gallium K-Edge X-Ray Absorption Spectroscopy. *Journal of Catalysis* **1993**, *140* (1), 209-225.
239. Dooley, K. M.; Price, G. L.; Kanazirev, V. I.; Hart, V. I., Gallium-loaded zeolites for light paraffin aromatization: evidence for exchanged gallium cation active centers. *Catalysis Today* **1996**, *31* (3), 305-315.
240. Rane, N.; Overweg, A. R.; Kazansky, V. B.; van Santen, R. A.; Hensen, E. J. M., Characterization and reactivity of Ga<sup>+</sup> and GaO<sup>+</sup> cations in zeolite ZSM-5. *Journal of Catalysis* **2006**, *239* (2), 478-485.
241. Kazansky, V. B.; Subbotina, I. R.; van Santen, R. A.; Hensen, E. J. M., DRIFTS study of the nature and chemical reactivity of gallium ions in Ga/ZSM-5: II. Oxidation of reduced Ga species in ZSM-5 by nitrous oxide or water. *Journal of Catalysis* **2005**, *233* (2), 351-358.
242. Mansoor, E.; Head-Gordon, M.; Bell, A. T., Computational Modeling of the Nature and Role of Ga Species for Light Alkane Dehydrogenation Catalyzed by Ga/H-MFI. *ACS Catalysis* **2018**, *8* (7), 6146-6162.
243. Ravel, B.; Newville, M., ATHENA, ARTEMIS, HEPHAESTUS: data analysis for X-ray absorption spectroscopy using IFEFFIT. *Journal of Synchrotron Radiation* **2005**, *12* (4), 537-541.

244. Newville, M., IFEFFIT : interactive XAFS analysis and FEFF fitting. *Journal of Synchrotron Radiation* **2001**, 8 (2), 322-324.
245. Shimizu, K.-i.; Takamatsu, M.; Nishi, K.; Yoshida, H.; Satsuma, A.; Tanaka, T.; Yoshida, S.; Hattori, T., Alumina-Supported Gallium Oxide Catalysts for NO Selective Reduction: Influence of the Local Structure of Surface Gallium Oxide Species on the Catalytic Activity. *The Journal of Physical Chemistry B* **1999**, 103 (9), 1542-1549.
246. Kresse, G.; Furthmüller, J., Efficiency of ab-initio total energy calculations for metals and semiconductors using a plane-wave basis set. *Computational Materials Science* **1996**, 6 (1), 15-50.
247. Kresse, G.; Hafner, J., Ab initio molecular dynamics for liquid metals. *Physical Review B* **1993**, 47 (1), 558-561.
248. Hjorth Larsen, A.; Jørgen Mortensen, J.; Blomqvist, J.; Castelli, I. E.; Christensen, R.; Duřak, M.; Friis, J.; Groves, M. N.; Hammer, B.; Hargus, C.; Hermes, E. D.; Jennings, P. C.; Bjerre Jensen, P.; Kermode, J.; Kitchin, J. R.; Leonhard Kolsbjerg, E.; Kubal, J.; Kaasbjerg, K.; Lysgaard, S.; Bergmann Maronsson, J.; Maxson, T.; Olsen, T.; Pastewka, L.; Peterson, A.; Rostgaard, C.; Schiøtz, J.; Schütt, O.; Strange, M.; Thygesen, K. S.; Vegge, T.; Vilhelmsen, L.; Walter, M.; Zeng, Z.; Jacobsen, K. W., The atomic simulation environment—a Python library for working with atoms. *Journal of Physics: Condensed Matter* **2017**, 29 (27), 273002.
249. Mortensen, J. J.; Kaasbjerg, K.; Frederiksen, S. L.; Nørskov, J. K.; Sethna, J. P.; Jacobsen, K. W., Bayesian Error Estimation in Density-Functional Theory. *Physical Review Letters* **2005**, 95 (21), 216401.
250. Henkelman, G.; Uberuaga, B. P.; Jónsson, H., A climbing image nudged elastic band method for finding saddle points and minimum energy paths. *The Journal of Chemical Physics* **2000**, 113 (22), 9901-9904.
251. Association, I. Z., International Zeolite Association (IZA) Structure Database.
252. Nowak, I.; Quartararo, J.; Derouane, E. G.; Védrine, J. C., Effect of H<sub>2</sub>-O<sub>2</sub> pre-treatments on the state of gallium in Ga/H-ZSM-5 propane aromatisation catalysts. *Applied Catalysis A: General* **2003**, 251 (1), 107-120.
253. Hu, J. Z.; Wan, C.; Vjunov, A.; Wang, M.; Zhao, Z.; Hu, M. Y.; Camaioni, D. M.; Lercher, J. A., 27Al MAS NMR Studies of HBEA Zeolite at Low to High Magnetic Fields. *The Journal of Physical Chemistry C* **2017**, 121 (23), 12849-12854.

254. Sun, C.; Deng, J.; Kong, L.; Chen, L.; Shen, Z.; Cao, Y.; Zhang, H.; Wang, X., Structure and Photoluminescence Properties of  $\beta$ -Ga<sub>2</sub>O<sub>3</sub> Nanofibres Synthesized via Electrospinning Method. *IOP Conference Series: Materials Science and Engineering* **2017**, *275*, 012046.
255. Golubev, N. V.; Ignat'eva, E. S.; Sigaev, V. N.; Lauria, A.; De Trizio, L.; Azarbod, A.; Paleari, A.; Lorenzi, R., Diffusion-driven and size-dependent phase changes of gallium oxide nanocrystals in a glassy host. *Physical Chemistry Chemical Physics* **2015**, *17* (7), 5141-5150.
256. Janda, A.; Bell, A. T., Effects of Si/Al Ratio on the Distribution of Framework Al and on the Rates of Alkane Monomolecular Cracking and Dehydrogenation in H-MFI. *Journal of the American Chemical Society* **2013**, *135* (51), 19193-19207.
257. Nishi, K.; Shimizu, K.-i.; Takamatsu, M.; Yoshida, H.; Satsuma, A.; Tanaka, T.; Yoshida, S.; Hattori, T., Deconvolution Analysis of Ga K-Edge XANES for Quantification of Gallium Coordinations in Oxide Environments. *The Journal of Physical Chemistry B* **1998**, *102* (50), 10190-10195.
258. Ma, D.; Shu, Y.; Zhang, C.; Zhang, W.; Han, X.; Xu, Y.; Bao, X., Synthesis and characterization of galloaluminosilicate/gallosilicalite (MFI) and their evaluation in methane dehydro-aromatization. *Journal of Molecular Catalysis A: Chemical* **2001**, *168* (1), 139-146.
259. Zheng, B.; Hua, W.; Yue, Y.; Gao, Z., Dehydrogenation of propane to propene over different polymorphs of gallium oxide. *Journal of Catalysis* **2005**, *232* (1), 143-151.
260. Arnold, A.; Steuernagel, S.; Hunger, M.; Weitkamp, J., Insight into the dry-gel synthesis of gallium-rich zeolite [Ga]Beta. *Microporous and Mesoporous Materials* **2003**, *62* (1), 97-106.
261. Dai, W.; Yang, L.; Wang, C.; Wang, X.; Wu, G.; Guan, N.; Obenaus, U.; Hunger, M.; Li, L., Effect of n-Butanol Cofeeding on the Methanol to Aromatics Conversion over Ga-Modified Nano H-ZSM-5 and Its Mechanistic Interpretation. *ACS Catalysis* **2018**, *8* (2), 1352-1362.
262. Fricke, R.; Kosslick, H.; Lischke, G.; Richter, M., Incorporation of Gallium into Zeolites: Syntheses, Properties and Catalytic Application. *Chemical Reviews* **2000**, *100* (6), 2303-2406.
263. Hsieh, M.-F.; Zhou, Y.; Thirumalai, H.; Grabow, L. C.; Rimer, J. D., Silver-Promoted Dehydroaromatization of Ethylene over ZSM-5 Catalysts. *ChemCatChem* **2017**, *9* (9), 1675-1682.
264. Ghorbanpour, A.; Rimer, J. D.; Grabow, L. C., Computational Assessment of the Dominant Factors Governing the Mechanism of Methanol Dehydration over H-ZSM-5 with Heterogeneous Aluminum Distribution. *ACS Catalysis* **2016**, *6* (4), 2287-2298.

265. Ghorbanpour, A.; Rimer, J. D.; Grabow, L. C., Periodic, vdW-corrected density functional theory investigation of the effect of Al siting in H-ZSM-5 on chemisorption properties and site-specific acidity. *Catalysis Communications* **2014**, *52*, 98-102.
266. Wang, C.-M.; Brogaard, R. Y.; Weckhuysen, B. M.; Nørskov, J. K.; Studt, F., Reactivity Descriptor in Solid Acid Catalysis: Predicting Turnover Frequencies for Propene Methylation in Zeotypes. *The Journal of Physical Chemistry Letters* **2014**, *5* (9), 1516-1521.
267. Matthew, D. O.; Jeffrey, D. R., Synthesis of zeolites in the absence of organic structure-directing agents: factors governing crystal selection and polymorphism. *Reviews in Chemical Engineering* **2014**, *30* (1), 1-49.
268. Oleksiak, M. D.; Muraoka, K.; Hsieh, M. F.; Conato, M. T.; Shimojima, A.; Okubo, T.; Chaikittisilp, W.; Rimer, J. D., Organic-Free Synthesis of a Highly Siliceous Faujasite Zeolite with Spatially Biased Q(4)(nAl) Si Speciation. *Angew. Chem. Int. Ed.* **2017**, *56* (43), 13366-13371.
269. Gounder, R.; Iglesia, E., Effects of Partial Confinement on the Specificity of Monomolecular Alkane Reactions for Acid Sites in Side Pockets of Mordenite. *Angew. Chem. Int. Ed.* **2010**, *49* (4), 808-811.
270. Knott, B. C.; Nimlos, C. T.; Robichaud, D. J.; Nimlos, M. R.; Kim, S.; Gounder, R., Consideration of the Aluminum Distribution in Zeolites in Theoretical and Experimental Catalysis Research. *ACS Catalysis* **2018**, *8* (2), 770-784.
271. Danilina, N.; Krumeich, F.; Castelanelli, S. A.; van Bokhoven, J. A., Where Are the Active Sites in Zeolites? Origin of Aluminum Zoning in ZSM-5. *The Journal of Physical Chemistry C* **2010**, *114* (14), 6640-6645.
272. Dwyer, J.; Fitch, F. R.; Qin, G.; Vickerman, J. C., Study of the surface composition of zeolites by fast atom bombardment mass spectrometry. *The Journal of Physical Chemistry* **1982**, *86* (23), 4574-4578.
273. Althoff, R.; Schulz-Dobrick, B.; Schüth, F.; Unger, K., Controlling the spatial distribution of aluminum in ZSM-5 crystals. *Microporous Materials* **1993**, *1* (3), 207-218.
274. Kessler, H.; Patarin, J.; Schott-Daric, C., The opportunities of the fluoride route in the synthesis of microporous materials. In *Studies in Surface Science and Catalysis*, Jansen, J. C.; Stöcker, M.; Karge, H. G.; Weitkamp, J., Eds. Elsevier: 1994; Vol. 85, pp 75-113.

275. Babitz, S. M.; Williams, B. A.; Miller, J. T.; Snurr, R. Q.; Haag, W. O.; Kung, H. H., Monomolecular cracking of n-hexane on Y, MOR, and ZSM-5 zeolites. *Applied Catalysis A: General* **1999**, *179* (1), 71-86.
276. Ong, L. H.; Dömök, M.; Olindo, R.; van Veen, A. C.; Lercher, J. A., Dealumination of HZSM-5 via steam-treatment. *Microporous and Mesoporous Materials* **2012**, *164*, 9-20.
277. Sano, T.; Ikeya, H.; Kasuno, T.; Wang, Z. B.; Kawakami, Y.; Soga, K., Influence of Crystallinity of HZSM-5 Zeolite on Its Dealumination Rate. *Zeolites* **1997**, *19* (1), 80-86.
278. Sano, T.; Yamashita, N.; Iwami, Y.; Takeda, K.; Kawakami, Y., Estimation of dealumination rate of ZSM-5 zeolite by adsorption of water vapor. *Zeolites* **1996**, *16* (4), 258-264.
279. Prodinge, S.; Shi, H.; Eckstein, S.; Hu, J. Z.; Olarte, M. V.; Camaioni, D. M.; Derewinski, M. A.; Lercher, J. A., Stability of Zeolites in Aqueous Phase Reactions. *Chemistry of Materials* **2017**, *29* (17), 7255-7262.
280. Vjunov, A.; Fulton, J. L.; Huthwelker, T.; Pin, S.; Mei, D.; Schenter, G. K.; Govind, N.; Camaioni, D. M.; Hu, J. Z.; Lercher, J. A., Quantitatively Probing the Al Distribution in Zeolites. *Journal of the American Chemical Society* **2014**, *136* (23), 8296-8306.
281. Holzinger, J.; Beato, P.; Lundegaard, L. F.; Skibsted, J., Distribution of Aluminum over the Tetrahedral Sites in ZSM-5 Zeolites and Their Evolution after Steam Treatment. *The Journal of Physical Chemistry C* **2018**, *122* (27), 15595-15613.
282. Palčić, A.; Ordonsky, V. V.; Qin, Z.; Georgieva, V.; Valtchev, V., Tuning Zeolite Properties for a Highly Efficient Synthesis of Propylene from Methanol. *Chemistry – A European Journal* **2018**, *24* (50), 13136-13149.
283. Persson, A. E.; Schoeman, B. J.; Sterte, J.; Otterstedt, J. E., Synthesis of stable suspensions of discrete colloidal zeolite (Na, TPA)ZSM-5 crystals. *Zeolites* **1995**, *15* (7), 611-619.
284. Morales-Pacheco, P.; Alvarez-Ramirez, F.; Del Angel, P.; Bucio, L.; Domínguez, J. M., Synthesis and Structural Properties of Zeolytic Nanocrystals I. MFI Type Zeolites. *The Journal of Physical Chemistry C* **2007**, *111* (6), 2368-2378.
285. Ding, K.; Corma, A.; Maciá-Agulló, J. A.; Hu, J. G.; Krämer, S.; Stair, P. C.; Stucky, G. D., Constructing Hierarchical Porous Zeolites via Kinetic Regulation. *Journal of the American Chemical Society* **2015**, *137* (35), 11238-11241.

286. Triantafyllidis, C. S.; Vlessidis, A. G.; Nalbandian, L.; Evmiridis, N. P., Effect of the degree and type of the dealumination method on the structural, compositional and acidic characteristics of H-ZSM-5 zeolites. *Microporous and Mesoporous Materials* **2001**, *47* (2), 369-388.
287. Wang, Z.; Jiang, Y.; Lafon, O.; Trébosc, J.; Duk Kim, K.; Stampfl, C.; Baiker, A.; Amoureux, J.-P.; Huang, J., Brønsted acid sites based on penta-coordinated aluminum species. *Nature Communications* **2016**, *7*, 13820.
288. Coster, D.; Blumenfeld, A. L.; Fripiat, J. J., Lewis Acid Sites and Surface Aluminum in Aluminas and Zeolites: A High-Resolution NMR Study. *The Journal of Physical Chemistry* **1994**, *98* (24), 6201-6211.
289. Gilson, J.-P.; Edwards, G. C.; Peters, A. W.; Rajagopalan, K.; Wormsbecher, R. F.; Roberie, T. G.; Shatlock, M. P., Penta-co-ordinated aluminium in zeolites and aluminosilicates. *Journal of the Chemical Society, Chemical Communications* **1987**, (2), 91-92.
290. Chen, J.; Chen, T.; Guan, N.; Wang, J., Dealumination process of zeolite omega monitored by <sup>27</sup>Al 3QMAS NMR spectroscopy. *Catalysis Today* **2004**, *93-95*, 627-630.
291. Pidko, E. A.; Almutairi, S. M. T.; Mezari, B.; Magusin, P. C. M. M.; Hensen, E. J. M., Chemical Vapor Deposition of Trimethylaluminum on Dealuminated Faujasite Zeolite. *ACS Catalysis* **2013**, *3* (7), 1504-1517.
292. Park, G. T.; Jo, D.; Ahn, N. H.; Cho, J.; Hong, S. B., Synthesis and Structural Characterization of a CHA-type AlPO<sub>4</sub> Molecular Sieve with Penta-Coordinated Framework Aluminum Atoms. *Inorganic Chemistry* **2017**, *56* (14), 8504-8512.
293. Wang, Z.; Jiang, Y.; Jin, F.; Stampfl, C.; Hunger, M.; Baiker, A.; Huang, J., Strongly enhanced acidity and activity of amorphous silica–alumina by formation of pentacoordinated AlIV species. *Journal of Catalysis* **2019**, *372*, 1-7.
294. Sazama, P.; Wichterlova, B.; Dedecek, J.; Tvaruzkova, Z.; Musilova, Z.; Palumbo, L.; Sklenak, S.; Gonsiorova, O., FTIR and <sup>27</sup>Al MAS NMR analysis of the effect of framework Al- and Si-defects in micro- and micro-mesoporous H-ZSM-5 on conversion of methanol to hydrocarbons. *Microporous and Mesoporous Materials* **2011**, *143* (1), 87-96.
295. Ghorbanpour, A.; Gumidyala, A.; Grabow, L. C.; Crossley, S. P.; Rimer, J. D., Epitaxial Growth of ZSM-5@Silicalite-1: A Core–Shell Zeolite Designed with Passivated Surface Acidity. *ACS Nano* **2015**, *9* (4), 4006-4016.

296. Grey, C. P.; Vega, A. J., Determination of the Quadrupole Coupling Constant of the Invisible Aluminum Spins in Zeolite HY with  $1\text{H}/27\text{Al}$  TRAPDOR NMR. *Journal of the American Chemical Society* **1995**, *117* (31), 8232-8242.
297. Deng, F.; Yue, Y.; Ye, C.,  $1\text{H}/27\text{Al}$  TRAPDOR NMR studies on aluminum species in dealuminated zeolites. *Solid State Nuclear Magnetic Resonance* **1998**, *10* (3), 151-160.
298. Liu, Y.; Müller, S.; Berger, D.; Jelic, J.; Reuter, K.; Tonigold, M.; Sanchez-Sanchez, M.; Lercher, J. A., Formation Mechanism of the First Carbon–Carbon Bond and the First Olefin in the Methanol Conversion into Hydrocarbons. *Angewandte Chemie* **2016**, *128* (19), 5817-5820.
299. Müller, S.; Liu, Y.; Kirchberger, F. M.; Tonigold, M.; Sanchez-Sanchez, M.; Lercher, J. A., Hydrogen Transfer Pathways during Zeolite Catalyzed Methanol Conversion to Hydrocarbons. *Journal of the American Chemical Society* **2016**, *138* (49), 15994-16003.
300. Wang, C.; Chu, Y.; Xu, J.; Wang, Q.; Qi, G.; Gao, P.; Zhou, X.; Deng, F., Extra-Framework Aluminum-Assisted Initial C–C Bond Formation in Methanol-to-Olefins Conversion on Zeolite H-ZSM-5. *Angewandte Chemie International Edition* **2018**, *57* (32), 10197-10201.
301. Arora, S. S.; Bhan, A., The critical role of methanol pressure in controlling its transfer dehydrogenation and the corresponding effect on propylene-to-ethylene ratio during methanol-to-hydrocarbons catalysis on H-ZSM-5. *Journal of Catalysis* **2017**, *356*, 300-306.
302. Martinez-Espin, J. S.; Mortén, M.; Janssens, T. V. W.; Svelle, S.; Beato, P.; Olsbye, U., New insights into catalyst deactivation and product distribution of zeolites in the methanol-to-hydrocarbons (MTH) reaction with methanol and dimethyl ether feeds. *Catalysis Science & Technology* **2017**, *7* (13), 2700-2716.
303. Liu, Y.; Kirchberger, F. M.; Müller, S.; Eder, M.; Tonigold, M.; Sanchez-Sanchez, M.; Lercher, J. A., Critical role of formaldehyde during methanol conversion to hydrocarbons. *Nature Communications* **2019**, *10* (1), 1462.
304. Hwang, A.; Kumar, M.; Rimer, J. D.; Bhan, A., Implications of methanol disproportionation on catalyst lifetime for methanol-to-olefins conversion by HSSZ-13. *Journal of Catalysis* **2017**, *346*, 154-160.
305. Yarulina, I.; Chowdhury, A. D.; Meirer, F.; Weckhuysen, B. M.; Gascon, J., Recent trends and fundamental insights in the methanol-to-hydrocarbons process. *Nature Catalysis* **2018**, *1* (6), 398-411.

306. Yarulina, I.; Bailleul, S.; Pustovarenko, A.; Martinez, J. R.; Wispelaere, K. D.; Hajek, J.; Weckhuysen, B. M.; Houben, K.; Baldus, M.; Van Speybroeck, V.; Kapteijn, F.; Gascon, J., Suppression of the Aromatic Cycle in Methanol-to-Olefins Reaction over ZSM-5 by Post-Synthetic Modification Using Calcium. *ChemCatChem* **2016**, *8* (19), 3057-3063.
307. Miyake, K.; Hirota, Y.; Ono, K.; Uchida, Y.; Tanaka, S.; Nishiyama, N., Direct and selective conversion of methanol to para-xylene over Zn ion doped ZSM-5/silicalite-1 core-shell zeolite catalyst. *Journal of Catalysis* **2016**, *342*, 63-66.
308. Chen, D.; Rebo, H. P.; Moljord, K.; Holmen, A., Influence of Coke Deposition on Selectivity in Zeolite Catalysis. *Industrial & Engineering Chemistry Research* **1997**, *36* (9), 3473-3479.
309. Čejka, J.; Centi, G.; Perez-Pariente, J.; Roth, W. J., Zeolite-based materials for novel catalytic applications: Opportunities, perspectives and open problems. *Catalysis Today* **2012**, *179* (1), 2-15.
310. van Laak, A. N. C.; Sagala, S. L.; Zečević, J.; Friedrich, H.; de Jongh, P. E.; de Jong, K. P., Mesoporous mordenites obtained by sequential acid and alkaline treatments – Catalysts for cumene production with enhanced accessibility. *Journal of Catalysis* **2010**, *276* (1), 170-180.
311. Groen, J. C.; Sano, T.; Moulijn, J. A.; Pérez-Ramírez, J., Alkaline-mediated mesoporous mordenite zeolites for acid-catalyzed conversions. *Journal of Catalysis* **2007**, *251* (1), 21-27.
312. Čejka, J.; Mintova, S., Perspectives of Micro/Mesoporous Composites in Catalysis. *Catalysis Reviews* **2007**, *49* (4), 457-509.
313. Zeng, J. L.; Xiong, Z. T.; Zhang, H. B.; Lin, G. D.; Tsai, K. R., Nonoxidative dehydrogenation and aromatization of methane over W/HZSM - 5 - based catalysts. *Catalysis Letters* **1998**, *53* (1), 119-124.
314. Liu, S.; Wang, L.; Ohnishi, R.; Ichikawa, M., Bifunctional Catalysis of Mo/HZSM-5 in the Dehydroaromatization of Methane to Benzene and Naphthalene XAFS/TG/DTA/MASS/FTIR Characterization and Supporting Effects. *Journal of Catalysis* **1999**, *181* (2), 175-188.
315. Mellmer, M. A.; Gallo, J. M. R.; Martin Alonso, D.; Dumesic, J. A., Selective Production of Levulinic Acid from Furfuryl Alcohol in THF Solvent Systems over H-ZSM-5. *ACS Catalysis* **2015**, *5* (6), 3354-3359.

## Appendix A Supplementary Information for Chapter 2

**Table A1.** Physicochemical Properties of MWW materials

sample <sup>a</sup>	BET surface area (m <sup>2</sup> /g)	External surface area (m <sup>2</sup> /g)	Micropore volume (ml/g)
MCM-22_15	634	149	0.19
d-MWW <sub>4</sub> _15	566	183	0.16
d-MWW <sub>5.5</sub> _15	558	164	0.16
d-MWW <sub>6</sub> _15	585	259	0.14
d-MWW <sub>7</sub> _15	592	348	0.11
d-MWW <sub>8</sub> _15	557	359	0.09
d-MWW <sub>9.5</sub> _15	345	350	0.00
MCM-22_30	626	109	0.21
d-MWW <sub>4</sub> _30	444	133	0.13
d-MWW <sub>5</sub> _30	392	138	0.10
d-MWW <sub>6</sub> _30	373	163	0.09
d-MWW <sub>7</sub> _30	370	228	0.06
d-MWW <sub>8</sub> _30	327	229	0.04
MCM-22_45	565	76	0.19
d-MWW <sub>4</sub> _45	251	144	0.06
d-MWW <sub>5</sub> _45	195	111	0.04
d-MWW <sub>6</sub> _45	171	131	0.02
ITQ-2_15	662	519	0.07
ITQ-2_45	612	506	0.06

a. surface area and micropore volume calculated from N<sub>2</sub> adsorption isotherms.

**Table A2.** Elemental composition of as-synthesized MWW materials

sample <sup>a</sup>	Si/Al	Na (wt%)	Al (wt%)	Si (wt%)
MCM-22_15	13.6	0.1	2.5	34.2
d-MWW <sub>5.5</sub>	13.7	0.4	2.5	34.2
d-MWW <sub>8.0</sub>	16.7	0.4	1.8	30.0
MCM-22_30	26.6	0.2	1.4	37.2
MCM-22_45	35.4	0.1	0.8	28.3

a. elemental composition determined by ICP elemental analysis.

**Table A3.** Solid-state  $^{31}\text{P}$  NMR peaks ( $\pm 2$  ppm) and fraction of adsorbed TMPO and TBPO on MWW zeolites

	Acid sites						Mobile			
TMPO peak	82	78	69	66	58	53	48	42	36	33
0 wt	0.007	0.02	-	0.16	0.07	-	-	0.72	-	0.02
5.5 wt	-	-	0.006	0.04	-	-	0.23	0.48	-	0.24
8 wt	-	-	-	0.04	0.02	0.01	-	0.85	0.01	0.06
ITQ-2	-	-	0.005	0.009	0.01	0.007	-	0.96	-	0.01
TBPO peak	75	62	-	-	-	-	50	46	-	-
0 wt	0.037	0.005	-	-	-	-	-	0.96	-	-
5.5 wt	0.02	0.008	-	-	-	-	-	0.97	-	-
8 wt	0.03	-	-	-	-	-	-	0.97	-	-
ITQ-2	0.03	-	-	-	-	-	0.19	0.78	-	-

**Table A4.** Catalytic results for the Friedel-Craft alkylation of benzene and benzyl alcohol

Catalyst	Conv. (%)	Yield DPM (%)	Yield DE (%)
MCM-22	63	22	41
d-MWW <sub>5.5</sub>	47	11	36
d-MWW <sub>8.0</sub>	96	33	63
ITQ-2_15	44 $\pm$ 6	12 $\pm$ 2	33 $\pm$ 4
ITQ-2_45	17	4	13

<sup>a</sup> Reaction conditions: benzene: 8.32 g, benzyl alcohol: 0.54 g, catalyst: 30 mg, 80 °C, 9 h

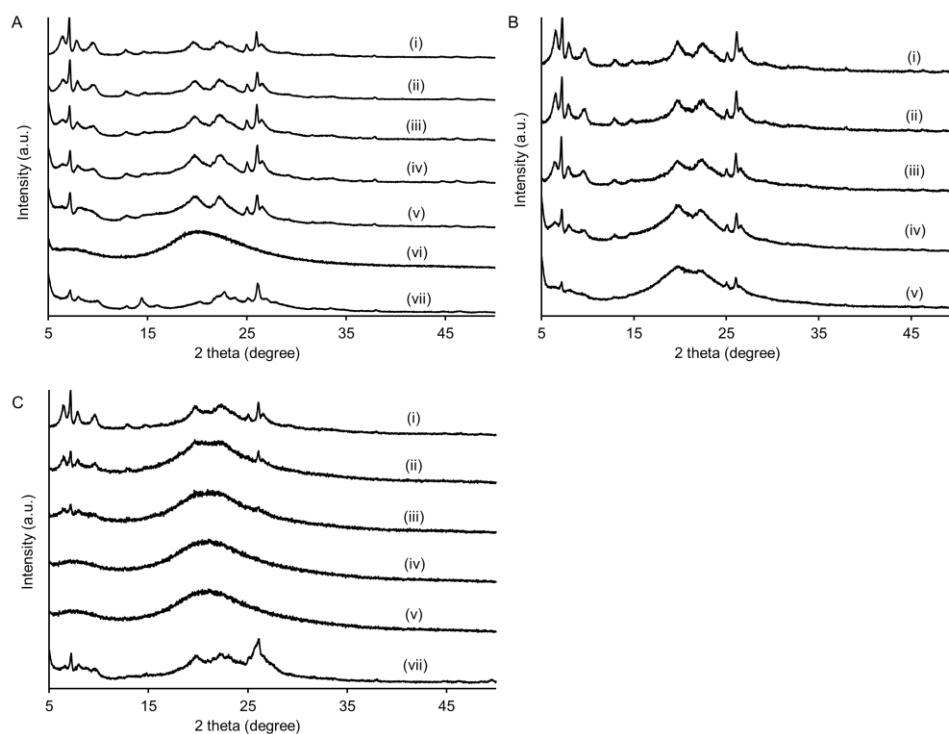


**Figure A1.** Powder XRD patterns of as-prepared MWW materials prepared with (i) 4, (ii) 5, (iii) 6, (iv) 7, (v) 8 wt%, (vi) 10wt% CTAB, and (vii) ITQ-2. MWW materials obtained in different gel Si/Al ratio: (A) 15, (B) 30, and (C) 45.

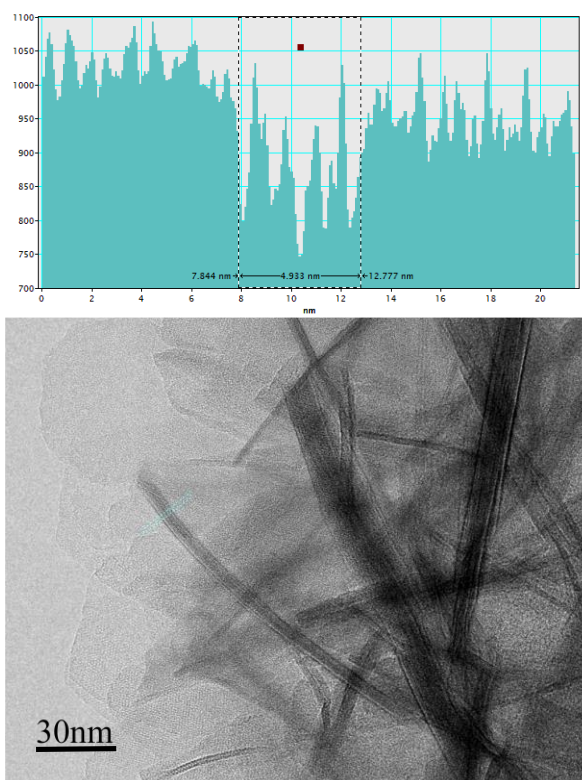


**Figure A2.** Example of sample thickness measurement for d-MWW<sub>8.0</sub> using Digital Micrograph. The line profile clearly shows the edge-on oriented MWW nanosheet is approximately 2 unit cells thick (~ 5 nm).

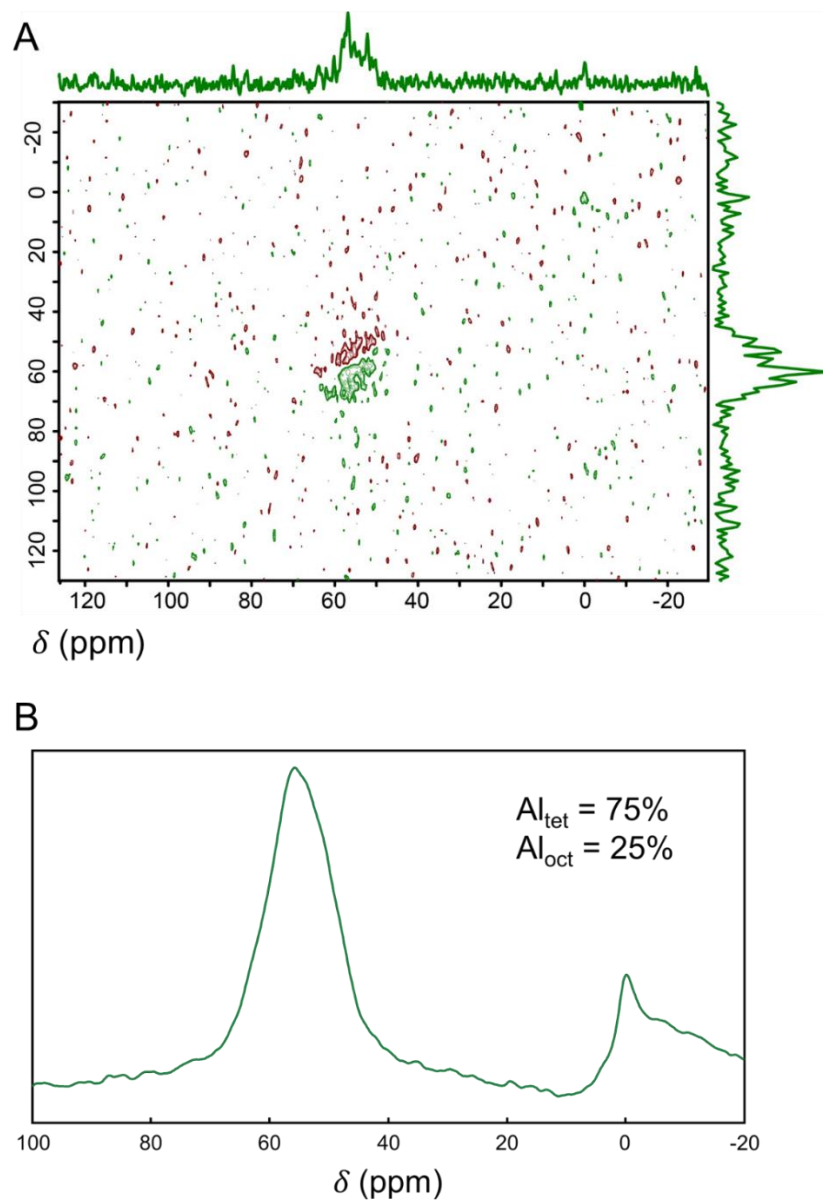


**Figure A3.** (A). Two-dimensional  $^{27}\text{Al}$  MQMAS NMR spectrum of ITQ-2\_15 (B). One-dimensional  $^{27}\text{Al}$  MAS NMR spectrum of ITQ-2\_15

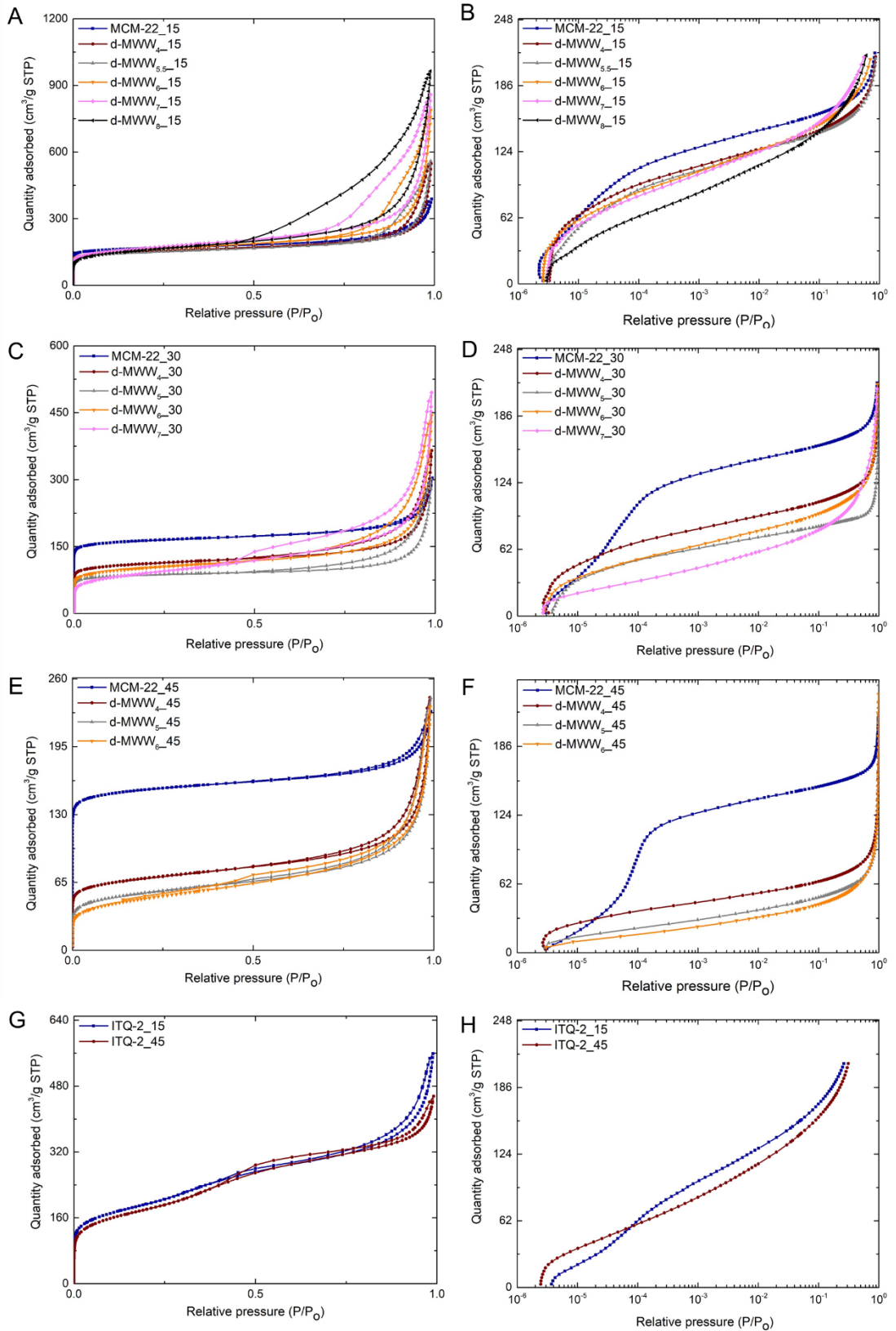


**Figure A4.** Nitrogen adsorption and desorption isotherms of calcined MWW materials.

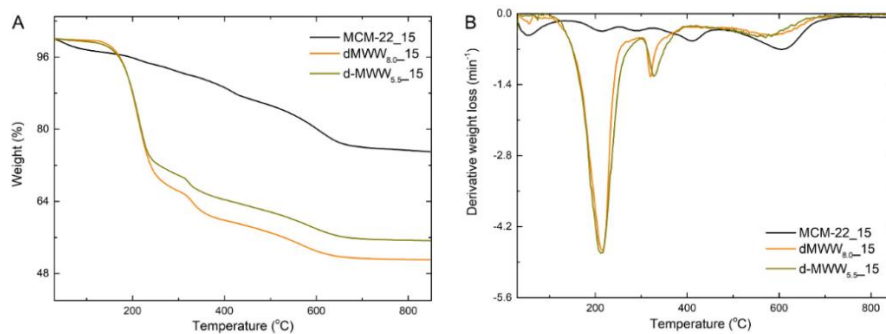


**Figure A5.** Thermogravimetric analysis (TGA) of as-synthesized MWW materials.

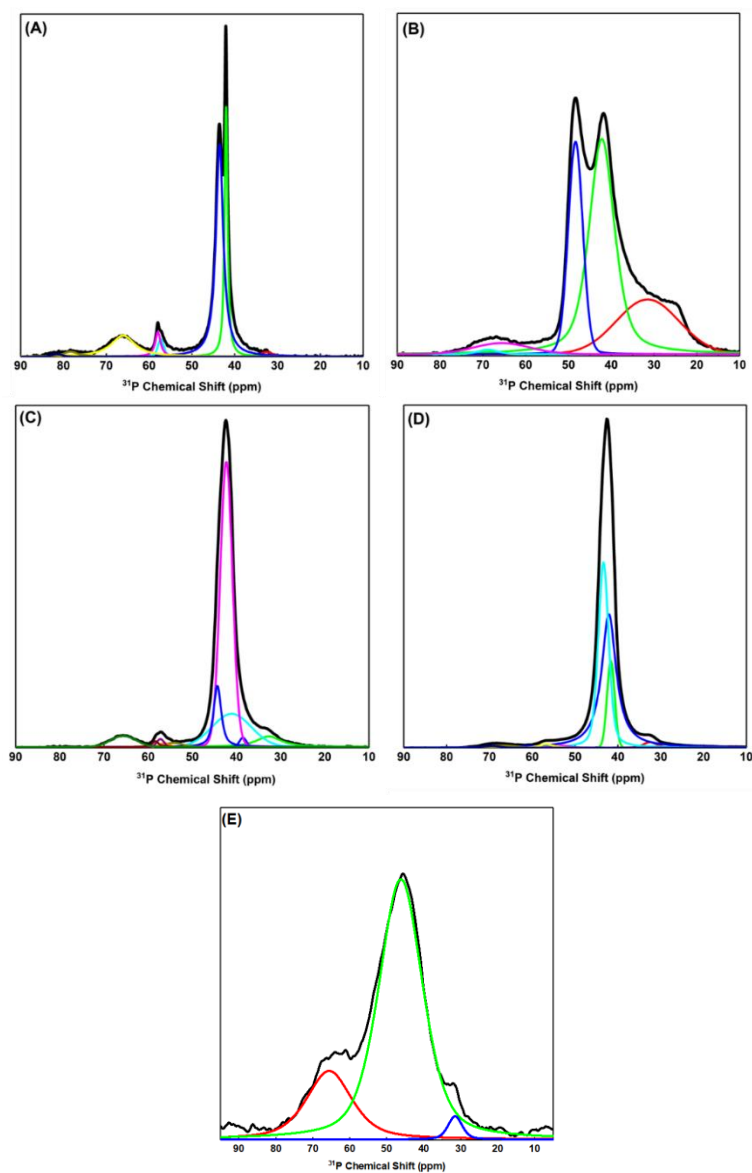


**Figure A6.** Deconvolution solid-state <sup>31</sup>P NMR spectra of TMPO adsorption on MWW-type zeolites: (A) MCM-22; (B) d-MWW<sub>5.5</sub>; (C) d-MWW<sub>8.0</sub>; (D) ITQ-2\_15; and (E) ITQ-2\_45.

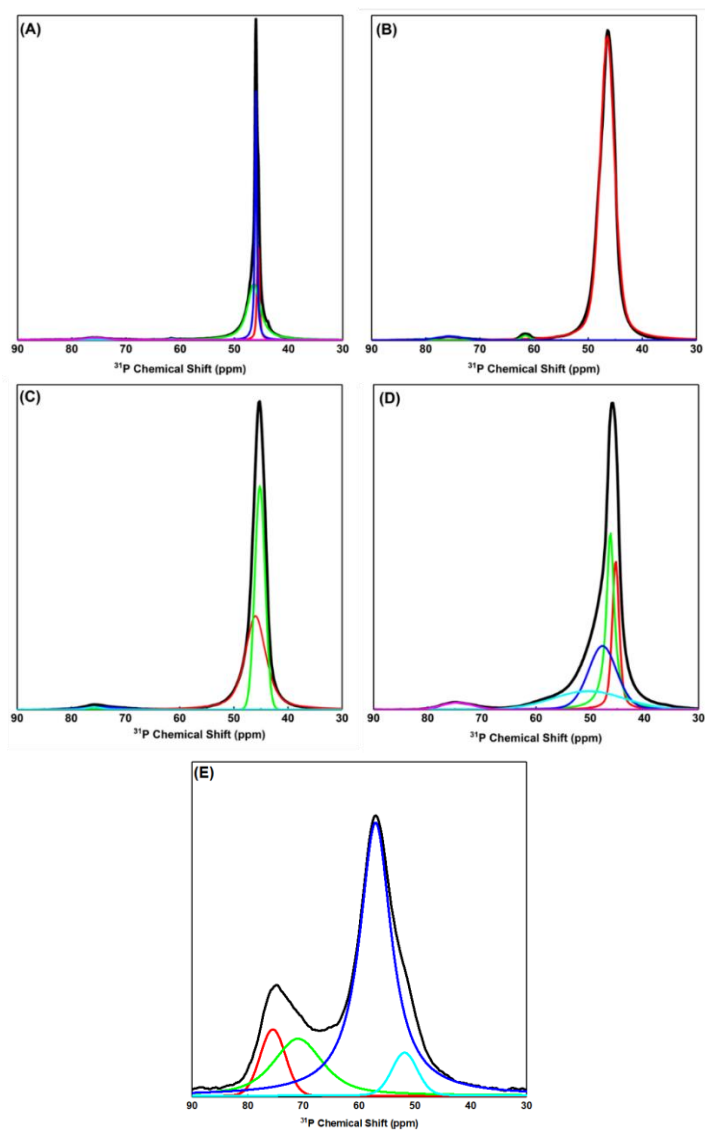


**Figure A7.** Deconvolution solid-state  $^{31}\text{P}$  NMR spectra of TMPO adsorption on MWW-type zeolites: (A) MCM-22\_15; (B) d-MWW<sub>5.5</sub>\_15; (C) d-MWW<sub>8.0</sub>\_15; (D) ITQ-2\_15 and (E) ITQ-2\_45.

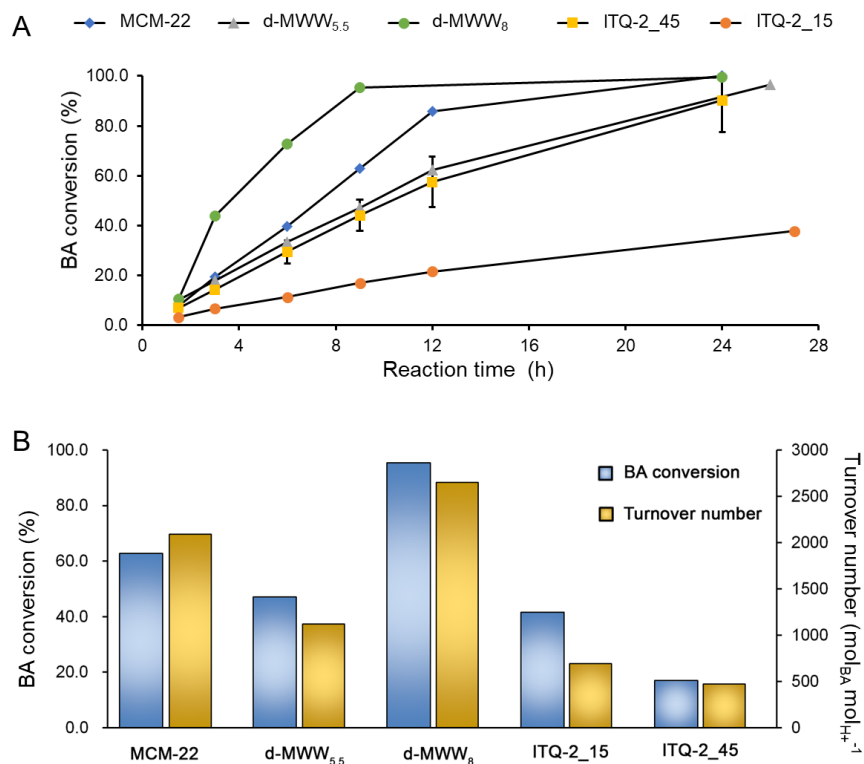


**Figure A8.** (A) Benzyl alcohol conversion as a function of reaction time over MWW-type catalysts. (B) Benzyl alcohol (BA) conversion (left axis) and turnover number (right axis). The results are shown for a single time point (9 h).

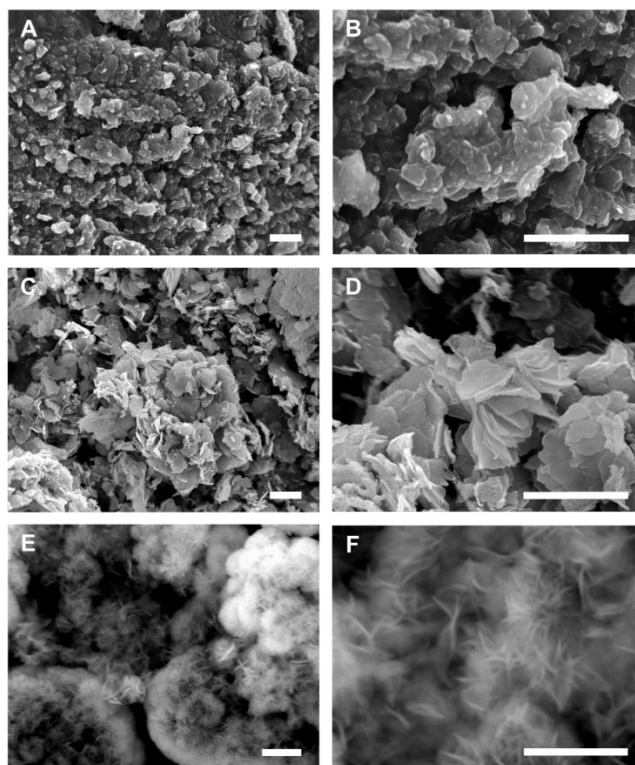


**Figure A9.** Scanning electron micrographs of calcined MWW type materials: (A and B) H-ITQ-2 (gel Si/Al = 15); (C and D) H-ITQ-2 (gel Si/Al = 45), and H-d-MWW<sub>5.5</sub> (gel Si/Al = 15). All scale bars are equal to 2  $\mu\text{m}$ .

### Appendix B Supplementary Information for Chapter 3

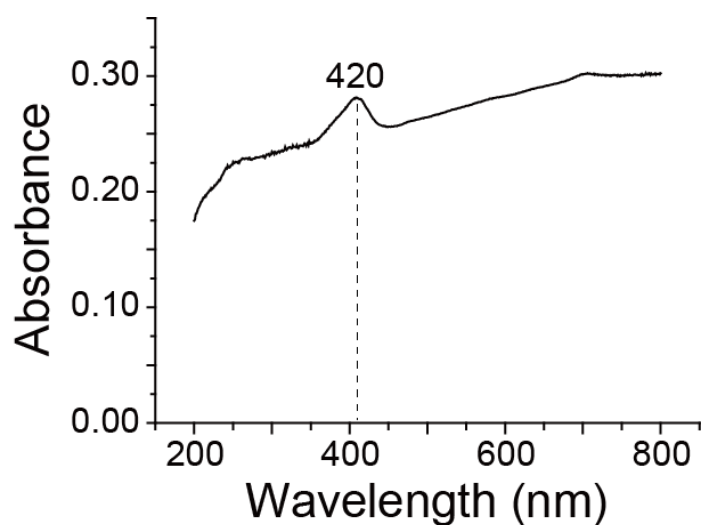


**Figure B1.** Solid-state UV-Vis spectrum of spent Ag<sub>25</sub>-ZSM-5 with an absorbance band at ca. 420 nm assigned to metallic Ag species.

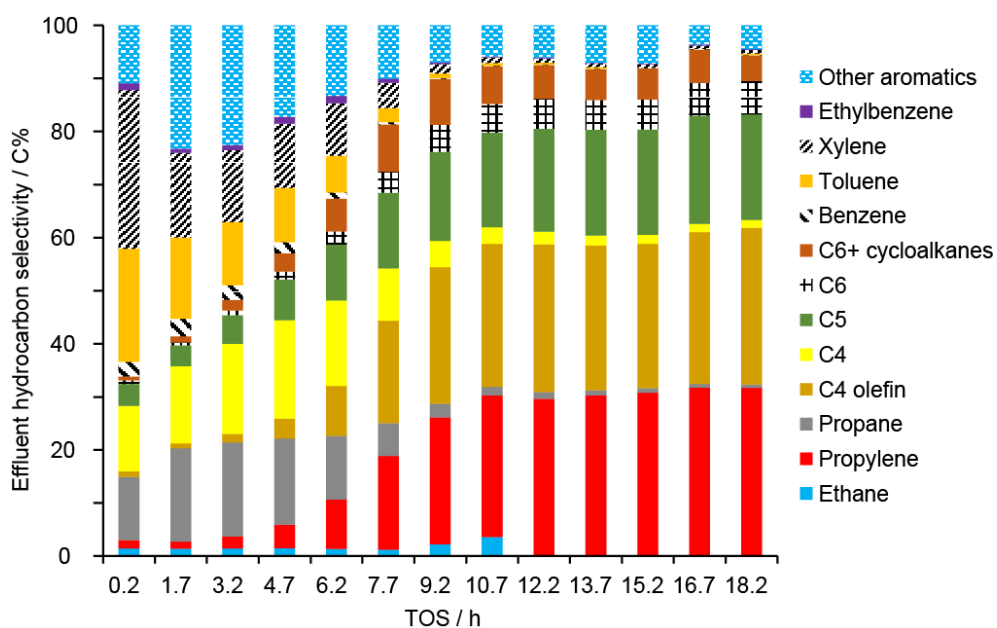


**Figure B2.** Product selectivity profile obtained in the NOC of methane and ethylene at over Ag<sub>25</sub>-ZSM-5. The space velocity was 2000 ml g<sup>-1</sup> h<sup>-1</sup> for both methane and ethylene.

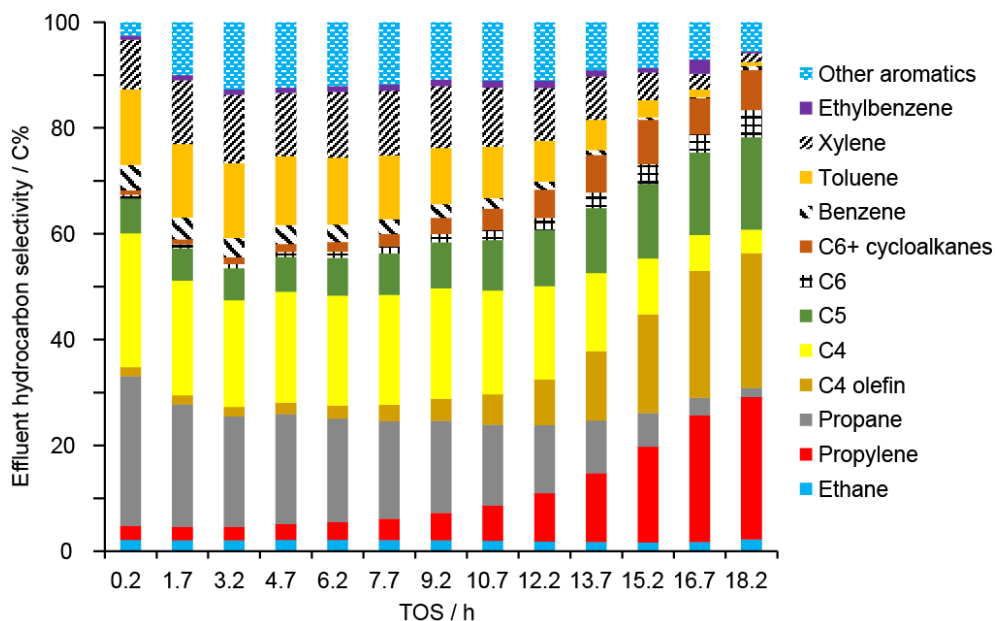


**Figure B3.** Product selectivity profile obtained in the NOC of methane and ethylene at over H-ZSM-5. The space velocity was  $2000 \text{ ml g}^{-1} \text{ h}^{-1}$  for both methane and ethylene.

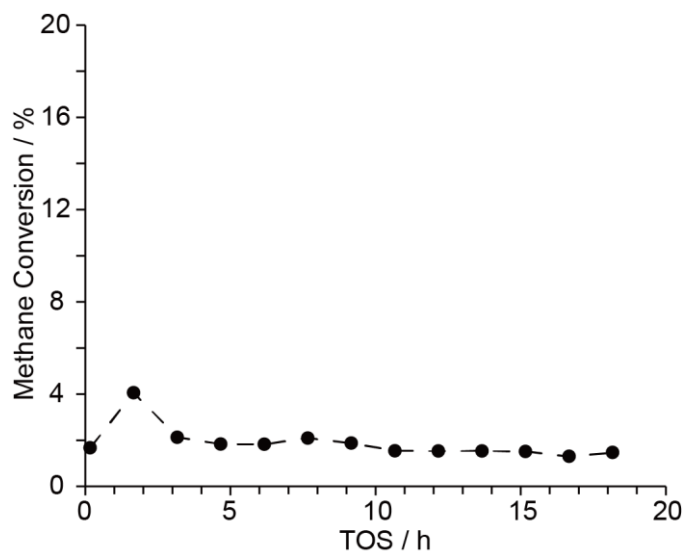


**Figure B4.** Performance of  $\text{Ag}_{25}\text{-ZSM-5}$  catalyst in NOC of methane. The space velocity was  $2000 \text{ ml g}^{-1} \text{ h}^{-1}$  for methane. Dashed lines are interpolations for improved visualization.

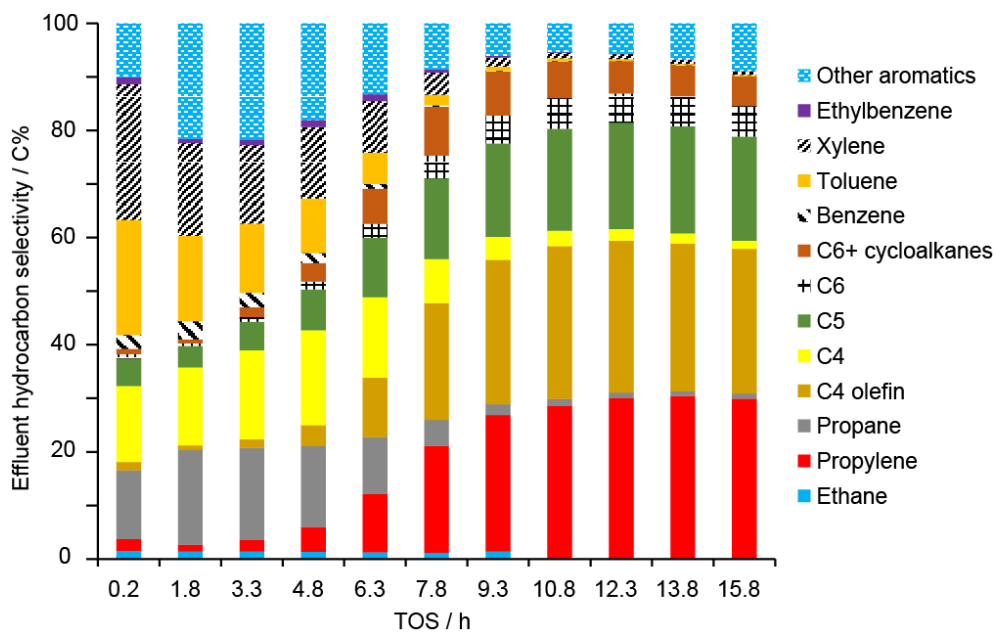


**Figure B5.** Product selectivity profile obtained in the ETL reaction over Ag<sub>25</sub>-ZSM-5. The space velocity was 2000 ml g<sup>-1</sup> h<sup>-1</sup> for ethylene.

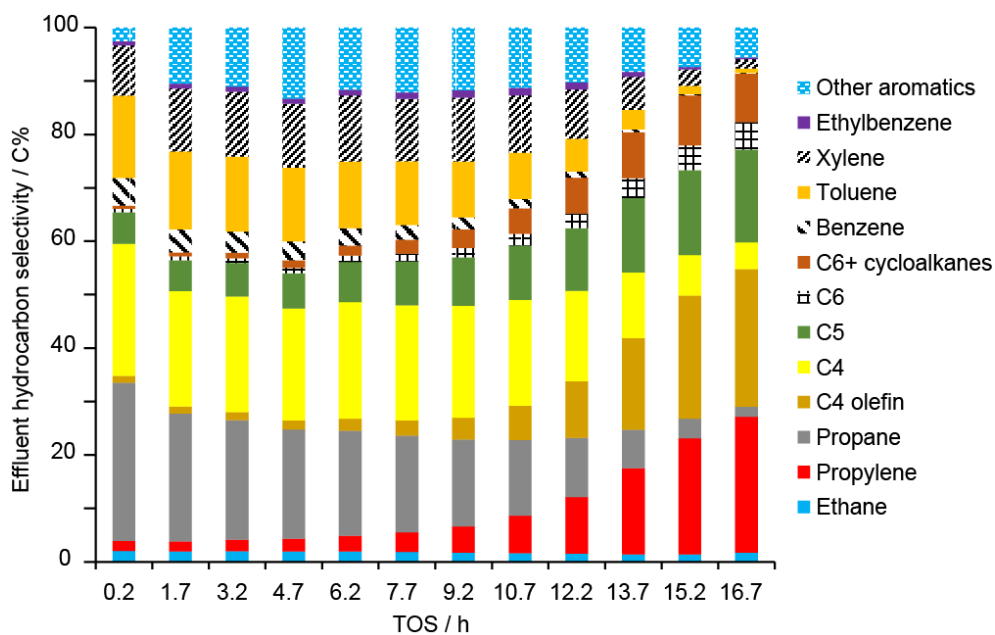


**Figure B6.** Product selectivity profile obtained in the ETL reaction over H-ZSM-5. The space velocity was 2000 ml g<sup>-1</sup> h<sup>-1</sup> for ethylene.

**Table B1.** Chemical compositions of Ag-ZSM-5 prepared using different AgNO<sub>3(aq)</sub> concentrations

Catalyst	AgNO <sub>3</sub> concentration (mM)	Ag/Al <sup>[a]</sup>	Brønsted acid site density (μmol g <sup>-1</sup> ) <sup>[b]</sup>	Lewis acid site density (μmol g <sup>-1</sup> ) <sup>[c]</sup>
Ag <sub>25</sub> -ZSM-5	10	0.24 ± 0.07	494	184
Ag <sub>15</sub> -ZSM-5	5	0.15 ± 0.01	552	125
Ag <sub>8</sub> -ZSM-5	2	0.08 ± 0.01	598	80

[a] Measured by EDX; [b] Estimated based on H-ZSM-5\_23 (650 μmol g<sup>-1</sup>) from Mellmer et al.<sup>315</sup>; [c] Estimated by considering that the number of Lewis acid sites in H-ZSM\_23 (28 μmol g<sup>-1</sup>) from Mellmer et al.<sup>315</sup> and assuming only Ag<sup>+</sup> present as the Lewis acid site.

**Table B2.** Comparison of aromatic selectivity in the ETL reaction over ZSM-5 catalysts

Catalyst	Ethylene conversion (%)	Benzene (%)	Toluene (%)	Xylene (%)	Total aromatics (%)
Ag <sub>25</sub> -ZSM-5	92.2	3.5	19.5	20.5	54.8
Ag <sub>8</sub> -ZSM-5	84.9	1.9	11.9	15.2	39.6
H-ZSM-5	89.9	1.2	5.8	7.1	20.4

## Appendix C Supplementary Information for Chapter 4

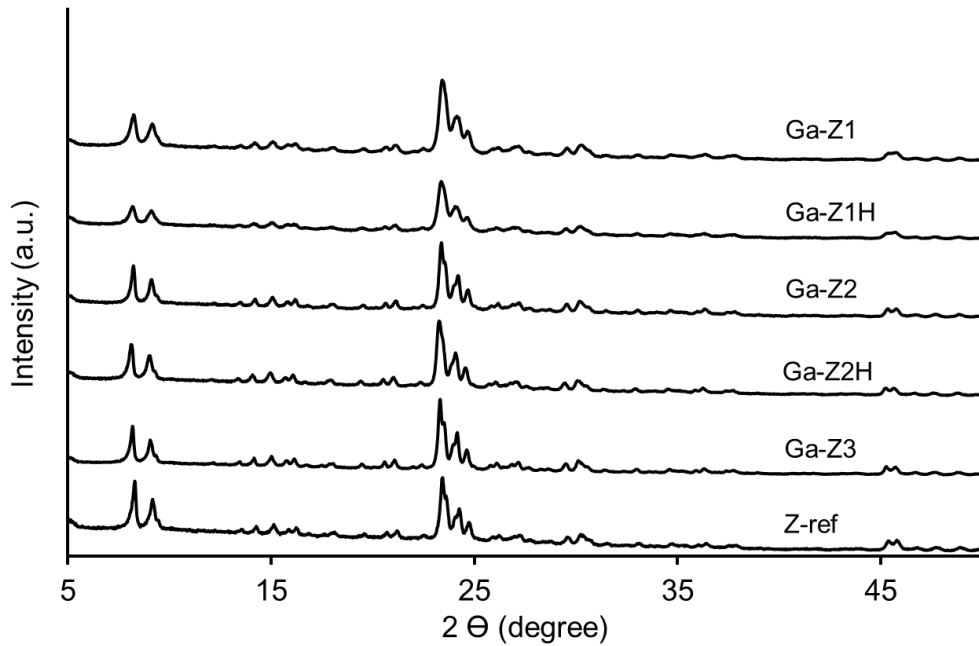


**Figure C1.** Powder X-ray diffraction (XRD) patterns of calcined H-form ZSM-5 samples prepared with different methods (Ga-Z1, Ga-Z1H, Ga-Z2, Ga-Z2H, and Ga-Z3) and calcined commercial ZSM-5 (Z-ref).

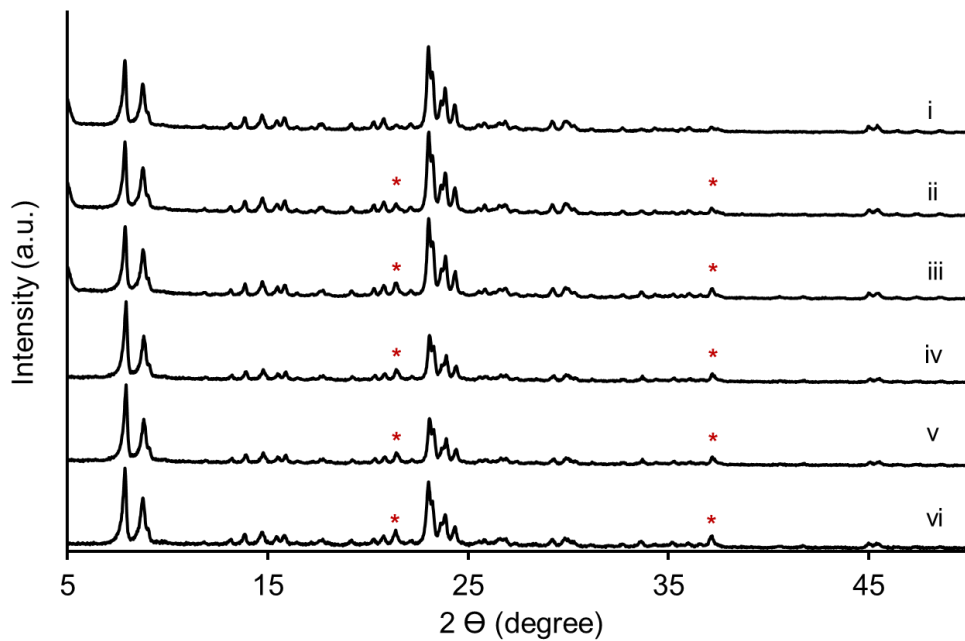


**Figure C2.** Powder X-ray diffraction (XRD) patterns of ZSM-5 samples prepared by ion exchange using different  $\text{Ga}(\text{NO}_3)_3$  concentrations: (i) 5 mM; (ii) 10 mM; (iii) 20 mM; (iv) 30 mM; (v) 40 mM; and (vi) 50 mM. Peaks marked with asterisks refer to crystalline  $\text{Ga}_2\text{O}_3$  species.<sup>254-255</sup>

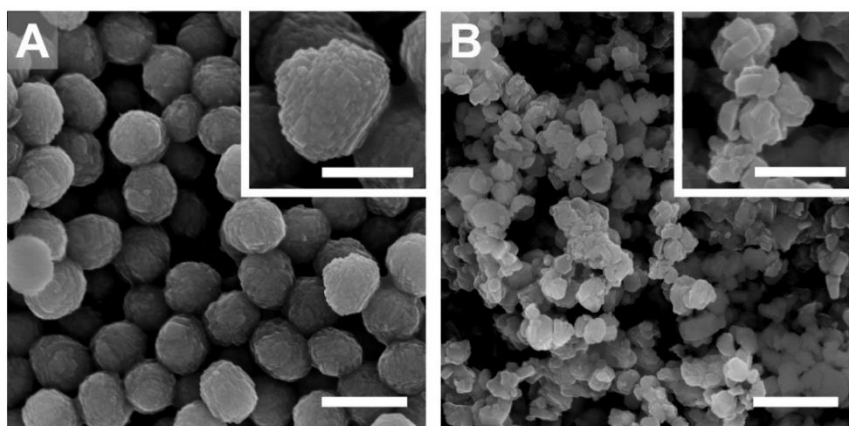


**Figure C3.** Scanning electron micrographs of the following as-synthesized samples: (A) Ga-Z1 and (B) Ga-Z2. Scale bars equal 1  $\mu\text{m}$ . Insets scale bars equal 500 nm.

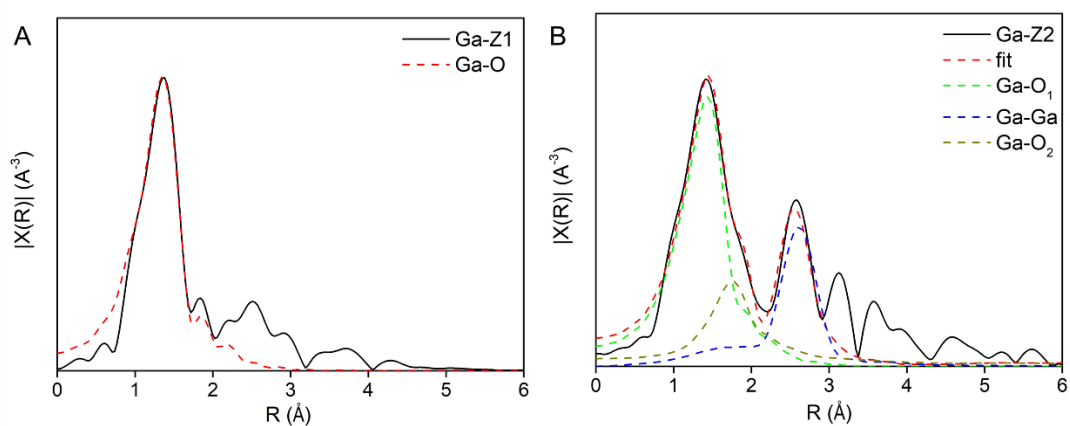


**Figure C4.** Magnitudes of  $k^2$ -weighted Fourier-transformed Ga K-edge EXAFS spectra of the following ZSM-5 samples: (A) Ga-Z1 (direct synthesis) with  $k$  range = 2-12  $\text{\AA}^{-1}$ ; and (B) Ga-Z2 (ion exchange) with  $k$ -range = 2-13  $\text{\AA}^{-1}$ .

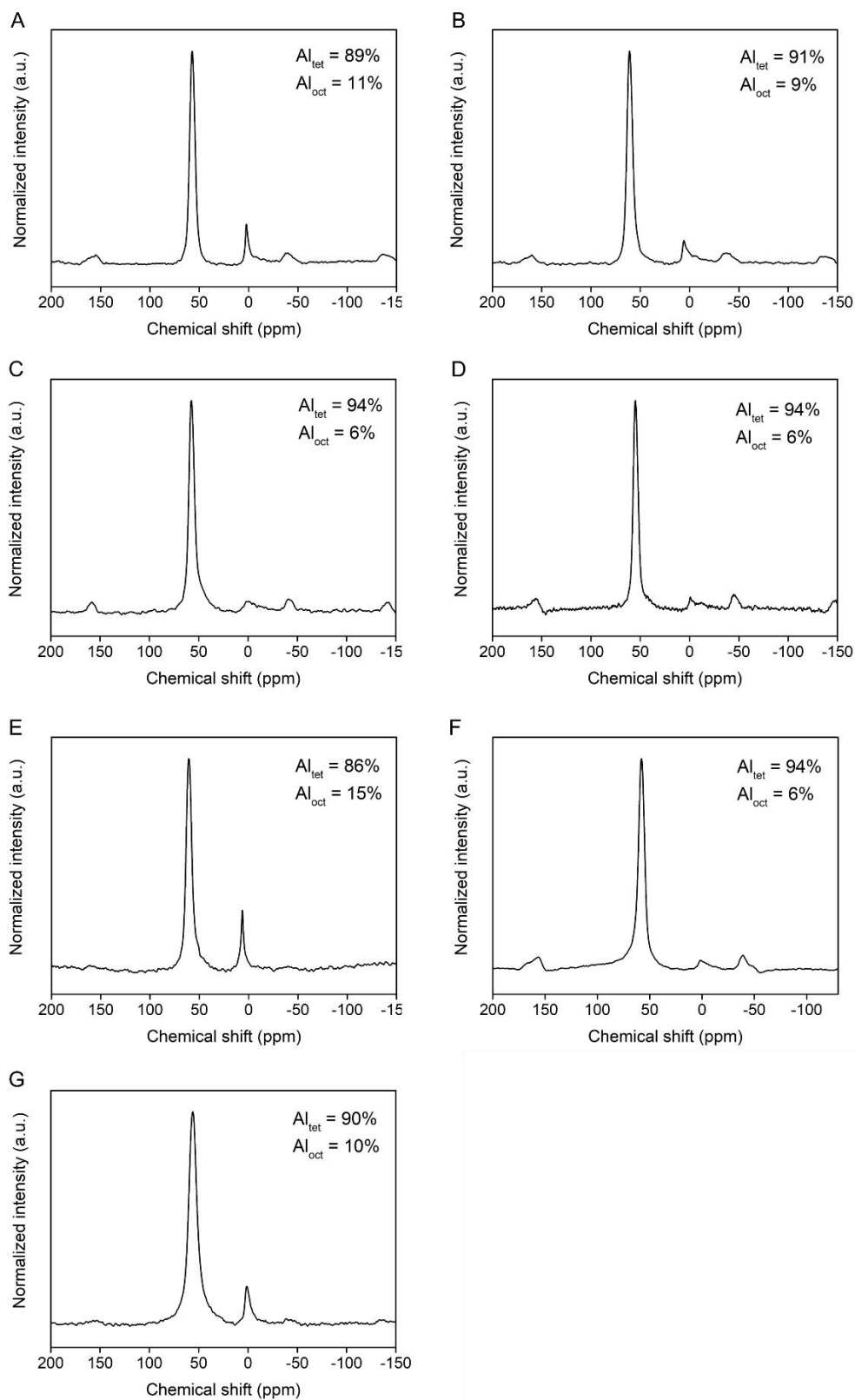


**Figure C5.**  $^{27}\text{Al}$  MAS NMR spectra of hydrated ZSM-5 materials: (A) Ga-Z1, (B) Ga-Z1H, (C) Ga-Z2, (D) Ga-Z2H, (E) Ga-Z3, (F) Z-ref, and (G) Z1 (obtained via the same approach of Ga-Z1 synthesis without the addition of Ga).

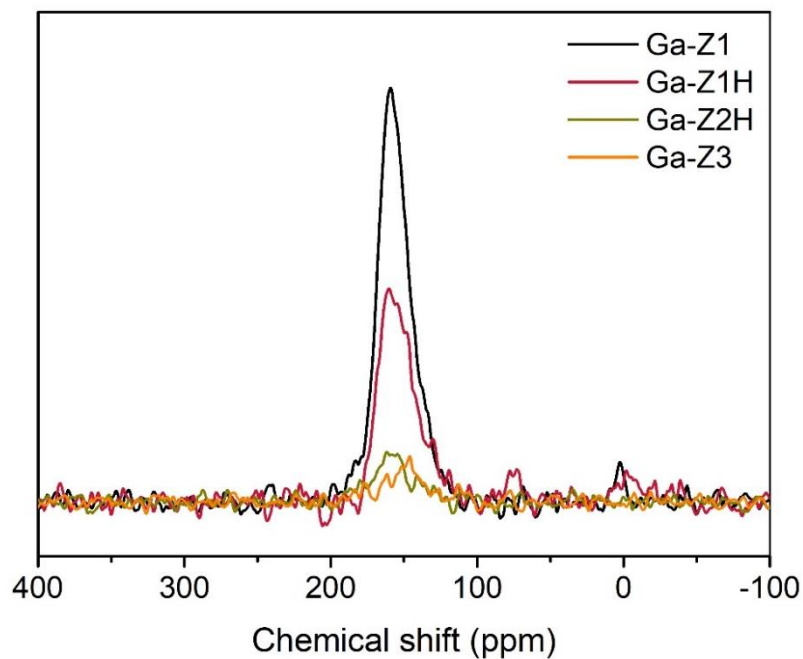


**Figure C6.**  $^{71}\text{Ga}$  MAS NMR spectra of hydrated ZSM-5 materials: Ga-Z1 (black), Ga-Z1H (red), Ga-Z2H (green), and Ga-Z3 (orange).

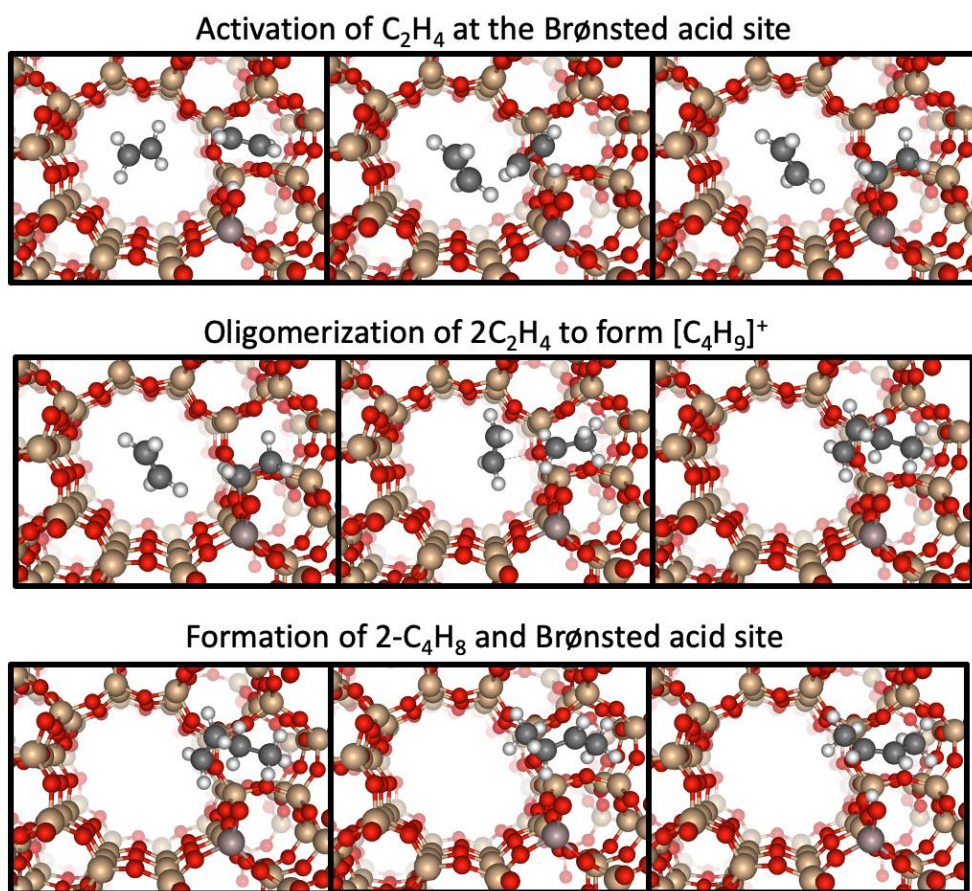


**Figure C7.** Illustration of ethylene dimerization to 2-butene at a Brønsted acid site located at the T-12 position of H-ZSM-5 (MFI framework).

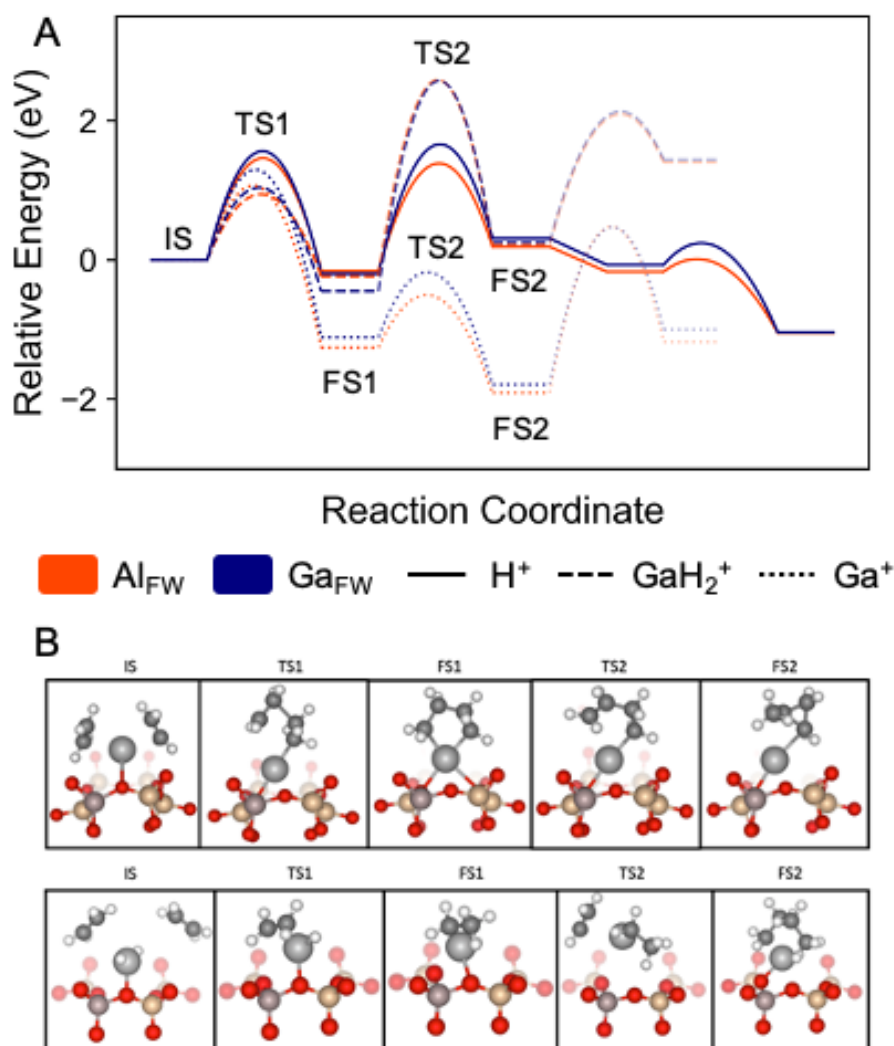


**Figure C8.** (A) Potential energy diagram for ethylene dimerization at Ga<sup>+</sup> and GaH<sub>2</sub><sup>+</sup> Lewis acid sites (B) The corresponding atomic configurations

Detailed description of Figure C8: The corresponding atomic configurations of initial states (IS), transition states (TS) and final states (FS) on Ga<sup>+</sup> (top) and GaH<sub>2</sub><sup>+</sup> (bottom) sites. The pathway for GaH<sub>2</sub><sup>+</sup> is discussed in the main text. On Ga<sup>+</sup> two ethylene molecules can react exothermically to form a [C<sub>4</sub>H<sub>8</sub>-Ga]<sup>+</sup> metallacycle (FS1). The barriers (TS1) are moderate and amount to 0.94 and 1.03 eV for H-(Al)- and H-(Ga)-ZSM-5, respectively. The formation of 2-butene as product requires two hydrogen transfer steps, which are both kinetically hindered. In particular, the first hydrogen transfer (TS2, FS2) requires activation energies in excess of 2.8 eV for both Al and Ga as heteroatoms. Alternatively, the cyclobutane may desorb without the need for

hydrogen transfer steps, but still requires an activation energy of over 2 eV. Overall, no feasible mechanism for ethylene oligomerization was found on Ga<sup>+</sup> sites.

**Table C1.** Chemical compositions of Ga-ZSM-5 prepared using different Ga(NO<sub>3</sub>)<sub>3(aq)</sub> concentrations

Ga(NO <sub>3</sub> ) <sub>3</sub> concentration (mM)	Si/Al <sup>[a]</sup>	Ga/Al <sup>[a]</sup>
50	19.4 ± 0.7	2.2 ± 0.3
40	19.9 ± 1.1	1.6 ± 0.6
30	20.0 ± 1.6	2.0 ± 1.2
20	19.2 ± 1.2	1.4 ± 0.4
10	21.0 ± 0.7	0.8 ± 0.3
5	20.0 ± 1.3	0.6 ± 0.3

[a] Measured by EDX

**Table C2.** Electronic energies from DFT calculations for all considered mechanisms for ethylene activation.

Acid Site	Pathway	Intermediate Steps	Energies (eV)			
			ΔE		E <sub>a</sub>	
			Al	Ga	Al	Ga
H <sup>+</sup>	P	1. 2C <sub>2</sub> H <sub>4</sub> + H <sup>+</sup> -Z → C <sub>2</sub> H <sub>4</sub> + C <sub>2</sub> H <sub>5</sub> <sup>+</sup> -Z	-0.16	-0.20	1.46	1.56
		2. C <sub>2</sub> H <sub>4</sub> + C <sub>2</sub> H <sub>5</sub> <sup>+</sup> -Z → C <sub>4</sub> H <sub>9</sub> <sup>+</sup> -Z	0.35	0.51	1.54	1.85
		3. C <sub>4</sub> H <sub>9</sub> <sup>+</sup> -Z → C <sub>4</sub> H <sub>9</sub> <sup>+</sup> -Z (H-transfer)	-0.36	-0.38	-	-
		4. C <sub>4</sub> H <sub>9</sub> <sup>+</sup> -Z → 2-C <sub>4</sub> H <sub>8</sub> + H <sup>+</sup> -Z	-1.15	-0.97	0.10	0.23
Ga <sup>+</sup>	P1	1. 2C <sub>2</sub> H <sub>4</sub> + Ga <sup>+</sup> -Z → C <sub>2</sub> H <sub>3</sub> -Ga + H <sup>+</sup> -Z + C <sub>2</sub> H <sub>4</sub> Further steps not explored	1.79	1.75	1.79	2.06
	P2	1. 2C <sub>2</sub> H <sub>4</sub> + Ga <sup>+</sup> -Z → H-Ga + C <sub>2</sub> H <sub>3</sub> <sup>-</sup> -Z + C <sub>2</sub> H <sub>4</sub> Further steps not explored	2.73	2.87	3.85	4.08
	P3	1. 2C <sub>2</sub> H <sub>4</sub> + Ga <sup>+</sup> -Z → C <sub>4</sub> H <sub>8</sub> -Ga-Z (cyclometallapentane)	-0.24	-0.45	0.94	1.03
2. C <sub>4</sub> H <sub>8</sub> -Ga-Z → C <sub>4</sub> H <sub>8, i1</sub> -Ga-Z (H-transfer from β-C to α-C)		0.45	0.70	2.82	3.01	
GaH <sub>2</sub> <sup>+</sup>	P1	1. 2C <sub>2</sub> H <sub>4</sub> + GaH <sub>2</sub> <sup>+</sup> -Z → C <sub>2</sub> H <sub>3</sub> -GaH <sub>2</sub> + H <sup>+</sup> -Z + C <sub>2</sub> H <sub>4</sub> Further steps not explored	0.93	1.09	1.14	1.47
		1. 2C <sub>2</sub> H <sub>4</sub> + GaH <sub>2</sub> <sup>+</sup> -Z → H-Ga + C <sub>2</sub> H <sub>3</sub> <sup>-</sup> -Z + C <sub>2</sub> H <sub>4</sub> Further steps not explored	1.98	2.25	2.21	2.49
	P3	1. 2C <sub>2</sub> H <sub>4</sub> + GaH <sub>2</sub> <sup>+</sup> -Z → C <sub>2</sub> H <sub>5</sub> <sup>+</sup> -GaH-Z + C <sub>2</sub> H <sub>4</sub>	-1.26	-1.11	0.97	1.22
2. C <sub>2</sub> H <sub>4</sub> + C <sub>2</sub> H <sub>5</sub> <sup>+</sup> -GaH-Z → C <sub>4</sub> H <sub>9</sub> <sup>+</sup> -GaH-Z		-0.65	-0.68	0.73	0.91	
		3. C <sub>4</sub> H <sub>9</sub> <sup>+</sup> -GaH-Z → 1-C <sub>4</sub> H <sub>8</sub> + GaH <sub>2</sub> <sup>+</sup> -Z	0.73	0.79	2.37	2.24

**Table C3.** Binding energies in eV from DFT calculations

	Al			Ga		
	H <sup>+</sup>	Ga <sup>+</sup>	GaH <sub>2</sub> <sup>+</sup>	H <sup>+</sup>	Ga <sup>+</sup>	GaH <sub>2</sub> <sup>+</sup>
ethylene	-1.83	-1.99	-0.66	-1.88	-2.45	-0.89
propene	-2.06	-1.89	-1.85	-2.12	-2.31	-2.14
1-butene	-2.03	-2.11	-1.94	-2.12	-2.57	-2.28
2-butene	-2.22	-2.37	-2.22	-2.28	-2.81	-2.56
1,3-butadiene	-2.26	-2.42	-2.24	-2.33	-2.87	-2.58
cyclobutene	-2.02	-2.26	-2.11	-2.07	-2.70	-2.44
cyclopentene	-2.22	-2.03	-1.87	-2.28	-2.46	-2.26
1-hexene	-2.38	-2.37	-2.31	-2.46	-2.80	-2.58
cyclohexene	-2.42	-2.17	-2.02	-2.51	-2.57	-2.32
benzene	-2.32	-2.22	-1.85	-2.39	-2.63	-2.30

**Table C4.** Lewis/Brønsted acid site redistribution energies across all 12 T-site combinations in ZSM-5

		Al at T <sub>j</sub> →											
		T01	T02	T03	T04	T05	T06	T07	T08	T09	T10	T11	T12
Ga at T <sub>i</sub> ↓	T01	-0.64	-0.27	-0.5	0.66	-0.03	-0.27	-0.09	0.43	-0.24	-0.68	-0.61	-0.09
	T02	-0.61	-0.24	-0.47	0.69	0	-0.24	-0.06	0.46	-0.21	-0.65	-0.58	-0.06
	T03	-0.38	-0.01	-0.24	0.92	0.23	-0.01	0.17	0.69	0.02	-0.42	-0.35	0.17
	T04	-1.43	-1.06	-1.29	-0.13	-0.82	-1.06	-0.88	-0.36	-1.03	-1.47	-1.4	-0.88
	T05	-0.36	0.01	-0.22	0.94	0.25	0.01	0.19	0.71	0.04	-0.4	-0.33	0.19
	T06	-0.72	-0.35	-0.58	0.58	-0.11	-0.35	-0.17	0.35	-0.32	-0.76	-0.69	-0.17
	T07	-0.67	-0.3	-0.53	0.63	-0.06	-0.3	-0.12	0.4	-0.27	-0.71	-0.64	-0.12
	T08	-0.62	-0.25	-0.48	0.68	-0.01	-0.25	-0.07	0.45	-0.22	-0.66	-0.59	-0.07
	T09	-0.05	0.32	0.09	1.25	0.56	0.32	0.5	1.02	0.35	-0.09	-0.02	0.5
	T10	0.38	0.75	0.52	1.68	0.99	0.75	0.93	1.45	0.78	0.34	0.41	0.93
	T11	-0.67	-0.3	-0.53	0.63	-0.06	-0.3	-0.12	0.4	-0.27	-0.71	-0.64	-0.12
	T12	-0.24	0.13	-0.1	1.06	0.37	0.13	0.31	0.83	0.16	-0.28	-0.21	0.31

## Appendix D Supplementary Information for Chapter 5

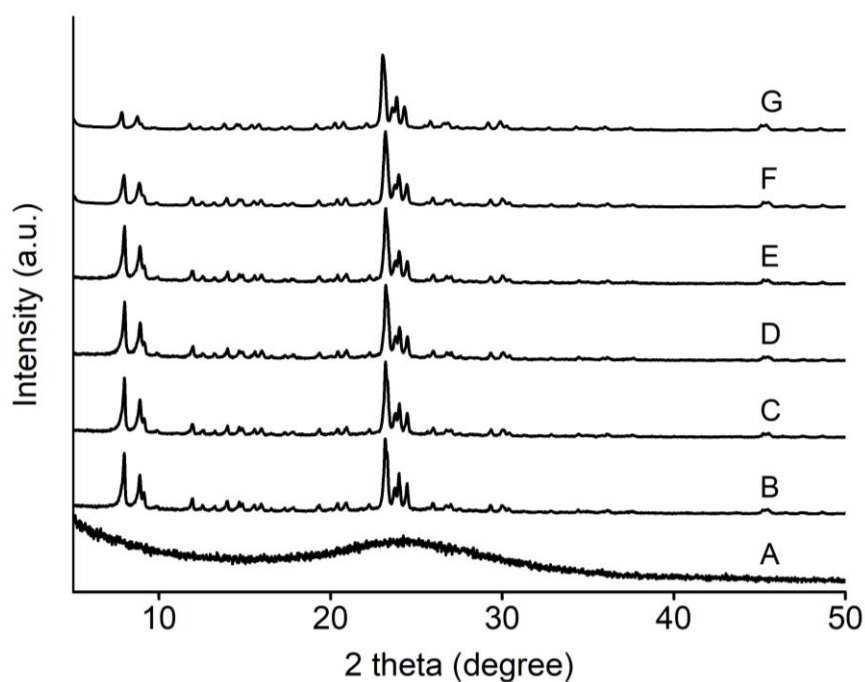


**Figure D1.** Powder X-ray diffraction (XRD) patterns of as-made ZSM-5 samples prepared with different sol gel Si/Al ratios: (A) Z20, (B) Z30, (C) Z50, (D) Z75, (E) Z100, (F) Z22-1, and (G) Z22-2.

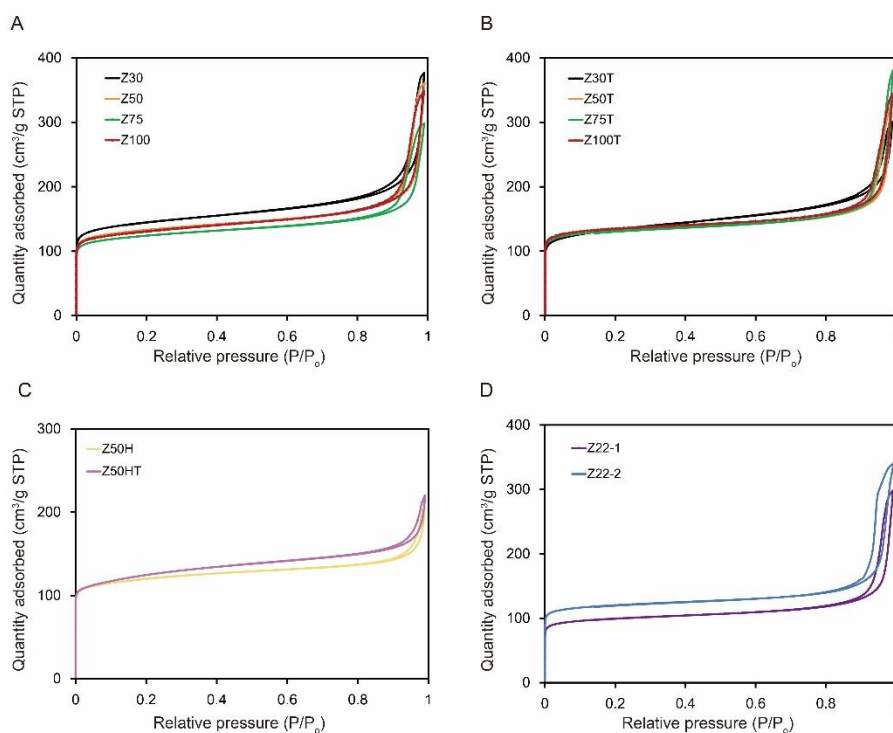


**Figure D2.** Nitrogen adsorption/desorption isotherms of calcined ZSM-5 samples.

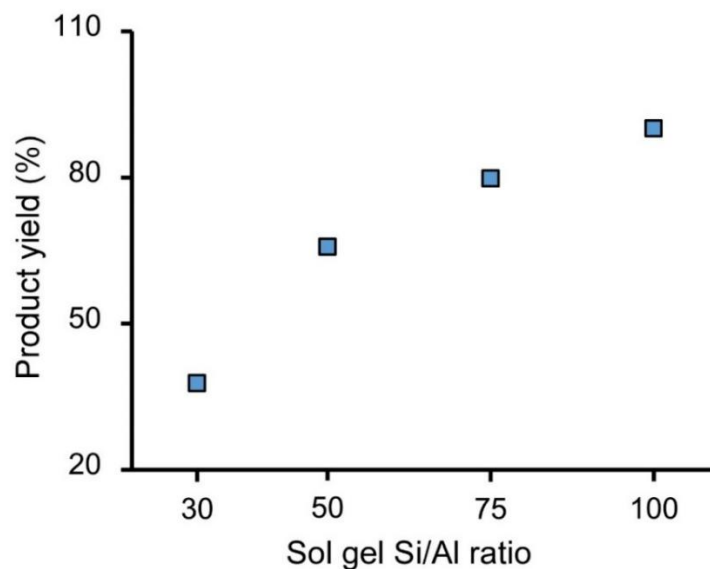


**Figure D3.** The approximate mass (yield) of collected ZSM-5 solid products from syntheses of varying sol gel Si/Al ratio. The samples contain residual OSDA and water.

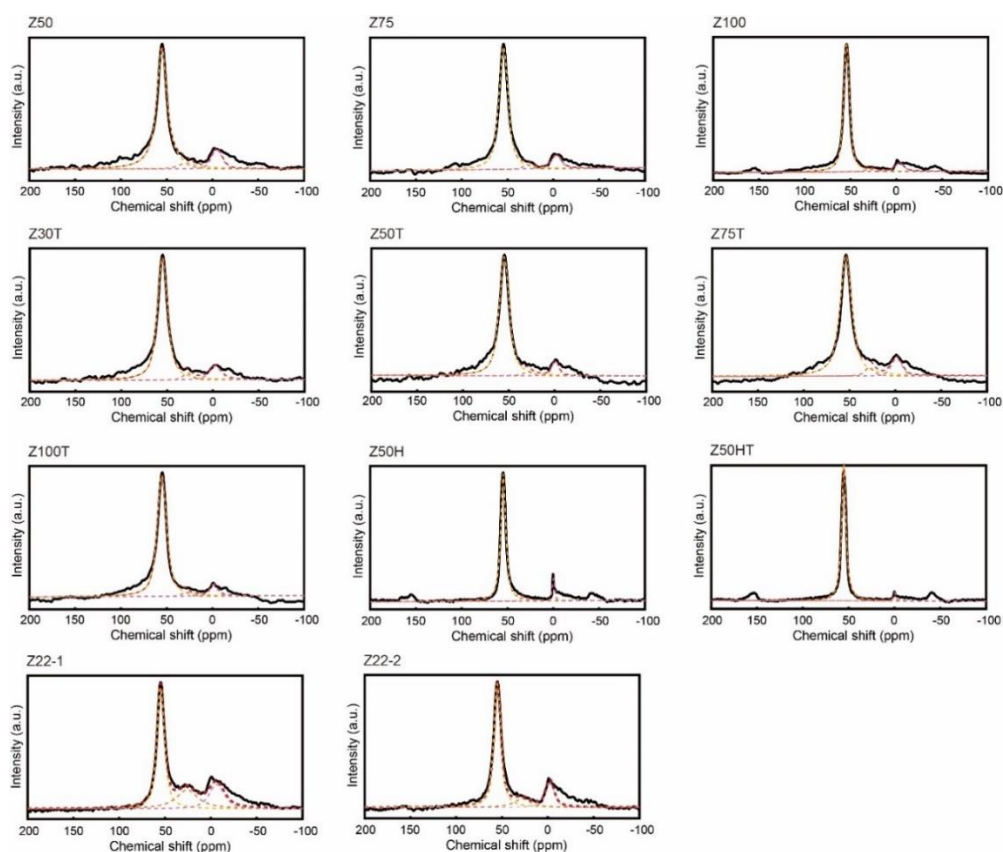


**Figure D4.** Deconvolution curve fittings of the  $^{27}\text{Al}$  MAS NMR spectra of H-Z50, H-Z75, H-Z100, H-30T, H-50T, H-75T, H-100T, H-50H, H-50HT, Z22-1, and Z22-2. Each sample is labeled above the respective NMR data.